Epitaxy of Hybrid Nanowires, Shadow Junctions and Networks

Sabbir A. Khan

University of Copenhagen
Microsoft Quantum Materials Lab

30th November 2020
Copenhagen, Denmark

Microsoft

UNIVERSITY OF COPENHAGEN

Ph.D. Thesis

Epitaxy of Hybrid Nanowires, Shadow Junctions and Networks

Sabbir A. Khan

Center for Quantum Devices
Niels Bohr Institute
University of Copenhagen
Microsoft Quantum Materials Lab Copenhagen,
2800 Lyngby, Denmark

Academic advisor: Prof. Peter Krogstrup
Assessment committee: Assoc. Prof. Kasper Grove-Rasmussen
Prof. Thomas Schäpers
Dr. Moïra Hocevar

November, 2020
This thesis has been submitted to the
Ph.D. School of the Faculty of Science,
University of Copenhagen

Publisher
First submitted in November, 2020 to
Niels Bohr Institute,
University of Copenhagen
Updated version: April, 2021

Abstract

This thesis explores the growth of hybrid semiconductor-superconductor nanowire (NW), which is considered as a potential material platform to host topologically protected Majorana fermions. Considering the requirements of strong spin-orbit interaction and large Landé-g factor, first, InAs and InSb semiconductor NWs are investigated using molecular beam epitaxy. Au catalyst assisted InAs NWs are directly grown from the InAs substrate, whereas InSb NWs are grown with a stem. Post growth structural analysis exhibits a wurtzite structure for InAs NWs and a pure zinc-blende structure for InSb NWs. Hybridization of these NWs are performed with Al and Sn superconducting films. To confirm the high interface quality, thin film deposition is executed *in situ*, right after the NW growth. With optimized growth conditions, uniform Al film is exhibited on both InAs and InSb NWs. Furthermore, a homogeneous Sn film is achieved on InSb NWs. However, under the same growth conditions, Sn film remains dewetted islands on InAs NWs due to the high interface energy density. Besides, structural analysis of Sn film displays $\alpha - \mathbf{Sn}$ phase domination in the presented growth conditions. On the other hand, the electrical measurements of the Sn film manifest superconducting transitions around 3.9K or higher. It is presumed that the superconducting $\beta - \mathbf{Sn}$ phases proximitized the neighboring $\alpha - \mathbf{Sn}$ phases during the measurements.

Epitaxially grown superconductors with *in situ* shadowed junctions on InAs, InSb and $InAs_{1-x}Sb_x$ NWs are shown next. The junction formation on the NW is studied as a function of interwire distances. It is found that, the morphology of the junction is directly dependent on the flux distribution, shadow geometry and material kinetics of the deposited film. With three deposited metal films (Al, Sn and Pb) on the NWs, the kinetic effect on the junction edge sharpness is investigated. Furthermore, the correlation between junction morphology and their electrical performance is examined. It is shown that the sharp-edge junctions exhibit high transparency with quantized conductance for all three NWs. In addition, a statistical comparison of shadowed and etched junction devices is presented, where the shadowed ones reveal better electrical performance.

In the last stage, the growth of quantum nanowire networks is presented with InAs, InSb, and $InAs_{1-x}Sb_x$ NWs. The emergence of a network is highly dependent on the Au catalyst position. With optimal growth conditions, the formation of InSb and $InAs_{1-x}Sb_x$ nanocrosses are shown. The growth dynamics of the nanocrosses are explained as a function of time-dependent axial and radial growth. Structural analysis of the nanocross demonstrates the single-crystalline zinc blende phase. By tuning the catalyst position, growth of InSb nanoplate and nanobridge structures are also shown, where the merging position plays a crucial role. In contrast to the Sb-based networks, reduced radial growth is observed in InAs networks. Thus, the final structure is driven by the axial growth. Varying

the distance of the Au positions, V-shaped, T-shaped and y-shaped junctions are created with InAs NWs. Unlike Sb-based networks, structural analysis of the InAs networks demonstrates a crystal phase change in the merging point. Finally, an *in situ* shadowing process for patterning nanocrosses is developed, exhibiting a material platform for NW based multi-terminal Josephson junction.

Sammenfatning

Denne afhandling undersøger væksten af hybrid halvleder-superleder nanowires (NWs), der betragtes som en potentiel materialeplatform til at være vært for topologisk beskyttede Majorana fermioner. I betragtning af kravene til stærk spin-orbit-interaktion og stor Landé-g-faktor undersøges først InAs og InSb halvleder-NWs ved hjælp af molekylær stråleepitaksi. Au-katalysator-assisterede InAs NWs dyrkes direkte fra InAs-substratet, mens InSb NWs dyrkes med en stamme. Strukturanalyse efter vækst viser en wurtzitestruktur for InAs NWs og en ren zinkblende struktur for InSb NWs. Hybridisering af disse NWs udføres med Al- og Sn-superledende film. For at bekræfte den høje interface-kvalitet udføres tyndfilmaflejring *in situ* lige efter NW-væksten. Med optimerede vækstbetingelser vises ensartet Al-film på både InAs og InSb NWs. Desuden opnås en homogen Sn-film på InSb NWs. Imidlertid forbliver Sn-film under de samme vækstbetingelser som fugtede øer på InAs NW'er på grund af den høje energitæthed for overfladerne. Desuden viser strukturanalyse af Sn-film $\alpha - \mathbf{Sn}$ fasedominering for de præsenterede vækstbetingelser. På den anden side viser elektriske målinger af Sn-filmen superledende overgange omkring 3.9K eller højere. Det formodes, at de superledende $\beta - \mathbf{Sn}$ faser proximiterede de tilstødende $\alpha - \mathbf{Sn}$ faser under målingerne.

Epitaksialt dyrkede superledere med *in situ* skyggede kryds på InAs, InSb og $InAs_{1-x}Sb_x$ NW vises derefter. Krydsdannelsen på NW studeres som en funktion af interwire-afstande. Det viser sig, at krydsets morfologi er direkte afhængig af fluxfordeling, skyggegeometri og materialekinetik af den deponerede film. Med tre aflejrede metalfilm (Al, Sn og Pb) på NWs undersøges den kinetiske effekt på krydskantens skarphed. Desuden undersøges sammenhængen mellem krydsmorfologi og elektriske egenskaber. Det er vist, at de skarpe kryds udviser høj gennemsigtighed med kvantiseret ledningsevne for alle tre NWs. Derudover præsenteres en statistisk sammenligning mellem skyggede og ætsede forbindelsesenheder, hvor de skyggede udviser bedre elektrisk ydelse.

I den sidste del præsenteres væksten af quantum nanowire-netværk med InAs, InSb og $InAs_{1-x}Sb_x$ NWs. Fremkomsten af et netværk er meget afhængig af Au-katalysator positionen. Med optimale vækstbetingelser vises dannelsen af InSb og $InAs_{1-x}Sb_x$ nanokryds. Vækstdynamikken i nanokrydsene forklares som en funktion af tidsafhængig aksial og radial vækst. Strukturel analyse af disse nanokryds demonstrerer den enkeltkrystallinske zinkblende-fase. Ved indstilling af katalysatorpositionen vises vækst af InSb nanoplade- og nanobro-strukturer, hvor den fusionerende position spiller en afgørende rolle. I modsætning til de Sb-baserede netværk observeres reduceret radial vækst i InAs-netværk. Således drives den endelige struktur af den aksiale vækst. Ved variation i afstanden fra Au-positionerne oprettes V-formede, T-formede og Y-formede kryds med InAs NWs. I modsætning til Sb-baserede netværk viser strukturanalyse af InAs-netværkerne en

krystalfaseændring i fusioneringspunktet. Endelig udvikles en *in situ* skyggeproces til mønstring af nanokryds, der udgør en materiel platform til NW-baseret multi-terminal Josephson-kryds.

Acknowledgement

First, I would like to thank Peter for the opportunity. It was a real pleasure to work with you. You have provided the freedom to explore and plan my experiments. At the same time, guided me in the proper direction whenever needed.

I would like to thank the thesis committee Kasper Grove-Rasmussen, Thomas Schäpers and Moïra Hocevar for your time and evaluating this thesis.

Big thanks to Thomas Sand Jespersen and his group (Lukas, Damon, Dags) for the collaboration and all the interesting measurements. Especially, I would like to mention Lukas Stampfer for utilizing the materials properly. I am grateful to Jordi Arbiol and his group for all the TEM analysis, without that growth progress would have been difficult. Particularly, Sara Marti-Sanchez, you were always helpful and enthusiastic about imaging new samples. Many thanks to Anna Fontcuberta i Morral for inviting me at LMSC, EPFL. It was fun to work in your lab. I can easily say it was one of the best time in my Ph.D. period. Nick and Wonjong, you both are amazing, thank you for all the help and fun times! I am grateful to Philippe Caroff and Leo Kouwenhoven for the warm welcome during my visit to TU Delft. At the beginning of my Ph.D., it was an effective training session on MBE with you, Philippe. Besides, at the conferences, you always introduced me to other researchers and advised with your experiences. Sadly, we couldn't attend MRS 2020, but let's hope for the next year again! I am extremely grateful to Michael Manfra for the invitation to visit Purdue University, which was also part of my research secondment. It is so kind of you that you provided time from your busy schedule and showed me the lab. Great thanks to Maja Cassidy and Sebastian Pauka, for all the measurements on InSb and InAs NWs.

To all the members of the Microsoft Quantum Materials team, I am extremely grateful for your support and help. Keita, you are like a mentor to me. Your ideas and suggestions were always valuable. Tomas, It was always nice talking with you and getting ideas on different topics. You can explain things very easily. Ajuan, thanks for all the great measurements. Jordan, thanks for the nice TEMs on networks. Martin, thanks for training me on the TEM and all the fun time at our old office. I really miss that. Sergej, I really appreciate our long discussions on different topics during the conference days and while traveling to different places. Mohana, you have always been a good friend, and thanks for training me in the new MBE. Besides, thank to: Jeanette, Signe, Daria, Gunjan, Steffen, Somya, Nikhil, Tue, Anna, David, Tobi, Rajib, Dmitrii, Yan, Khoa and Morten. I must mention our old group members: Filip, Joachim and Rawa, thank you for all the help and guidelines initially. Especial mention to my partners in the lab, Yu and Harry. Thanks, Yu for the great coordination in MBE, you were always there when needed. Thanks,

Harry for being such a good friend both at work and outside. We always had great time together. Gratitude to all Qdev members for creating a nice working environment. I must thank the great admin team from Qdev: Dorthe, Maria, Marianne. You took care of all my administrative issues regarding Marie Curie project, that made my Ph.D. life much easier. My utmost appreciation to Claus for teaching me how to operate MBE and answering all the questions that I had. I can't even think of my Ph.D. project without you. Thank you Shiv, for helping with the fab related issues. I am grateful to Tobi, Steffen, Daria, Jordan, Juan Carlos, Raktim and most importantly Audhuna for proof-reading this thesis.

I am particularly grateful to the Marie Curie INDEED network to fund my Ph.D. project. Special thank goes to Dagou for leading the project nicely and the warm welcome during our Durham visit. I really enjoyed talking with you at the INDEED events. I acknowledge all the project leaders and their effective guidance. Huge thanks to Natalia for arranging all the events and providing reminders about the next steps. Also for taking care of all our EU reports. I made wonderful friends in the INDEED events and always waited for the next event. It's sad that the project time is over and we are not going to meet on a regular basis. My thesis will be incomplete without mentioning you all: Alex, Nuño, Aswathi, Timur, Wonjong, Vasilii, Anton, Nemanja, Egor, Ridvan, Pablo, Manuel and Michal.

In the end, Mom and Audhuna, it is difficult where to start. I do not think I could come to this point without both of you. Just want to say, I am grateful for everything.

Sabbir A. Khan

List of Publications

1. **Sabbir A. Khan**, Charalampos Lampadaris, Ajuan Cui, Lukas Stampfer, Yu Liu, Sebastian J Pauka, Martin E Cachaza, Elisabetta Maria Fiordaliso, Jung-Hyun Kang, Svetlana Korneychuk, Timo Mutas, Joachim E Sestoft, Filip Krizek, Rawa Tanta, Maja C Cassidy, Thomas Sand Jespersen, Peter Krogstrup, *Highly Transparent Gatable Superconducting Shadow Junctions*, ACS Nano, 14, 11, 14605–14615, 2020.

2. **Sabbir A. Khan***, Lukas Stamfer*, Timo Mutas, Jung-Hyun Kang, Peter Krogstrup, Thomas S. Jespersen, *Multiterminal Quantized Conductance in InSb Nanocrosses*, Advanced Materials (Accepted).

3. **Sabbir A. Khan**, Charalampos Lampadaris, Sara Martí-Sánchez, Yu Liu, Maria Chiara Spadaro, Dags Olsteins, Damon Carrad, Jordi Arbiol, Thomas Sand Jespersen, Peter Krogstrup, *Epitaxy of Sn on Semiconductor Nanowires*, (In Preparation).

4. Ajuan Cui, **Sabbir A. Khan**, Keita Otani, Mohana Rajpalke, Charalampos Lampadaris, Jung-Hyun Kang, Rajib Batabyal, Roman Lutchyn, Peter Krogstrup, *Field Effect Extraction of Electronic Properties from Hybrid Epitaxial Semiconductor-Metal Nanowires*, (In Preparation).

5. Yu Liu, Saulius Vaitiekenas, Sara Marti-Sanchez, Christian Koch, Sean Hart, Zheng Cui, Thomas Kanne, **Sabbir A. Khan**, Rawa Tanta, Shivendra Upadhyay, Martin Espineira Cachaza, Charles M Marcus, Jordi Arbiol, Kathryn A Moler, Peter Krogstrup, *Semiconductor-Ferromagnetic Insulator-Superconductor Nanowires: Stray Field and Exchange Field*, Nano Letters, 20 (1),pp. 456-462, 2019.

6. Yu Liu, Alessandra Luchini, Sara Martí-Sánchez, Christian Koch, Sergej Schuwalow, **Sabbir A. Khan**, Tomaš Stankevič, Sonia Francoua, Jose RL Mardegan, Jonas A Krieger, Vladimir N Strocov, Jochen Stahn, Carlos AF Vaz, Mahesh Ramakrishnan, Urs Staub, Kim Lefmann, Gabriel Aeppli, Jordi Arbiol, Peter Krogstrup, *Coherent Epitaxial Semiconductor-Ferromagnetic Insulator InAs/EuS Interfaces: Band Alignment and Magnetic Structure*, ACS Applied Materials and Interfaces, 12, 7, 8780–8787, 2020.

7. Filip Krizek, Joachim E. Sestoft, Pavel Aseev, Sara Marti-Sanchez, Saulius Vaitiekenas, Lucas Casparis, **Sabbir A. Khan**, Yu Liu, Tomas Stankevic, Alexander Whiticar, Alexandra Fursina, Frenk Boekhout, Rene Koops, Emanuele Uccelli, Leo P. Kouwenhoven, Charles M. Marcus, Jordi Arbiol and Peter Krogstrup, *Field Effect Enhancement in Buffered Quantum Nanowire Networks*, Physical Review Materials 2, 093401, 2018.

8. Lukas Stamfer, Damon Carrad, Dags Olsteins, Timo Mutas, **Sabbir A. Khan**, Peter Krogstrup, Thomas S. Jespersen, *Multiterminal Josephson Effect in InAsSb Nanocrosses*, (In Preparation).

9. Lukas Stamfer, Damon Carrad, Dags Olsteins, **Sabbir A. Khan**, Peter Krogstrup, Thomas S. Jespersen, *Little Parks Effect in Half-shell Al/InAsSb Nanowires*, (In Preparation).

10. Lukas Stamfer, Damon Carrad, Dags Olsteins, **Sabbir A. Khan**, Peter Krogstrup, Thomas S. Jespersen, *Photon Assisted Tunneling of High Order Multiple Andreev Refections in Epitaxial Nanowire Josephson Junctions*, (In Preparation).

Contents

Abstract iv

Sammenfatning vi

Acknowledgement viii

List of Publications x

Contents xii

1 Introduction 1
- 1.1 Semiconductor Nanowires . . . 1
  - Growth Overview . . . 1
  - Applications in Different Fields . . . 1
- 1.2 Majorana Fermions in Semiconductor Nanowires . . . 2
  - Majorana in Condensed Matter . . . 2
  - Majorana Ingredients in Nanowire . . . 3
- 1.3 Thesis Outline . . . 6

2 Epitaxy of Hybrid Nanowires 7
- 2.1 Introduction . . . 7
- 2.2 Molecular Beam Epitaxy . . . 8
- 2.3 Vapor-liquid-solid Mechanism . . . 10
- 2.4 VLS Grown InAs Nanowire . . . 14
- 2.5 VLS Grown InSb Nanowire . . . 16
  - Why Interest on InSb Nanowires? . . . 16
  - Stem Assisted Growth . . . 17
  - Diameter Increment . . . 18
  - Interface Analysis . . . 20
  - Defect-free Zinc Blende Structure of InSb NW . . . 20
- 2.6 Thin Film Epitaxy on Semiconductor Nanowire . . . 22
  - Nucleation Stage (Adatom Diffusion and Temperature Effect) . . . 24
  - Islands Growth (Surface Driven Growth) and Coalescence . . . 26
  - Reconstruction and Grain Boundary . . . 27
- 2.7 Al Growth on Nanowire . . . 29
  - Al Thin Film on InAs NWs . . . 29
  - Al Thin Film on InSb NWs . . . 31
- 2.8 Sn Growth on Nanowire . . . 32
  - Thin Film Formation . . . 33
  - Structural Analysis . . . 35
  - Migration of Sn into the InSb Core . . . 38
  - Superconducting Transition . . . 40
- 2.9 Conclusion . . . 41
- 2.10 Experimental Details . . . 42
  - Substrate Preparation . . . 42
  - Nanowire Growth . . . 43
  - Thin Film Deposition . . . 43
  - Characterization . . . 44

3 Shadowed Nanowire Junctions **47**
3.1 Introduction . . . 47
3.2 Epitaxy of SE-SU Shadow Junctions . . . 48
NW Growth Optimization . . . 48
SU Deposition and Shadow Schemes . . . 50
3.3 Comparison of Shadowed and Etched Junctions . . . 54
3.4 Evaluation of Sharp-edge Shadowing . . . 56
3.5 Junctions Transparency . . . 60
Quantized Conductance . . . 60
Low Temperature Measurements . . . 62
3.6 Conclusion . . . 66
3.7 Experimental Details . . . 66
Substrate Fabrication . . . 66
Hybrid NWs Synthesis in the Trenches. . . . 67
Structural Characterization . . . 68
NW Device Fabrication . . . 68
NW Device Measurements . . . 69
Resistance Calculation and Mobility Fit . . . 70

4 Semiconductor Nanowire Networks **71**
4.1 Introduction . . . 71
4.2 VLS and SAG Networks . . . 71
4.3 InSb Nanocrosses . . . 72
Substrate Preparation . . . 72
Growth of InSb Nanocrosses . . . 73
Structural Analysis of InSb Nanocrosses . . . 78
4.4 InSb Nanoplate and Other Nanostructures . . . 80
"Type-I" merging: Nanoplate with Elongated Arm . . . 81
"Type-II" merging: Nanoplate without Arm . . . 83
"Type-III" merging: Nanobridge . . . 85
4.5 InAs Nanowire Networks . . . 86
Networks from Two Trenches . . . 86
Networks from Single Trench . . . 88
Long Distance Networks . . . 89
4.6 InAsSb Nanocrosses . . . 91
4.7 Shadowing VLS Nanocrosses . . . 92
Substrate Preparation . . . 92
Nanocrosses Growth and Shadowing . . . 94
4.8 Conclusion . . . 95

5 Conclusion and Outlook **97**

Bibliography **101**

List of Figures

1.1 **Energy spectrum and topological phase transition of hybrid nanowire. a**, Schematic of the semiconductor-superconductor hybrid NW. Here the NW is positioned in the x-direction. The spin-orbit interaction is along the z-direction and the magnetic field is applied in x-direction perpendicular to the spin-orbit interaction. **b**, The dispersion relation of energy as a function of momentum in a one-dimensional system, which is a simple parabola. **c**, The second term of the Hamiltonian, where spin-orbit interaction is introduced to the system. It splits the band depending on the spin-polarization with a spacing $k_{SO} = m\alpha$ in the K-axis and also moves the energy level down to $E_{SO} = \frac{m \cdot \alpha^2}{2m}$, as indicated in the image. **d**, Magnetic field B is introduced to the system, which opened a Zeeman energy gap, E_Z at K=0, indicated in the image. The spin-polarization direction will be determined by the momentum [40]. **e**, Superconductivity is induced in the system, as a result, a superconducting gap is opened between the bands. Here Zeeman energy is smaller than the gap size, hence the system is in the trivial superconducting phase. **f**, The magnetic field further increased resulting in the increased Zeeman energy. The transition point when, $E_Z = \Delta$, the superconducting gap closes. The closed spectrum in particle-hole band is linear forming a Dirac cone, which leads to the Berry-phase cancellation [42, 43]. **g**, If the magnetic field is high enough to reach $E_Z > \Delta$, the gap reopens and the phase transition from trivial to topological superconductivity happens. Here the gap size, $E_G = 2(E_Z - \Delta)$ [45]. Although it's difficult to visualize, the re-opened gap is actually an inversed gap (negative gap). The idea of the schematic is adapted from Ref. [40, 45] 5

2.1 **Molecular beam epitaxy. a**, MBE system with *in vacuo* connected electron beam physical vapor deposition (EBPVD) system situated at Niels Bohr Institute. Two systems are connected with a long buffer tunnel as indicated with a white arrow. Load lock is connected at the end of the buffer tunnel. **b**, MBE growth chamber at one end of buffer tunnel, where, as source materials: In, Ga, As, Sb, Au, Al, Bi, and Si are loaded in the effusion cells. **c**, Schematic of the MBE growth chamber presented in (b). **d**, EBPVD growth chamber connected at the other end of the buffer tunnel. Here, all the superconducting and ferromagnetic materials are loaded. After growth, the NW sample is transferred in this chamber and cooled down with liquid nitrogen before depositing metals, which will be discussed later. **e**, Inside of the buffer tunnel, where the transfer rods are connected to load/unload or shuffling the samples. **f**, Load lock inside, where samples are loaded and degassed before transferring to the buffer tunnel. Load lock and buffer tunnel are separated with a gate-valve. The sample is only transferred when a high vacuum is achieved. There is a mass-spectrometry connected to the load lock to analyze the chemical components of the substrate before transferring to the buffer tunnel. **g**, Crucible with a source material inside the PVD chamber. The material is heated with a guided electron gun. 9

2.2 **Layer-by-layer VLS NW growth. a**, Supersaturation of the catalyst particle (assume Au) with precursors. **b**, Nucleation started from the supersaturated catalyst, resulting in a 2D layer growth through the liquid-solid transition. It continues within the diameter of the Au catalyst. **c**, The first layer completed. Simultaneously restoration of supersaturation begins with continuous precursor supply, that leads to a new nucleation as indicated. **d**, New layer completed and new nucleation begins. Repetition of this process continues making layer-by-layer NW growth. The idea of the schematic is adapted from Ref. [85] 11
2.3 **Kinetic pathway during nanowire growth.** Schematic of the NW with different kinetic process associated with it. (i)-(viii) discuss different phases of transitions. The circular dots shows area of the adatom collection for the NW. λ is the adatom diffusion length. The idea of the schematic is refereed to [4]. 13
2.4 **Au assisted InAs nanowire growth. a**, Schematic of the InAs NW growth steps. The growth is divided into four sections. (i) Annealing of InAs growth substrate with As over-pressure. Later, *in situ* Au is deposited. With the mounted temperature the Au forms liquid on the substrate. (ii) Supersaturation of Au with the presence of In+As and the precipitation begins. (iii) Layer-by-layer growth of NW with continuous feeding of In and As (iv) Growth completes and the substrate is cooled down. Corresponding substrate temperatures are provided. **b**, Tilted scanning electron microscopy (SEM) image of *in situ* Au assisted InAs NW. Catalyst position is indicated at the top. **c**, High resolution transmission electron microscopy (TEM) of representative InAs NW structure. The TEM image is taken from a different batch. Defect-free InAs wurtzite NW structure can be observed. Corresponding FFT is presented at the bottom. . . 15
2.5 **Contact angle evolution with presence of Sb. a**, Contact angle of Au-III liquid alloy without Sb in the chamber. Here, the contact angle is bigger than 90° and the axial NW growth is possible with presence of As or P in the chamber. **b**, Au alloy is wetting due to the presence of surfactant Sb. Here, the contact angle is smaller than 90° and in-plane random directional growth may happen instead of axial NW growth. Sb chain sticks on the corresponding surface and alters the surface energy. Hence, VLS axial growth is not possible directly from the substrate. **c**, With presence of As, an InAs stem is grown and later, Sb can be introduced in the chamber. The Au alloy is restricted to wet within the finite {111} facet on InAs stem. Hence, in this case the contact angle is bigger than 90° and InSb NW growth is possible. 17

2.6 **Top to bottom structural investigation of thick InSb NWs. a**, TEM image of InAs to InSb transition segment. Magnified InAs segment shows defect free WZ crystal. **b**, InAs to InSb transition from another NW. Magnified transition section demonstrates a line of stacking-fault induced while growing from InAs to InSb. **c**, TEM image of InSb body where the crystal phase is complete ZB. Zoomed in TEM image in green segment shows ZB crystal. **d**, TEM image of the InSb body of another NW and zoomed in edge also demonstrate pure single crystalline ZB quality. **e**, TEM image of half of Au catalyst, which is a round shape. **f**, TEM image of other half of Au catalyst, which is faceted. This can be attributed to the cooling effect. During the cooling process Au droplet solidifies and forms the faceted shape. In both cases, ZB crystal is found beneath the Au catalyst. **g**, TEM image of the Au catalyst and solidified InSb segment beneath. Magnified TEM section demonstrates stacking fault line right beneath the Au catalyst. We also attribute this stacking fault to the cooling effect after the growth. Scale bars in the images are 10 nm and scale bars in the magnified sections are 5 nm. (TEM presented here is performed by Jung-Hyun Kang at DTU CEN) 19

2.7 **Structural analysis of thin InSb NWs. a** and **b**, Tilted SEM image of thin b-polar InSb NWs (diameter ~ 100nm) grown from InAs (111) substrate. The length of the NWs are around 2-2.5 μm. Scale bars are 100 nm. **c**, Representative TEM image of the InAs-InSb interface. **d**, Magnified section demonstrates two twin boundaries (shown with arrows) in the InAsSb transition section before reaching the full diameter of the InSb segment. This is the only defect observed in the analyzed structure. **e**, Magnified HR-TEM shows pure ZB structure in the InSb segment. **f**, TEM Analysis of the Au catalyst and Au-InSb interface. As shown in the previous case, Au solidified at room temperature resulting a faceted structure. **g**, Magnified HR-TEM shows the interface between Au-InSb demonstrating defect-free ZB alloy in Au and pure ZB InSb structure. **h**, Further analysis with high magnification micrograph of the Au section shows the $AuIn_2$ FM3-M cubic crystal phase, oriented through its [1-10] zone axis, confirming high concentration of In in the catalyst. 21

2.8 **Thin film growth on semiconductor.** Thin metal film growth on semiconductor surface as a function of time and temperature. (**a**-**e**), stage by stage metal film growth at low temperature (T). At low T, adatom diffusion length (λ_a) is small, leading to close proximity islands that merge and create surface driven thin film. (**f**-**j**), Metal film evolution at high T. Here, λ_a is big, resulting in largely spaced islands. Continuous film may create in long growth run. The idea of the schematic is adapted from Ref. [52, 160] 23

2.9 **Thin Al epitaxy on InAs NWs. a**, 30° tilted SEM image of InAs/Al NW. White arrow shows the Al deposition angle. The schematic shows the cross section of hexagonal NW with two-facets Al. Yellow arrow shows the viewing angle in the TEM inspection. Inset SEM image shows the well-defined facets of the wire with the Al deposition shadow on the substrate. **b**, Low magnified TEM image of the NW segment showing no crystal defects in the InAs and also an uniform Al thin film deposited along the NW. White arrow shows the growth direction of the NW. **c**, High resolution TEM image from highlighted area, which shows sharp interface between InAs and Al. (111) out-of-plane orientation Al film is grown on InAs $\{1\bar{1}00\}$ facets. Scale bars for (a), (b) and (c) are respectively 100 nm, 50 nm and 5 nm. (TEM presented here is performed by Martin Espineira Cachaza at DTU CEN) 30

2.10 **Thin Al epitaxy on InSb NWs. a**, 30° tilted SEM image of InSb/Al NW. The white arrow shows the Al deposition angle. The schematic of hexagonal cross-section shows two-facets Al deposition that we intended in this experiment. The yellow arrow shows the viewing angle in the TEM inspection. **b**, High resolution TEM image of InSb and Al section. The arrow shows (111) growth direction. **c**, High resolution TEM image of the magnified section from panel (b). A clear and abrupt interface between InSb and Al is observed. InSb is ZB structure and Al is cubic structure. The arrow on InSb shows the <110> facets direction. 17 (111) Al planes are counted from the image referring to ~ 3.5 nm thickness. Scale-bar for panel (a) is 100 nm and panel (b) and (c) are 2 nm. (TEM presented here is performed by Emrah Yucelen at Microsoft Quantum Lab, Delft.) 31

2.11 **Evolution of Sn thin film on nanowire. a-c**, shows progression of Sn film as a function of substrate temperatures. Substrate temperatures are varied from -50° C to -150°C. A constant Sn flux rate of ~ 5 Å/s is maintained for all the samples. NWs are grown around the diameter of ~ 120 nm and hybridized with 20 nm thin Sn for all the samples. For the InSb/Sn segments, the morphology of the Sn enhances with lower temperature. On the other hand, Sn on InAs sections remain discrete even with the lowest temperature. Scale bars for all the sections are 100 nm. 34

2.12 **Sn epitaxy on InSb NWs. a**, Tilted scanning electron micrograph (SEM) of InSb NW hybridized with Sn thin film. A uniform layer of Sn segment can be distinguished. **b**, InAs-InSb interface, where no Sn film is observed in the initial curvature region of InSb. **c**, Transmission electron microscopy (TEM) of a section from InSb/Sn NW. The black dotted line indicates the interface between two segments. **d**, Magnified high-resolution TEM from highlighted section of panel (c). Epitaxial Sn segment on InSb with interface line can be seen. No crystal defects in both sides are found. **e**, Further, magnification in the interface area implies cubic phase crystal both in InSb and Sn section. InSb segment demonstrates cubic ZB crystal phase, which we have discussed in section 2.5 of this chapter. On the other hand, $\alpha - \mathbf{Sn}$ demonstrates cubic crystal. Hence the epitaxial section is contribution from ZB InSb and $\alpha - \mathbf{Sn}$. **f**, Crystal structure of InSb and both $\alpha - \mathbf{Sn}$ and $\beta - \mathbf{Sn}$ with their corresponding lattice constant. **g**, HR-TEM from other section of the film showing multiple defects on the Sn crystal. White dashed lines show of twinning in the {111} plane oblique to the growth direction (white arrow) for low temperature film. Magnified section in the right shows clear picture of the twining event. The highlighted section shows (-1-11) twin overlaps. **h**, Sn film in high temperature, multiple planar defects in random orientation, unlike low temperature film. Arrow shows the growth direction and dashed lines show the defect orientations. Diffraction pattern in the right from non-defective highlighted segment shows [110] plane $\alpha - \mathbf{Sn}$ Sn. Scale bars for (**a**), and (**c**) are 100 nm. Scale bar for (**b**) is 20 nm. . . 36

2.13 **Sn growth on InAs NW. a**, Tilted SEM image of the InAs/Sn segment (stem), where Sn seems to discrete faceted islands. Scale bar is 100 nm. **b**, Low magnification TEM of a InAs/Sn section. Magnified high resolution TEM in the right shows defect-free single crystalline quality of Sn grain on InAs. However, due to the high difference symmetry, no epitaxy is observed in the interface and Sn seems to be out of axis. **c**, Diffraction patterns confirms (orange circles) out-of-plane Sn direction in {002} Sn planes. 37

2.14 **Diffusion of Sn during post-growth processing. a**, High resolution TEM image of cross-sectional InSb/Sn structure. InSb/Sn is protected with AlO_x and Pt-C layer during TEM lamella preparation. **b**, Magnified structural analysis of InSb/Sn section, where defect-free ZB crystal is observed and presented in the inset. **c**, Elemental analysis with electron energy loss spectroscopy (EELS), where InSb section covers the whole hexagonal structure. **d**, EELS at the edge of the NW shows oxide layer and deposited Pt protection layer in purple color. In the bottom, SiO_x substrate, where NWs are transferred using a micromanipulator. **e**, Elemental analysis of the Sn on the NW facets. Sn presence can be identified on the bottom two facets. Unexpected spreading of the Sn signal is observed. **f**, A combined signal of InSb and Sn, where Sn diffusion from facets to the NW core is clearly observed. Sn thickness on the facets is almost reduced to half, and the rest is alloyed with InSb. 39
2.15 **Superconducting transition on InSb/Sn devices. a**, SEM image of the fabricated four-terminal device with InSb/Sn NW. **b**, The critical temperatures and magnetic field for four measured devices, where Dev#1-2 consist nominal 20 nm Sn shell and Dev#3-4 consists 15 nm Sn shell. (Device fabrication and measurements are done by Charalampos Lampadaris.) 40

3.1 **Fabricated substrate.** SEM image of wet-etched (111)B faceted trenches with deposited Au disks (scale bar is 1 μm). 48
3.2 **InAs nanowire growth on the trenches. a**, Scanning electron micrograph (SEM, 30° tilted) of Au-assisted InAs NW array grown on the preprocessed "V" groove (111)B faceted InAs trenches. Scale bar is 1 μm. **b**, V/III ratio as a function of InAs NW growth temperature (T_G). The plot is divided into six regions (A-F), and NW growth outcome (yield, morphology, etc.) of each region is investigated. Region "D" ($T_G \sim$ 401-415°C with V/III ratio ~ 9-10.5) shows the highest yield and uniform InAs NW growth (dark green circles). 48
3.3 **InAs NW growth optimization.** SEM micrographs of the InAs NWs growth on the trenches in different growth conditions. Region **D** demonstrates the highest yield (> 90%) with uniform NWs growth. Scale bars are 1 μm. 49
3.4 **High-quality InAs nanowire.** High-resolution TEM of the InAs NW demonstrating stacking fault-free WZ structure. Inset shows the FFT of corresponding structure. 50
3.5 **InSb NWs from trenches.** Tilted SEM image of InSb NWs grown with InAs stems. Scale bar is 1 μm. 50
3.6 **Nanowires growth on the (111)B trenches. a**, Schematic with crystal orientation of the hybrid NWs. Dashed arrow shows the superconductor deposition direction. In the right, schematic of superconductor deposition geometry on the NW with respect to the beam flux direction and the NW growth axis. Here, α is the angle between these two vectors to calculate effective flux (f') on the NW facet. **b**, Schematic of 3-facets and 2-facets superconductor on the NWs. The table provides the beam angle requirements in the case when ϕ=0, for 2-facets and 3-facets superconductor coverage. 51
3.7 **InSb NWs with different SU. a**, Tilted SEM image of InSb NWs with epitaxially grown Al. **b**, SEM image of InSb/Sn NWs with junctions. **c**, SEM image of InSb/Pb NW with junction. Orange arrows indicate the shadowed junctions. Dashed arrows indicate the direction of superconductor deposition. Scale bars for (a), (b) and (c) are 1 μm. Scale bar for (a) inset is 100 nm. 51

3.8 **Shadow schemes.** SEM micrographs and schematic of different shadow junction schemes grown on the trenches. SU deposition directions are shown with arrows. 52
3.9 **Al epitaxy on InAsSb NWs.** SEM (30° tilted) of $InAs_{0.3}Sb_{0.7}$/Al NW array (scale bar is 1μm). The highlighted section shows double shadowed junctions on the NWs (scale bar is 500 nm). 52
3.10 **$InAs_{0.3}Sb_{0.7}$ NWs with different superconductors. a**, SEM micrograph of $InAs_{1-x}Sb_x$/Al NW junction. Scale bar is 100 nm. Blue arrow to right is the HAADF-STEM tomography of the NW demonstrating junction morphology. **b**, STEM-EDX of the junction shows In, As, Sb and Al composition. As shown in the bottom, the grown $InAs_{1-x}Sb_x$ NWs consist 30% of As and 70% Sb and the composition remain homogeneous along the individual NW. **c**, $InAs_{0.3}Sb_{0.7}$ NWs with Sn. **d**, $InAs_{0.3}Sb_{0.7}$ NWs with Pb. Scale bars for (**c**) and (**d**) are 1 μm. Insets scale bars are 100 nm. All the white arrows in the SEM images show directions of superconductor deposition. 53
3.11 **Gate response statistics of shadowed and etched junctions.** Pinch-off statistics of the back-gated devices with shadowed (green) and etched (blue) junctions. 54
3.12 **Shadowed and etched single NW. a**, Schematic of the test device with comparable size shadowed and etched junctions in a single NW. **b**, Electrical measurements of the test device where conductance is shown as a function of gate voltage for shadowed (green) and etched (blue) junctions. The shadowed junction shows quantized plateaus as highlighted with inset. Applied magnetic field, **B**=6 T in both cases. SEM image of the exact NW is shown inset with a scale bar of 100 nm. 54
3.13 **Additional low temperature electrical measurements of shadow and etched junctions in single NW. a**, SEM image of NW devices with shadowed and etched junctions in individual wires. Blue colour stands for the etched junctions and green for the shadowed. Measurements are taken in a dilution refrigerator at 20 mK. **b**, The etched junction is not pinched-off and shadowed junction is pinched-off. **c**, Both junctions are pinched-off, whereas the shadowed device shows quantized conductance (inset) for high field (6 T). **d**, The results of the etched junctions obtained from the PPMS at 2 K. None of the junctions are pinched-off within the voltage range. **e**, and **f**, Two shadowed NW junctions that have not pinched-off due to the ambiguous junction region pointed by the white arrows in the relevant SEM images. The scale bars of all the SEM images are 1μm. 55
3.14 **Post-growth etching of the junctions. a**, AFM image of etched InAs/Al NW device (scale bar 500 nm). Zoomed-in junction (scale bar 100 nm) exhibits a disorder-free semiconducting segment. **b**, AFM image of double junctions device (scale bar 500 nm) where magnified segments of the junctions (scale bar 100 nm) exhibit Al residue, rough InAs surface, and damaged SE/SU interfaces. 55
3.15 **Junction formation and edge profile. a**, Schematic of the SE-SU junction formation and the edge profile. The broadening (Δ_b) and profile of the junction edge can be determined by the flux distribution in the transition region, inter-wire distances (l_s), source to wire distance (L_{SW}) and effective width of the source (W_s). The junction length (ℓ_j) depends on the size of the Δ_b and the diameter of the shadowing NW (d_{NW}). (diagram is not drawn to scale). 56
3.16 **Measurements of edge broadening. a**, Geometry for determining the shadow position. **b**, Δ_b as a function of l_s. Blue dots are measured Δ_b for Al junctions on $InAs_{0.3}Sb_{0.7}$ NWs and green dashed lines are calculated Δ_b. 57

3.17 **Post-growth etching of the junctions. a**, Atomic force micrograph (AFM) of the $InAs_{0.3}Sb_{0.7}$/Al junction for $l_s > 500$ nm. Large Al broadening with multiple Al grains are observed in the junction. Depending on the effective flux distribution on the transition region the junction is divided into three segments. **b**, AFM of the $InAs_{0.3}Sb_{0.7}$/Al NW junction for $l_s < 250$ nm, where the junction is clean with sharp-edge profile. **c**, Zoomed-in TEM image from (**b**) shows the epitaxial SE-SU interface and small Al broadening in the junction. Scale bars are 5 nm and 1 nm respectively. 58
3.18 **AFM of InSb/Sn and InSb/Pb junctions. a**, AFM of the sharp-edge InSb/Sn junction shadowed by thinner InSb NW for $l_s < 250$ nm. The line scans, taken at the positions marker by black lines show the broadening of ~ 13 nm. **b**, AFM of the InSb/Pb junction for $l_s < 250$ nm. The line scans show the broadening of ~ 75 nm. 59
3.19 **Edge profile effect on the junction performance. a**, The gate-independent resistance of the shadow junction devices as a function of l_s. Inset is the schematic of standard device where R_{Δ_b} is the broadening resistance, R_c is the contact resistance and R_{int} is the interface resistance. The dotted line till 0.8 kΩ represents the statistical value of contact resistance obtained by four-probe measurements. **b**, The conductance saturation as a function of l_s. 60
3.20 **Nanowire junction devices. a**, Pseudo colored SEM image of a typical single-junction back-gated device. Scale bar is 1 μm. **b**, Pinch-off voltage statistics for InAs, $InAs_{0.3}Sb_{0.7}$ and InSb NW junction devices. 60
3.21 **Quantized $InAs_{0.3}Sb_{0.7}$/Al NW junction. a**, Differential conductance as a function of gate voltage and magnetic field of a $InAs_{0.3}Sb_{0.7}$/Al NW junction. **b**, Hysteresis of the device shown in (**a**) where sweep up and down follows closely. Inset is a comparison of a statistical value of hysteresis between quantized and non-quantized devices. 61
3.22 **Quantized conductance on InAs/Al and InSb/Al junctions.** Conductance is drawn as a function of gate voltage for InAs/Al (**a**), and InSb/Al NW (**b**) junctions. All the plots shown here are measured with 9 T magnetic field, which is applied perpendicular to the NWs. The measurement is done at 2 K and the length of the junction is ~ 100 nm. 62
3.23 **Quantized InSb/Sn junction device a**, An SEM image of the NW prior to deposition of contacts. Contacts are deposited such that the only center junction is being probed. The measured dimension of this junction is 210 nm. **b**, Differential conductance as a function of gate voltage and magnetic field for InSb/Sn NW junction. 62
3.24 **Additional measurements in InSb/Sn junction device. a**, A two-terminal source-drain measurement is taken at **B**=0 T, while **b**, shows the same measurement taken at **B**=6 T. The source-drain bias (V_{SD}) at the device is extracted for both measurements using the known resistance of the filters and contacts in the fridge. In both sets of data, quantized conductance plateaus are visible, suggesting transport in the junction is ballistic on the order of a few hundred nanometres. As is expected, at zero field the first plateau has a conductance of $2e^2/h$, while at 6 T, spin degeneracy is broken leading to the emergence of a plateau at e^2/h. In the zero-field data, features relating to the superconducting shell are visible near zero bias and as two dips symmetric around zero bias. . 63

3.25 **Supercurrent and multiple Andreev reflections in the sharp-edge junctions.** **a**, Typical VI-curve for an $InAs_{0.3}Sb_{0.7}$/Al shadow Josephson junction (Device S#1). The switching and retrapping currents are indicated. **b**, Differential resistance as a function of current and gate potential. The black region corresponds to the zero-voltage state. I_C and normal state conductance g_N measured at $B_\perp = 0.3\,T$ are shown. **c**, I_C *vs.* g_N for all measured devices. Dashed lines are the theoretical expectations. **d**, Voltage-biased measurement of the sub-gap structure of S#1 showing resonances of multiple Andreev reflections. The high-conductance region asymmetric around zero bias (∗) is related to a supercurrent branch enabled by the finite resistance of the cryostat wiring. 64

3.26 **Supercurrent measurements for other devices.** First column of this figure shows the SEM before metallization of the 6 other devices shown in Figure 3.25. The shadowed region is hinted with an arrow. In the case of the crosses, the merged NW is fully metalized with the corresponding contact in order to avoid floating pieces of SU close to the junction. Second column indicates the I-V characteristics of the junctions with up and down sweep at V_{bg}= 0 V. In device S#3, we note a presence of a step like feature which qualitatively looks like a Fiske step. The third column shows the differential resistances as a function of applied current and back-gate voltage. 65

3.27 **Substrate fabrication and molecular beam epitaxy of hybrid nanowires. a**, An image of 2-inch wafer with lithography-defined patterns. Zoomed-in SEM image of the (111) B faceted trenches with deposited Au disks (scale bar is 1 μm). **b**, Schematic of the fabricated substrate and NW growth scheme. The angle of the etched trenches are 54.7°C. An offset (m) from the bottom of the trenches is maintained in order to avoid competition between bulk growth and NW growth in the trenches. Regarding the position of the Au, if it is close to the lower edge of the trench, the wire may not be able to grow before it gets covered by planar growth. If the catalyst is too close to the upper edge, it migrates to the (100) facet while annealing. Hence, perfectly aligned lithography to place the Au seeds in the middle of the sidewall is crucial. Red arrow is an example SU deposition direction along the trenches. **c**, InAs NWs growth from the trench substrate. 67

3.28 **Fitting of a pinch-off curve.** Blue line: forward sweep of the gate voltage and the evolution of the differential conductance in units of $2e^2/h$. Red dashed line: the fitted model. On the right, field-effect mobility as a function of interwire distances. 70

4.1 **Conditions for different InSb networks. a**, Tilted scanning electron micrograph (SEM) of InAs (111)B trenches with deposited Au catalyst particles. Trenches are created by wet-etching in InAs (100) substrate. Here, Δx is the distance between two Au catalysts from opposite trenches, Δz is the offset between two Au catalysts, and h_{tr} is the height or the etch depth of the trench. The schematic is not drawn to scale. **b**, Three possible schemes of the NWs, grown from the opposite directions depending on their Au positions. First, when the final diameters of the NWs (d_{NW}) are smaller than the offset of the Au catalyst ($d_{NW} < \Delta z$), then the wires are used for shadowing as elaborated in Chapter 3. Second, if the diameter of the NWs (d_{NW}) are bigger than the offset of the Au catalyst ($d_{NW} \geqslant \Delta z$ and $\Delta z \neq 0$), a nanocross can be formed. Finally, if Au catalysts are positioned face-to-face which means, NWs are grown without offset a nanoplate shape structure can be formed. Later two networks will be discussed broadly in this chapter. **c**, Tilted SEM image of InAs stem assisted InSb NWs grown from the opposite trenches. Predesigned Au positioning on the trenches confirms NWs growth direction towards each other and condition for nanocross formation. The highlighted section shows an example of proper nanocross formation, where the NWs merge through the side-wall and combined as one structure. **d**, Schematic of the nanocross from the trenches with the condition $d_{NW} > \Delta z$. Scale bars for (**a**) and (**c**) are 1 μm. . 73

4.2 **Morphology evaluation of InSb nanowires on the trench. a**, InSb NW growth analysis as a function of In and Sb flux ratio. Tilted SEM images for four different conditions and corresponding growth times are presented. The growth temperature is maintained constant for all different conditions. With the highest In growth rate and Sb pressure (1.8×10^{-6} Torr, V/III ratio 4.49), the diameters of the InSb NWs are significantly larger compared to the other three conditions. On the other hand, lowering the In growth rate 0.289 ML/s with Sb pressure 1.3×10^{-6} Torr (panel (iii)) provides a high aspect ratio meaning longer length with smaller diameter compared to the other three conditions in the same growth time. The scale bars for all the images are 1 μm. **b**, Length, and diameter as a function of the V-III ratio on the same samples presented in panel (**a**). **c**, Aspect ratio as a function of V-III ratio, where V/III ratio 4.49 demonstrates the lowest aspect ratio and V/III ratio 4.30 shows the highest aspect ratio. **d**, Axial and radial growth rate as a function of V/III ratio. It is further evidence that high In and Sb flux causes larger radial growth to compare to the axial growth. Reduced Sb flux and In growth rate helps to lessen the radial growth and results in a higher aspect ratio. 75

4.3 **Understanding InSb nanocross formation. a**, Length and diameter as a function of growth time. Here, the In growth rate is fixed to 0.289 ML/s. **b**, Aspect ratio as a function of growth time while maintaining other growth conditions fixed. **c**, Radial growth rate as a function of growth time. **d**, Schematic of the nanocross geometry, where Δx is the trench-to-trench distance between the Au catalysts, MP is the point where NWs merge or cross each other and L_{MP} is the length of the NW before merging. **e**, Schematic of the evolution of NWs to merge and form nanocrosses. Here, d_0 is the initial diameter of the InSb NW without radial growth, Δr is the thickness of the radial growth, Δz is the offset between two Au catalyst. In the growth time scale, t_0 is the time when growth starts, $t_{(MP)}$ is the time when merging happens or NWs pass through each other and t is the final growth time. Here, three different merging possibilities are shown depending on the growth condition, which will be discussed in detail in the text. 76

4.4 **TEM analysis of the InSb nanocrosses. a**, Tilted SEM image of InSb nanocrosses, where all the NWs are crossed with assistance of the radial growth in longer growth time as the schematic is shown in Figure 4.3**e**. Scale bar is 1 μm. **b**, Representative TEM of a nanocross. Scale bar is 100 nm. **c**, High resolution TEM from highlighted section of (**b**) confirming ZB crystal structure before and after merging. **d**, Highlighted TEM of the curved section from (**b**). Couple of stacking faults are observed only at the edge (indicated by white arrow) of merged section. On the other hand, pure ZB structures maintains to the center of the merged section and in all arms. **e**, Representative TEM image of the pure WZ InAs stem. Scale bars for (**c**) and (**d**) are 2 nm, and (**e**) is 5 nm. 78

4.5 **Structural analysis of marginally overlapped and partially intersected InSb nanocrosses. a**, Schematic of the opposite directional InSb NWs partially intersected through the sidewall due to radial growth. **b**, Tilted SEM image of InSb nanocrosses, where NWs are moderately meet (or overlap) each other through the facets when final InSb diameter is reached. **c**, TEM analysis of the similar nanocross, as shown in panel (**b**), where NWs are slightly touched but not intersected through each other. The magnified TEM image in the right confirms the overlapping, as no intersection is observed. **d**, Tilted SEM image of the nanocrosses, where NWs are marginally intersected from the sidewall after final growth time. **e**, TEM image of the similar nanocross. It is clearly observed that NWs are intersected to each other, unlike the previous one. Scale bars are 100 nm. 79

4.6 **Head-to-head Au catalyst position. a**, Tilted SEM image of the trenches, where the Au catalysts are lithographically positioned without any offset. **b**, Initial InSb section grown with InAs stem. **c**, Schematic of the three possible types of nanostructure formation when InSb NWs are grown head-to-head towards each other. Here, Δm is the distance of the merging point from the Au catalyst. Scale bars for (**a**) and (**b**) are 1 μm. 80

4.7 **Formation of different types of network.** Histogram presents percentage of different types of InSb structures created from Au catalyst positioned without offset. Total 321 data are counted. 81

4.8 **"Type-I" merging. a**, Schematic of the "Type-I" InSb network. Here, one NW hit on the side-wall of another NW with an offset. **b**, Tilted SEM image of the "Type-I" merging. **c**, TEM analysis of the similar phenomena, where Au catalysts are well separated from each other after merging. **d**, Magnified highlighted section from panel **c**. Scale bars for (**b**), (**c**), (**d**) are 100, 50 and 5 nm respectively. 81

4.9 **InSb nanoplate with elongated arm. a**, Schematic of the InSb nanoplate with a long arm. Inset SEM image demonstrates the top view of the elongated arm. **b**, Tilted SEM image, where all the arms are in the same direction. **c**, Tilted SEM image, where arms are shown two different directions demonstrating domination of kinetics of the Au catalyst to determine the direction of the arm. Inset is the top view demonstrating the triangular nanoplate section. Scale bar for (**a**) is 100 nm. Scale bars for (**b**) and (**c**) are 1 μm. 82

4.10 **InSb network with "Type-II" merging. a**, Schematic of the InSb network created after "Type-II" merging. **b**, Tilted SEM image of InSb network where Au catalysts of NW_L and NW_R slide through each other facets after the meeting. The highlighted red circle shows the Au catalyst's position after the final growth time. **c**, SEM image shows the similar phenomena as (**b**), but in the opposite directions. **d**, Schematic of the Au position to create network shown in panel (**b**) and (**c**). **e**, Schematic and inset SEM shows the condition, where Au catalysts sit on the top and bottom facets of the NWs instead of side facets. **f**, Tilted SEM image of the nanoplate where upper NW slides on $(10\bar{1})$ and $(0\bar{1}\bar{1})$ facets and at the same time bottom NW crawl through (011) and $(\bar{1}01)$ facets in opposite <111> directions. **g**, Tilted SEM image of the nanoplate structure, where Au catalyst of NW_L stays in the top facet, whereas the NW_R catalyst crawl through the sidewall similar to other conditions. 84

4.11 **"Type-III" merging with InSb network. a**, Schematic of the "Type-III" merging. Here, Δz and Δm are zero, as a result, Au droplets of both NWs merge. **b**, Initial stage of the merging, where two Au droplets meet. **c**, Second stage of the merging, where Au droplets are combined into one. On the right, SEM image of such structure. **d**, In the last stage, Au droplet assists growing in $< 100 >$ direction for longer growth time. SEM image on the right shows similar results in long growth time. Scale bars for (**c**) and (**d**) are 100 nm. 85

4.12 **InAs network from two neighbouring trenches. a**, SEM image of the junctions, where the NWs meet tip-to-tip and Au catalysts merge into one. Later, the merged catalyst choose to slide into one of the NWs' arms. **b**, SEM image of the "T"-shaped junctions, where one catalyst hit the sidewall of another one and crawl down to [-1-1-1] direction. **c**, TEM image of the junction interface from similar NW highlighted from (**c**). A trapezoidal ZB inclusion is observed after merging. A couple of stacking faults (indicated with arrows) are observed close to the boundary area of the ZB segment. Scale bars for (**a**) and (**b**) are 1 μm and (**c**) is 20 nm. 87

4.13 **InAs network from one trench. a**, SEM image of the single trench with Au catalysts positioned in both side of the (111) facets. Au catalysts are placed head-to-head. **b**, Tilted SEM image of the "y"-shaped InAs network with a 2D nano-plate overgrown area in the junction. Scale bars for (**a**) and (**b**) are 1 μm. 88

4.14 **Formation of branched InAs NW. a**, Schematic of the branched InAs NWs junction, where opposite <111> directional NWs merge from the side and a third new directional NW grows in parallel to the substrate (<110> direction). **b**, SEM image of the three parallel trenches with EBL positioned Au catalysts. Dotted highlighted Au from the last trenches are positioned "head to head" to merge and form a network. **c**, SEM image of the grown brunched NWs, where the orange highlighted NW grows in <110> direction after merging. Scale bars are 1 μm. 89

4.15 **Crystal structure of an arbitrary branched InAs NW junction. a**, TEM image of a branched InAs NW junction in the grid. **b**, Magnified TEM image of the junction area. Coloured boxes are our sections of interest, where we will perform high-resolution TEM and present in later panels. **c**, HR-TEM image in the segment of InAs NW_R, which is uninfluenced to merging and shows pure WZ crystal structure. **d**, Coexistence of WZ and ZB crystal structure after merging, which is also shown in Ref.[261]. Here Shockley partial dislocation leads to a couple of stacking faults induced in the structure during transition [282]. **e**, Interface between NW_L and the junction area. Although merged, a clear distinction between NW_L and NW_R is observed. Several stacking faults are also appeared in the process of relaxing the crystal structure. **f**, Magnified TEM image of the interface section reveals the transformation of two WZ structures into ZB while merging. **g**, HR-TEM from NW_L before merging. The NW shows mostly WZ crystal structure with the inclusion of several stacking faults. **h**, HR-TEM of the junction progression after merging. The clear distinction between NW_L and NW_R (which initiated in the interface, shown in panel (**e**)) continues. A dotted line in the contrast area is indicated. The growth of both NW segments side by side is a unique phenomenon. **h**, Au catalyst position at the top of the branched NW. The separation between both structures continues beneath the catalyst. 90

4.16 **Nanocrosses with InAsSb NWs. a**, Tilted SEM image of the InAsSb NW growth on the trenches, where the spacing between the catalysts are different from right to left. Based on that, NCs are created only on the sections where $d_{NW} \geq \Delta z$. **b**, Tilted SEM image of the magnified InAsSb nanocrosses, where less radial overgrowth is observed compared to InSb. Scale bars for (**a**) and (**b**) are 10 μm and 1μm respectively. 91

4.17 **Substrate preparation for nanocross shadowing. a**, Schematic of the InAs (100) wafer, where 150 nm of PECVD SiO_x is deposited for masking. In the right, color codes are mentioned for different materials. **b**, First electron beam lithography (EBL) is used for defining the pattern for the bridges. Buffered HF is used to remove the SiO_x from the developed area. As a result, the bridge for shadowing is formed. **c**, Second EBL process is used to pattern the area to make the trenches. Sulfuric acid based wet-etching is used to etch the developed area and create (111)B facted trenches [54]. **d**, Third EBL process is used to define the position of the Au catalyst on the (111)B faceted wall. E-beam evaporation is used to deposit the Au film. After lift-off, only developed areas are left with Au catalysts. 93

4.18 **Shadowing InSb nanocrosses with Al. a**, Tilted SEM image of the fabricated substrate. Related parameters for the shadow geometry is shown in the inset. **b**, Tilted SEM image of the shadowed nanocross. The arrows show the direction of the Al deposition. Indicated dotted lines show the shadow bar and the overgrowth on SiO_x mask. Scale bars for (**a**) and (**b**) are 1 μm. 94

List of Tables

2.1 Possible single element superconductors (bulk value) [70, 73–78]. 8

Introduction 1

1.1 Semiconductor Nanowires

Growth Overview

One dimensional (1D) semiconductor nanowire (NW) has been an important topic of research for the last few decades [1–5]. Control synthesis of length and diameter, versatile choice of compositions, and the ability to tune the intrinsic properties are some of the key reasons behind this vast interest. Till date, significant progress has been made in the synthesis technique, materials development, and embedding these materials into functional device applications. The availability of diverse bulk semiconductor materials lead to explore both single element and the compound NWs. Capitalizing on the 1D nature, interesting electrical and optical properties can be engineered in the binary and ternary compounds NWs (from different element groups). So far, the most explored semiconductor NWs are: Si NW, group III-V NWs (GaAs, InAs, InP, InSb and their ternary compounds, etc.), group II-VI NWs (ZnO, ZnS, CdS, CdTe, etc.), and III-N NWs (GaN, AlN, InN, and their ternary compounds, etc.) [2–8]. Several growth mechanisms have been developed to grow these NWs. Among them, the conventional and most popular method is vapor-liquid-solid (VLS) grown NWs, demonstrated by Wagner and Ellis in 1964 [9]. Apart from the VLS method, vapor-solid- solid (VSS), solution-liquid-solid (SLS) and selective area growth (SAG) are also well-known methods for NW growth [1–4]. The systems that have been used for NW growth are molecular beam epitaxy (MBE), metal-organic vapor phase epitaxy (MOVPE), metal-organic chemical vapor deposition (MOCVD), chemical vapor deposition (CVD), plasma-enhanced chemical vapor deposition (PECVD), chemical beam epitaxy (CBE), etc [2–5, 8]. Besides, a low cost, high yield continuous gas-phase synthesis called Aerotaxy (industry suitable) has been demonstrated in Ref. [10] to grow semiconductor NWs.

Applications in Different Fields

Semiconductor NWs have been widely studied as a building block for electronic and photonic devices. The 1D geometry of the NWs not only assists in scaling down the device dimension but also provides flexibility towards on-chip integration in circuits [4, 11]. Low power, high mobility NW-field-effect transistors (FET) has been widely demonstrated in in-plane device geometry (top/bottom gate) and in as-grown vertical (gate-all-around) device architecture [2, 12], which is considered as a direction for next-generation large-scale integration of NWs [6, 13]. Furthermore, NWs have been explored for memory devices [14], resonant tunneling diodes [15], p-n junction diode [16], light-emitting diodes [17], photodetectors [18], chemical [19] and biological sensors [20] etc. In recent years, the investigation of semiconductor NWs for third-generation

photovoltaics has increased significantly, as it holds the promise for high efficiency with low-cost solar cell [21, 22]. Due to the possibility of tuning the band structure with different compounds and effective reduction of thermal conductivity in 1D structure (compare to the bulk), NWs are considered as an efficient thermoelectric material; therefore prominently used for thermoelectric devices [2, 23]. Utilizing the mechanical properties, semiconductor NWs are used as resonators and piezoelectric devices [24, 25]. NW applications are further extended to electrodes for lithium-ion batteries [26], artificial photosynthesis [27] and in many more research fields. Moreover, parallel theoretical proposals of new devices with NWs play an integral role in providing future research directions.

The fact that hasn't been mentioned yet is, with quantum confinement, semiconductor NWs are one of the appealing platforms to study quantum transport in the 1D system. With the reduced dimension, physical phenomena such as single impurity scattering, electron-phonon coupling and the influence of interface (in hybrid) get amplified. Hence, these can be studied with NWs, which otherwise would not be possible in bulk materials system [5]. It enables a better understanding of the material properties and helps to engineer the device at an atomic-scale. Recently, the proposal of topological superconductivity in hybrid NWs and their potential application in future Majorana based quantum computation [28, 29], resulted in significant attention to study semiconductor NWs. Following the theoretical proposal, a possible signature of Majorana fermion (or Majorana bound state) in hybrid NW has been demonstrated in the following references [30–32]. Further study to achieve robust Majorna signature (through braiding) and utilize it as quantum bits (qubit) for logic operation is in progress [33–35]. Hence, this is a highly active research field, where the advancement in materials science plays a key role. In the next section, I will briefly discuss the Majorana fermions in condensed matter systems and the ingredients require to host Majorana fermions in semiconductor NWs.

1.2 Majorana Fermions in Semiconductor Nanowires

Majorana in Condensed Matter

In particle physics, every particle has an anti-particle with an opposite physical charge, which is called Dirac fermion, named after Paul Dirac [36]. As an example, a positron is the anti-particle of an electron or, a proton has an antiproton, etc. There is another kind of fermion, which is its own antiparticle, called Majorana fermion, named after Ettore Majorana, who proposed it from a real solution of the Dirac equation in 1937 [37]. In high energy physics, researchers are still investigating on Majorana fermion as an elementary particle. However, there are few theoretical proposals to realize Majorana fermions (or Majorana bound states) as quasiparticles in a condensed matter system [28, 38, 39]. In a solid-state system, we can consider electron ("filled") and hole ("empty") as equivalent to the particle and antiparticle respectively. A linear superposition of fermionic operators for the electron (creation operator) and the hole (annihilation operator) will lead us to the Majorana creation and annihilation operator,

which are equal: $\gamma_i = \gamma_i^\dagger$, and is the fundamental condition of Majorana fermions. Following is the qualitative summary of Majorana fermions' properties, listed from Ref. [40]: i) An ordinary fermion can be formed with two Majorana fermions, ii) Majorana fermion obeys non-Abelian exchange statistics, iii) Four Majorana fermions (two ordinary fermions) instead of two are needed to create Majorana qubit. Due to the parity conservation, braiding operation is not possible with two Majorana fermions. Such properties make Majorana qubits robust from any local perturbations and are expected to have a long coherence time [40]. Hence, for fault-tolerant quantum computation, Majorana qubit is the most potential candidate.

As discussed above, Majorana fermion is a superposition of electron and hole. Although direct superposition of such opposite charges seems unrealistic, an equivalent system can be considered in superconductors. A crowd of Cooper pairs (bound electron pairs [41]) are present in the superconductor, where an additional injection of hole or electron leads to an unpaired electron. That means a pair of electron and a hole will be combined as an electron, considerably similar to the superposition of electron and hole. Due to this particle-hole symmetry, a potential place to find a Majorana fermion is superconductor [40, 42]. For the equal and opposite energy (E), Majorana creation and annihilation operator can be expressed as $\gamma_i(E) = \gamma_i^\dagger(-E)$. From this relation, it can be said that the Majorana fermion condition fulfills if the superconducting energy state is zero. However, this zero energy state cannot be directly realized in a superconductor due to the superconducting gap. We may consider vortices or quantum dot in the superconductor, where the superconducting gap is locally suppressed, resulting in multiple energy states in the potential trap [40, 42]. Nevertheless, due to the quantum mechanical zero-point motion, the energy states can only appear in finite energies (1/2, 3/2, 5/2..), and no zero energy state is possible. According to Volovik et. al. [43], the zero energy state is possible using p-wave superconductors. In p-wave superconductors, Berry-phase of π cancels zero-point motion and a stable zero energy state is created [42, 43].

Majorana Ingredients in Nanowire

In 2001, Kitaev [44] demonstrated with a toy model that Majorana could appear in a pair at the edge of a one-dimensional spin-less p-wave superconductor. For a detailed description of Kitaev's model please read Ref. [40, 44]. In reality, a spin-less p-wave superconductor does not exist, which made it difficult to experimentally demonstrate Majorana fermion right after Kitaev's proposal [44]. Followed by continuous theoretical development, in 2010 Lutchyn et. al. [29] and Oreg et. al. [28] proposed an engineering way to develop a material platform that can essentially function as a p-wave superconductor and most importantly can be realized experimentally to host Majorana fermion. Their proposal included conventional semiconductor NW (as discussed in the previous section) proximitized with the s-wave superconductor. The combination of both elements required to have specific ingredients to function as a spin-less p-wave superconductor. The proposed simplified Hamiltonian from

Kitaev's model is as following [28]:

$$H = \left[p^2/2m - \mu\right]\tau_z + \alpha k \sigma_z \tau_z + B\sigma_x + \Delta\tau_x \tag{1.1}$$

Here, p is the momentum, m is effective electron mass and μ is chemical potential. The terms σ and τ are the Pauli matrices operating in spin space and particle-hole space respectively. α is the spin-orbit strength and B is the magnetic field providing Zeeman energy. Finally, Δ is the superconducting gap. These four terms reflect the fundamental ingredients to host Majorana. The first term shows the kinetic energy and chemical potential of the one-dimensional system. The parabolic dispersion relation is shown in Figure 1.1**b**. The second term shows the spin-orbit interaction in this 1D system. The spin-orbit interaction splits the conduction band and shifts them in both sides of the k-axis with a spacing of $k_{SO} = m\alpha$, as shown in the Figure 1.1**c**. The new energy scale for this shifted band is $E_{SO} = \frac{m \cdot \alpha^2}{2m}$. The third and fourth terms show applied magnetic field perpendicular to the spin-orbit direction and the proximitized superconductivity respectively. Magnetic field opens Zeeman energy gap, E_Z at k=0 and induced superconductivity opens a gap Δ close to the Fermi energy as shown in Figure 1.1**d** and **e**.

The magnetic field removes spin degeneracy and assist the 1D system to be completely spin-less. It also polarizes the spins (singlet to triplet), breaking the Cooper pairs from the superconductor. As a result, superconductivity is reduced leading to the suppression of the gap size. The energy gap at k=0 can be expressed as a function of Zeeman energy and chemical potential [28, 38]:

$$E_G = \left| E_Z - \sqrt{\Delta^2 + \mu^2} \right| \tag{1.2}$$

Here, $E_Z = g\mu_B B$, where μ_B is the Bohr magneton and g is the Landé-g factor. From the above equation, we can see that the gap can be mainly tuned by the applied magnetic field. The particle-hole pair is fixed by the choice of semiconductor and superconductor. If the applied field is smaller than the gap $E_Z < \sqrt{\Delta^2 + \mu^2}$, then the system is in trivial superconducting phase. Increasing the magnetic field, when the Zeeman energy is equal to the gap size $E_Z = \sqrt{\Delta^2 + \mu^2}$, the superconductivity gets completely suppressed and the gap closes. Further with high magnetic field, $E_Z > \sqrt{\Delta^2 + \mu^2}$, the gap reopens, that is the emergence of spin-less superconductivity (equivalent to the spin-less p-wave superconductor) as the spin degeneracy is completely removed by Zeeman energy. The reopening of gap is actually an inversion of gap, that's why it is also called a negative gap. The point from closing the gap to opening again with high Zeeman energy is referred as the transition from trivial superconducting phase to the topological superconducting phase (or topological superconductivity). Hence, the Majorana is expected to appear, when $E_Z \geq \sqrt{\Delta^2 + \mu^2}$. [28, 29, 38, 42, 46, 47]

In the real Majorana devices, chemical potential can be controlled by the fabricated gates close to the NWs and the magnetic field can be applied externally. However, in the recent reports (Paper 5) [48, 49] ferromagnetic insulator hybridized with semiconductor NW showed an alternative

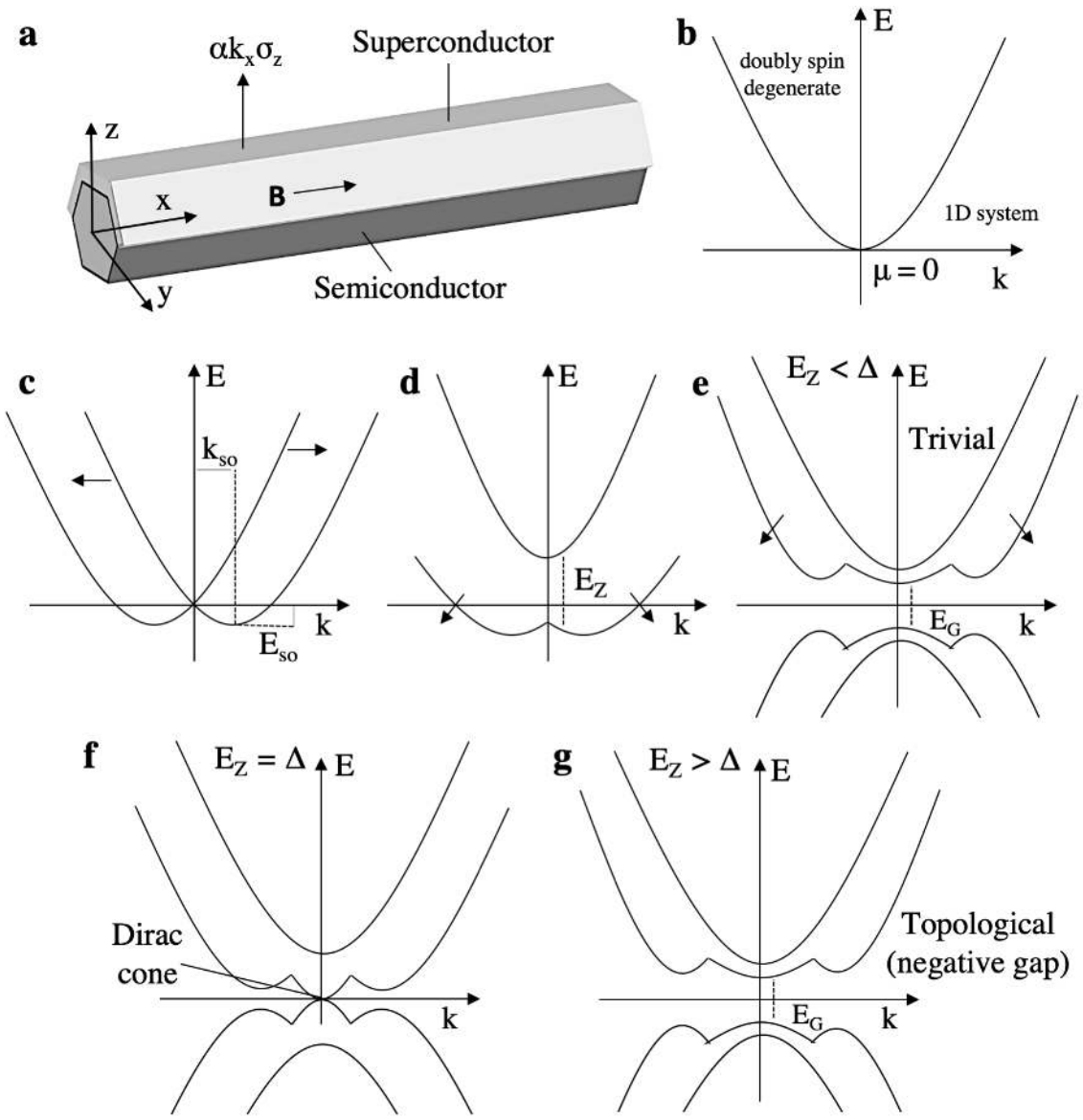

Figure 1.1: Energy spectrum and topological phase transition of hybrid nanowire. a, Schematic of the semiconductor-superconductor hybrid NW. Here the NW is positioned in the x-direction. The spin-orbit interaction is along the z-direction and the magnetic field is applied in x-direction perpendicular to the spin-orbit interaction. **b**, The dispersion relation of energy as a function of momentum in a one-dimensional system, which is a simple parabola. **c**, The second term of the Hamiltonian, where spin-orbit interaction is introduced to the system. It splits the band depending on the spin-polarization with a spacing $k_{SO} = m\alpha$ in the K-axis and also moves the energy level down to $E_{SO} = \frac{m \cdot \alpha^2}{2m}$, as indicated in the image. **d**, Magnetic field B is introduced to the system, which opened a Zeeman energy gap, E_Z at K=0, indicated in the image. The spin-polarization direction will be determined by the momentum [40]. **e**, Superconductivity is induced in the system, as a result, a superconducting gap is opened between the bands. Here Zeeman energy is smaller than the gap size, hence the system is in the trivial superconducting phase. **f**, The magnetic field further increased resulting in the increased Zeeman energy. The transition point when, $E_Z = \Delta$, the superconducting gap closes. The closed spectrum in particle-hole band is linear forming a Dirac cone, which leads to the Berry-phase cancellation [42, 43]. **g**, If the magnetic field is high enough to reach $E_Z > \Delta$, the gap reopens and the phase transition from trivial to topological superconductivity happens. Here the gap size, $E_G = 2(E_Z - \Delta)$ [45]. Although it's difficult to visualize, the re-opened gap is actually an inversed gap (negative gap). The idea of the schematic is adapted from Ref. [40, 45]

in situ route. In summary, from a material growth point of view, the following list of ingredients are required in the 1D NW for generating Majorana fermions:

- Semiconductor NWs with strong spin-orbit coupling and large Landé-g factor.
- High crystal quality of semiconductor NWs to avoid unwanted

disorders, that could create fluctuation in chemical potential and eventually hindrance to the topological phase [46].
- Induced superconductivity in the semiconductor NW, where high interface quality between them is essential [50].

1.3 Thesis Outline

In this thesis, I have explored the growth of hybrid NW based materials platform. Considering the fundamental requirements of strong spin-orbit coupling, large Landé-g factor, I have narrowed down the investigation to InAs, InSb, and InAsSb semiconductor NWs. For superconductor hybridization, I have mainly focused on Al and Sn thin film. Demonstration of single-step *in situ* patterning for high-quality NW based Josephson junction is also a key study of this thesis. Finally, the synthesis of nanowire networks has also been presented in the thesis.

The chapters outlines are the following:

Chapter 2 [1] reports the epitaxy of hybrid NWs. Introducing the VLS theory of semiconductor NW growth, the experimental results of VLS-grown InAs and InSb NWs are presented. Next, the theoretical background of metal thin film growth on NWs is discussed. Based on the theoretical understanding, hybridization of Al and Sn are presented.

1: This chapter is based on Paper 3 and Paper 4

Chapter 3 [2] reports the high quality *in situ* shadowed junction in hybrid NWs. The substrate fabrication technique and optimized growth conditions for shadowing NWs are presented. The shadowing is demonstrated with Al, Sn, and Pb on the NWs. The evolution of the junction edge profile and morphology are studied as a function of shadow geometry and material kinetics. The electrical measurement of the shadowed junction is performed to evaluate the junction's transparency. Finally, by showing the challenges of the etched junctions, a statistical comparison of the etched and shadowed junctions is presented.

2: This chapter is based on Paper 1

Chapter 4 [3] discusses the growth of quantum nanowire networks. Conditions for different network formation in VLS grown NWs are presented. Furthermore, an advanced architecture for shadowing the nanocrosses is shown that opens up the possibility for creating *in situ* multi-terminal junctions.

3: This chapter is based on Paper 2

Chapter 5 summarizes the outcomes of the thesis. By discussing the core findings and experimental challenges, a possible next step is suggested from a material science perspective.

Epitaxy of Hybrid Nanowires 2

2.1 Introduction

One-dimensional (1D) semiconductor (SE)-superconductor (SU) hybrid system serves as the platform for topological superconductivity with the presence of magnetic field [28, 29, 44, 51]. The realization of such system largely depends on the right combination of the hybrid and its interface quality. Hence, the choice of appropriate materials pair along with optimized growth condition is essential. The requirements of high crystal quality, strong spin-orbit coupling and large Landé-g factor provide the direction for semiconductor choice. As of today, the most investigated semiconductor NWs are InAs and InSb [30, 31, 52–61]. On the other hand, from a wide range of superconducting materials, most reported ones on NWs are NbTiN [30, 61–63] and Al [52–55, 58, 64].

Both NbTiN and Al hybridized with NWs demonstrated a signature of topological superconductivity in the earlier reports [30, 58]. NbTiN has a gap size of ~ 3meV and critical field > 10T. However, it is challenging to perform *in situ* hybridization of NbTiN with NWs, as it requires a sputtering tool for the deposition [61, 63, 65]. Consequently, the deposition is executed *ex situ*, that rises issues like interface disorders. On the contrary, as a single element metal, Al is possible to deposit *in situ* after the NW growth. This provides epitaxially grown disorder-free interface [52, 54, 66]. Therefore, Al is a widely reported superconductor for Majorana and other superconducting devices. On the flip side, Al has a relatively low critical temperature, $\mathbf{T_c} \sim 1.2$ K and field $\mathbf{B_c} \sim 0.01$ T, as well as a small gap size (~ 100 μeV). Thus, hunting for new material continues, which can retain similar epitaxial benefit as Al, but manifest high $\mathbf{T_c}$ and larger gap size.

In recent years, growth of niobium (Nb) [67], vanadium (V) [68], tantalum (Ta) [69] and lead (Pb) [70] metals are reported on InAs NWs. All of these superconductors demonstrate high $\mathbf{T_c}$ and $\mathbf{B_c}$ value (see Table 2.1 on the following page), hence probable alternative for hybridization. The thin film of Nb, V and Ta on semiconductor NWs are amorphous or polycrystalline [67–69], that impedes the accuracy of the measurements due to the disoriented grains and sometimes discontinuity [69]. Conversely, Pb deposition on the InAs NW exhibits epitaxial relation, similar to Al [70]. Considering the single-crystalline quality, higher mobility and larger Landé-g factor, InSb NW provides a better semiconducting platform compare to InAs NW [51]. Therefore, InSb NW with Pb epitaxy is more promising combination to explore. Nevertheless, uniform Pb film on InSb NW seems to be challenging as there is no low index domain match without high residual mismatch [54]. Recently, lattice-matched Sn is reported on the InSb NWs exhibiting another alternative route for hybridization [71]. Difficulties with Sn lie in its fundamental material properties. Crystalline Sn has two phases: $\alpha - \mathbf{Sn}$ and $\beta - \mathbf{Sn}$; among them only $\beta - \mathbf{Sn}$ exhibits superconducting properties [72]. Due to the low-temperature growth and favorable interface energy, both

Summary

This work presents both the theoretical background and experimental demonstration of the hybrid semiconductor-superconductor NWs. The growth of InAs and InSb NWs are carried out using the MBE system. Hybridization of Al and Sn on these NWs are performed *In situ* using either MBE growth chamber or *in vacuo* connected physical vapor deposition chamber. The epitaxy of hybrid materials depends on the interfacial domain matching. Additionally, the uniformity of the thin film depends on the non-equilibrium growth condition during deposition. Therefore, the thin film growth is conducted by cooling the substrate at a low temperature to limit the adatom diffusion length and increase the incorporation rate. Besides, extensive structural analysis of the grown hybrid NWs using TEM are presented.

allotropes can grow on the NW, which makes it difficult to configure as a single-domain superconducting film.

Based on the above discussion, in this chapter, I will present *in situ* hybridization of SE-SU NWs. The chapter is divided into two sections: semiconductor NW growth and thin-film growth. With a theoretical understanding of Au-assisted VLS NWs, the first section will show experimental results of MBE-grown InAs and InSb NWs. In the next section, initially, a theoretical framework for understanding the thin film growth on semiconductor NW will be given. I will then describe experimental results of *in situ* Al growth on both NWs. Finally, the synthesis of Sn film on semiconductor NWs and the associated challenges will be discussed. Detailed experimental procedures will be provided at the end of this chapter.[1]

Table 2.1: Possible single element superconductors (bulk value) [70, 73–78].

Materials	$\mathbf{T_c}$ (K)	$\mathbf{B_c}$ (T)
Al	1.2	0.01
Nb	9.46	0.82
V	5.03	0.98
Ta	4.47	0.1
Tl	2.39	0.017
Pb	7.2	0.08
In	3.4	0.028
Sn	3.7	0.03

1: TEM analysis of the grown NWs presented in this chapter are performed by Sara Martí-Sánchez, Maria Chiara Spadaro under the supervision of Prof. Jordi Arbiol from Catalan Institute of Nanoscience and Nanotechnology (ICN2). Few cases, where the TEMs are performed elsewhere, will be mentioned in the corresponding sections.

2.2 Molecular Beam Epitaxy

Molecular beam epitaxy (MBE) system has been used for semiconductor NW growth since early 2000 [3, 79]. MBE is known for the ultra-high-vacuum growth system, providing a highly pure environment for crystal growth. In the typical MBE system, depending on the growth history, pressure can be achieved as low as $\sim 10^{-12}$ Torr. With such low pressure the mean free path of the atoms/molecules from the source is very long (»10 meters) and certainly much longer than the geometrical distance between the source and the substrate (approximately 20 cm in our system) [3, 80]. Therefore, the atom deposition towards the substrate is referred to "line-of-sight" impingement, as no collisions happen during travel time [3, 80]. The additional atoms those are not landed on the substrate are immediately pumped out from the growth chamber. This leads to the possibility of the atomically sharp interface during multi-layer growth without intermixing [80]. Thus, MBE is used as a primary instrument for growing a high-quality two-dimensional electron gas (2DEG), where multi-layer epitaxy is required. Another key feature of the MBE is controlled and low growth rate (ML/s) generated from the effusion or Knudsen cell. A low growth rate confirms epitaxial growth on the substrate with the lowest possible contamination (confirming the low pressure). Furthermore, a low growth rate with high vacuum enhances the possibility of *in situ* characterization. The most commonly used real-time surface analysis system in MBE is reflection high-energy electron diffraction (RHEED), which is used to investigate microstructure growth on the surface. Besides, for chemical analysis of the progressing surface, the reflection mass spectrometry (REMS) or modulated beam mass spectrometry (MBMS) can be used [80]. This real-time monitoring provides control growth with compositional analysis and increases the reproducibility of the intended surface structure.

All the NWs growth presented in this thesis has been performed in the Varian GEN II MBE system (see Figure 2.1) at Niels Bohr Institute. It consists of three main sections: i) load lock chamber (see Figure 2.1**f**) for loading/unloading and pre-baking the mounted samples with the holder to remove impurities, ii) buffer or transport tunnel (see Figure 2.1**e**), that is used for moving the samples around and also baking the samples for further cleaning, iii) growth chamber (see Figure 2.1**b**), where

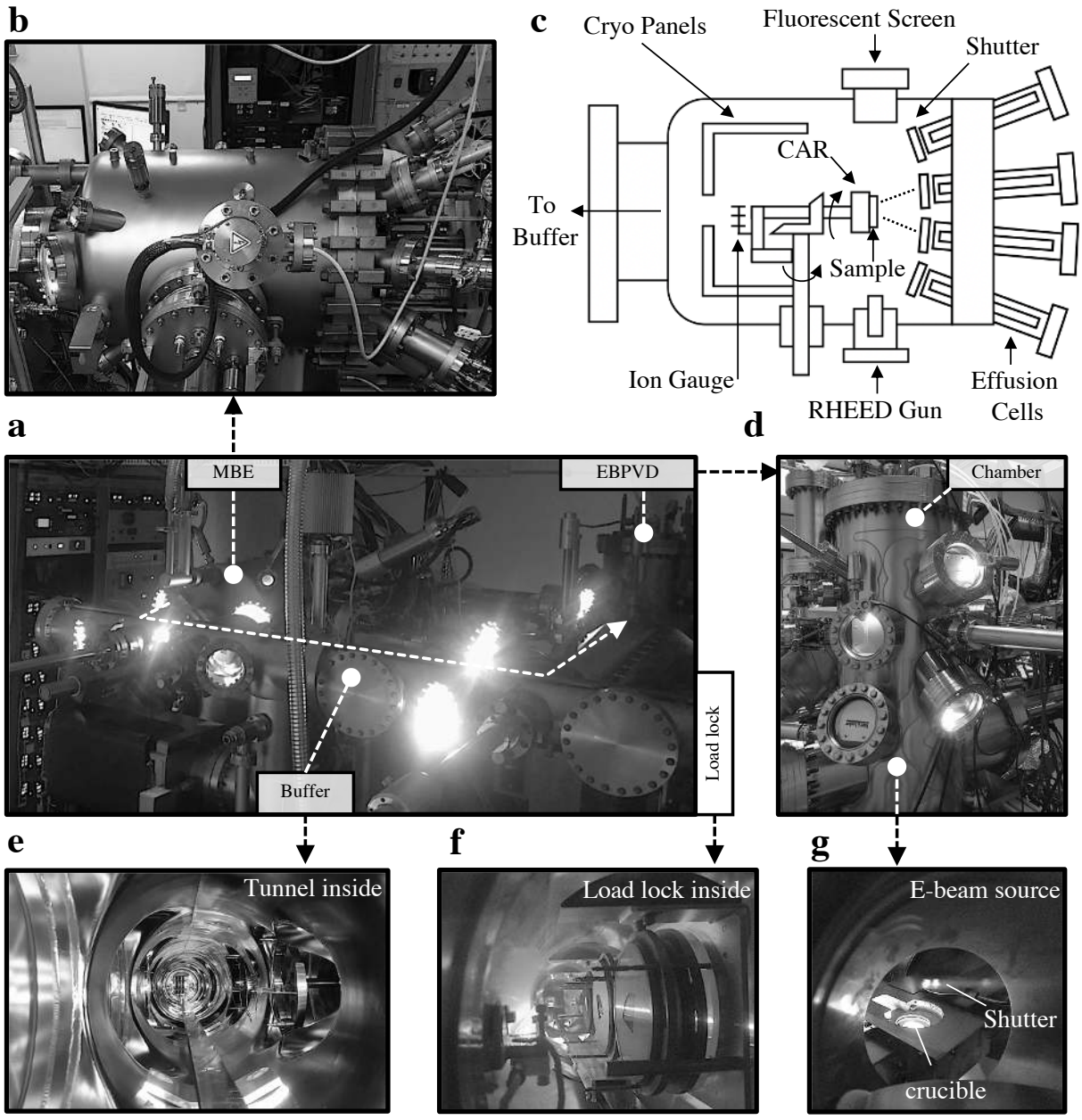

Figure 2.1: Molecular beam epitaxy. a, MBE system with *in vacuo* connected electron beam physical vapor deposition (EBPVD) system situated at Niels Bohr Institute. Two systems are connected with a long buffer tunnel as indicated with a white arrow. Load lock is connected at the end of the buffer tunnel. **b**, MBE growth chamber at one end of buffer tunnel, where, as source materials: In, Ga, As, Sb, Au, Al, Bi, and Si are loaded in the effusion cells. **c**, Schematic of the MBE growth chamber presented in (b). **d**, EBPVD growth chamber connected at the other end of the buffer tunnel. Here, all the superconducting and ferromagnetic materials are loaded. After growth, the NW sample is transferred in this chamber and cooled down with liquid nitrogen before depositing metals, which will be discussed later. **e**, Inside of the buffer tunnel, where the transfer rods are connected to load/unload or shuffling the samples. **f**, Load lock inside, where samples are loaded and degassed before transferring to the buffer tunnel. Load lock and buffer tunnel are separated with a gate-valve. The sample is only transferred when a high vacuum is achieved. There is a mass-spectrometry connected to the load lock to analyze the chemical components of the substrate before transferring to the buffer tunnel. **g**, Crucible with a source material inside the PVD chamber. The material is heated with a guided electron gun.

all the material sources are connected. Usually, the growth chamber and other sections are constructed with stainless-steel. To maintain the high vacuum in the MBE system, different pumps can be used, such as ion pumps, cyro pump, turbomolecular pumps, diffusion pumps, titanium sublimation pumps, etc [81]. In our MBE, cyro pumps, ion pumps, Ti-sublimation pumps, turbo pump and roughing pump are

used for keeping the high vacuum. The chamber wall is surrounded by the cryo panels with continuous liquid nitrogen supply (see Figure 2.1**c**), which confirms low desorption from the chamber wall. As shown in the schematic of Figure 2.1**c**, sources are connected to the growth chamber facing the substrate at a certain angle. The single element highly pure materials are loaded on the crucible, that is placed inside the Knudsen or effusion cells. Effusion cell is the heating device and can operate in ultra-high vacuum. During the deposition, the cell is heated to a stable temperature and material is evaporated from the crucible. A shutter is placed in front of the cell to block the materials when needed. Thus, simultaneously opening the shutters from multiple elements will lead to the alloy growth. Temperature fluctuation is very crucial for high vapor pressure materials, such as As and Sb. A small variation in the temperature may lead to the deviation in the deposition rate [82]. Hence, for high vapor pressure materials, a different type of effusion cell is used, called cracker cell. It has a valve attached to it in order to control the flux amount. Besides, in a cracker cell, a higher temperature is induced at the top of the cell that helps to crack bigger molecules, for example, Sb_4 to Sb_2 [82]. The purity of the source materials is also crucial for high mobility crystal growth in MBE. Typically the source materials are purchased with "six nines" (99.9999%) or more purity, that makes the commercial elemental source material very expensive. Beam flux monitor (BFM) or ion gauge (at the back of the sample holder shown in Figure 2.1**c**) are used to read incoming flux and calibrate it from the effusion cell [83]. As shown in Figure 2.1**c**, the sample is loaded in the heated substrate holder with a rotational mechanism. A thermocouple is attached with the substrate holder to measures the wafer temperature from the backside. Due to the temperature deviation, this measurement is not as reliable as pyrometer reading in MBE. Pyrometer reads the thermal emission from the substrate through view-port. Thus, the transparency of the view-port is important to maintain. Usually, the view-port is heated after the growth to desorb the attached materials. Additionally, in a customized MBE system, transfer tunnel can be used for connecting other instruments for different growths or *in situ* processes. Such as, more growth chambers with separate sources, atomic layer deposition system (ALD), e-beam evaporation system, etc. Besides, characterization tools, for instance, atomic force microscopy (AFM) or scanning tunneling microscopy (STM) can be connected for *in vacuo* analysis. As shown in Figure 2.1, in our MBE system, the transfer tunnel is connected with an e-beam evaporation system, that we use for *in situ* metal film deposition to hybridize semiconductor NWs.

2.3 Vapor-liquid-solid Mechanism

In 1964, Wagner and Ellis [9] first demonstrated the nanowire growth using Vapor-Liquid-Solid (VLS) mechanism, where they grew <111> directional Si NW on Si (111) substrate using Au as a catalyst particle. Since then VLS is one of the most realized mechanisms for growing 1D, high crystal quality NWs [4]. The research interest on VLS mechanism increased significantly since 2000 with the expansion of semiconductor NWs applications in the nano-electronic devices [3, 4]. In the VLS mechanism, NWs are grown from the catalyst particle. The liquid catalyst

particle is supersaturated with the precursor. As a result, a solid crystal is precipitated in the interface of the supersaturated catalyst and substrate. Briefly, from vapor flux to solid crystal outcome happens through the transition of vapor to liquid and liquid to solid, providing the process name of VLS mechanism [4, 9]. This process assists to attain the distinctive properties of the grown structure. Here we list a few of them [4]:

- Diameter, length, and uniformity of the NWs are controlled by the catalyst particle. That gives the possibility to synthesize NW arrays of the desired morphology with predefined catalyst particles. Moreover, engineering the catalyst position during the growth offer branching of the NWs [84].
- By tuning the growth conditions (temperature, flux ratio, etc.), the crystal phase changing is possible. In other word, control polytypism, especially in III/V NWs, that rises interesting properties of the NW.
- Efficient relaxation mechanism (through sidewall) of the VLS grown NW provides the opportunity to explore heterostructure properties of the lattice-mismatched materials. Otherwise, it is not possible in the planar structure. Hence, core-shell heterostructure with different semiconductors can be achieved.
- VLS-grown NWs can be easily doped, enhancing their p-type or n-type properties. Also, it is possible to create a p-n junction in the same NWs, that opens up different device applications.

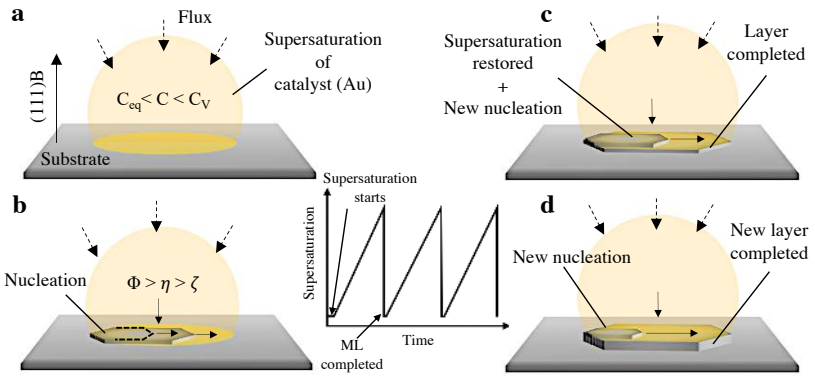

Figure 2.2: Layer-by-layer VLS NW growth. a, Supersaturation of the catalyst particle (assume Au) with precursors. **b**, Nucleation started from the supersaturated catalyst, resulting in a 2D layer growth through the liquid-solid transition. It continues within the diameter of the Au catalyst. **c**, The first layer completed. Simultaneously restoration of supersaturation begins with continuous precursor supply, that leads to a new nucleation as indicated. **d**, New layer completed and new nucleation begins. Repetition of this process continues making layer-by-layer NW growth. The idea of the schematic is adapted from Ref. [85]

Several studies have been performed to model the growth kinetics of VLS grown NWs and explain the mechanism [4, 86–93]. The fundamental understanding initiates with the supersaturated liquid catalyst, the chemical potential relates to that and the phase diagram of the given materials. Let's consider a solid metal (usually Au) deposited on the <111> directional III-V substrate (the reason behind choosing <111> direction will be discussed in the next section). This nano-sized solid metal can be melted to liquid with a given annealing temperature, depending on the size of the nanoparticle [94]. Simultaneously, if the flux of the growth materials is introduced in the growth chamber, it will dissolve in the droplet making vapor to liquid transition. In parallel, there will be some desorption of materials from liquid to vapor, however, the net incorporation rate will be higher. At a given temperature, the concentration of the provided materials alloyed with liquid (C) will be higher than their equilibrium

concentration (C_{eq}) [4, 91]. To continue dissolving materials on the liquid catalyst, higher vapor concentration is required, so $C < C_V$, where C_V is the concentration of material in the vapor. The change in chemical potential ($\Delta\mu$) of these three phases will determine the solidification from supersaturated alloy. Based on the deposited material concentration on liquid (C) and equilibrium (C_{eq}), the $\Delta\mu$ can be expressed as [52, 95]:

$$\Delta\mu = k_B T \ln \frac{C}{C_{eq}} \tag{2.1}$$

Here, k_B is the Boltzmann's constant, T is the absolute temperature. The chemical potential difference of liquid-solid and vapor-solid are respectively expressed as [4, 91]:

$$\Delta\mu_{LS} = \mu(C) - \mu\left(C_{eq}\right) \tag{2.2}$$

$$\Delta\mu_{VS} = \mu(C_V) - \mu\left(C_{eq}\right) \tag{2.3}$$

For positive vapor to liquid flux transition, $\Delta\mu_{LS} < \Delta\mu_{VS}$ and positive liquid to solid transition, $\Delta\mu(C) > \Delta\mu(C_{eq})$, that means $\Delta\mu_{LS}$ require to be positive [4, 91]. Effective vapor supersaturation (Φ) can be defined as a function of $\Delta\mu_{VS}$ and liquid supersaturation (ζ) as a function of $\Delta\mu_{LS}$ [4]:

$$\Phi = \exp\left(\frac{\Delta\mu_{VS}}{k_B T}\right) - 1; \zeta = \exp\left(\frac{\Delta\mu_{LS}}{k_B T}\right) - 1 \tag{2.4}$$

From the above discussion, solidification of the nanowire crystal through the VLS mechanism (without considering diffusion effect) requires following condition [4]:

$$\Phi > \zeta > 0 \tag{2.5}$$

Satisfying the above requirements, a solid crystal will precipitate in the liquid-solid interface and the solidified concentration will be defined by the materials phase diagram. Solidified material in the interface is confined laterally within the diameter of the liquid catalyst, hence, the driving force of growing the NWs is in the vertical direction. Based on the *in situ* TEM analysis reported by different research articles [85, 96–98], NW growth steps can be shown in Figure 2.2. From Figure 2.2, after supersaturation, a 2D island initiates in the interface and it completes within the diameter of the NW. With monolayer completion, the alloyed material concentration in the liquid gets lower. Thus, for restoring the supersaturation, an uninterrupted flux deposition is maintained, that leads to the initiation of the next nucleation. In this way, layer-by-layer growth continues until the final termination.

The growth of the VLS NW is driven by the continuous supersaturation of the catalyst via collection of materials. Therefore, an understanding of the kinetic pathway of materials to incorporate in the liquid catalyst is crucial. Multiple events may appear simultaneously during this process, as depicted in the Figure 2.3 and summarized below [4, 87, 99]:

- Starting with direct impingement of the materials on the catalyst particle, which leads to the vapor to liquid transition. At the same time, desorption happens from the liquid catalyst to the vapor. See (i) and (ii).
- Vapor to solid transition through direct impingement from vapor to the NW sidewall. Desorption also happens from the sidewall of the NW, leading to the solid to vapor transition. See (iii) and (iv).
- High amount of flux impinges on the substrate. Depending on the surface diffusivity, adatom from a certain area will diffuse to the NW side-wall (see (v)). For certain conditions, it is possible to ignore the diffusion process from the substrate and from the NW side-wall. Then it becomes an adsorption-driven growth process, for instance, the high-temperature chemical vapor deposition (CVD) process [4]. However, in the MBE or MOVPE, adatom diffusion through the substrate and the sidewall is crucial and cannot be ignored. Tuning of the adatom diffusion is possible through the choice of substrate and growth conditions.
- Adatoms of the substrate will also create a quasi-two-dimensional (2D) growth. This will increase the thickness of the area around NW (see (vi)). Hence, the actual grown length of the NW is the visible length and the 2D grown thickness of the substrate.
- Diffusion of adatoms from the NW sidewall to the liquid catalyst, helps to accelerate the supersaturation (see (vii)). Nevertheless, incorporation or desorption (as shown in (iii) or (iv)) during the process may hinder the diffusion rate. If the effective density of the adatom increases in the NW sidewall, then the incorporation rate increases compare to the desorption rate. As a result, NW starts growing radially. This scenario mostly happens when the NW's length is comparable to the adatom diffusion length. We will discuss this elaborately in Chapter 4. If the NW length gets longer than the adatom diffusion length of the sidewall, then tapering of the NW happens with radial growth.
- In Figure 2.3 (viii), a transition between liquid and solid interface is shown (liquid-solid transition), which is the driving force of the NW crystal growth.

From the discussed points, material collection happens either from the direct impingement on the catalyst or from the adatom diffusion to the catalyst. During MBE growth of III-V NWs, the substrate temperature is maintained $\sim 450^{\circ}$C, which is certainly below the evaporation temperature of the group III materials. Therefore, the adatom diffusivity in the growth substrate is considerably high. We can certainly say that adatom diffusion on the substrate and the side-wall (step (v) and (vii)) are major components in the MBE-grown NWs, that lead to the significant material collection in the catalyst [4, 87]. Adatom diffusion from one point to another depends on their difference in chemical potential. Similarly, adatom diffusion from the substrate to the NW sidewall (step (v)) or from sidewall to liquid catalyst (step (vii)) will be driven by their chemical potential difference. If we consider the diffusion from sidewall to the liquid, then the condition should be $\Delta\mu(\mathrm{AS}) > \Delta\mu(\mathrm{LS})$, where, $\Delta\mu(\mathrm{AS})$ and $\Delta\mu(\mathrm{LS})$ are chemical potential difference of adatom-solid and liquid-solid respectively. Now, similar to the equation 2.4, diffusion

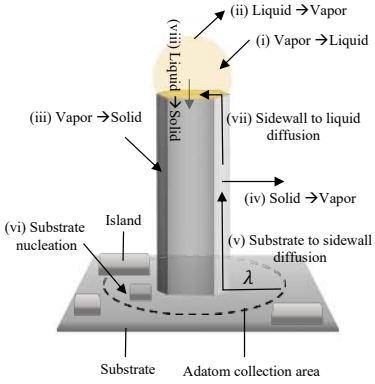

Figure 2.3: Kinetic pathway during nanowire growth. Schematic of the NW with different kinetic process associated with it. (i)-(viii) discuss different phases of transitions. The circular dots shows area of the adatom collection for the NW. λ is the adatom diffusion length. The idea of the schematic is refereed to [4].

related effective adatom supersaturation (η) can be expressed as [4]:

$$\eta = \exp\left(\Delta\mu_{AS}/k_BT\right) - 1 \tag{2.6}$$

Here, $\eta > \zeta$, for the adatom transport to the liquid. Adatom also incorporate on the substrate or the sidewall and desorbs (step (iii) and (iv)), hence $\eta < \Phi$, leading to a diffusion related modified condition for VLS NW growth [4]:

$$\Phi > \eta > \zeta \tag{2.7}$$

So, the typical long length of the III-V NWs can be attributed to the diffused adatom, that otherwise would not have been possible only with impinged atoms on the catalyst [4, 87, 100, 101]. Besides, the liquid particle during the growth can be considered as both catalyst and the collection center of the materials.

In a nutshell, the discussions presented here are basic understanding for VLS grown NW. The entire process is more complicated and deals with several different conditions. Recent progress with *in situ* TEM observation helped researchers to analyze the growth mechanics and propose additional analytical models [85, 92, 93, 96–98]. Further reading on the theoretical model and analysis, can be found in the following references [4, 86–93]. Next, I will present the experimental results of the VLS grown III-V semiconductor NWs.

2.4 VLS Grown InAs Nanowire

InAs NWs are one of the most studied III-V NWs, both in terms of growth and device applications. Comparatively high electron mobility than other III-V semiconductors (lower than InSb), small direct bandgap and electron effective mass make InAs an interesting material choice for applications like high-performance transistors or optoelectronic devices [102, 103]. It is also a commonly used material for Majorana devices. Besides, InAs NWs are compatible with the standard device fabrication process, that makes it easier to play with different device architectures [104, 105]. From a growth perspective, InAs NWs can be realized in most of the available growth systems (MBE, CBE, MOVPE, etc.). It can be grown using Au catalyst or self-catalyst mechanism [106]. Usually, base substrates such as, InAs, InP [106, 107], GaAs [108, 109] and Si [108, 110–112] are used for the InAs NW growth. Here, we choose to grow InAs NWs on the InAs (111)B substrate. The planar growth is minimal in the <111> substrate [4] and it is energetically favourable direction for NW growth [99]. As a catalyst, we choose to use Au particles. Au constitutes binary eutectic alloys with a wide selection of materials [7]. Also in most of the cases, alloyed-Au droplets create growth facilitated contact angle ($\theta_c > \pi/2$) with the substrate, that makes it an ideal choice for VLS NW growths. Outside Au, other metals such as, Pt [113], Ag [114], Cu [115] and Sn [116] have also been reported as catalysts. An argument may arise regarding Au-assisted NW's compatibility in the C-MOS processes [7]. Thus, several studies have been conducted to eliminate Au catalysts after

the NW growth maintaining the NW properties [117, 118]. This could still hold the promise for Au-assisted NWs in large applications. In this thesis, I have only focused on individual high-quality NW growth. Hence, Au related issues will not be considered.

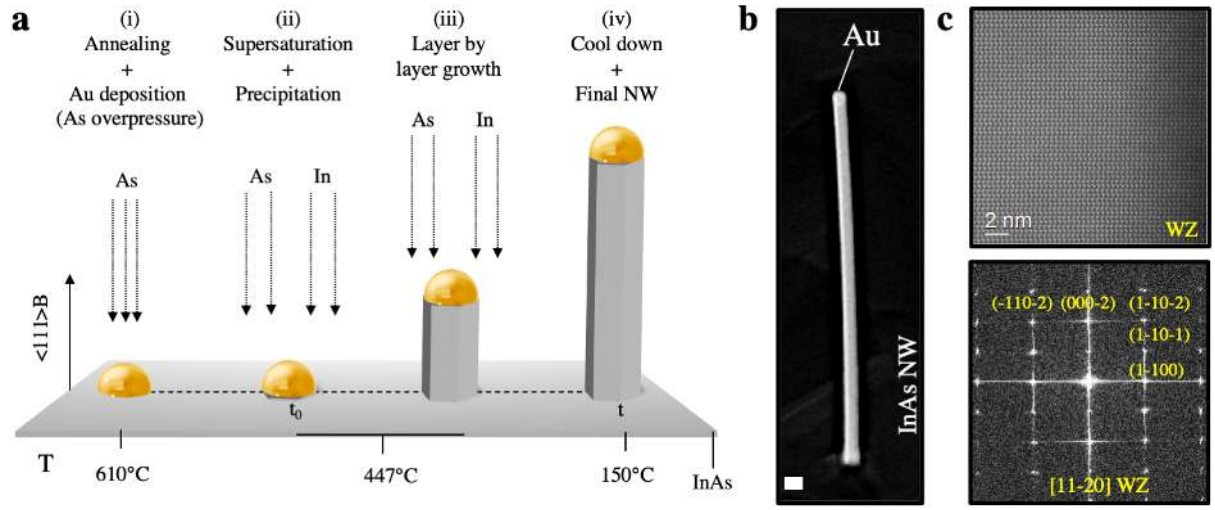

Figure 2.4: Au assisted InAs nanowire growth. a, Schematic of the InAs NW growth steps. The growth is divided into four sections. (i) Annealing of InAs growth substrate with As over-pressure. Later, *in situ* Au is deposited. With the mounted temperature the Au forms liquid on the substrate. (ii) Supersaturation of Au with the presence of In+As and the precipitation begins. (iii) Layer-by-layer growth of NW with continuous feeding of In and As (iv) Growth completes and the substrate is cooled down. Corresponding substrate temperatures are provided. **b**, Tilted scanning electron microscopy (SEM) image of *in situ* Au assisted InAs NW. Catalyst position is indicated at the top. **c**, High resolution transmission electron microscopy (TEM) of representative InAs NW structure. The TEM image is taken from a different batch. Defect-free InAs wurtzite NW structure can be observed. Corresponding FFT is presented at the bottom.

InAs NW growth from Au catalyst is presented in Figure 2.4. Substrate preparation and MBE growth steps are discussed in the experimental section of this chapter. As shown in Figure 2.4**a**, standard *in situ* Au assisted NW growth process consists four steps. (i), InAs substrate requires to anneal at a temperature significantly higher than the growth temperature. Here the substrate is annealed at 610 °C with high As_4 overpressure. During high-temperature annealing, a substantial amount of group V (As) materials desorb from the substrate. As a result, high net As pressure is needed for simultaneous reconstruction of the substrate. This also confirms the cleaning of the substrate through vaporizing the surface contaminations. Au is deposited subsequently, with the presence of As overpressure. Due to the high substrate temperature, Au doesn't get wet on the substrate and remains as droplets. (ii), In flux is introduced to the growth chamber, and at the same time, As pressure is reduced to achieve V/III ratio ~ 9.78. The In planar growth rate is fixed to 0.289 ml/s. The Au catalysts are supersaturated with In and As atoms. Upon supersaturation, the nucleation starts at the liquid and solid interface. The nucleation site evolves and terminates after completing a full monolayer, as no new nucleation site is present. (iii), Maintaining the growth temperature, the uninterrupted In and As flux generate layer-by-layer growth. (iv), After the final growth time, the substrate temperature is cooled down. To avoid decomposition from the NWs, the cooling process is also performed under As_4 overpressure. The standard InAs NW growth is performed for 30 min, that provides around 4-5 μm long NWs. As mentioned before, with 447 °C growth temperature, there

is a significant adatom diffusion effect in our NW growth. Since the NWs are randomly spaced, few of them will have shared adatom distribution, whereas others will grow independently. That leads to the NW diameter distribution across the substrate. For the given growth conditions, the diameter range varies from 100nm to 150nm. Difference in Au volumes is also the reason behind the diameter deviation. We haven't statistically measured the diameter distributions across the substrate after *in situ* Au deposition. However, an assumption can be drawn from the post-growth NWs diameter. The supersaturated Au catalysts define the NW diameter and we also have observed the identical diameter size of the Au catalyst and the NWs (see Figure 2.4**b**). Besides, no tapering is found along the NW, as shown in the Figure 2.4**b**. Thus, the adatom diffusion length at the sidewall of the NWs is believed to be longer than 3 μm at the presented growth conditions, unlike the previous report [101].

Structural analysis of the InAs NW is presented in Figure 2.4**c**, where a defect-free WZ phase is observed and confirmed with FFT. Stacking faults in the InAs NWs are also observed in several cases (WZ to ZB transform). Nonetheless, in the presented growth conditions, we observed an improved NW quality, particularly, for the InAs NWs that are grown from (111)B trenches (will be discussed in the next chapter). The bulk InAs is ZB crystal, whereas, the InAs NWs usually grow in the WZ crystal phase. This WZ formation in NWs of ZB III-V semiconductors depends on the supersaturation, the contact angle and the nucleation position in the interface [119, 120]. All these parameters can be controlled by the growth temperature and V/III ratio. It is reported [119] that, high supersaturation via III/V materials with a certain interface energy usually lead to nucleate WZ phase in the interface (on the ZB substrate beneath). Furthermore, if the triple line position and the nucleation initiate at the edge of the NW facet, then the crystal phase continues to be WZ during the growth [120]. It alters for the scenarios where due to the growth condition deviation, the supersaturation changes, and the contact angle get enhanced. As a result, the triple line shifts from the edge of the facets to the top of the NW, that leads to the energetically ZB favorable condition [120]. This also explains the formation of stacking faults or crystal phase change during the NW growth. If the local condition is stable during the growth, then the contact angle and the triple line will not shift frequently, resulting in a less defective crystal structure.

2.5 VLS Grown InSb Nanowire

Why Interest on InSb Nanowires?

Among the other III-V semiconductor materials, III-Sbs attract significant attention due to their extraordinary optical and electrical properties. Hence, for the last two decades, there have been notable efforts to synthesize III-Sb NWs both for studying fundamental material properties and for investigating device applications. Out of the III-Sb family, InSb exhibits the narrowest bandgap of 0.17 eV at room temperature (only InAsSb with certain As and Sb composition can achieve bandgap of around 0.084 eV) and large lattice constant (6.47 Å) [121, 122]. Thus, InSb NWs are used for different optoelectronic devices, like, photodetectors

[123]. Besides, InSb has the highest bulk electron mobility (≈ 77000 cm^2/Vs) among the III-V materials, which makes it interesting for low power, high-speed electronics [122]. Moreover, as discussed in Chapter 1, with defect-free crystal structure InSb NWs are perfect candidate for Majorana devices [51], spin-orbit qubit devices [124] and other quantum transport experiments [125]. Nevertheless, the enormous potential of InSb NW comes with fundamental challenges to synthesize the materials [54, 122]. In this section, I will discuss the constraints associated to InSb NW growth and present a detailed structural analysis.

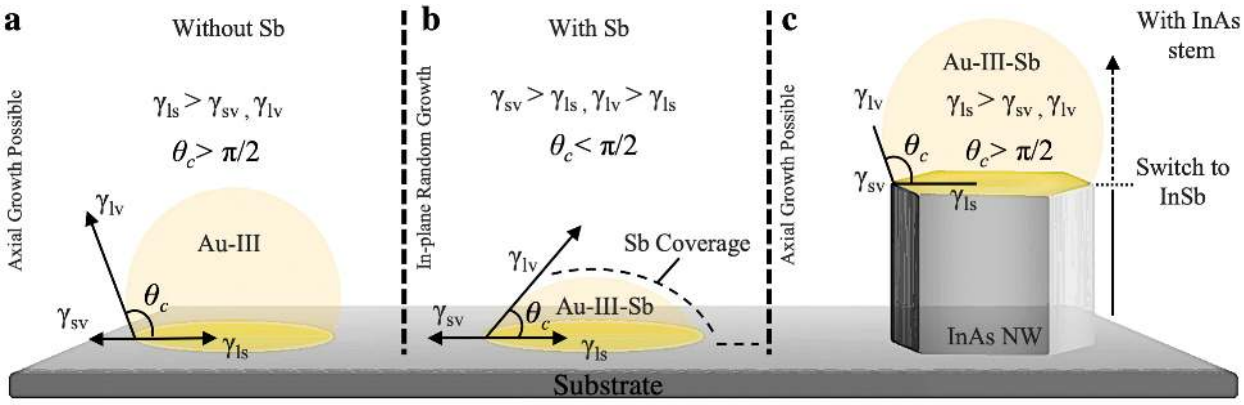

Figure 2.5: Contact angle evolution with presence of Sb. a, Contact angle of Au-III liquid alloy without Sb in the chamber. Here, the contact angle is bigger than 90° and the axial NW growth is possible with presence of As or P in the chamber. **b**, Au alloy is wetting due to the presence of surfactant Sb. Here, the contact angle is smaller than 90° and in-plane random directional growth may happen instead of axial NW growth. Sb chain sticks on the corresponding surface and alters the surface energy. Hence, VLS axial growth is not possible directly from the substrate. **c**, With presence of As, an InAs stem is grown and later, Sb can be introduced in the chamber. The Au alloy is restricted to wet within the finite {111} facet on InAs stem. Hence, in this case the contact angle is bigger than 90° and InSb NW growth is possible.

Stem Assisted Growth

As shown in Figure 2.6, InSb NWs are not grown directly on the substrate. Instead, a different III-V NW platform (usually, InAs or InP stem) is grown before the InSb segment. The stem-assisted growth is observed for all III-Sb related NWs [54, 122, 126–128]. Let's focus on the challenges of Sb related NW growth directly from the substrate, and how a stem can facilitate the growth conditions.

There are couple of difficulties connected to each other, that complicate the Au assisted InSb NW growth. It is known that, Sb (Z=51) is a strong surfactant [129, 130]. Thus, it sticks on the surface and modifies the surface energy drastically. With the presence of Sb, the contact angle (θ_c) of the liquid Au is changed, which eventually affects the NW growth. The contact angle of the liquid Au can be expressed with Young's equation:

$$\theta_c = cos^{-1}\left(\frac{\gamma_{sv} - \gamma_{ls}}{\gamma_{lv}}\right) \tag{2.8}$$

here,

γ_{sv} = solid-vapor interface energy;

γ_{ls} = liquid-solid interface energy;

γ_{lv} = liquid-vapor interface energy;

Moriarty et. al [131] experimentally demonstrated that Sb deposition on the GaAs (111)B-(2×2) surface at high annealing temperature (300-525°C) exhibits surface reconstruction to (1×3), consisting of long Sb trimmer chain. Such reconstruction leads to high surface energy. Similar Sb-rich surface reconstruction is demonstrated by Whitman et al. [132, 133] on AlSb and GaSb surfaces. Hence, the insertion of Sb in the VLS system increases the surface energy of liquid-vapor (γ_{lv}) and solid-vapor (γ_{sv}) interfaces. Conversely, the liquid-solid interface energy (γ_{ls}) is not altered by Sb, as it tends to stay on the surface and does not incorporate with the liquid Au. Therefore, according to the Young's equation, the increase of γ_{lv} and γ_{sv} in the multi-phase system is adjusted through a change in liquid shape to minimize the overall energy of the system. If $\gamma_{sv} > \gamma_{ls}$ and $\gamma_{lv} > \gamma_{ls}$ due to Sb deposition, then $\theta_c < \pi/2$. That means, because of the acute θ_c, the Au liquid will wet while trying to grow directly on the substrate. For stable NW growth, $\theta_c > \pi/2$ is required, leading to $\gamma_{ls} > \gamma_{sv}, \gamma_{lv}$ [4, 93, 120, 134]. In brief, Sb inclusion in VLS system changes the related interfacial surface energy, that lowers the contact angle of the liquid Au, resulting in an unfavorable conditions to grow axial InSb NWs directly on the substrate. Instead, the Au liquid will move around and an in-plane growth will be observed [4, 122, 135–137]. An illustration of Sb effect on the Au droplet is shown in Figure 2.5**a** and **b**. As shown in Figure 2.5**a**, without Sb the contact angle is larger than $\pi/2$ and favorable to axial NW growth. But, in Figure 2.5**b** with Sb coverage, the surface energy is increased and the Au droplet wets on the substrate.

In order to create a favorable axial growth condition, a foreign III-V material stem is grown. As shown in the TEM image of Figure 2.6**a-b**, InAs stem is a popular one, since it has a closer lattice match with InSb compare to other III-V materials [121]. InP NW stem is also demonstrated from InP substrate [127], but, later switched into the InAs stem before growing InSb. As illustrated in Figure 2.5**c**, an InAs stem creates a finite space of (111)B facet for Au liquid on top of the NW. Thereby, the liquid does not wet and extends solid-liquid interface. Maintaining θ_c above $\pi/2$, InSb NW is possible to grow after InAs stem. In the next section, I will try to explain the possible reasons behind the diameter increment of InSb segment.

Diameter Increment

As already elaborated in the VLS section, NW diameter depends on the size of the deposited catalyst and the composition of the supersaturated liquid during the growth. Generally, for III-V heterostructure NWs (except III-Sbs), the diameter alteration is not observed during the transition [138–140]. In contrary, for InAs-InSb and GaAs-GaSb NWs, an increased diameter after the transition from the stem is observed [122, 126, 128, 135, 136, 141]. There are few factors that play a role in the diameter change. According to Guo et. al [141], diameter increment is due to the lattice mismatch in the interface of two materials, resulting in the strain relaxation of crystal through lateral expansion. They demonstrated the results with GaAs-GaSb NWs. This can also be true for InAs-InSb NWs, considering InSb has a larger lattice parameter than InAs. Later, Carroff et

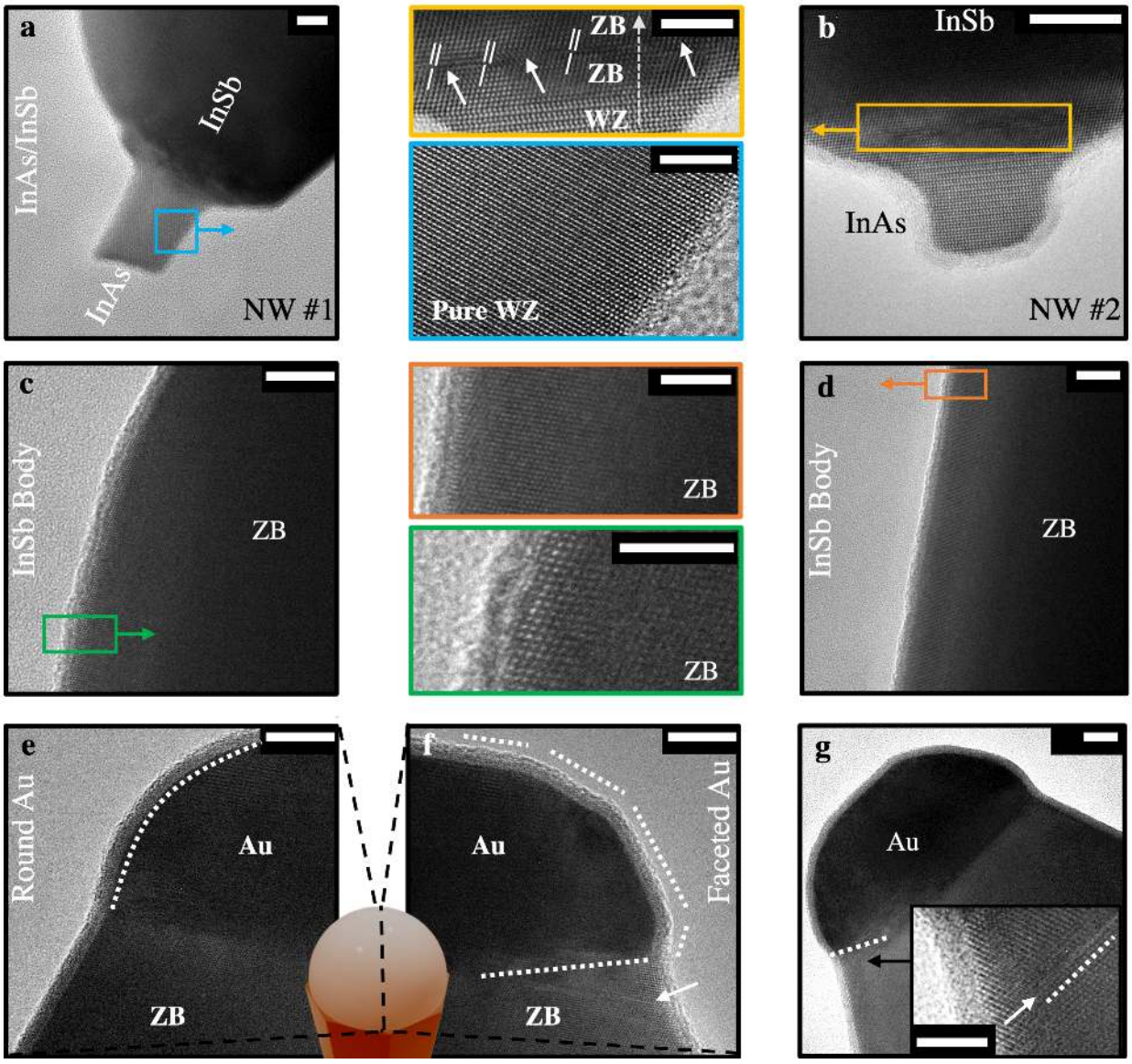

Figure 2.6: Top to bottom structural investigation of thick InSb NWs. a, TEM image of InAs to InSb transition segment. Magnified InAs segment shows defect free WZ crystal. **b**, InAs to InSb transition from another NW. Magnified transition section demonstrates a line of stacking-fault induced while growing from InAs to InSb. **c**, TEM image of InSb body where the crystal phase is complete ZB. Zoomed in TEM image in green segment shows ZB crystal. **d**, TEM image of the InSb body of another NW and zoomed in edge also demonstrate pure single crystalline ZB quality. **e**, TEM image of half of Au catalyst, which is a round shape. **f**, TEM image of other half of Au catalyst, which is faceted. This can be attributed to the cooling effect. During the cooling process Au droplet solidifies and forms the faceted shape. In both cases, ZB crystal is found beneath the Au catalyst. **g**, TEM image of the Au catalyst and solidified InSb segment beneath. Magnified TEM section demonstrates stacking fault line right beneath the Au catalyst. We also attribute this stacking fault to the cooling effect after the growth. Scale bars in the images are 10 nm and scale bars in the magnified sections are 5 nm. (TEM presented here is performed by Jung-Hyun Kang at DTU CEN)

al. [126] and Borg et. al. [122, 136] attributed the larger diameter of InSb to the change of group III composition (In) in the liquid particle from InAs to InSb growth. It is reported that [126, 136, 142], the In concentration in the Au particle increased significantly while switching from InAs to InSb segment. With the increased In concentration, the diameter of the liquid Au is increased. This is also assisted by the change in contact angle (smaller compare to the pre-InAs growth) of the Au particle during the introduction of Sb in the growth chamber [136]. Eventually, this increased Au diameter leads to the larger diameter of InSb compare to the InAs segment. Further *in situ* investigation of the Au particle evolution during

the transition is required to draw a proper conclusion.

Interface Analysis

Figure 2.6**a-b** and Figure 2.7**a-d** show TEM analysis of InAs WZ stem to InSb ZB crystal phase transition. Blue highlighted section from Figure 2.6**a** exhibits pure WZ structures in InAs segment. Here the diameter of InAs is 24 nm. Defect-free InAs WZ crystal has already been demonstrated in previous section and will also be discussed in next chapter [54]. Figure 2.6**b** shows TEM analysis of NW#2 and yellow magnified section in the left is detailed of the transition section. Further, in Figure 2.7**d** shows the interface analysis for a thin InSb NW.

In contrary to the bulk system, it is possible to combine highly mismatched materials in the NWs due to their structurally assisted strain relaxation close to the interface. This leads to a possibility of exploring interesting material properties in the heterostructures. TEM image of Figure 2.6**b** shows a high contrast in the interface of InAs and thick InSb NW, indicating the presence of strain. We magnified into the contrast interface area in the yellow box to understand the strain relaxation mechanism. The transition of the interface segment can be divided into three regions: pure WZ, small ZB in the interface, and later pure ZB section. Pure WZ section is the boundary of the InAs stem before the transition. When Sb is introduced, the crystal changes to the initial ZB segment until the formation of misfit-dislocation. Similar phenomenon is also observed in previous investigations [126, 143–146]. For the case of thin InSb NW presented in Figure 2.7**c-d**, the transition of ZB seems to be less defective, where only two twin boundaries are observed. The small ZB segment can be attributed to the presence of Sb. It is known that a small Sb incorporation in the crystal assists it to switch into ZB crystal phase [147]. So, when the Sb flux is provided, with a small amount of As present in the system, that leads to a ternary InAsSb section with a minimum incorporation of Sb. The Sb gradient in the InAs-InSb is also observed by Caroff et. al. [126], and later, Mata et al. [144] confirmed the presence of InAsSb segment with an atomic resolution analysis. This ternary segment is very small and in the range of a couple of nm. Right at the edge of ternary segment, couple of misfit dislocations or twining events occur depending on the diameter of the InSb segment. Since InAsSb with small Sb composition has a smaller lattice parameter than InSb, this leads to the misfit dislocations to take place as a mechanism of strain relaxation and assists in transit into relaxed disorder-free InSb ZB. Similar to the previous reports [144], we also observe the misfit dislocations mostly identified in the center of the interface (in Figure 2.6**b**), but not in the edges. Further moving from the interface area, we can see the stacking of the pure ZB crystals, a characteristic outcome of the InSb and will be discussed in the next section.

Defect-free Zinc Blende Structure of InSb NW

The single-crystalline InSb segment is examined in Figure 2.6**c-d** and Figure 2.7**e**. Such high crystal quality is also evident in the electrical measurements, showing ballistic transport in the measured InSb NW devices

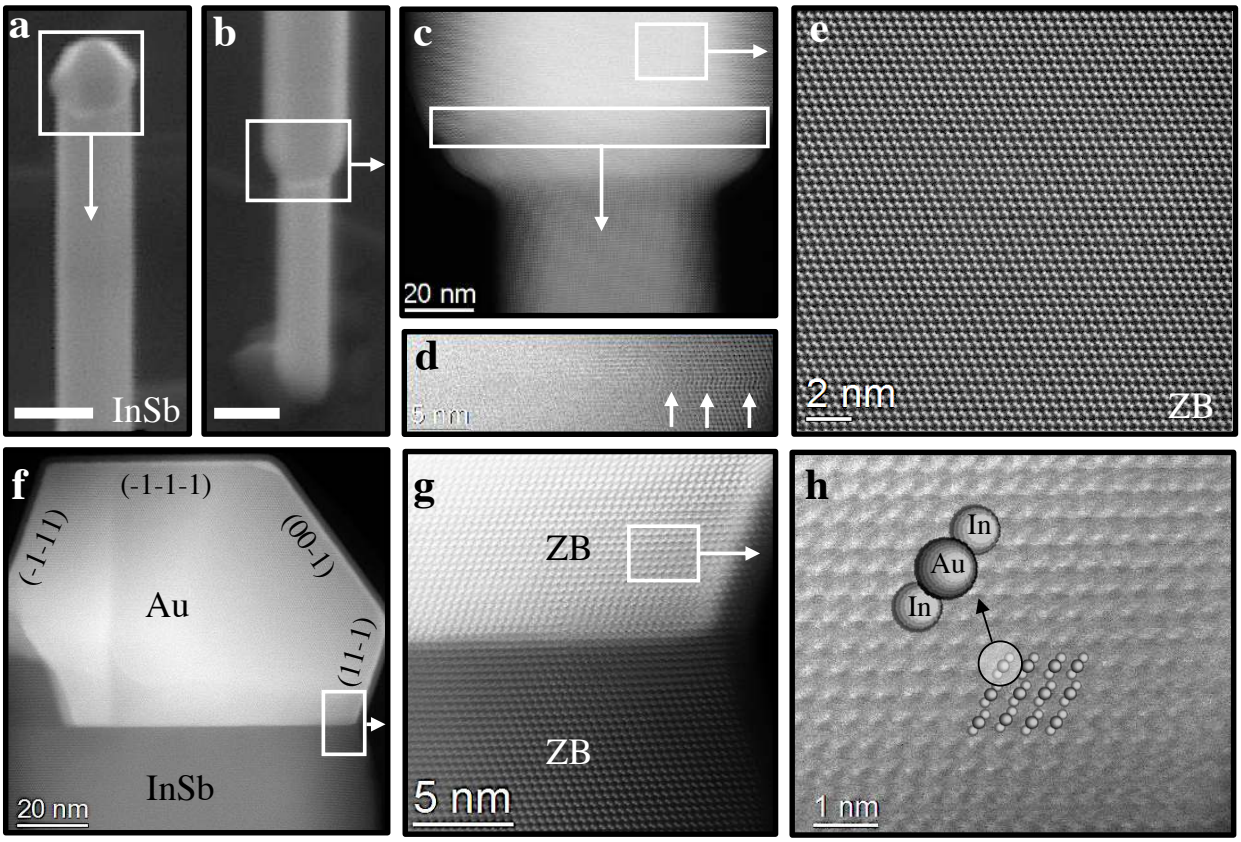

Figure 2.7: Structural analysis of thin InSb NWs. a and **b**, Tilted SEM image of thin b-polar InSb NWs (diameter ~ 100nm) grown from InAs (111) substrate. The length of the NWs are around 2-2.5 μm. Scale bars are 100 nm. **c**, Representative TEM image of the InAs-InSb interface. **d**, Magnified section demonstrates two twin boundaries (shown with arrows) in the InAsSb transition section before reaching the full diameter of the InSb segment. This is the only defect observed in the analyzed structure. **e**, Magnified HR-TEM shows pure ZB structure in the InSb segment. **f**, TEM Analysis of the Au catalyst and Au-InSb interface. As shown in the previous case, Au solidified at room temperature resulting a faceted structure. **g**, Magnified HR-TEM shows the interface between Au-InSb demonstrating defect-free ZB alloy in Au and pure ZB InSb structure. **h**, Further analysis with high magnification micrograph of the Au section shows the $AuIn_2$ FM3-M cubic crystal phase, oriented through its [1-10] zone axis, confirming high concentration of In in the catalyst.

[54, 148–152]. [2] The defect-free ZB crystals can be attributed to several factors. Starting with ionicity (f_i) value and energy difference (ΔE_{WZ-ZB}) to form WZ and ZB crystal structures for III-V NWs. Correlation of ionicity, relative energy difference among the crystal phases and stacking disruption or rotational twinning both for bulk and NW structures has been observed before [153–155]. Among the other III-V materials, InSb demonstrates low value of ionicity ($f_i = 0.19$) and eventually high energy difference to form WZ ($\Delta E_{WZ-ZB} = 8.2$ meV/atom). In addition to InSb, GaSb also demonstrates relatively low ionicity ($f_i = 0.15$) and high energy difference $\Delta E_{WZ-ZB} = 9.9$ meV/atom [154]. In both cases, NWs demonstrate a strong possibility of formatting only ZB crystals. In contrast, with relatively high ionicity and low energy difference, most of the III-As and III-P materials demonstrate WZ formation of NW with ZB inclusion. Besides, for the highest ionicity value, III-N groups show pure WZ phase both in bulk and NW structure [155]. A table containing ionicity information of III-V materials can be found in Ref. [154, 155]. In a nutshell, the ZB crystal phase is assumed to be more stable in III-Sb NWs since relatively high energy is required to transform into a WZ phase. Hence, no WZ or high order of polytypisms are seen in the InSb NW. Nevertheless, only low ionicity crystal stability may not be good enough

2: See Chapter 3 for examples.

to explain the reason for the pure ZB phase. Confusion arises when the nearby ionicity value of GaAs (with InSb) demonstrates WZ NW with ZB defects. Thus, other factors may also play a role in defining the InSb crystal.

It has been reported [155–157] that, a critical diameter may dominate the crystal phase transition of WZ to ZB in the NWs. For InSb NWs, theoretically predicated critical diameter to transform into WZ is very small, in the range of 10-20 nm [155], which may be experimentally challenging in InAs assisted InSb NWs. The InSb NWs grown in this thesis are > 80 nm in diameter, and hence, more favorable to ZB crystal. Even so, the critical diameter effect on the InSb crystal may be arguable, since some crystal defects on large diameter have already been observed [158]. Eventually left us to consider the supersaturation and growth conditions of InSb NWs for being pure ZB. Mandl et al. [159] experimentally demonstrated with In-Sb catalyst particle that, the defect formation of InSb NWs depends on the Sb concentration of the catalyst. It has been reported that, with low to high Sb concentration, the InSb crystal phase shifts from pure ZB to mix crystal to long WZ segment. Au assisted InSb typically demonstrates a very small Sb concentration on the catalyst particle and mostly In-Au alloy, as shown in Figure 2.7**h**. Such a small Sb concentration helps to grow single-crystalline ZB InSb as presented in Figure 2.6 and Figure 2.7. The high-resolution TEM images in both cases show defect-free ZB layers (post-growth analysis) in the catalyst particle, which favors solidifying single-crystalline InSb stacks. As shown in Figure 2.7**g**-**h**, $AuIn_2$ alloy creates a perfect epitaxy with InSb segment maintaining the same crystal symmetry and very close lattice constant. $AuIn_2$ alloy (FM3M) shows a lattice constant of 6.51 Å, meaning only 0.4% residual mismatch with InSb (6.48 Å), that leads to the disorder-free InSb crystallization.

2.6 Thin Film Epitaxy on Semiconductor Nanowire

Understanding the controlled growth of semiconductor NWs from previous sections, now I am going to move our focus on hybridizing semiconductor NWs with a thin metal film. Thin-film growth on semiconductor planar structure is well-studied and opened enormous opportunities for semiconductor industry [161–166]. As mentioned before, with the recent proposal of topological superconductivity in hybrid NW system, investigation of thin-film growth on semiconductor NWs is in high demand [29, 34, 44, 51, 167, 168]. Here, the concentration will be on growing thin-film *in situ* right after the NW growth. First, I will explore the theoretical understanding of thin film growth on NW.

Thermodynamically stable and continuous metal thin film on the semiconductor NW facets is challenging due to the limited temperature space and growth kinetics. As a result, a non-equilibrium growth parameter window is required to grow a uniform metal film on the semiconductor. The morphology of the metal thin film directly depends on the growth surface and the kinetics of the adatoms on that surface, which is determined by the parameters like temperature and beam flux, that we

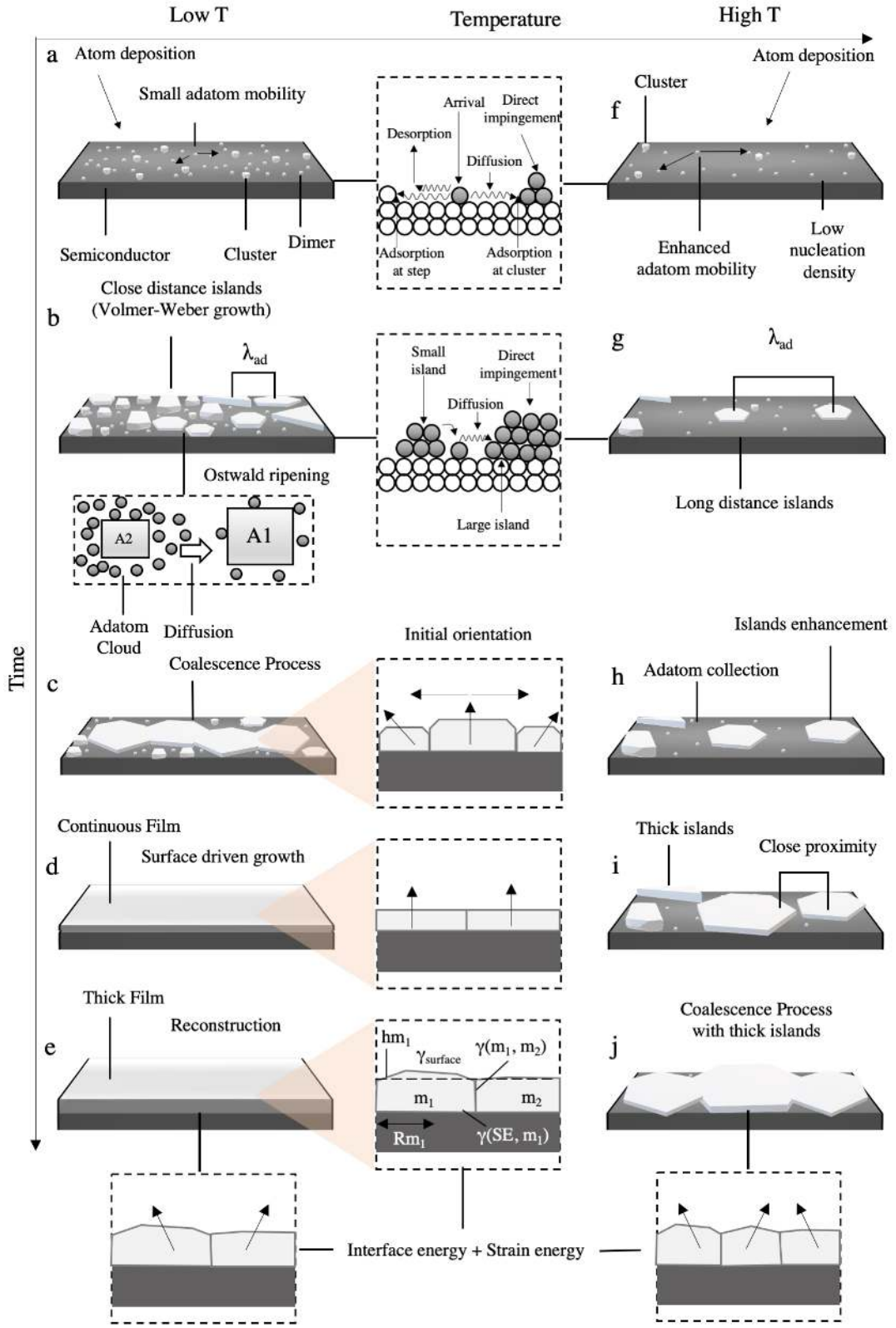

Figure 2.8: Thin film growth on semiconductor. Thin metal film growth on semiconductor surface as a function of time and temperature. (**a-e**), stage by stage metal film growth at low temperature (T). At low T, adatom diffusion length (λ_a) is small, leading to close proximity islands that merge and create surface driven thin film. (**f-j**), Metal film evolution at high T. Here, λ_a is big, resulting in largely spaced islands. Continuous film may create in long growth run. The idea of the schematic is adapted from Ref. [52, 160]

control during the growth. Thin metal film growth can be divided into three stages: nucleation stage, islands growth (surface driven growth) and grain boundary evolution.

Nucleation Stage (Adatom Diffusion and Temperature Effect)

Metal atoms impinge on the semiconductor surface with an average kinetic energy of the molecules, which is determined by the source temperature. After interaction with the surface, the atoms compromise their kinetic energy and get adsorbed on the surface (become adatoms). The adatom will diffuse randomly until it incorporates with a group of other adatoms, at the adatom cluster or other nucleation site. However, the initial incorporation site may not be stable for the adatom. Depending on the substrate temperature, atomic structure, surface chemistry and presence of impurities, [3] the potential difference and stability of different nucleation sites can vary a lot. Hence, the adatom may continuously triumph the potential barrier of one site and diffuse into another one in a random walk process, until it reaches the kinetically relaxed stage. Such jumping rate (Γ) of adatom from one diffusion site to another is determined by the attempt frequency (v) (comes from vibration frequency of the atom), substrate temperature (T), the potential energy barrier of diffusion (E_d). The relation can be described as the following:

3: Usually a significant effort is conducted to minimize the impurities in the surface, such as multiple cleaning before mounting in the growth chamber and later, high-temperature annealing to get rid of unintended impurities. However, some impurities may still be embedded due to the surface chemistry, which can create a potential difference.

$$\Gamma = v\exp(-\frac{E_d}{k_B T}) \tag{2.9}$$

Here, k_B is the Boltzmann's constant. If the adatom has energy bigger than E_d, then, it may stay a certain period on the substrate before it has a finite probability of desorption. In order to minimize the desorption rate from the substrate and endure the diffusion process, E_d requires to be smaller than the desorption energy. As we can see from the equation 2.9, substrate temperature plays a crucial role in adatom diffusion, which we will elaborate later. We can also relate Γ to adatom diffusivity or diffusion coefficient as follows [161, 169–171]:

$$D = \frac{\Gamma a^2}{z} \tag{2.10}$$

Here "a" is the distance between the incorporation sites, and "z" is the number of the neighboring sites, where adatoms can jump in. The factor "z" will be different depending on the nature of diffusion. Since we are considering 2D diffusion nature, here z = 4, leading us:

$$D = \frac{\Gamma a^2}{4} = \frac{v a^2}{4}\exp(-\frac{E_d}{k_B T}) \tag{2.11}$$

We can consider constant $a^2 v = D_0$,

$$D = D_0\exp(-\frac{E_d}{k_B T}) \tag{2.12}$$

Now, adatom travels a certain distance before get incorporated into the energetically favorable incorporation site. The time when an adatom starts traveling, to the time of incorporation is called adatom lifetime (τ_a), which can be expressed as [161, 172]:

$$\tau_a = \frac{1}{v}\exp(\frac{E_a}{k_B T}) \tag{2.13}$$

Here, E_a is the activation energy for the incorporation. Finally, adatom diffusion length λ_a can be expressed in relation with adatom coefficient and adatom lifetime:

$$\lambda_a = \sqrt{D\tau_a} \tag{2.14}$$

According to Ref [52, 87], λ_a can be expressed as a function of substrate temperature (T), chemical potential of the incorporation site (μ_a) and adatom density (ρ_a, which depends on the beam flux): [4]

$$\lambda_a\left(\rho_a, T\right) \propto \rho_a^{-\frac{1}{2}} \exp\left(-\frac{E_d - \delta\mu_a}{2k_B T}\right) \tag{2.15}$$

4: Check Ref [52] and Ref. [87] for detailed derivation.

From the equation 2.15, we can find the influence of beam flux and the temperature to determine the adatom diffusion length. From the exponential relation, T and μ_a has crucial role to govern λ_a. Lower substrate temperature reduces λ_a, as a result, adatom incorporates in neighboring incorporation site quickly. From this equation increment in ρ_a (high beam flux rate) will also decrease the λ_a. With decreasing λ_a adatoms will incorporate quickly reducing ρ_a. Hence, low temperature and high beam flux are desirable for thin metal film growth on the semiconductor surface.

Figure 2.8 shows a schematic of thin-film evolution in all stages as a function of growth time and substrate temperature. Figure 2.8 **a-e** are the illustrations for low temperature condition, and Figure 2.8 **f-j** are scenarios for the high-temperature growth. Figure 2.8 **a** shows at sufficiently low-temperature, adatoms have small mobility (small adatom diffusion length), as a result, incorporates with nearest sites. On the other hand, in Figure 2.8 **f** with high-temperature, adatoms have more kinetic energy, hence, they are more mobile and do not incorporate in nearest incorporation site (long diffusion length). In a high enough temperature, the desorption rate of adatoms can increase significantly. Inset connected to Figure 2.8 **a** and **f** shows multiple events that can occur upon the arrival of an atom on the semiconductor surface depending on the diffusion barrier. As mentioned in the beginning, not only does the new arrival adatom diffuse, but also already incorporated adatom diffuses from one site to another. As a result, some clusters can get larger with attachment, while others shrink due to the detachment. It is reported that [160, 173], clusters with more atoms (more than two) are unlikely to lose atom due to the supersaturation, hence, they become the energetically favorable site to grow bigger. In other words, we can say that nucleation density on the substrate depends on the probability of two or more atoms incorporation together (making dimer) and the probability increased with ρ_a, which can be controlled by increasing incoming flux [160, 174]. If nucleation

density is n, it can be expressed as a function of incoming flux (f) and diffusivity (D) [70, 174, 175]:

$$n \sim \left(\frac{f}{D}\right)^{\frac{i}{i+2}} \exp\left(\frac{-E_b}{(i+2)k_bT}\right) \tag{2.16}$$

Here, $\mathbf{E_b}$ is the binding energy and "i" is the critical cluster size. Also, low temperature provides reduced λ_a, that increases the probability further to encounter adatoms to each other, whereas in high temperature, adatoms tend to incorporate with big cluster or step site. Hence, the nucleation density in Figure 2.8 **a** is more than Figure 2.8 **f**.

Islands Growth (Surface Driven Growth) and Coalescence

In the next stage of the thin film growth, the nucleation or incorporation sites (clusters, steps and others) grow larger with the continuous growth process and spread as islands on the semiconductor surface. Multiple parallel events take place during this island growth stage. Spacing between the larger clusters diminishes and they combine as an island. Direct impingement of the atoms from vacuum also plays a role in islands' evolution. In addition to that, the continual diffusion process of adatom along with detachment and attachment from the progressive nucleation sites contribute to the island dimension. Island growth and merging stage for low temperature is displayed in Figure 2.8 **b**-**c** and high temperature substrate is shown in Figure 2.8 **g**-**h**.

Size evolution of the islands (or grains) can be understood from Ostwald ripening process [176–178]. For simplicity of the explanation, let's consider the merging process of two nearby islands or grains, $\mathbf{A_1}$ and $\mathbf{A_2}$. As shown in Figure 2.8 **b**, adatom cloud is usually present around the islands. However, cloud density depends on the size of the islands. If we consider one island is bigger than the other one, $\mathbf{A_1} > \mathbf{A_2}$, as shown in Figure 2.8 **b** inset, then a gradient in cloud density between $\mathbf{A_1}$ and $\mathbf{A_2}$ will be seen, which is determined the binding energy of the adatom on the surface. Binding energy on the surface depends on the curvature of the island and the island size is inversely related to the curvature [160, 178, 179]. Hence, there will be more detachment of the adatom from $\mathbf{A_2}$ island, which means the surrounding adatom cloud will be larger compare to the $\mathbf{A_1}$ islands. A diffusion from large cloud (around $\mathbf{A_2}$) to small adatom cloud (around $\mathbf{A_1}$) will happen. As a result, the adatom density around $\mathbf{A_1}$ island will increase significantly, which will lead to enhanced incorporation of the adatom on $\mathbf{A_1}$ island. With the continuation of this process, the size difference will increase, and bigger island dominates over the smaller neighboring islands.

The crystal orientation of the islands can be determined by the semiconductor surface or arbitrary orientation and hence, can differ from island to island [160]. Magnified section in Figure 2.8 **c** shows the orientation with arrow. Depending on the island size (number of atoms), inaugural crystal orientation may not be the energetically favorable one and subjected to change depending on the growth time. If the island with a small number has a high energy crystal phase orientation initially, in a longer growth

period it will change to a lower energy crystal phase orientation. An exception can happen due to the kinetic restriction, in that case, the surface structure may change [160]. On the other hand, bigger size islands are kinetically bound to remain in their initial crystal orientation and cannot change with further growth. Hence, the size of the islands plays a crucial role to determine later crystal orientation [70]. It can be presumed that, eventually, lower surface energy orientation will dictate over a long growth period.

The coalescence process begins when islands are grown big enough to come into close proximity, as shown in Figure 2.8 **c**. When islands merge, they start reforming the interface to attain minimum surface energy. During this process, a grain boundary is formed in the interface of two islands due to the plastic deformation of the impinging island [180, 181]. Now, the time frame of this coalescence process depends on the size of the islands, where process time for the larger island is slower compare to the smaller one. The coalescence period τ_{coal} can be expressed as following [160, 182]:

$$\tau_{coal} = \frac{R^4}{B} \tag{2.17}$$

Where, R is the radius of the curvature and B is the coalescence parameter and can be expressed as a function of diffusion co-efficient [182]:

$$B = \frac{D\gamma\Omega^2 S_0}{kT} \tag{2.18}$$

Here, γ is the surface energy, Ω is the atomic volume and S_0 is adatom density. τ_{coal} plays a role defining the crystal shape when multiple big islands interact at the same time. From the equation 2.18, we can also see τ_{coal} has a dependence on temperature.

As depicted in Figure 2.8 **d**, at low temperature small islands can merge and create a continuous thin film on semiconductor surface, where lowest surface energy dominates over other. On the other hand, in high temperature, large islands are still sparsely spaced (see Figure 2.8 **i**), hence, surface driven continuous film cannot form.

Reconstruction and Grain Boundary

Diffusivity (D) of the adatom and hence, adatom diffusion length (λ_a) change to a large extent depending on whether adatoms are on semiconductor surface or grown metal surface. During surface driven growth (discussed previously), crystal reconstruction happens through minimization of surface energy. On the other hand, in growth time when metal is covered on the semiconductor surface, (as shown in Figure 2.8, in low temperature it happens early) crystal reconstructions mainly happen through minimization of the grain boundary energy.

Surface diffusion happens through the grain boundary and mitigates the chemical potential of the system, leading to the reconstruction of the grains in an equilibrium shape. The crystal orientation of the merged structure depends on the individual crystal orientation of the islands

before merging and evolution of grain boundary, which will be elaborated next. If the islands have the same crystal orientations then the new merged island will also follow the same. However, if the islands have different crystal orientations, then the final merged island may follow one of their parents' crystal orientations depending on the migration of the grain boundary. On the other hand, if the kinetic energy barrier of the grain boundary is very high to overcome, then the grain boundary will be stationary, where two crystal orientations may stay together [52, 70, 183]. Merged grain boundary with single crystal orientation is shown in Figure 2.8 **d** magnified section. A detailed theoretical framework for grain growth mechanism is demonstrated by Krogstrup et al. [52], which is summarised below for a further understanding of grain boundary effect on crystal morphology.

Let's consider, $\mathbf{m_1}$ and $\mathbf{m_2}$ are two neighbouring grains. The average growth rates of the grain can be expressed as a function of chemical potential [52]:

$$\Delta\Gamma_{(m_1 m_2)} \propto \exp\left(-\frac{\delta g_{m_1 m_2}}{k_B T}\right)\left(\exp\left(\frac{\delta\mu_{m_1}}{k_B T}\right) - 1\right) \tag{2.19}$$

The growth of $\mathbf{m_1}$ will be driven by the chemical potential difference between $\mathbf{m_1}$ and $\mathbf{m_2}$:

$$\delta\mu_{m_1} = \frac{\partial G}{\partial n_{m_1}} - \mu_{m_2} \tag{2.20}$$

Here, "G" is the Gibbs free energy and "n" is number of atoms in $\mathbf{m_1}$. According to the above equation, the value of $\mu_{\mathrm{m_1}}$ determines whether $\mathbf{m_1}$ expands over $\mathbf{m_2}$, remain same or diminish. Hence, further elaboration of $\mu_{\mathrm{m_1}}$ will provide the understanding behind thermodynamic driving force of reconstruction and grain boundary mobility. $\mu_{\mathrm{m_1}}$ can be derived as a function of two core parameters of the metal film: 1) height or thickness of $\mathbf{m_1}$, $\mathrm{h_{m_1}}$ and 2) in-plane radius curvature of $\mathbf{m_1}$, $\mathrm{R_{m_1}}$ [52]:

$$\delta\mu_{m_1}^{R_{m_1}} = \Omega\frac{\gamma_{surface,m_1} + \gamma_{m_1\|m_2}}{h_{m_1}} + \Omega\frac{\gamma^{j}_{m_1\|m_2}}{R_{m_1}} + \frac{\Omega\mathbf{S}\varepsilon^2}{(1-v)} - \mu_{m_2}^{R_{m_2}} \tag{2.21}$$

Here, γ is the interface energy, **S** is the shear modulus, "v" is the and Poisson's ratio. The equation 2.21 is divided into three sections, where the first part dominates in the initial stage when the thickness of the film is small, which has been discussed in the previous section. The second and third terms play a role when metal films grow thicker, which is our matter of interest in this section. As we can see from this equation, the surface energy is exchanged into the interface or boundary energy (second section) and strain energy (third section). If the grain boundary energy of $\mathbf{m_1}$ is high, it will feel the driving force towards equilibrium by diffusing materials into the neighboring grain $\mathbf{m_2}$. The crystal orientation may alter from the initial one depending on the value of $\mu_{\mathrm{m_1}}$, if it is large enough to overcome the reconstruction barrier.

2.7 Al Growth on Nanowire

With theoretical understanding, I will now explore the experimental results of thin-film deposition on semiconductor NWs. In this section, I am going to focus on the classical Al film growth on NWs with high interface quality. Al is still the most used metal for topological SE/SU quantum devices. Compatibility with the standard fabrication process, uniform film morphology with epitaxial quality and passivation possibility with native oxide are few reasons behind the popularity [52]. Together with the low-temperature deposition technique (as discussed in the previous section) and being a well-studied group III material, no customized state-of-the-art equipment is required for depositing Al in MBE (compared to other dedicated materials). As a result, Al-based SE/SU hybrids are more accepted research platform and several successful devices have already been demonstrated with this hybrid. [64, 184, 185].

Remark 2.7.1 The Al hybridization with NWs presented in this section are part of the research project of "Paper 4" (In Preparation).

Thin Al film ($\leqslant 15$ nm) on semiconductor NWs is required to withstand a high magnetic field without suppressing the superconductivity. However, thermodynamically stable such thin film is challenging to grow. Keeping this in mind, in this experiment, I will grow Al on InAs and InSb NWs.

Al Thin Film on InAs NWs

As discussed before, the semiconductor NWs are grown on InAs (111)B substrate and *in situ* deposited Au are used as catalyst particles. Besides, hybridization is also performed on the NWs, grown from InAs (100) substrate with (111)B etched trenches. [5] For Al deposition, standard calibrated Al flux is used from the MBE system. After NW growth [6], the substrate temperature is cooled down to $\sim -36^{\circ}$C over 8-10 hours. The substrate is aligned with an angle with respect to the Al source for the selective depositing on the NW facets (for the half shell case). On the other hand, for a full shell case, deposition is done with the continuous rotation of the substrate. A detailed deposition technique is presented in the "Experimental Details" section.

5: Detail about this will be discussed in chapter 3.

6: See "Experimental Details" for semiconductor NW growth.

In this experiment, Al is grown on the <0001> directional InAs NWs. NWs are grown hexagonal, and deposition is performed on the selected facets along the NW. The <0001> direction on (111)B substrate provides options to deposit Al on any of the six $\{1\bar{1}00\}$ facets. In Figure 2.9**a**, Al is deposited on two-facets of the InAs NW with a stationary substrate and fixed angle. The deposition direction is shown with a white arrow in Figure 2.9**a** and the inset schematic shows two-facets of Al on hexagonal InAs cross-section. Al growth direction can also be understood from the shadow on the substrate, as shown in the Figure 2.9**a** inset. InAs NWs diameter are in the range of 100-150 nm with well-defined facets, can also be seen in the magnified inset image. An example of long InAs segments is presented in Figure 2.9**b**, where a clear distinction between InAs and ~ 15 nm continuous Al thin film is observed. The requirement for thermodynamically driven thin film formation on the NW is discussed in the theory section. Following that, Al is grown at low substrate temperature and with high flux rate leading to complete Al wetting on the NW facets. High-resolution TEM of the interface is

presented in Figure 2.9**c**, where a sharp interface between InAs and Al is observed.

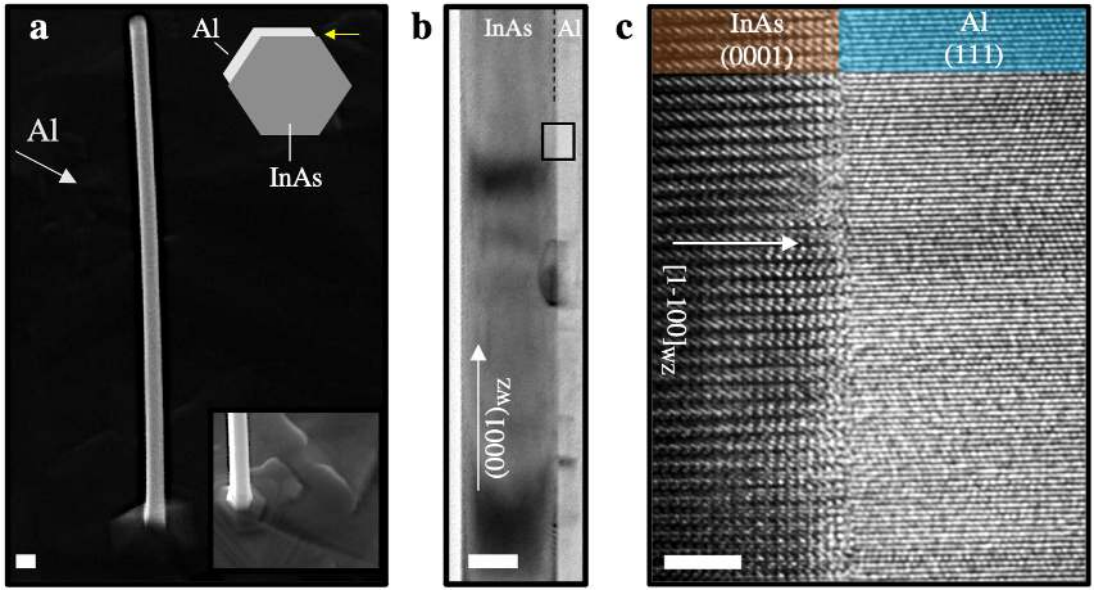

Figure 2.9: Thin Al epitaxy on InAs NWs. a, 30° tilted SEM image of InAs/Al NW. White arrow shows the Al deposition angle. The schematic shows the cross section of hexagonal NW with two-facets Al. Yellow arrow shows the viewing angle in the TEM inspection. Inset SEM image shows the well-defined facets of the wire with the Al deposition shadow on the substrate. **b**, Low magnified TEM image of the NW segment showing no crystal defects in the InAs and also an uniform Al thin film deposited along the NW. White arrow shows the growth direction of the NW. **c**, High resolution TEM image from highlighted area, which shows sharp interface between InAs and Al. (111) out-of-plane orientation Al film is grown on InAs $\{1\bar{1}00\}$ facets. Scale bars for (a), (b) and (c) are respectively 100 nm, 50 nm and 5 nm. (TEM presented here is performed by Martin Espineira Cachaza at DTU CEN)

Recalling the facts that crystal orientation of Al will depend on the thickness of the grown film, surface energy, interface energy and grain boundary mobility. With an initial thickness, the continuous film is expected to form, where the crystal orientation is driven by surface and interface energy. Later, with continuous growth and increased thickness, the grain boundary energy is expected to reconstruct the crystal orientations. According to Ref. [52], Al on InAs forms a large domain with a small residual mismatch, hence, from equation 2.15, moderately low temperature will help to drive initial thin film with a certain orientation. In the following articles [52, 67, 70, 186], two out-of-plane Al orientations, (111) or $(11\bar{2})$ are reported on the InAs $\{1\bar{1}00\}$ facets. In fact, (111) is the low energy Al plane normal to the $\{1\bar{1}00\}$ facets. Thus, it can be expected from the theory that, with initial thickness, InAs surface energy minimization will lead to a (111) out-of-plane Al film perpendicular to the NW [52]. Consistent with this, in Figure 2.9**c** we also observe (111) out-of-plane orientation Al thin film perpendicular to the wire facets. Furthermore, transition from (111) to $(11\bar{2})$ plane is reported with the thicker film [52]. In a long-growth time, according to equation 2.21, boundary energy and interface energy minimization determines the crystal orientation. High boundary energy grain will diffuse into the neighboring lower one and drive for the reconstruction until reaches to an equilibrium. $(11\bar{2})$ out-of-plane orientation of Al shows single crystalline and small residual domain mismatch with wire facets, hence changing from (111) to $(11\bar{2})$ plane is more energetically favorable for thick Al

film. However, in Figure 2.9**b** and **c**, $(11\bar{2})$ plane is not observed, which implies that the Al thickness is still in the lower side and hence, crystal orientation is surface driven, resulting in only (111) Al planes.

Al Thin Film on InSb NWs

Similar to the previous section, InSb NWs are either grown from InAs (111)B substrate or (111)B trenches. As elaborated in section 2.5, InSb NWs are grown with InAs stems. [7] The diameter of InSb NWs varies from 120 nm to 150 nm. Al is deposited in two facets out of six {110} ZB facets. Figure 2.10**a** shows a standard <111> directional ~ 120 nm InSb NW grown on InAs (111)B substrate. Al deposition angle is shown with the white arrow. In the cross-section schematic, Al-grown facets are shown, and also viewing angle for the imaging is indicated with a yellow arrow.

7: See section 2.5 for InSb NW growth details.

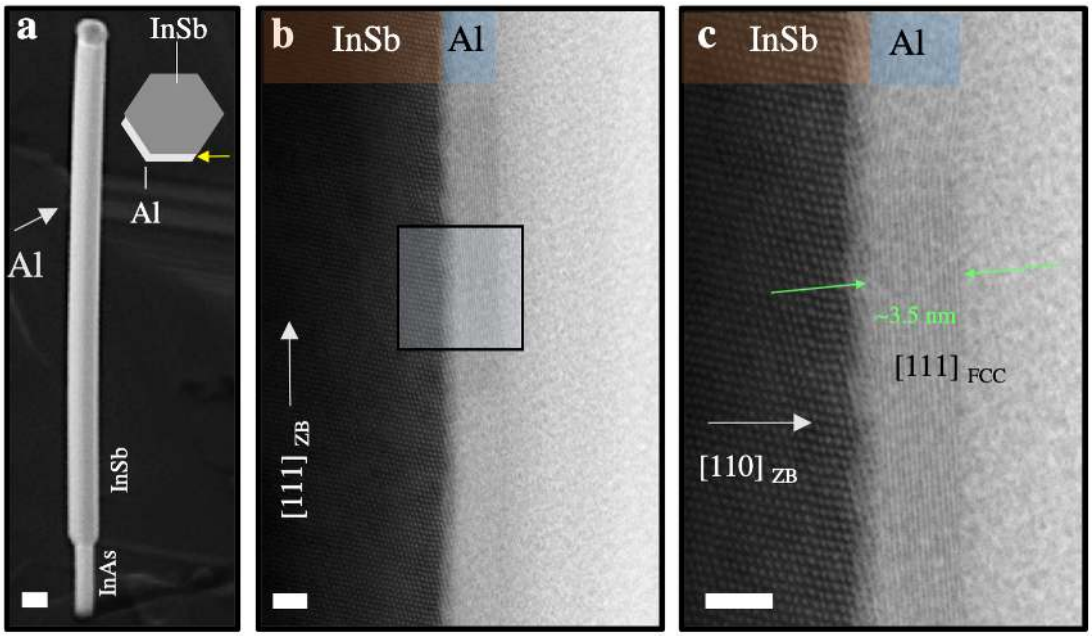

Figure 2.10: Thin Al epitaxy on InSb NWs. a, 30° tilted SEM image of InSb/Al NW. The white arrow shows the Al deposition angle. The schematic of hexagonal cross-section shows two-facets Al deposition that we intended in this experiment. The yellow arrow shows the viewing angle in the TEM inspection. **b**, High resolution TEM image of InSb and Al section. The arrow shows (111) growth direction. **c**, High resolution TEM image of the magnified section from panel (b). A clear and abrupt interface between InSb and Al is observed. InSb is ZB structure and Al is cubic structure. The arrow on InSb shows the <110> facets direction. 17 (111) Al planes are counted from the image referring to ~ 3.5 nm thickness. Scale-bar for panel (a) is 100 nm and panel (b) and (c) are 2 nm. (TEM presented here is performed by Emrah Yucelen at Microsoft Quantum Lab, Delft.)

Figure 2.10**b** shows a low magnified TEM of hybrid InSb/Al, where a continuous and uniform Al segment can be seen in-contact with InSb. As drafted in the previous section, low temperature along with high Al flux drive the thin Al film formation, and the same parameters as InAs/Al are used for the InSb/Al hybridization. For interface quality analysis magnified HR-TEM section is presented in Figure 2.10**c**. The distinct interface of ZB InSb and FCC Al can be seen. Here, all the Al planes are <111> oriented on the {110} ZB side-facets (showed with white arrow). Al and InSb have a large lattice mismatch (4.05Å and 6.47Å respectively). Thus, an interfacial domain will form to minimize the interfacial strain

[52, 187]. Interfacial domain mismatch of 4% is calculated to be the best match combination between InSb and Al for 5 Al cubic planes and 3 InSb ZB planes [52]. It is reported that [52], for cubic metal like Al, <111> orientation on (111) ZB is favorable as the bi-crystal symmetry allows epitaxial match and extensive single crystal section, which is also observed in Figure 2.10**c**. Further, as the film is thin enough and no grain boundary assisted reconstruction happened. This is also the reason why no strain assisted bending is observed in the NW, which is usually observed for much thicker shell and for the interfacial domain mismatch. [8] In total, 17 uninterrupted [111] Al planes can be counted from HR-TEM indicating to ~ 3.5 nm continuous film formation on the InSb facets. As mentioned earlier, thin Al film on the NW is important to withstand high magnetic field in the Majorana devices and Figure 2.10**c** is a possible demonstration of a uniform ultra-thin film on InSb NWs. In addition to that, the ternary composition of InAsSb is also an interesting material to explore with Al hybridization, and will be demonstrated in chapter 3.

8: See section 3.2 for examples of bending with thick Sn and Pb shell.

After exhibiting the thin film deposition, it is important to mention that, one should follow a careful fabrication process with InSb/Al hybrid. InSb/Al is susceptive to the high temperature and starts creating In/Sb-Al alloy immediately. Hence, no resist baking should be performed, which may damage the interface. Additionally, one needed to be careful about imaging as well, as high energy long exposure imaging may damage the NW. Therefore, a low energy short exposure SEM or performing AFM on the devices are better options.

Before wrapping up the discussion about Al hybridization on the NWs, I would like to note an important point about dewetting phenomena, when unloading or exposing to room temperature. Even if it is possible to grow such a thin metal film, it is away from the equilibrium condition. Therefore, with an elevated temperature during unloading from the growth chamber, Al film starts dewetting. Consequently, discrete islands of the Al film can be seen in the post-growth analysis. With a sudden increase in the temperature, the grains are reconstructed again towards the minimization of surface energy. To avoid this situation, it is possible to lock the Al film with a passivation layer. The advantage of Al is, a self-terminated AlO_x can be formed before unloading, that will help to confine and protect the film from dewetting. For this reason, we oxidize the Al hybridized samples for a certain period before unloading. [9] This procedure is also applicable for other deposited metals.

9: See the "Experimental Details" section for the detailed procedure of Al deposition and unloading.

2.8 Sn Growth on Nanowire

Sn (group IV material) has a wide range of applications spans in the arena of metal coating, soldering electronic devices and optoelectronics [188–193]. Recent discoveries have enhanced Sn's appeal to the energy applications (next-generation battery) [194], and topological insulator [195, 196]. Further, in the hunt for alternative superconductors with high $\mathbf{T_c}$ and $\mathbf{B_c}$ value [10] for topological superconductivity, Sn on semiconductor NWs opens a promising route [54, 71]. Being an unconventional chemical element, Sn exhibits two crystal phases depending on the temperature: $\beta - \mathbf{Sn}$ (also called white tin) and $\alpha - \mathbf{Sn}$ (also called gray tin) [197–204]. $\beta - \mathbf{Sn}$ is the high temperature stable phase with tetragonal crystal

10: See Table 2.1 on page 8

structure [72, 193, 202–204]. On the other hand, $\alpha - \mathbf{Sn}$ is the low-temperature stable phase with less dense diamond cubic structure [197–201]. Such different crystal structures also affect their electrical properties. $\beta - \mathbf{Sn}$ is metallic and demonstrate superconductivity below 3.7K [72]. In contrast, $\alpha - \mathbf{Sn}$ is a semi-metal and known for its use as a topological insulator [71, 195, 196, 205]. A transition between these two phases occurs around 13.2°C [206]. This phase transition also modifies their volume and can be attributed to the minimization of the surface energy at transition temperature [193]. During the thin film growth, both $\beta - \mathbf{Sn}$ and $\alpha - \mathbf{Sn}$ can coexist depending on the growth conditions and the surface energy [71, 202, 207].

Remark 2.8.1 The Sn hybridization with NWs presented in this section is part of the research project of "Paper 3" (In Preparation).

In this experiment, I will study the thin film formation of Sn on semiconductor NWs and the related growth conditions. I will further investigate the film morphology, their crystal structures on different NWs, and the associated challenges. Finally, the Sn hybridized NW devices will be presented, demonstrating superconducting transitions.

Thin Film Formation

Hybridization of Sn is performed in the EBPVD system, which is *in vacuo* connected with the MBE chamber, as shown in the MBE section. [11] For studying Sn hybridization, we grow InAs assisted InSb NWs on InAs (111)B substrate. Similar to the previous sections, the NWs are grown via *in situ* deposited Au catalysts, that ensures the maximum purity of the substrate. The interesting fact is, by growing such dual segments, we can simultaneously study the Sn deposition on both InAs and InSb NWs under the same growth conditions. [12] . The diameter of the InSb segment is maintained ~ 120-140 nm and the InAs segment is ~ 50-70 nm. With this diameter, hexagonal NWs will be well-faceted, and the interface energy will be comparatively minimized, which is important for the metal wetting on the semiconductor surface.

11: The detailed deposition process is presented in the experimental section.

12: See section 2.3-2.5 for detail understanding of the NW growth.

As presented in the theory section, adatom density and substrate temperature plays a crucial role by thermodynamically driving the element to assemble as a continuous thin film. From equation 2.15 and 2.16, a higher flux rate will increase the Sn adatom concentration, ρ_a on the semiconductor facets. Enhanced ρ_a will reduce the adatom diffusion length λ_a and will also increase the nucleation density ("n") on the NW facets. Thus, supplying high Sn flux will reinforce the possibility of a continuous thin film. Keeping this in mind, the Sn flux rate is set very high, ~ 5 Å/s. Moreover, λ_a and "n" on the NW facets are exponentially (equation 2.15 and 2.16) related to the substrate temperature, T and the chemical potential of the incorporation site, μ_a. Hence, only high Sn flux will not be able to play a role until favorable T and μ_a is present. Here, sufficiently low temperature is crucial to thermodynamically drive the Sn film to wet on the NW surface by making small λ_a. On the NW facets, μ_a will depend on the change in Gibbs free energy, which again will depend on the interface energy density (γ) between Sn and given NW surface, determined by the residual mismatch. γ also depends on the area of interface, "A" and strain energy in the later stage of the growth [52], as shown in equation 2.20 and 2.21. [13] InSb and Sn have low residual mismatch [71, 200, 207, 208], hence low interface energy. As a result, with the presence of low enough temperature, thermodynamic driving force

13: Detailed elaboration is provided in section 2.6.

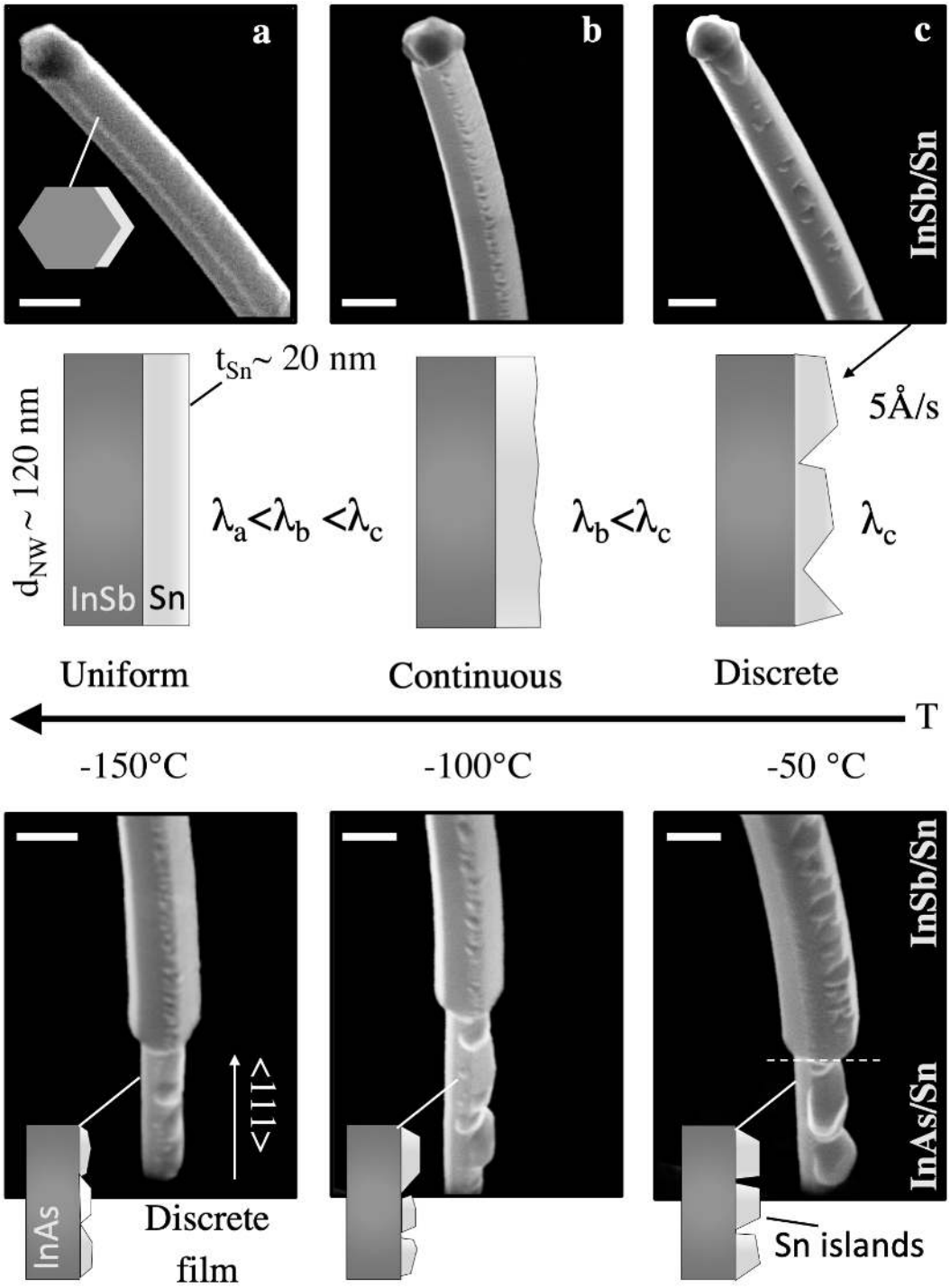

Figure 2.11: Evolution of Sn thin film on nanowire. a-c, shows progression of Sn film as a function of substrate temperatures. Substrate temperatures are varied from -50° C to -150°C. A constant Sn flux rate of ~ 5 Å/s is maintained for all the samples. NWs are grown around the diameter of ~ 120 nm and hybridized with 20 nm thin Sn for all the samples. For the InSb/Sn segments, the morphology of the Sn enhances with lower temperature. On the other hand, Sn on InAs sections remain discrete even with the lowest temperature. Scale bars for all the sections are 100 nm.

favors Sn to wet on the InSb NW facets making a continuous thin film. In contrast, InAs and Sn show high residual mismatch [70], leading to high interface energy density. Therefore, with the same growth conditions and low temperature (as InSb/Sn), Sn on InAs is expected to be a dewetted film. A further lower temperature is required to make a continuous Sn film on InAs.

Figure 2.11 experimentally proves the hypothesis of Sn film growth on NWs. InSb/Sn segments are shown at the top of the Figure 2.11 and InAs/Sn segments are shown at the bottom. Temperatures are varied from -50° C to -150°C and corresponding Sn film morphology is presented. At -50° C, [14] the morphology of the film is rough and in some places discrete, as shown in Figure 2.11**c**. The temperature here is not sufficiently low to decrease λ_c, that means adatoms are kinetically energetic and do not easily incorporate into the neighboring nucleation sites. As a result, the continuous film does not form in the surface driven growth stage. [15] Consequently, in the given 20 nm thickness of Sn film, morphology remains rough and discrete. In a thicker deposition, the continuous film will be formed, however, the morphology will persist as rough. In Figure 2.11**b**, the temperature is lowered to -100°C, which provides $\lambda_b < \lambda_c$. Here, more adatoms incorporate into the neighboring sites, leading to a continuous Sn thin film formed by 20nm thickness with improved film morphology. Nevertheless, small surface roughness is observed in some sections, that can further be improved by lowering the temperature. In Figure 2.11**a**, the substrate temperature is lowered to -150°C, granting $\lambda_a < \lambda_b < \lambda_c$, hence, adatom diffusion is almost confined and sticks where it lands. Therefore, surface-driven continuous film is formed within a few monolayers and in 20nm, atomically smooth Sn thin film emerges on InSb. Moreover, after a certain thickness, film morphology will become rough, as the grain boundary mobility will play a significant role to determine the crystal orientations, as shown in Figure 2.8 and elaborated in equation 2.21. On the contrary, as hypothetically predicted, Sn film on InAs remains dewetted film within the available temperature space. Not much effect is seen with the temperature variation range. Two possible approaches can be considered in this case (will also be elaborated later). First, with increased thickness, after a critical value, the islands will impinge on each other and a continuous film will be formed. Second, further lowering the temperature will kinetically lock the adatom diffusion and drive to wet the film. That said, further lowering the temperature will not be possible in our current system.

14: Thermocouple reading in the PVD chamber, the real substrate temperature can be much lower.

15: Please see the theory section "Islands growth and coalescence" paragraph for details.

Structural Analysis

With the uniform deposition of Sn shell, an extensive study is performed to evaluate the crystal structure of the film. Figure 2.12 **a** presents a micrograph of continuous and homogeneous 20 nm Sn shell morphology on two-facets of the InSb. A slight bend on the hybrid NW is observed that can be attributed to the different thermal expansion coefficient of both materials, experienced due to the elevated temperature while unloading the sample [52, 54]. Thus, in TEM analysis a slim tilt is also observed in the InSb/Sn interface, that supposedly doesn't have any effect on Sn morphology. The continuous film initiates when InSb reaches to full diameter. [16] Prior to that, no Sn is observed at the curvature of the InSb segment (right after InAs/InSb interface) as shown in Figure 2.12 **b**. This is due to the high surface energy in the curvature section or shadowed by the thick InSb diameter section. Similar to the previous report [71], we also observed polycrystalline Sn film on semiconductor NWs. Simultaneously, defect-free and planar-defected regions are noticed in the Sn shell, which is valid for several examined NWs in TEM. Figure 2.12 **c** and Figure 2.12 **d** shows perfect epitaxy of InSb and Sn. Careful

16: See section 2.5 for understanding of InAs/InSb interface and diameter change

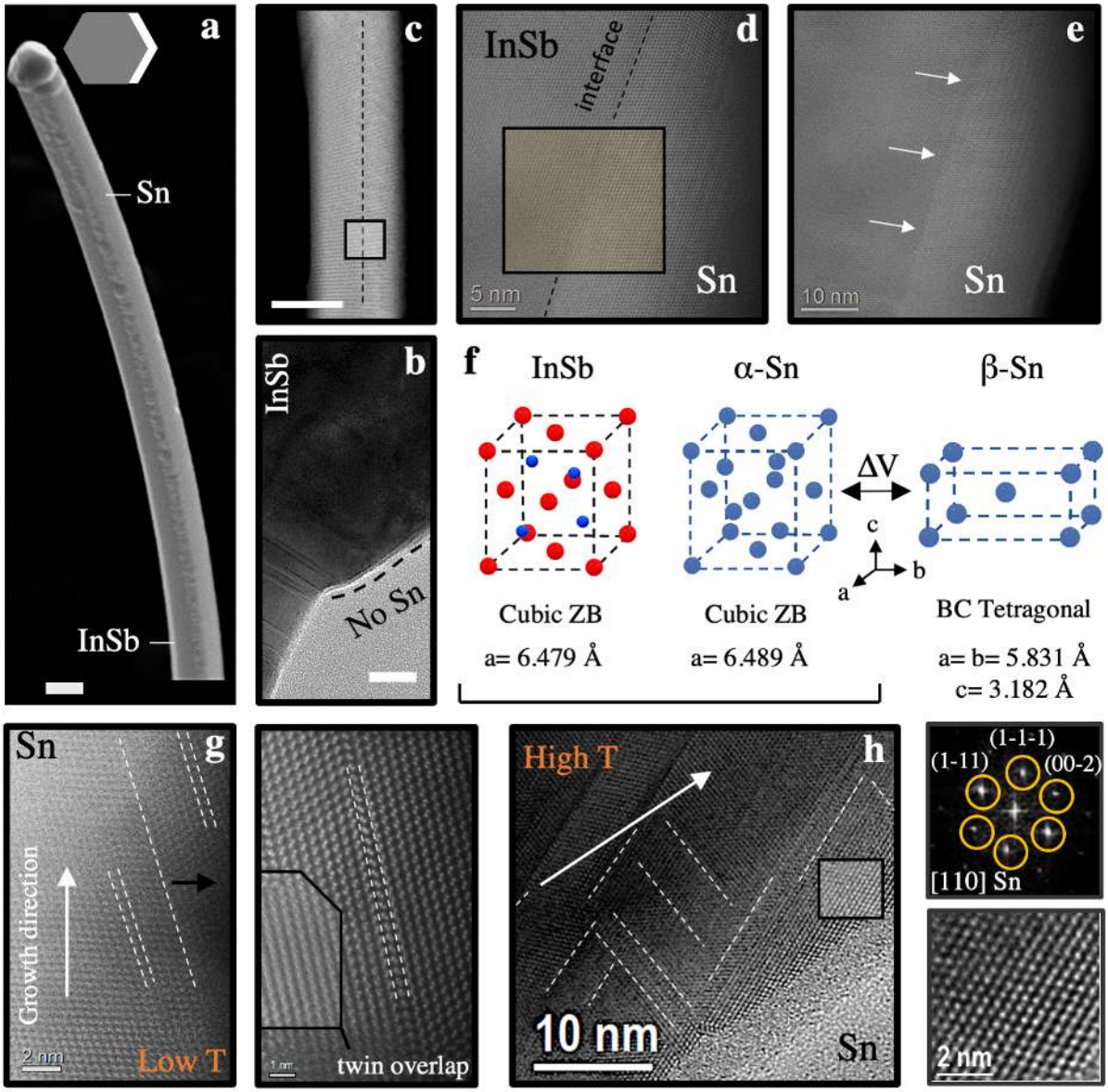

Figure 2.12: Sn epitaxy on InSb NWs. a, Tilted scanning electron micrograph (SEM) of InSb NW hybridized with Sn thin film. A uniform layer of Sn segment can be distinguished. **b**, InAs-InSb interface, where no Sn film is observed in the initial curvature region of InSb. **c**, Transmission electron microscopy (TEM) of a section from InSb/Sn NW. The black dotted line indicates the interface between two segments. **d**, Magnified high-resolution TEM from highlighted section of panel (c). Epitaxial Sn segment on InSb with interface line can be seen. No crystal defects in both sides are found. **e**, Further, magnification in the interface area implies cubic phase crystal both in InSb and Sn section. InSb segment demonstrates cubic ZB crystal phase, which we have discussed in section 2.5 of this chapter. On the other hand, $\alpha - \mathbf{Sn}$ demonstrates cubic crystal. Hence the epitaxial section is contribution from ZB InSb and $\alpha - \mathbf{Sn}$. **f**, Crystal structure of InSb and both $\alpha - \mathbf{Sn}$ and $\beta - \mathbf{Sn}$ with their corresponding lattice constant. **g**, HR-TEM from other section of the film showing multiple defects on the Sn crystal. White dashed lines show of twinning in the {111} plane oblique to the growth direction (white arrow) for low temperature film. Magnified section in the right shows clear picture of the twining event. The highlighted section shows (-1-11) twin overlaps. **h**, Sn film in high temperature, multiple planar defects in random orientation, unlike low temperature film. Arrow shows the growth direction and dashed lines show the defect orientations. Diffraction pattern in the right from non-defective highlighted segment shows [110] plane $\alpha - \mathbf{Sn}$ Sn. Scale bars for (**a**), and (**c**) are 100 nm. Scale bar for (**b**) is 20 nm.

examination on both sides of the interface reveals a cubic crystal structure with almost the same lattice constant. As shown in Figure 2.12 **f**, InSb has ZB crystal structure with lattice constant a~ 6.479 Å and $\alpha - \mathbf{Sn}$ phase has similar cubic structure with a lattice constant a~ 6.489 Å. Therefore, with lattice mismatch ϵ ~0.15%, it is very difficult to distinguish between both elements, that leads to the less contrasted interface even with HR-TEM.

Conversely, β − **Sn** has a large lattice mismatch with InSb that would provide clear contrast in the interface. A well-known phenomenon of Sn is the transition between both phases depending on the growth condition, which also modifies the crystal volume (**ΔV**) about 27% [209].

As shown in Figure 2.12 **g** and Figure 2.12 **h**, several planar defects appear in different sections of the shell. The defect characteristics seem to be dependent on the growth temperature. Figure 2.12 **g** shows TEM analysis of the region from low T grown shell, where multiple twining events can be seen. In low T samples, such twining events are only seen in the {111} planes oblique to the growth direction, as highlighted with dashed lines. There are no other directional defects are observed in low T samples. In contrary, in the high-temperature Sn shell (continuous but less uniform), presented in the Figure 2.12 **h**, planar defect density increases substantially. Defects appear in multiple directions including periodic twining perpendicular to the growth direction, that leads to the frequent alternation of the Sn crystal orientation along the shell. Eventually, makes it difficult to understand the right crystal phase. The places with perfect epitaxy and single-crystalline quality can easily be identified as cubic phase α − **Sn**, as shown in the diffraction pattern and HR-TEM inset in Figure 2.12 **h**. In our analysis from both low and high-temperature shells, it is observed that a high amount of α − **Sn** segments are present in the shell. Especially, investigating low-temperature samples, where more perfect epitaxy is observed, indicate the large domination of α − **Sn** domains. This convinces us to state that, our growth condition of low T, high flux rate together with InSb surface energy is favorable to grow more α − **Sn** shell, compare to β − **Sn**. In fact, we cannot unequivocally identify β − **Sn** in our TEM analysis. However, we cannot exclude the certainty of β − **Sn** presence in the shell and co-existence of both phase, as reported in Ref. [71]. In the electrical measurements (will be presented later section), most of the devices evince superconducting transition around 3.9K or higher. This can only come from the existence of β − **Sn** in the shell, which will proximitized the α − **Sn** segments (as α − **Sn** is semi-mental, and do not manifest superconductivity in our given shell thickness). Presumably, defect density and a lower concentration of β − **Sn** sections in the samples make it difficult for us to clearly identify them in the post-growth TEM investigation.

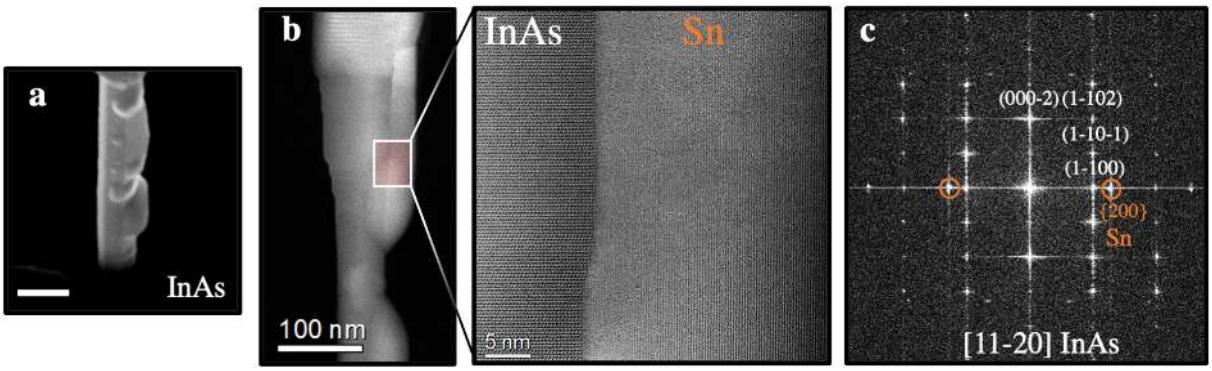

Figure 2.13: Sn growth on InAs NW. a, Tilted SEM image of the InAs/Sn segment (stem), where Sn seems to discrete faceted islands. Scale bar is 100 nm. **b**, Low magnification TEM of a InAs/Sn section. Magnified high resolution TEM in the right shows defect-free single crystalline quality of Sn grain on InAs. However, due to the high difference symmetry, no epitaxy is observed in the interface and Sn seems to be out of axis. **c**, Diffraction patterns confirms (orange circles) out-of-plane Sn direction in {002} Sn planes.

Next, Sn growth phenomena on InAs NW segments (that we used as the stem) are examined. As elaborated in Figure 2.11 and presented in Figure 2.13 **a**, Sn deposition on InAs leads to discrete and randomly oriented faceted-islands. In contrast to InSb/Sn, low index domain match for InAs and Sn induces large residual mismatch [52, 70]. This leads to the high interface energy between InAs and Sn. Eventually, a significant thermodynamic driving force is required to wet Sn on the InAs surface. As a result, Sn remains separated islands in our given growth conditions and limited reach to the lower substrate temperature. Continuous islands can be achievable by further lowering the substrate temperature, which will completely freeze the adatoms. Therefore, quick island formation and coalescence process will lead them to a thin film. Though, such a film will be very susceptive to elevated temperature and hence, a passivation layer would be needed to confine the film. A passivation layer can be done with thin Al film [71]. Furthermore, continuous Sn thin film on InAs can also be attainable if we increase the adatom concentration or the thickness of the film. After a critical thickness, the islands will merge and grain boundary evolution will determine the crystal orientation. The critical thickness will be determined by the substrate temperature, adatom density and island size. [17] . In such cases, the film morphology can be rough compare to the InSb/Sn. Similar phenomena are observed for Pb on the InSb surface and will be shown in Chapter 3.

17: Described in section "reconstruction and grain boundary".

In the TEM analysis of InAs/Sn crystals, no planar defects are observed in the several examined samples, which is opposite to InSb/Sn samples. Although the discrete grains are not in-axis with InAs surface due to the high residual mismatch, but are mostly single crystalline. We also observed a domination of $\alpha - \mathbf{Sn}$ film due to our growth condition as shown in high resolution image of Figure 2.13 **b** and confirmed with diffraction pattern in Figure 2.13 **c**. As we can see from Figure 2.13 **b**, high difference symmetry and residual mismatch restrain Sn to exhibit epitaxial interface with InAs, in contrast to what we have seen for InSb/Sn interface in Figure 2.12, **e**.

Migration of Sn into the InSb Core

For further investigation in the interface of InSb/Sn, we take a cross-sectional look at the structure. NWs are transferred into the SiO_x substrate using micromanipulator for this experiment. Later, protected with deposited AlO_x and Pt-C layer before preparing the cross-sectional lamella using FIB (focused ion beam). Parameters and procedures are discussed in the experimental section of this chapter. In total, three cross-sectional InSb NWs are examined with identical results. In Figure 2.14**a**, presents cross-section of one of the analyzed NW.

As we have seen in Figure 2.12, due to proximity atomic number between In (49), Sb (51) and Sn (50), it is difficult to attain elemental contrast during HAADF-STEM (High-angle annular dark-field imaging-scanning transmission electron microscope). The only contrast is seen can be attributed to the NW thickness variation. Hence, proper elemental identification can be done with energy dispersive X-Ray analysis (EDX) and electron energy loss spectroscopy (EELS). First, EDX analysis on the sample cross-section is performed, which provides the information of Sn presence at the edge of the facets with some additional signals of Sn

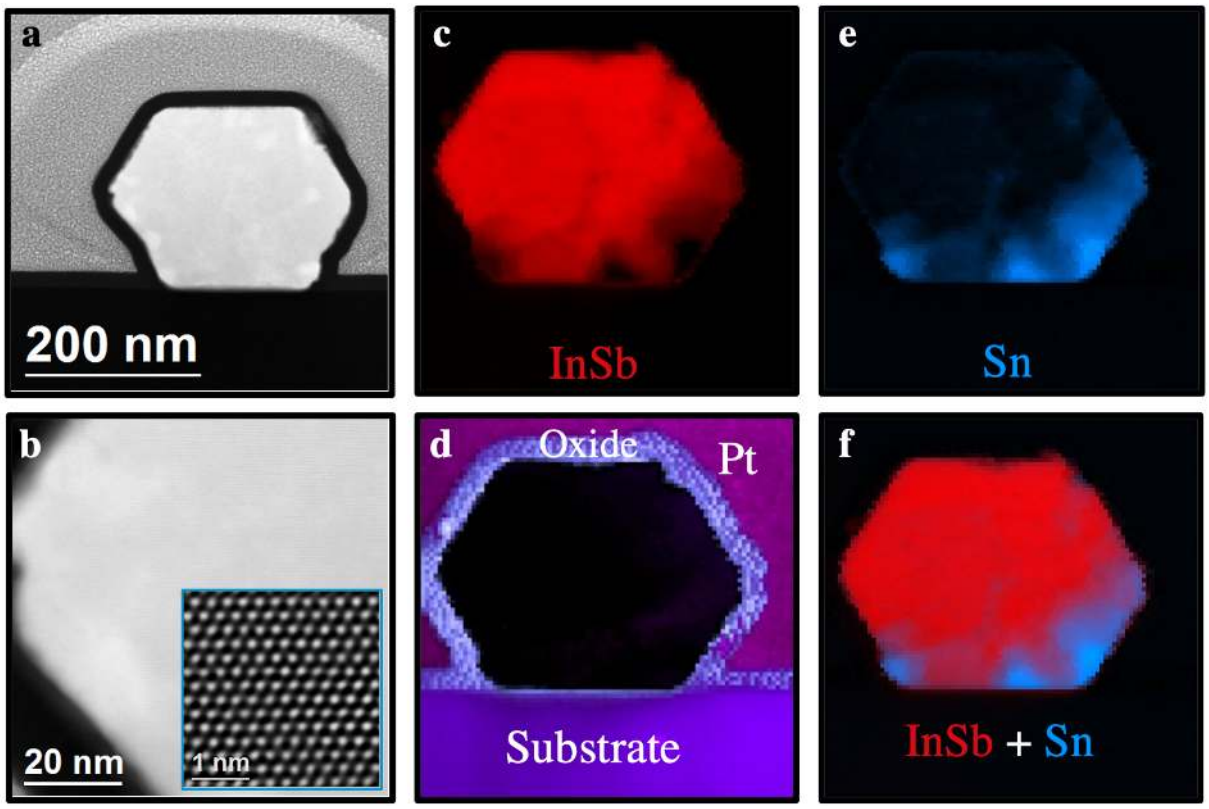

Figure 2.14: Diffusion of Sn during post-growth processing. a, High resolution TEM image of cross-sectional InSb/Sn structure. InSb/Sn is protected with AlO_x and Pt-C layer during TEM lamella preparation. **b**, Magnified structural analysis of InSb/Sn section, where defect-free ZB crystal is observed and presented in the inset. **c**, Elemental analysis with electron energy loss spectroscopy (EELS), where InSb section covers the whole hexagonal structure. **d**, EELS at the edge of the NW shows oxide layer and deposited Pt protection layer in purple color. In the bottom, SiO_x substrate, where NWs are transferred using a micromanipulator. **e**, Elemental analysis of the Sn on the NW facets. Sn presence can be identified on the bottom two facets. Unexpected spreading of the Sn signal is observed. **f**, A combined signal of InSb and Sn, where Sn diffusion from facets to the NW core is clearly observed. Sn thickness on the facets is almost reduced to half, and the rest is alloyed with InSb.

around the core of InSb, indicating a possibility of Sn migration. For precise distribution of the elements and further verification, an EELS map is presented in Figure 2.14 **c**-**f**, where panel (**c**) shows only InSb elements and panel (**e**) presents Sn distribution. As we can see from the map, Sn can be traced from the lower two facets of the NW. A wider range of Sn distribution can be observed ranging from the edge of the facets to the inside of the NW. In principle, Sn should only be present in the outer edge of the wire facets. It is believed that Sn diffused through the InSb crystal by making alloys with In. Such type of alloys still keep the same ZB crystal structure at [111] orientation, as shown in Figure 2.14**b**, that is assisted by the close lattice parameter (InSb=6.48Å and of Sn=6.49Å). Geometrical Phase Analysis (GPA) analysis is also performed to understand the crystal relaxation. No hidden strain that may be caused by the alloying or difference between the alloyed section and pure InSb section is observed in the GPA analysis, which further confirms lattice-matched alloying. Quantitatively around 11-19 nm Sn remains on the upper facets, and the rest is diffused in the InSb NW. Due to the overlap and peaks' shape, the core-loss signal of the EELS is not very conclusive. Hence, the map is performed in a certain way. It is attained by the spectrum from the low-loss region. Then, the spectrums are fitted with the corresponding plasmons for the individual pure compounds. Such kind of fitting leads to uncertainty in the individual compound segments

owing to the plasmon delocalization. However, the extracted information from the low-loss region is in good agreement with the understanding achieved from the core-loss region, with a small uncertainly spread.

Now, the question arises regarding the reason behind such alloying and in which stage it may happen: during growth or post-growth analysis. We examined the Sn thickness with AFM in post-growth analysis and found the exact thickness as deposited. The AFM was performed in the junction area, that provided accurate measurement. [18] On the contrary, the thickness of the Sn almost get halved during the migration, as shown in Figure 2.14 **f**. Hence, the possibility of alloying in the interface during shell growth can be eliminated. As discussed in the previous section, InSb/Metal thin film is very susceptive to the processing conditions, such as elevated temperature. This is also the reason why any heating is avoided during InSb/SU (Al or Sn) device fabrication [54, 71]. The processing for cross-sectional TEM involves multiple steps, where InSb/Sn is exposed to high thermal energy such as ALD or FIB. Also, long exposure in the high energy electron can cause inter-diffusion. However, that's unlikely in our case, as unstable materials can be easily identified through the evolution of structure in HAADF STEM or EELS analysis. From Figure 2.14 **a** the structure seems stable after beam exposure. Judging from different steps and activities related, our best assumption is the diffusion and alloying happen during the ALD step. As in this step, the substrate is heated to a high temperature for deposition of AlO_x, that leads to the intermixing of Sn and InSb. To summarize this section, InSb/Sn is sensitive to the increased thermal energy, and an immediate interfacial diffusion is possible to happen. This is eventually detrimental to the device performance. Therefore, it is suggested to optimize the steps carefully while processing InSb/Sn structure.[19]

18: Detailed about the junctions on NWs are presented in chapter 3.

19: Our optimized InSb/Sn device fabrication recipe is presented in the experimental section of Chapter 3.

Superconducting Transition

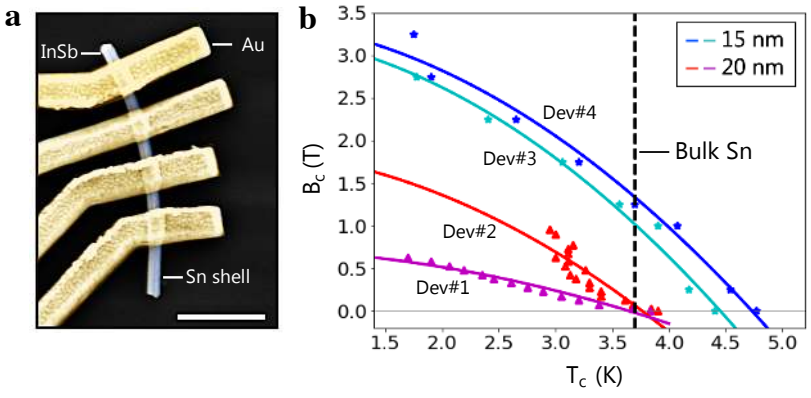

Figure 2.15: Superconducting transition on InSb/Sn devices. a, SEM image of the fabricated four-terminal device with InSb/Sn NW. **b**, The critical temperatures and magnetic field for four measured devices, where Dev#1-2 consist nominal 20 nm Sn shell and Dev#3-4 consists 15 nm Sn shell. (Device fabrication and measurements are done by Charalampos Lampadaris.)

Demonstrating the Sn epitaxy on semiconductor NWs and analyzing their structural properties in our given growth conditions, now we would like to investigate the electrical property of this hybrid system. We are particularly interested in hunting if Sn shell exhibits any superconducting properties, considering that our presented growth condition favors $\alpha - \mathbf{Sn}$ domination in the shell, which is a semi-metal. For this, we

fabricated four-terminal devices with InSb/Sn NW, as shown in Figure 2.15**a**. The diameter of the InSb NWs are ~ 150 nm and continuous Sn is deposited on three facets of the NWs. Careful device fabrication steps have been followed without any high-temperature treatment in order to avoid intermixing of Sn with InSb NWs. Detailed fabrication steps for InSb/Sn devices will be shown in the next chapter along with other devices. The superconducting transition of the four measured devices as a function of magnetic field and temperature is presented in Figure 2.15**b**, where two different thickness of the Sn are used: nominal ~ 15 nm and ~ 20 nm. The magnetic field is applied perpendicular to the NW. We can see from the data that all four devices demonstrate superconducting transition. Each data is collected from the maximum transition point in their corresponding applied magnetic field. The superconducting transition we observe despite of the presence of $\alpha - \mathbf{Sn}$ presumably due to the proximity effect. It is believed that the superconducting $\beta - \mathbf{Sn}$ phase in the Sn shell (which is not detected in TEM) proximitized the $\alpha - \mathbf{Sn}$ phase during measurement. The similar proximity effect of two phases with thin Sn film on InSb substrate was observed by Didschuns et. al. [202] and very recently reported on NW [71]. However, there are few other devices we measured that didn't show any transition. That leads us to believe that in our discussed growth condition, there is a percolation threshold of $\beta - \mathbf{Sn}$ phase, below which the Sn shell doesn't act as a superconductor (further investigation is ongoing). The measured all four devices also show transition temperature (at 0T) higher than the bulk Sn one (3.7K, presented by the dotted line). Further, critical temperature and field are dependent on the Sn shell thickness. Dev#3 and Dev#4 with nominal ~ 15 nm thickness show a critical temperature of ~4.6K and ~4.9K respectively at 0T. These two devices persist magnetic field up to 2.8 T and 3.3 T at 1.7K. However, Dev#1 and Dev#2 with ~ 20 nm nominal Sn shell demonstrate critical temperature of ~3.9K, and their persistency against the magnetic field are also dropped significantly. Hence, the data presented in Figure 2.15**b** recommends that the thinner Sn shell may provide a better superconducting platform with the enhanced critical temperature and field value. Besides, with the favorable thin film growth conditions presented in the previous section, it is possible to grow ultra-thin Sn film on InSb NW similar to Al (presented in section 2.6), which we will try in the future.

2.9 Conclusion

In conclusion, MBE-grown InAs and InSb NWs hybridized with Al and Sn are demonstrated in this work. Initially, growth details are discussed, where both types of NWs are grown from *in situ* deposited Au catalysts. InAs NWs can be directly grown from the InAs (111)B substrate, whereas InSb NWs are required a stem to initialize the growth. This is due to the low contact angle of Au in presence of Sb, which leads to the wetting of Au on the InAs substrate. Structural analysis on these materials shows a less-defective WZ phase for InAs and highly pure ZB phase InSb NWs. The high purity of ZB InSb is attributed to the low ionicity value, critical diameter range, and supersaturation condition of Au-In_2 alloy. Furthermore, a non-equilibrium metal film growth condition is presented to hybridize Al and Sn on these grown NWs. With low substrate and

high deposition flux, the continuous Al thin film can be grown on the InAs and InSb NWs. Here, a continuous Al thin film as low as 3.5 nm is demonstrated on InSb NWs. With the temperature growth map, it is shown that Sn forms an epitaxy relation with InSb, however, a dewetted morphology on the InAs NW. It is presumed that a further lower temperature would require to create a uniform Sn film on InAs NW. Structural analysis of the Sn shell shows $\alpha - \mathbf{Sn}$ domination, which is a semi-metal. However, the measurements in the four-terminal devices show a superconducting transition with a critical temperature larger than the bulk Sn. It is believed that superconducting property is exhibited due to the proximity effect from the limited $\beta - \mathbf{Sn}$ phase exists in the shell. Besides, varying the Sn shell thickness, it is observed that thinner shell exhibits higher critical temperature and magnetic field. For consistent device performance, further effort is required from the growth side to find an optimal condition to selectively grow $\alpha - \mathbf{Sn}$ and $\beta - \mathbf{Sn}$ phase on the NW.

2.10 Experimental Details

Substrate Preparation

Substrate fabrication for all types of NW growth is done either with InAs (100), InAs (111)B, or InAs (111)A wafer. InAs (100) substrates are used to create trenches and to grow angled NWs. Such (111)B trench creation involves multiple fabrication steps, which will be discussed in Chapter 3. [20] . Further, InAs (111)B substrates are mostly used for *in situ* Au assisted NW growth. *In situ* Au confirms the high purity of the growth substrate as no chemicals and process-related contamination or defects are induced. Au deposition steps on the (111)B substrates before growth will be discussed later in the NW growth step. In some cases, we also pre-pattern the InAs (111)B (or sometimes InAs (111)A) substrates for growth study. For patterning, we take InAs (111)B 2-inch substrate and spin coat the electron sensitive PMMA resist with 4000 RPM for 45 sec. Then, the resist is baked for 2 min at 180°C. Then, the substrate is patterned in the electron beam lithography (EBL, Elionix ELS-7000) system. The typical EBL parameters that we use: write field size: 60000 dots, 300 μm; current: 500 pA; aperture: 40 μm. After exposure, The resist is developed using, 1:3 MIBK: IPA for 45 sec and IPA for 30 sec. The sample is checked carefully with an optical microscope. If the resist is finely developed, the wafer is transferred to the metal deposition chamber (AJA evaporation system). After development, we try to move the sample in the metal deposition chamber as quickly as possible to avoid native oxide growth on the unmasked dots. Depending on our desired NW diameter $\sim$ 10-15 nm Au film is deposited with the rate of 1Å/s. Then, lift-off process is performed with the acetone. Initially, the sample is dipped into the acetone for 1 hour with 50°C heated bath. Later, clean acetone dipping is done until Au films are completely removed. The cleaning procedure is done with acetone (10 sec), IPA (10 sec) and milli q water (30 sec). Next, the sample is further cleaned with oxygen plasma ashing for 2 min. Finally, to adjust the substrate with our MBE growth holder, we cleave the 2-inch wafer into four quarters using a manual scriber. The growth from the pre-patterned substrate was not largely

20: See experimental section: "substrate fabrication" in chapter 3

presented in this chapter. Here, I mainly focused on *in situ* Au assisted NW growth and hybridization.

Nanowire Growth

Nanowire growth step starts with heating the source materials to our desired temperature and stabilizing it for at-least 6 hours. In addition to the III-V materials, we also heat up the Au cell for *in situ* deposition. Our optimized typical cell temperatures are: In (865/815)°C, As (400/345)°C, Sb (680/500)°C and Au (1100)°C. Before loading in the MBE load lock, we dip the fabricated substrate into HF for 10 sec and milli-q water for 20 sec. This additional steps are performed only for a fabricated substrate to confirm further cleanness of the substrate along with removing additional native oxide. Pristine InAs (111)B substrates are not cleaned with HF, and directly loaded. Here, I will only focus on the growth steps for *in situ* Au assisted VLS NWs. Growth details for trench NWs will be discussed in the next chapter. [21] There are dedicated holders depending on the type of materials involved in the growth (As or Sb) and it's highly recommended to use the specific holder for the growth. Next, the substrate is loaded in the load lock and baked for 2 hours at 200°C until the pressure reaches around $5e^{-8}$ Torr. The trolley with the substrate is subsequently transferred to the connected buffer chamber, where the sample holder is annealed for 1 hour at 200°C. This removes further impurities from the substrate. After that, the sample is cooled down and wait until the pressure drops below $5e^{-10}$ Torr. Then, the sample is transferred to the growth chamber. Before starting the growth, all the corresponding flux ratios are checked, and the stability is verified. During the growth, the substrate is annealed at 610°C for 6 min with high As_4 over-pressure. In the annealing step, the Au temperature is raised to 1220°C. After annealing, the substrate is cooled down 590°C for Au deposition. Upon the temperature is reached, Au is deposited for 3 sec. The deposition time may vary depending on our desired diameter of the NWs. With the hot substrate, sparsely deposited Au is formed as liquid droplets around the substrate. Then the substrate is further cooled down to our growth temperature. For *in situ* Au assisted NWs, the growth temperature is 447°C. The standard InAs or InAs assisted InSb or InAsSb NWs are grown with corresponding shutter opening. The growth time of each section is determined by the desired length of the NW. After the growth, the substrate is cooled down and then, either unloaded or prepared for the metal hybridization (most common cases), which is elaborated in the next section.

21: See experimental section: "Nanowire Growth" in chapter 3, for the NW growth on the trench substrates.

Thin Film Deposition

***In situ* Al** deposition is usually performed in the MBE growth chamber. It's important to know the Al growth rate (through calibration) before deposition. Right after the growth, all the heated sources are cooled down to their base temperatures and also the substrate is returned to the standing temperature (150°C in our case). We wait until the beam flux monitor reading reaches to the pressure around $< 10^{-9}$ torr. As the pressure achieved, substrate power and other heating station power are turned-off leading to the initiation of substrate cooling. We wait again

until the substrate holder is cooled down to $\sim -36^{\circ}$C and stable. It usually takes about 8-10 hours right before the MBE chamber is ready for Al deposition. When the desired temperature is reached, the substrate is aligned in parallel with the major flat (of the wafer) and rotated in $\sim 337.5^{\circ}$ clockwise to adjust the angle with our Al source. This angle correction is required if we deposit Al on the selected facets of our NWs (half-shell). For the all-around shell (full-shell), we rotate the substrate at a given rate, so that the shell is homogeneous around the core NW. Before deposition, the Al cell is heated 1140°C, and flux is stabilized for more than 2 hours. Then, the flux rate is checked at least twice within half an hour interval to confirm the stability. Depending on the required thickness, flux rate, and threshold of forming a continuous film, the deposition time is determined. Immediately after the deposition, the unloading process starts (before elevating the temperature). To avoid the dewetting issue when introduced to room temperature, 15 min of oxidization is performed in the load lock. During this period AlO_x is formed on top of the film, which locks the films and prevents reconstruction.

***In situ* Sn** is deposited in a standard electron beam evaporation system connected with our MBE system as shown in Figure 2.1. Similar to Al deposition, after the NW growth, we wait for the growth temperature to cool down to the base temperature. When the temperature is reached, the substrate is moved to the e-beam chamber through the transfer tunnel. Next, the substrate holder is cooled with liquid nitrogen. We wait until the lowest temperature is reached $\sim -150^{\circ}$C (thermocouple reading) and completely stabilized. Once the temperature is reached, we start melting the Sn source with magnetically guided energetic electron beam. Then, the flux rate is measured through a quartz crystal monitor, when material evaporation starts (making sure that the substrate shutter is closed). We tune for the desired deposition rate and open the substrate shutter for thin-film growth with the intended thickness. Depending on the growth conditions, we aim for a deposition rate around 3-5 Å/s for Sn film. Alike Al film deposition, we also correct the angle of the substrate position with respect to the source, based on the selected NW facets. After deposition, the sample is unloaded from the e-beam chamber and oxidized (similarly as described above) in the load lock before exposing to room temperature.

Characterization

Morphology of the hybrid NWs is initially characterized with standard **scanning electron microscopy** (SEM, JEOL JSM-7800F). Normally, operating parameters are secondary electron detector and 15KV accelerating voltage with 10-15 mm working distance. For the tilted view, we usually use a 30-degree angle. For identification of the NW facets or hybrid layers, sometimes we also use 2-5KV accelerating voltage with 5mm working distance. We try to avoid long exposure of the samples with electrons, as NWs can be contaminated with carbons and that eventually detrimental for the device performances. If a section of the growth sample is thoroughly characterized with SEM for analyzing the length and the diameter, then, for device fabrication, NWs are collected from a different section of the growth substrate.

VLS grown NWs require to transfer onto the separate substrate for further characterization or device fabrication. NWs can be transferred randomly using a simple dry transfer technique or selectively by using **micromanipulator**. A random dry transfer is a fast method and is only used where precise positioning is not needed. Usually, the edge of a cleanroom wipe is used to pick the NWs and then, mechanically transferred on the separate substrate. A gentle touch with the wipe corner is good enough to collect the wires. Further, for NW collection on the TEM grid, we directly use the grid to slide over a small section of the growth substrate. Careful soft sliding is important with the TEM grid in order to avoid damaging the grid membrane. Such kind of dry transfer maximizes the density of the NWs and makes it easy to find the NWs for TEM or AFM investigation and enhance the statistics. On the downside, collections of the NWs are completely random. If the NWs are not uniform throughout the substrate, then such kind of dry transfer is ineffective and proper statistical analysis is not possible. In addition to that, a large number of the wires get bundled or overlapped with each other, which may increase the difficulties to characterize through TEM, AFM, or even unable to fabricate the device out of this. On the other hand, for the precise positioning on the transferred substrate or device fabrication with a specific type of NW, a selective collection of NW is required. In this case, we use the micromanipulator with an optical microscope attached to it, which assists to locate the collection area. First, we use SEM to precisely locate the place of our desired NWs. Designated alignment marks or numbering scheme of the growth segment helps to identify the NW. Next, we take the NW batch to the micromanipulator and try to track down the same position with the optical microscope. Then, we set the device chip or TEM grid next to it and adjust the needle position with respect to growth substrate and the substrate, where NWs will be transferred. The convenient needle height and position can be saved in the system so that we can return to the same selected place after transferring NWs. We use the 100 nm tungsten needle to transfer the NWs. During the transfer, the needle approaches close to the bottom of the NWs. Then, with a gentle force, NW breaks from the bottom and sticks with the needle due to the electrostatic force. Collected NW is transferred into the desired substrate and pushed around to precisely position or align in a certain direction. Such an accurate positioning or alignment is needed primarily on the device chip or for cross-sectional lamella preparation, where all the NWs are required to be parallel to each other. Although NW collection with micromanipulator confirms high precision and selectivity, it can be a time-consuming process.

Further, for measuring the thickness of the metal shell and surface roughness (in case of half-shell NW) we use standard **atomic force microscopy** (AFM, Bruker Dimension Icon PT). For AFMing the hybrid samples, we use the tapping mode and the probe is: ScanAsyst-Air, with a nominal tip radius of 2 nm. We start with a scan size of 1μm, 0-degree scan angle, sample/line is 512, and the scan rate is 1 Hz. Later, based on the image condition and the scan noise, we optimize the scan parameters. Usually, for our desired image section, we increase sample/line up to 1024 for better data acquisition. Post-AFMed images are analyzed with Gwyddion software. Typically, for AFM characterization the NWs are transferred onto the device chip, so that the same NWs can also be used for fabricating devices.

For **transmission electron microscopy** (TEM), [22] NWs are either transferred on the TEM grid as discussed before or on SiO_x substrate using micromanipulator for lamella preparation. First, for the cross-sectional analysis, NWs are positioned parallel to each other on the SiO_x substrate. Then, 30 nm of AlO_x is deposited using an atomic layer deposition (ALD) system to protect the NWs during the cross-sectional cut. Further, Pt-C is deposited using a focused ion beam (FIB) prior to the cut. The transversal cross-sectional lamella is prepared by FIB in an FEI Helios Nanolab 600 system situated at the 'Laboratorio de Microscopías Avanzadas' of the 'Instituto de Nanociencia de Aragón' (INA-LMA), Zaragoza, Spain. After lamella preparation, the cross-sections of the NWs are transferred to the TEM chamber for analysis. Atomically resolved high-angle annular dark-field (HAADF) micrographs are obtained in a probe-corrected FEI Titan system, which is operated at 300 kV. Electron energy-loss spectroscopy (EELS) spectrum imaging (in the transversal cross-sections) is performed in the same microscope at two different energy ranges: i) - 250 eV to 1274 eV with 0.5 eV energy dispersion. The full-width half-maximum (FWHM) of the zero-loss peak (ZLP) of 1 eV to investigate the spatial distribution of the core-loss edges of In, Sb, and Sn (In M4,5 at 443 eV; Sb N4,5 at 528 eV and Sn M4,5 at 485 eV), ii) 0-185 eV with 0.1 eV energy dispersion. The FWHM of the ZLP of 1 eV (Sn N4,5 at 24 eV) for second cross-check, given the energy proximity between the different energy loss edges in the core-loss regime.

Next, for the typical TEM analysis, the nanowires are transferred to a Cu-grid with carbon using a micromanipulator or simple dry transfer. In this case, HAADF is performed using the same microscope and imaging conditions, as mentioned above for the cross-section. High resolution (HR)-TEM is obtained in an FEI Tecnai F20 microscope, (located in the Catalan Institute of Nanoscience and Nanotechnology (ICN2)) and operated at 200 kV. EELS is performed in the samples focusing in the core-loss region, with energy range from 370 eV to 2418 eV with energy dispersion of 1 eV and a ZLP FWHM (energy resolution) of approximately 2 eV. EELS S/N ratio is enhanced by applying principal component analysis (PCA) to the spectrum image before mapping (filtering high order components).

22: Detail information about the parameters and conditions of the TEM operation are provided by Sara Martí-Sánchez from Catalan Institute of Nanoscience and Nanotechnology (ICN2).

Shadowed Nanowire Junctions 3

Remark 3.0.1 This chapter is reprinted with permission from Ref. [54] (Paper 1) [Sabbir A. Khan, Charalampos Lampadaris, Ajuan Cui, Lukas Stampfer, Yu Liu, Sebastian J Pauka, Martin E Cachaza, Elisabetta Maria Fiordaliso, Jung-Hyun Kang, Svetlana Korneychuk, Timo Mutas, Joachim E Sestoft, Filip Krizek, Rawa Tanta, Maja C Cassidy, Thomas Sand Jespersen, Peter Krogstrup, *Highly Transparent Gatable Superconducting Shadow Junctions*, ACS Nano, 14, 11, 14605–14615, 2020]. Copyright [2020] by the American Chemical Society.

Summary

Gate tunable junctions are key elements in quantum devices based on hybrid semiconductor-superconductor materials. They serve multiple purposes ranging from tunnel spectroscopy probes to voltage-controlled qubit operations in gatemon and topological qubits. Common to all is that junction transparency plays a critical role. In this study, we grow single crystalline InAs, InSb and $InAs_{1-x}Sb_x$ nanowires with epitaxial superconductors and *in situ* shadowed junctions in a single-step molecular beam epitaxy process. We investigate correlations between fabrication parameters, junction morphologies, and electronic transport properties of the junctions and show that the examined *in situ* shadowed junctions are of significantly higher quality than the etched junctions. By varying the edge sharpness of the shadow junctions we show that the sharpest edges yield the highest junction transparency for all three examined semiconductors. Further, critical supercurrent measurements reveal an extraordinarily high $I_C R_N$, close to the KO−2 limit. This study demonstrates a promising engineering path towards reliable gate-tunable superconducting qubits.

3.1 Introduction

Josephson junctions (JJs) are critical circuit elements for superconducting quantum computing. Gate tunable junctions based on proximitized semiconducting segments in hybrid semiconductor (SE)-superconductor (SU) materials are an interesting class of junctions with potential as JJ elements in transmons qubits [210, 211] as well as critical operators in topological qubits [212]. Similar to all semiconducting circuit elements, they are highly susceptible to disorder and require dedicated optimization for development towards high-fidelity gate operations. In the case of topological quantum computing, achieving disorder-free junctions is desirable on several levels. Coupling a one-dimensional semiconductor with strong spin-orbit interaction and large Landé-g factor to a conventional s-wave superconductor has the fundamental ingredients to generate topologically protected Majorana bound states (MBS) [28, 29, 51, 167, 168].

If the material fulfills the set of requirements, MBS are expected to tolerate local perturbations and therefore makes it a promising candidate for scalable quantum computing [212–214]. In recent years, there has been significant progress in the development of epitaxially grown SE-SU hybrid materials to fulfill these requirements [48, 52, 184, 215, 216]. Even though electronic tunnel spectroscopy has yielded results that have been interpreted as signatures of MBS [30, 31, 55–61], direct evidence for topologically protected MBS is still missing. Complications in the process of verifying the MBS with tunnel spectroscopy relate not only to the hybrid SE-SU nanowire (NW) segments but also to the tunnel junctions, which may contain random disorders that may give rise to local Andreev bound states that mimic the zero-bias conductance peaks expected from MBS [217–219]. Avoiding such misinterpretations is certainly desirable and a crucial reason to aim for disorder-free junctions. Junctions in spectroscopy devices have been demonstrated with a top-down etching process [58, 220, 221], whereas a more recent alternative approach has been using an *in situ* method [66, 69, 185]. However, until now, a detailed investigation of the disorder-free junction formation along with correlations between fabrication and junction quality has been missing,

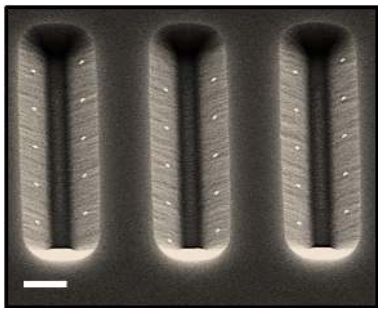

Figure 3.1: Fabricated substrate. SEM image of wet-etched (111)B faceted trenches with deposited Au disks (scale bar is 1 μm).

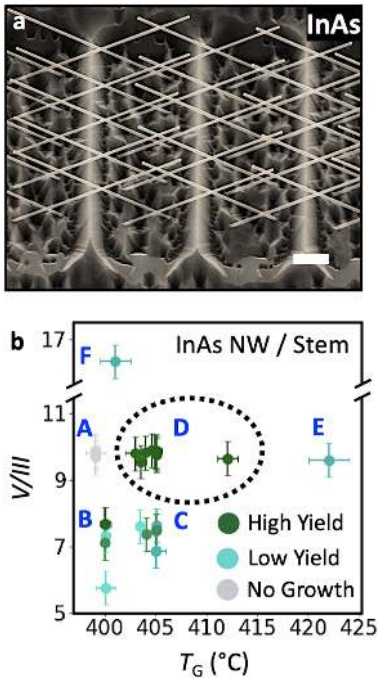

Figure 3.2: InAs nanowire growth on the trenches. a, Scanning electron micrograph (SEM, 30° tilted) of Au-assisted InAs NW array grown on the preprocessed "V" groove (111)B faceted InAs trenches. Scale bar is 1 μm. **b**, V/III ratio as a function of InAs NW growth temperature (T_G). The plot is divided into six regions (A-F), and NW growth outcome (yield, morphology, etc.) of each region is investigated. Region "D" (T_G ~ 401-415°C with V/III ratio ~ 9-10.5) shows the highest yield and uniform InAs NW growth (dark green circles).

which is highly required for further development of the gate-tunable junctions.

In this work, we study the synthesis of stacking-fault-free InAs, InSb and $InAs_{1-x}Sb_x$ NWs with epitaxially grown superconductors containing shadowed junctions in a single-step growth process using molecular beam epitaxy (MBE). To obtain shadowed junctions at predefined positions, we use (111)B faceted trenches on InAs (100) substrates for NW growth [185, 222]. This method provides freedom for controlled positioning of the shadow junctions due to the specified NW growth directions. We study the formation of junctions as a function of the interwire distance between the shadowing NW and the junction NW. We also analyze the junction profile, which directly depends on the flux distribution from the source and geometry of the shadowing. Further with different superconductors we investigate the influence of growth kinetics on the junction sharpness. Developing a pregrowth substrate fabrication process including optimized growth condition and sharp-edge shadowing, we show high junction transparency with reproducible ballistic transport. Correlations between the structural and electronic properties of the junctions are done by statistical characterization of the junction morphology and transport properties of junction NWs from selected positions on the growth substrate. We compare *in situ* shadowed and etched junctions on statistical ensembles of NW devices as well as on the same $InAs_{1-x}Sb_x$/Al NWs and confirm the superior electrical quality for the shadowed junctions. Finally, measurements at mK temperatures show $I_C R_N$ products over seven samples close to the KO−2 and KO−1 limit. Voltage bias measurements reveal the size of the induced superconducting gap, as well as a phase coherence of at least 5 times the junction length.

["Experimental Details" section is presented at the end of this chapter.]

3.2 Epitaxy of SE-SU Shadow Junctions

NW Growth Optimization

The NW substrates are fabricated using electron beam lithography (EBL) and wet-etching process to form (111)B facets in planar InAs (100) substrates, where the Au catalysts are positioned with a subsequent EBL process as shown in Figure 3.1. As opposed to earlier works [185, 222], we do not use any masks to confine the Au particles, which significantly reduces the preprocessing efforts and minimizes contamination during fabrication. This makes the process suitable for exploring different material combinations with high throughput. Step-by-step substrate fabrication details are presented in "Experimental Details" section.

Figure 3.2**a** shows an SEM image of InAs NWs grown from (111)B trenches. However, the NW growths on the trenches require careful optimization of the growth conditions. We find out that As_4 beam flux is necessary to enhance the initial NW growth rate to escape the competition with planar growth in the trenches. In Figure 3.2**b** we show a map of InAs NW growth yield, which resembles the design of growth parameter optimization. Dark to light green color represents high (> 90%) to low yield (< 50%) growth of NWs and gray resembles no growth. To help

tuning in the right growth parameter space, we distinguish between six growth parameter regions. As can be seen from Figure 3.2**b**, the growth temperature window in region "D" with V/III ratio ~ 9-10.5 provides the highest yield and uniform morphology of the NWs, whereas outside of this region, the growth either has uneven yield issue or has nonuniform NWs.

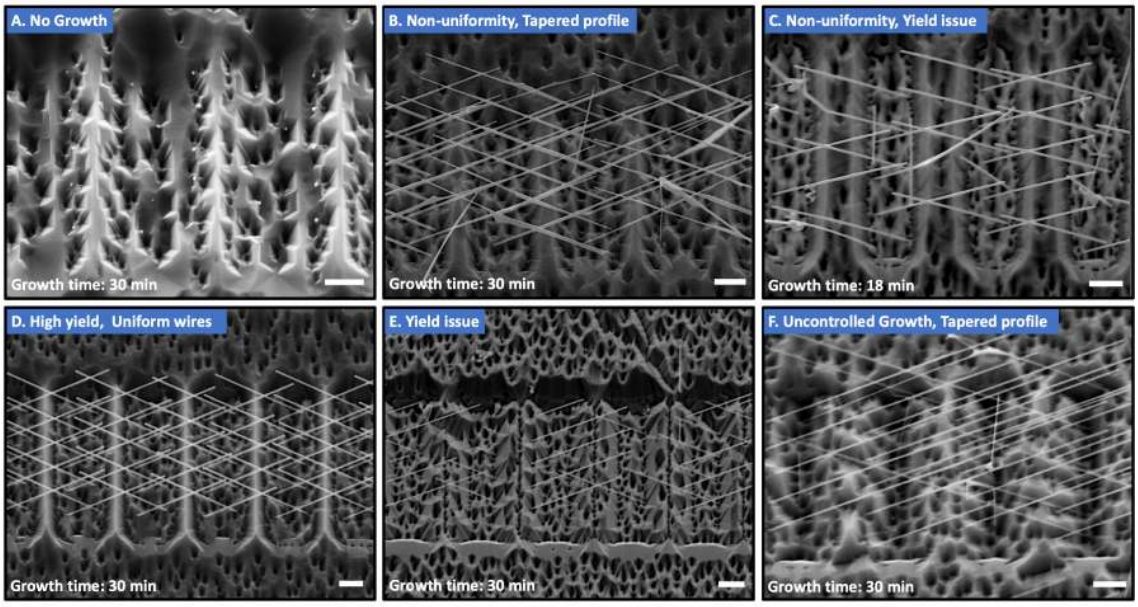

Figure 3.3: InAs NW growth optimization. SEM micrographs of the InAs NWs growth on the trenches in different growth conditions. Region **D** demonstrates the highest yield (> 90%) with uniform NWs growth. Scale bars are 1 μm.

Figure 3.3 is the extended demonstration of Figure 3.2**b**. Starting from region **A**, with growth temperature < 400°C (pyrometer reading) and V/III ratio ~ 10, none of Au seed particles nucleate and grow NWs. Most of the trenches are filled with InAs planar growth. Reducing the V/III ratio from **A** to region **B**, increased the yield of InAs NWs. However, we observe non-uniformity along the wires such as diameter change and tapered profile. Maintaining the V/III ratio as **B**, we increase the temperature ~ 5°C in region **C** (~ 405°C). We still observe non-uniformity along the wires with decreased yield. Maintaining the growth temperature, from **C** to region **D**, we only increase the V/III ratio ~10, which improves both yield (> 90%) and morphology of the NWs. For instance, the growth time of 30 min results homogeneous ~ 5-5.5 μm long NWs with diameter varied from 70-90 nm depending on the deposited thickness of the Au seed particles. It is also possible to grow longer wires maintaining the uniformity, however, we choose to grow in the above-mentioned length, considering our shadow design, which will be discussed later in this chapter. Further, if we increase the V/III ratio in **F** (~ 16), we observe uncontrolled NWs length and diameter with a tapered profile. Finally, in **E** with increased growth temperature (more than 20°C from **D**), we start observing yield issue again across the substrate.

We mostly grow in the lower side of the growth temperature window in region **D**, as we get pure wurtzite (WZ) crystal structure at lower temperatures. As shown in Figure 3.4, post-growth TEM analysis in

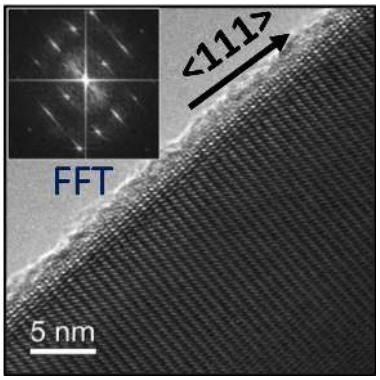

Figure 3.4: High-quality InAs nanowire. High-resolution TEM of the InAs NW demonstrating stacking fault-free WZ structure. Inset shows the FFT of corresponding structure.

multiple growth sections of the wafer confirms pure wurtzite (WZ) InAs structures with minimal crystal defects along the individual NW. We believe this less crystal defects can also be attributed to the high incident materials flux on the angled NW surface, however systematic study is required for proper understanding. Small structural defects are observed at the top of NW near seed particles which can be attributed to the cooling effect.

Confirming previous reports [223], we are also not able to grow InSb NWs directly from the trenches. As discussed before, the Au-alloy forms a small contact angle to the substrate when Sb is present, which prevents initiation of NW growth [223]. However, once the InAs NW stem is formed it is possible to switch into InSb NW growth. With optimized growth conditions (in region "D"), we achieve high yield InSb NWs across the substrate as shown in Figure 3.5. Post-growth TEM analysis confirms high-quality zinc blende crystal structure for the InSb segment, as discussed in previous chapter. [See chapter 2 for TEM analysis of InSb NWs]

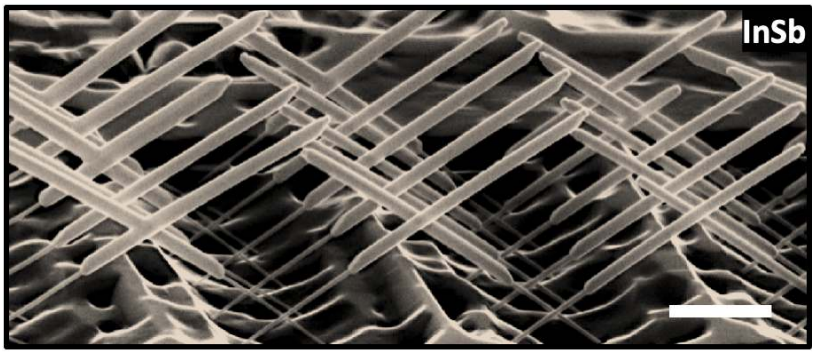

Figure 3.5: InSb NWs from trenches. Tilted SEM image of InSb NWs grown with InAs stems. Scale bar is 1 μm.

SU Deposition and Shadow Schemes

Figure 3.6**a** shows the schematic of the NWs with a shadow junction as grown on the substrate. On the right, the hemisphere diagram shows the coordinates used to describe the superconductor beam flux direction with respect to NWs. Depending on the angle of the incoming flux and orientation of the NW facets, the superconductor can be grown on selected facets. The table in Figure 3.6**b** contains information on beam flux angles required for 2-facet and 3-facet superconductor coverage on $[1\bar{1}0]_{ZB}/[11\bar{2}0]_{WZ}$ and $[11\bar{2}]_{ZB}/[1\bar{1}00]_{WZ}$ oriented NWs. The amount of superconductor that is grown on each facet (for a given growth time) is proportional to the effective beam flux (f') on the selected facet. Here f' is defined as the flux impinging on the midfacet facing the source during 3-facet deposition (see Figure 3.6**b**). If we consider 2-facet depositions, then both facets receive equal amounts of material, as an instance, for ϕ=0 and θ=35°, $f_{[\bar{1}01]} = f_{[011]} = \frac{\sqrt{3}}{2} f'$. For 3-facet depositions, the facet facing towards the beam receives f', whereas the adjacent facets get $f'/2$.

The SEM images of InSb/Al NWs with *in situ* junctions are demonstrated in Figure 3.7**a**, where the inset shows a ~ 100 nm long junction. As the

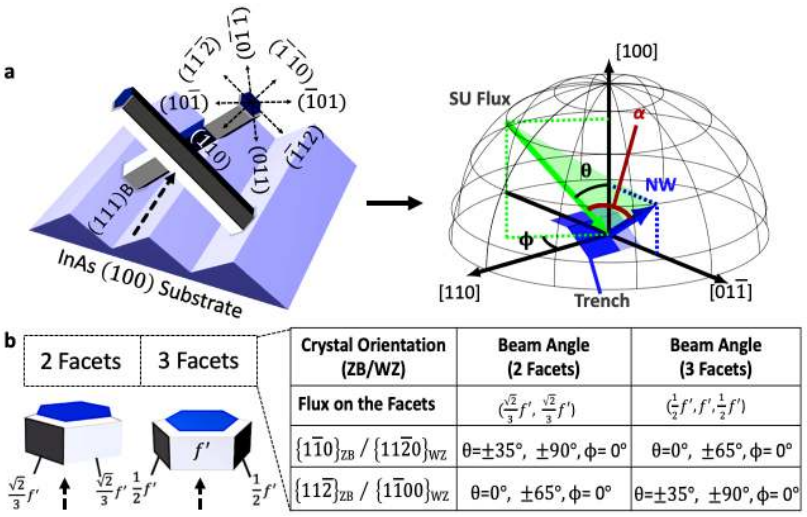

Crystal Orientation (ZB/WZ)	Beam Angle (2 Facets)	Beam Angle (3 Facets)
Flux on the Facets	$(\frac{\sqrt{2}}{3}f', \frac{\sqrt{2}}{3}f')$	$(\frac{1}{2}f', f', \frac{1}{2}f')$
$\{1\bar{1}0\}_{ZB}$ / $\{11\bar{2}0\}_{WZ}$	θ=±35°, ±90°, ϕ= 0°	θ=0°, ±65°, ϕ= 0°
$\{11\bar{2}\}_{ZB}$ / $\{1\bar{1}00\}_{WZ}$	θ=0°, ±65°, ϕ= 0°	θ=±35°, ±90°, ϕ= 0°

Figure 3.6: Nanowires growth on the (111)B trenches. a, Schematic with crystal orientation of the hybrid NWs. Dashed arrow shows the superconductor deposition direction. In the right, schematic of superconductor deposition geometry on the NW with respect to the beam flux direction and the NW growth axis. Here, α is the angle between these two vectors to calculate effective flux (f') on the NW facet. **b**, Schematic of 3-facets and 2-facets superconductor on the NWs. The table provides the beam angle requirements in the case when ϕ=0, for 2-facets and 3-facets superconductor coverage.

NW positions are controlled, it is possible to engineer multiple junctions in a single NW. Advanced junction schemes are presented in Figure 3.8. Synthesis of hybrid InSb/Sn NWs has recently been reported [71], showing a route for deposition of alternative superconductors on bare semiconductor NW facets. Due to the simplicity of the single UHV-step process in our work, it is easy to vary not only semiconductor compositions but also the superconducting materials, providing a versatile platform for exploring the wide range of interesting hybrid material combinations. Two promising superconductor alternatives to Al are Sn and Pb, which both have higher T_c (for bulk it is around 3.7 K for Sn and 7.2 K for Pb, compared to 1.2 K for Al). As these superconducting materials are challenging to etch selectively without damaging the semiconducting NW segments, the shadowing method may be critical for the realization of high-quality junctions. Figure 3.7**b** and Figure 3.7**c** we demonstrate Sn and Pb films grown on InSb NWs. After the semiconductor NW growth, the Sn and Pb are grown on liquid nitrogen cooled stage in a UHV chamber connected to the MBE, which has already been discussed in Chapter 2. Compared to Al and Sn, the growth of uniform Pb films on multiple facets of VLS NWs seems more challenging. Especially for InSb/Pb and $InAs_{1-x}Sb_x$/Pb interfaces, there is no obvious low index domain match without a high residual mismatch [52]. This indicates that the interface energy density is relatively high, which increases the thermodynamic driving force for dewetting; that is, it requires a lower growth temperature to prevent kinetic dewetting to occur.

Having growth conditions for InAs and InSb NWs on the trenches, the As and Sb fluxes can be tuned to grow $InAs_{1-x}Sb_x$/Al NWs [184], as shown in Figure 3.9. Similar to InSb NWs, we initiate the $InAs_{1-x}Sb_x$ NW growth with an InAs stem (using the recipe from Figure 3.2**b**, region "D"). The InAs stem is not visible in Figure 3.9**a** due to the over-growth on the substrate. To enhance spin-orbit interaction [224] while maintaining an efficient field effect response by keeping the carrier density low [184, 225], we aim for Sb composition around x=0.7 (nominal Sb/As flux ratio of 0.8). The composition of the $InAs_{0.3}Sb_{0.7}$/Al NWs is measured applying Vegard's law [226] for the lattice parameter in ternary alloys.

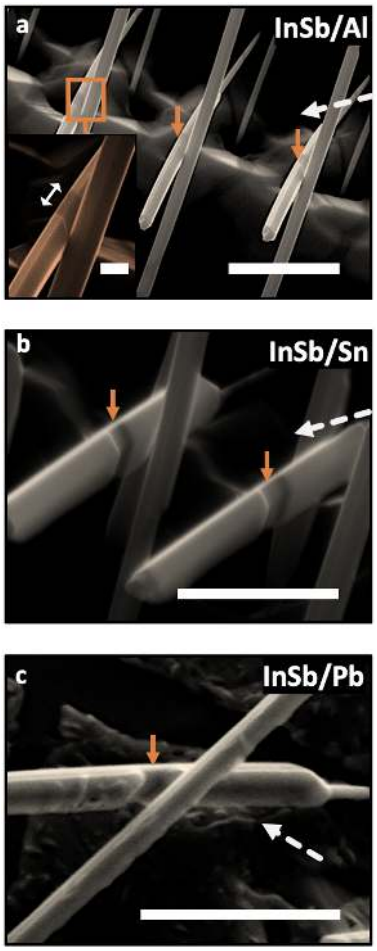

Figure 3.7: InSb NWs with different SU. a, Tilted SEM image of InSb NWs with epitaxially grown Al. **b**, SEM image of InSb/Sn NWs with junctions. **c**, SEM image of InSb/Pb NW with junction. Orange arrows indicate the shadowed junctions. Dashed arrows indicate the direction of superconductor deposition. Scale bars for (a), (b) and (c) are 1 µm. Scale bar for (a) inset is 100 nm.

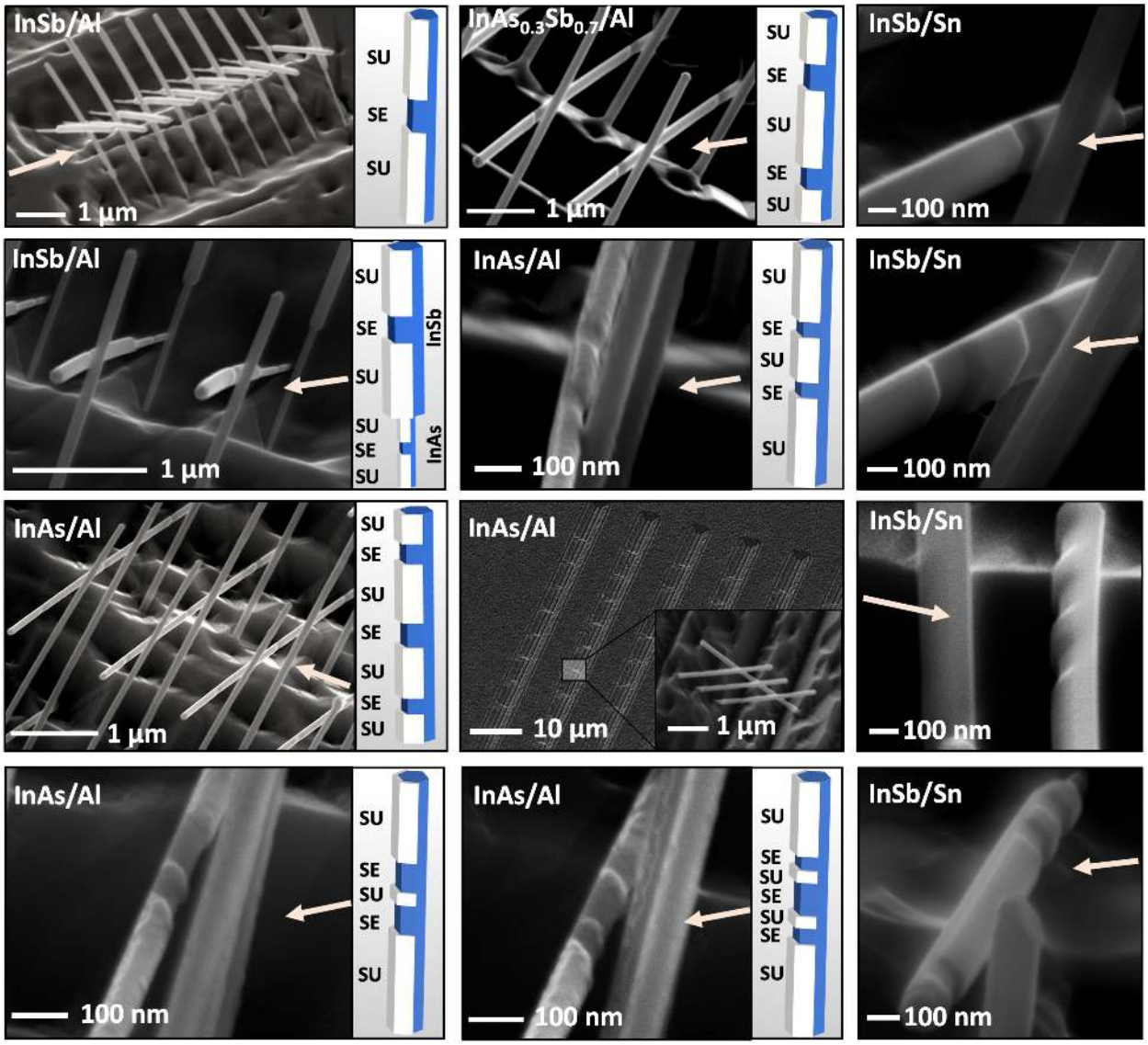

Figure 3.8: Shadow schemes. SEM micrographs and schematic of different shadow junction schemes grown on the trenches. SU deposition directions are shown with arrows.

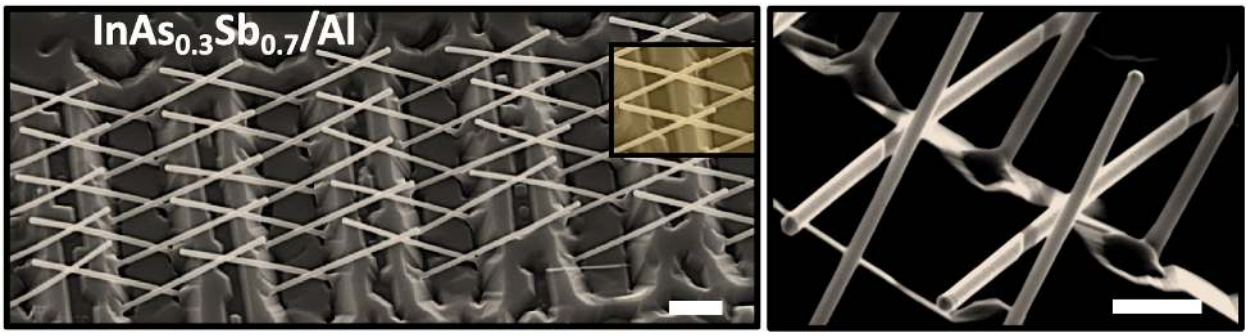

Figure 3.9: Al epitaxy on InAsSb NWs. SEM (30° tilted) of $InAs_{0.3}Sb_{0.7}$/Al NW array (scale bar is 1µm). The highlighted section shows double shadowed junctions on the NWs (scale bar is 500 nm).

We also investigate the $InAs_{1-x}Sb_x$ NW junction quality with STEM tomography as shown in Figure 3.10**a**.The detail tomography procedure is discussed in Experimental section. In tomography image, we can see abrupt junction. However, in some cases, we also observe homogeneous

2-facet Al and discontinuous third facet Al. This non-uniformity of the SU on NW can be related to the large interwire distances. Besides, SU deposition angle with respect to the NW facets and inhomogeneous growth of the NW can also be responsible. We confirm the composition of the $InAs_{1-x}Sb_x$ NW with STEM-EDX analysis and shown in Figure 3.10**b**. Further, $InAs_{0.3}Sb_{0.7}$/Sn hybrid is shown in Figure 3.10**c**, where nominal ~ 20 nm Sn is deposited on the wire facet at very low temperature. The continuous thin film of Sn is formed on NW facets, however, rough morphology is observed compared to the InSb/Sn NWs. After deposition, NWs seem to bend away from the Sn. This bending could be due to the different thermal expansion coefficient between the ternary $InAs_{0.3}Sb_{0.7}$ NW and Sn during temperature increment after NW growth. $InAs_{0.3}Sb_{0.7}$ NW with continuum Pb hybridization is shown in Figure 3.10**d**. Magnified NW and junction segments are shown in the inset, where $InAs_{0.3}Sb_{0.7}$/Pb demonstrates opposite bending. Such bending can be due to the compressive strain in the interface of $InAs_{0.3}Sb_{0.7}$ and Pb along the NWs, that is also comparable in some cases of InAs/Al interfaces [52].

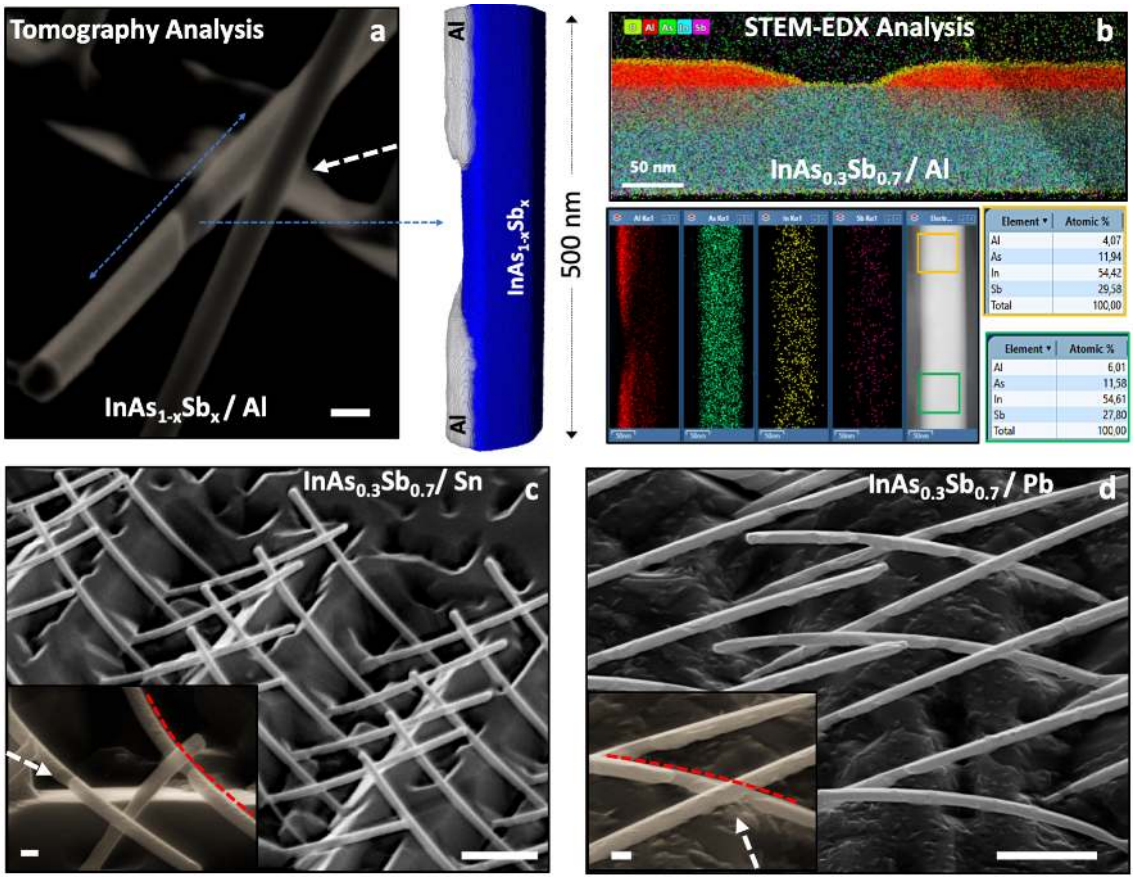

Figure 3.10: $InAs_{0.3}Sb_{0.7}$ NWs with different superconductors. a, SEM micrograph of $InAs_{1-x}Sb_x$/Al NW junction. Scale bar is 100 nm. Blue arrow to right is the HAADF-STEM tomography of the NW demonstrating junction morphology. **b**, STEM-EDX of the junction shows In, As, Sb and Al composition. As shown in the bottom, the grown $InAs_{1-x}Sb_x$ NWs consist 30% of As and 70% Sb and the composition remain homogeneous along the individual NW. **c**, $InAs_{0.3}Sb_{0.7}$ NWs with Sn. **d**, $InAs_{0.3}Sb_{0.7}$ NWs with Pb. Scale bars for (**c**) and (**d**) are 1 μm. Insets scale bars are 100 nm. All the white arrows in the SEM images show directions of superconductor deposition.

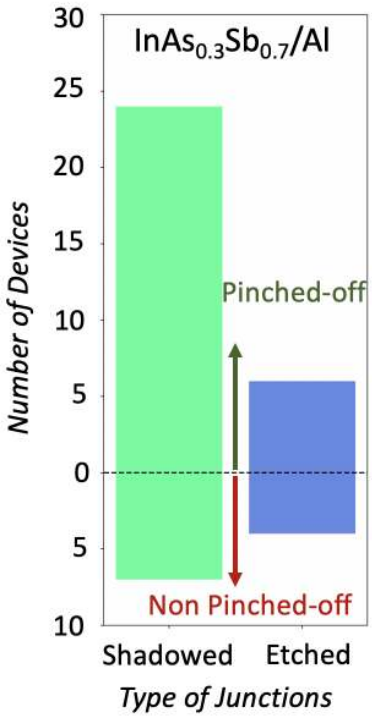

Figure 3.11: Gate response statistics of shadowed and etched junctions. Pinch-off statistics of the back-gated devices with shadowed (green) and etched (blue) junctions.

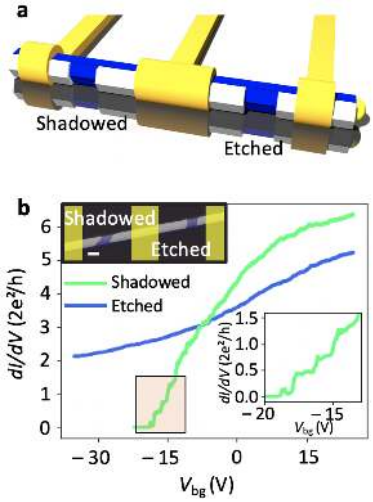

Figure 3.12: Shadowed and etched single NW. a, Schematic of the test device with comparable size shadowed and etched junctions in a single NW. **b**, Electrical measurements of the test device where conductance is shown as a function of gate voltage for shadowed (green) and etched (blue) junctions. The shadowed junction shows quantized plateaus as highlighted with inset. Applied magnetic field, **B**=6 T in both cases. SEM image of the exact NW is shown inset with a scale bar of 100 nm.

3.3 Comparison of Shadowed and Etched Junctions

The $InAs_{0.3}Sb_{0.7}$/Al NWs are used to compare the field-effect response of etched and shadowed junctions, as shown in Figure 3.11. The challenge for etched junctions is to find conditions that selectively etch Al while leaving the semiconductor unharmed. For instance, we have not been able to find selective etch conditions for Al on InSb. For $InAs_{0.3}Sb_{0.7}$ and InAs NWs, we use etch conditions which were optimized in previous studies and apparently leave the semiconductor intact [64, 184]. Because the electron transport characteristics vary from device to device, we need statistics for comparing quality measures. For this purpose, we compare 41 back-gated devices: 31 with shadowed and 10 with etched junctions; see Figure 3.11. For etched junctions, 7 out of the 10 devices are first measured at 20 mK, out of which 6 pinch off with a threshold voltage of -3 ± 1 V, a mean saturation conductance of $1.6 \pm 0.2\ 2e^2/h$ and the field-effect mobility $\mu_{FE} \approx 1900 \pm 600$ cm^2/Vs (highest $\mu_{FE} \approx 4400$ cm^2/Vs). As a comparison, we measure 9 shadowed devices under identical conditions, where four devices pinch off with a mean threshold voltage of -36.0 ± 2.5 V and rest have not pinched-off within the applied gate voltage. The mean saturation conductance of all shadowed devices is $9 \pm 1\ 2e^2/h$.

For a higher throughput, we turn to measurement at 2 K and measure 22 devices with shadowed junctions where 20 devices pinched-off with a mean $\mu_{FE} \approx 17000 \pm 400$ cm^2/Vs (highest $\mu_{FE} \approx 35000$ cm^2/Vs). The mean threshold voltage and saturation conductance of these devices are -13 ± 2 V and $5.1 \pm 0.5\ 2e^2/h$ respectively. In comparison, three etched junctions are characterized at 2 K, showing a low gate response and no pinch off within the voltage limits of the system and with mean saturation conductance of $4.1 \pm 0.7\ 2e^2/h$. In short, according to the statistics presented above, shadow junctions exhibit a significantly higher conductance and mobility compared to the etched junctions.

As an additional comparison, we fabricate 11 devices with comparable size etched and shadowed junctions in the same $InAs_{0.3}Sb_{0.7}$/Al NW (shown in Figure 3.12**a**). Among them, only three devices are functional on both sides, where the electrical measurement of one of these devices is demonstrated in Figure 3.12**b**. Despite the almost identical appearance of the etched and shadowed junctions in these devices, a radical difference is observed in the transport properties. Here the shadow junction pinched off with clear quantized conductance plateaus around magnetic field, **B** > 4 T, whereas the etched junction is not pinched-off within the available voltage range. Similar differences are observed for the other two devices presented in Figure 3.13**b** and **c**. We note that there can be many reasons for disorders associated with etching, such as undercut during wet etching, increased SE surface roughness, impurities left from etchant and leftovers from the etched metal. There are most likely ways to improve etch recipes; however, unless the etch actively provides protection, it is reasonable to assume that optimized shadowed junctions will generally be of the highest possible quality. Besides obtaining higher quality junctions, shadowed junctions allow flexibility in the choice of material combinations, where selective etching may be infeasible. Based on this and the above results, we choose to solely focus on shadow junctions for all material combinations.

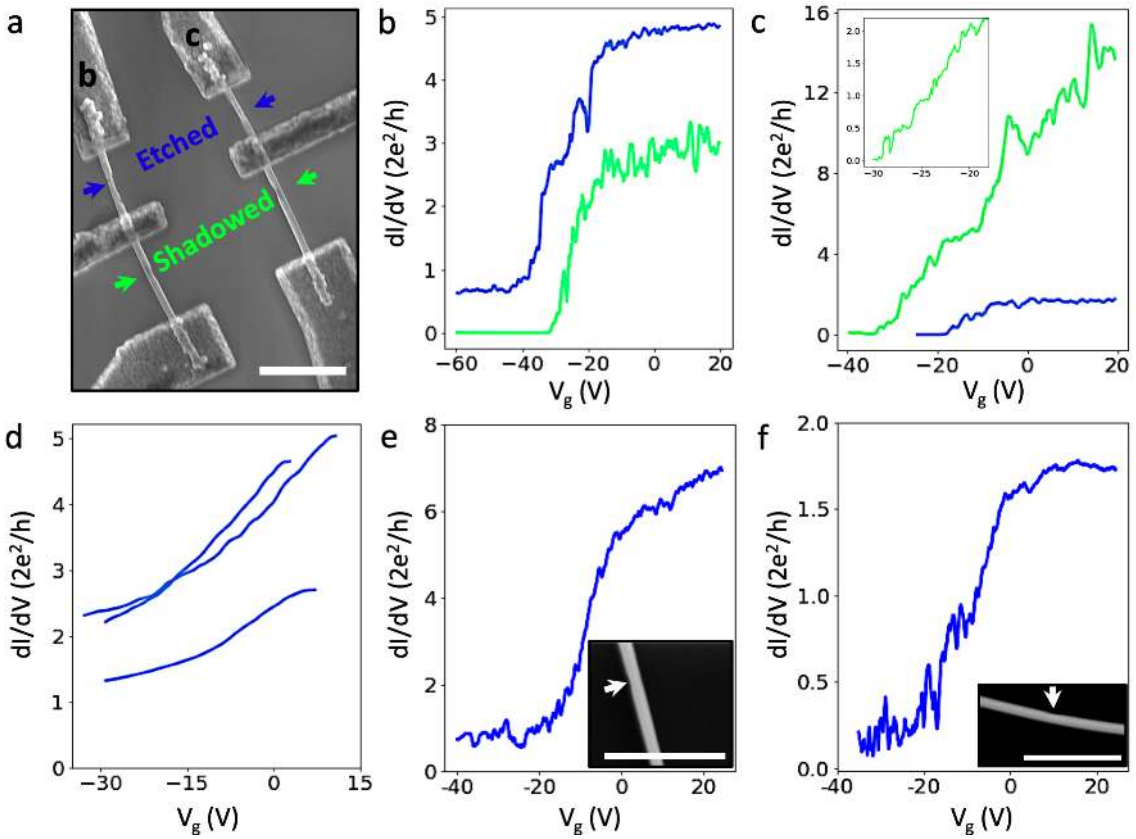

Figure 3.13: Additional low temperature electrical measurements of shadow and etched junctions in single NW. a, SEM image of NW devices with shadowed and etched junctions in individual wires. Blue colour stands for the etched junctions and green for the shadowed. Measurements are taken in a dilution refrigerator at 20 mK. **b**, The etched junction is not pinched-off and shadowed junction is pinched-off. **c**, Both junctions are pinched-off, whereas the shadowed device shows quantized conductance (inset) for high field (6 T). **d**, The results of the etched junctions obtained from the PPMS at 2 K. None of the junctions are pinched-off within the voltage range. **e**, and **f**, Two shadowed NW junctions that have not pinched-off due to the ambiguous junction region pointed by the white arrows in the relevant SEM images. The scale bars of all the SEM images are 1μm.

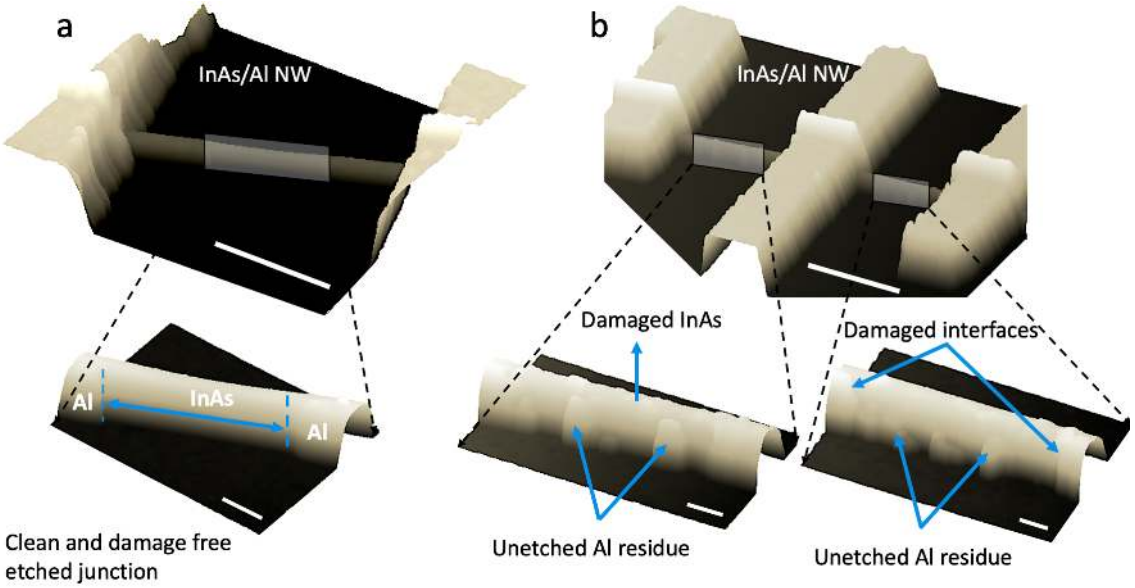

Figure 3.14: Post-growth etching of the junctions. a, AFM image of etched InAs/Al NW device (scale bar 500 nm). Zoomed-in junction (scale bar 100 nm) exhibits a disorder-free semiconducting segment. **b**, AFM image of double junctions device (scale bar 500 nm) where magnified segments of the junctions (scale bar 100 nm) exhibit Al residue, rough InAs surface, and damaged SE/SU interfaces.

Examples of etched InAs/Al junction devices are shown in Figure 3.14**a** and **b**. The etching is performed using standard Transene Aluminum etchants-type D with optimal etch time [64, 211, 227]. In Figure 3.14**a** and **b**, both devices are fabricated in the same chip and junctions are etched under the same etching conditions. However, the junction in device Figure 3.14**a** is clean and damage-free, whereas junctions in Figure 3.14**b** exhibit incomplete etching and damaged profile. As a result, in the same chip, junctions performance in different devices will be deviated and non-reproducible due to the uncontrolled etching. This phenomenon justifies the statistics of inadequate performances in the etched junctions, compare to the shadowed junctions. On the other hand, optimized *in situ* shadow junctions avoid disorders and exhibit high yield reproducible superconductive devices.

3.4 Evaluation of Sharp-edge Shadowing

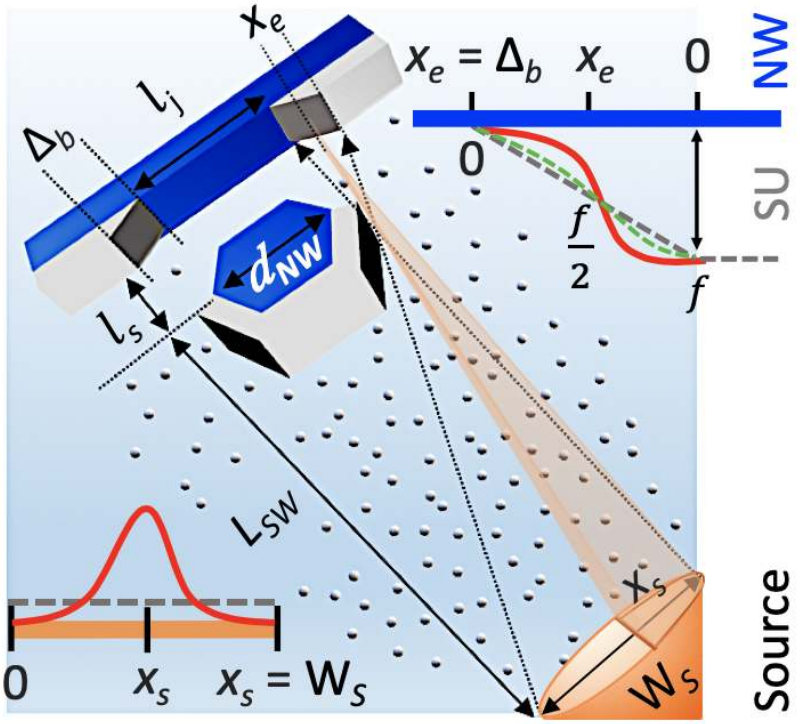

Figure 3.15: Junction formation and edge profile. a, Schematic of the SE-SU junction formation and the edge profile. The broadening (Δ_b) and profile of the junction edge can be determined by the flux distribution in the transition region, interwire distances (l_s), source to wire distance (L_{SW}) and effective width of the source (W_s). The junction length (ℓ_j) depends on the size of the Δ_b and the diameter of the shadowing NW (d_{NW}). (diagram is not drawn to scale).

The influence of the junction edge morphology on the junction transparency is studied by comparing devices with varying edge sharpness. The edge sharpness is varied by changing interwire distance, l_s, between the shadowing and the shadowed NW. A junction is sketched in Figure 3.15, where the transition region going from a fully shadowed region to a fully unblocked region (with nominal beam-flux f) is given by

$$\Delta_b = \frac{W_S l_s}{L_{SW}} \tag{3.1}$$

Here, L_{SW} is the "source to wire" distance, and W_S is the width of the source opening. The effective flux in the transition region $f'(x_e)$

as a function of coordinate $0 < x_e < \Delta_b$ is directly related to the flux distribution across the source opening as

$$f'(x_e) \propto \int_0^{W_S - \frac{L_{SW}}{l_s} x_e} f_{\text{source}}\, \mathrm{d}r \tag{3.2}$$

Here, f_{source} is the beam-flux originating from a point source within a cutoff area up to $W_S - \frac{L_{SW}}{l_s} x_e$ of the source opening (cut-off determined by x_e) as shown in Figure 3.15. Thus, a point in the transition region x_e sees a fraction of the source from where the effective impinging flux originates. If the outgoing flux distribution within the source opening is uniform, it can be shown that the effective flux in the transition region is given by:

$$f'(x_e) = \frac{f}{\pi}\left[\frac{\pi}{2} - X_e\sqrt{1 - X_e^2} - \arcsin X_e\right] \tag{3.3}$$

where

$$X_e = \frac{2L_{SW}}{l_s W_S} x_e - 1 \tag{3.4}$$

Such an outgoing flux distribution originating from a uniform circular source opening would give a flux distribution in the transition region, as shown in the dashed green line in the inset of Figure 3.15, whereas a uniform beam estimated from a 2D model (or from a hypothetical squared source opening) would provide a linearly increasing flux distribution as a reasonable approximation (as shown with the dashed black line). On the other hand, for a circular source opening with a Gaussian flux distribution, the transition region will see an effective flux closer to a step-profile flux distribution shown as red solid line.

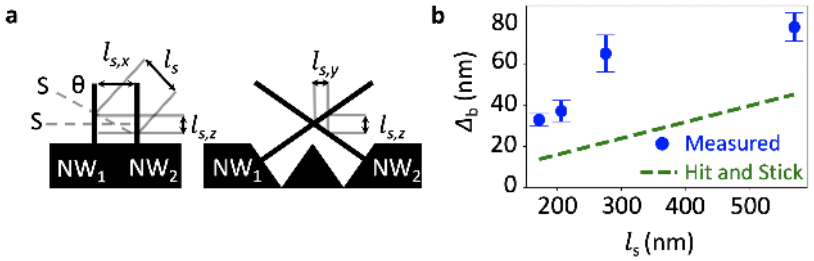

Figure 3.16: Measurements of edge broadening. a, Geometry for determining the shadow position. **b**, Δ_b as a function of l_s. Blue dots are measured Δ_b for Al junctions on $InAs_{0.3}Sb_{0.7}$ NWs and green dashed lines are calculated Δ_b.

If the temperature is sufficiently low, such that the adatoms are kinetically limited to stick where they land ("hit and stick" model), the shape of the junction edges will directly map the flux distribution from the source opening as described above. However, the "hit and stick" model collapse if the adatoms are mobile. This will alter the broadening towards equilibrium shaped morphologies. The length scale at which kinetics

plays a role can be described by a characteristic adatom migration length [52, 87]:

$$\lambda_{\mathrm{a}} \propto \sqrt{\frac{1}{\rho_{\mathrm{a}}}} \exp\left(-\frac{\delta h_{\mathrm{aa}} - \delta\mu_{\mathrm{inc}}}{k_{\mathrm{B}}T}\right) \tag{3.5}$$

where, ρ_a is the adatom density, δh_{aa} and $\delta\mu_{inc}$ are a characteristic activation barrier for migration and chemical potential of the adatoms respectively. As seen from this equation, also the beam flux (f) can play a role on λ_a, which complicates the analysis of the adatom kinetics due to the effective flux gradient in the transition region. To limit the adatom mobility, we grow the SU thin film at low substrate temperatures, where λ_a is sufficiently short to allow the formation of a uniform thin film at the given flux.

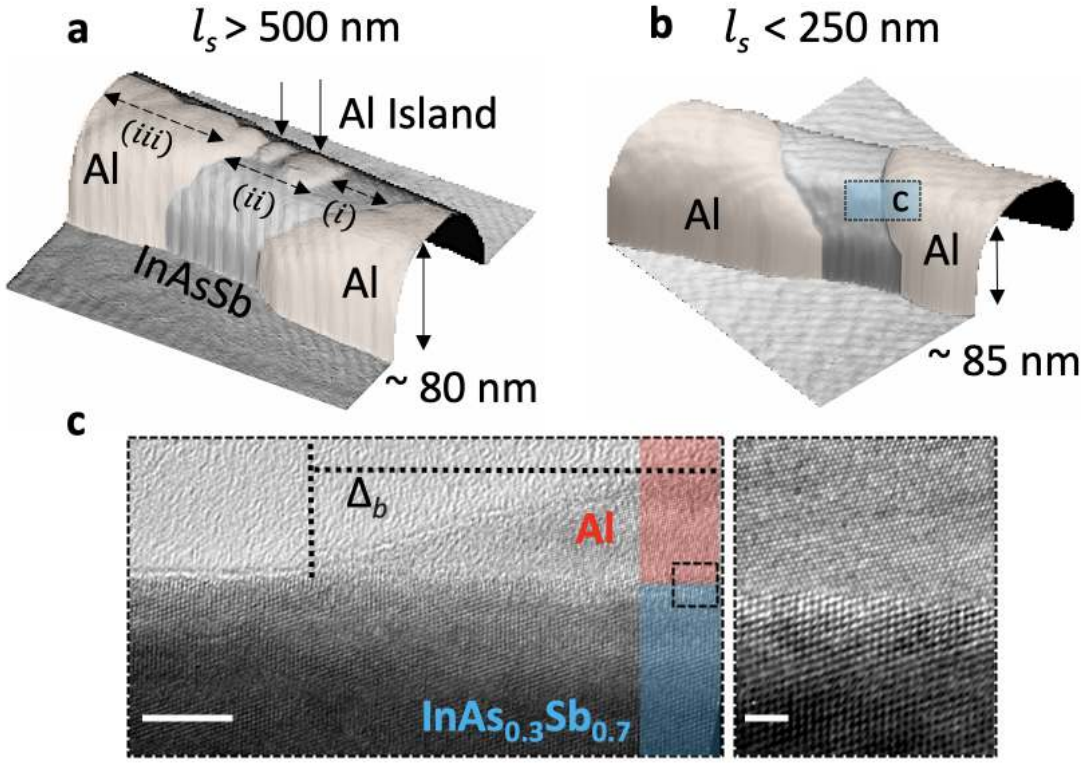

Figure 3.17: Post-growth etching of the junctions. a, Atomic force micrograph (AFM) of the $InAs_{0.3}Sb_{0.7}$/Al junction for $l_s > 500$ nm. Large Al broadening with multiple Al grains are observed in the junction. Depending on the effective flux distribution on the transition region the junction is divided into three segments. **b**, AFM of the $InAs_{0.3}Sb_{0.7}$/Al NW junction for $l_s < 250$ nm, where the junction is clean with sharp-edge profile. **c**, Zoomed-in TEM image from (**b**) shows the epitaxial SE-SU interface and small Al broadening in the junction. Scale bars are 5 nm and 1 nm respectively.

The determination scheme of shadow location is sketched in Figure 3.16**a** where l_s (and therefore Δ_b) is controlled with two parameters, θ and $l_{s,x}$, the spacing between the Au dots along opposite trenches. For $\phi = 0$ the relation is simply

$$l_{\mathrm{s}} = \frac{l_{\mathrm{s},x}}{\sin\theta} \tag{3.6}$$

These two parameters also determine the position of the shadow on the NW via the equations $l_{s,y} = \frac{l_s \cos\theta}{\tan 35.3°}$ and $l_{s,z} = l_s \cos\theta$. As described above, Δ_b depends on $l_{s,x}$, which is controlled by the Au droplet positioning during substrate preparation. If the Au droplets offset on the opposite facets are within the d_{NW} range, then the NWs will merge to form nano-crosses or other type of networks [66, 222] (see chapter 4). However, for obtaining sharp-edged junctions, l_s needs to be as small as possible without merging. We vary l_s from ~ 170 nm to ~ 570 nm from trench to trench on a given substrate and measure the broadening on selected NWs with AFM. Figure 3.16**b** shows measured broadening (blue points) together with the calculated "hit and stick" broadening (green dashed line) for $InAs_{0.3}Sb_{0.7}$/Al junctions. Here, W_s ~ 1.6 cm and L_{SW} ~ 20 cm for Al deposition in our MBE. The measured mean broadening follows the trend of "hit and stick" model with an offset, which indicates that adatom kinetics plays an important role for Al shadow junction formation under these conditions.

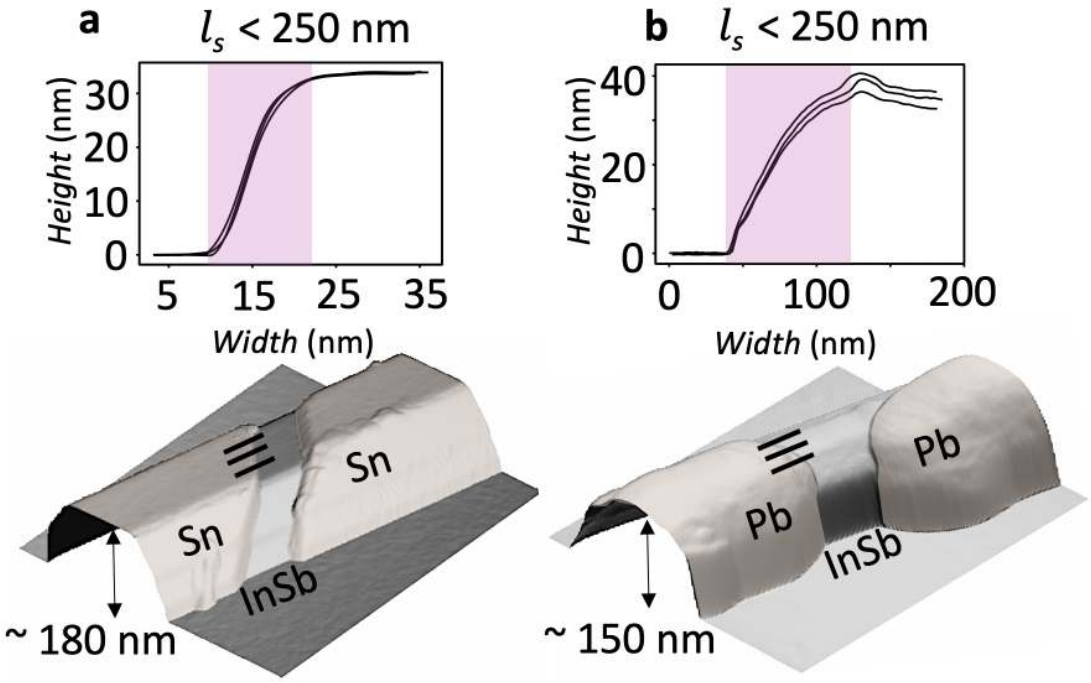

Figure 3.18: AFM of InSb/Sn and InSb/Pb junctions. a, AFM of the sharp-edge InSb/Sn junction shadowed by thinner InSb NW for l_s < 250 nm. The line scans, taken at the positions marker by black lines show the broadening of ~ 13 nm. **b**, AFM of the InSb/Pb junction for l_s < 250 nm. The line scans show the broadening of ~ 75 nm.

A general trend is that small Al islands are formed in the junction region for l_s > 500 nm (as shown in Figure 3.17**a**). The junction edge broadening with discrete Al islands are estimated from fitting a curve over the measure islands. For l_s < 250 nm, we observe well-defined single junctions with no Al islands, as shown in Figure 3.17**b** and confirmed by a TEM image in Figure 3.17**c**. We attribute the larger broadening profile of Al shadow edges than predicted by the "hit and stick" model to the kinetically driven equilibrium shape. For l_s < 250 nm, the Sn and Pb-based junctions on InSb exhibit sharpe-edge shadows, as shown in

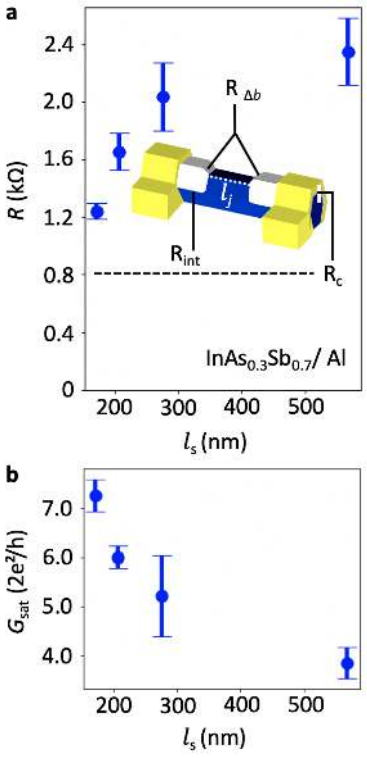

Figure 3.19: Edge profile effect on the junction performance. a, The gate-independent resistance of the shadow junction devices as a function of l_s. Inset is the schematic of standard device where R_{Δ_b} is the broadening resistance, R_c is the contact resistance and R_{int} is the interface resistance. The dotted line till 0.8 kΩ represents the statistical value of contact resistance obtained by four-probe measurements. **b**, The conductance saturation as a function of l_s.

Figure 3.18**a** and Figure 3.18**b**. In contrast to the Al deposition, we used e-beam evaporation of Sn and Pb, where the source opening W_S depend on how the electron beam is focused on the targeted materials. In the case of Sn, the effective area is visibly smaller than the area of the total target, which means that the effective source opening W_S and therefore Δ_b will be smaller for a given l_s in case of "hit and stick" conditions. The outgoing flux distribution can be estimated with a Gaussian profile, as discussed in Figure 3.15, leading to a sharp-edge flux profile in the transition region. Figure 3.18**a** with line scan showing $\Delta_b \sim 13$ nm confirms a sharp-edge profile of the Sn edge. Here, the measured sharpness may be underestimated due to the AFM tip diameter. On the other hand, for Pb-based shadowing, the outgoing flux distribution is more uniform from the source; as a result, Δ_b for the Pb-based junction is larger than that of Sn, ~ 75 nm, as extracted from line cuts in Figure 3.18**b**.

We study correlations between the junction transparency and the critical parameter for the junction profile l_s on the Al shadowed NWs. For this purpose, we calculate the gate-independent resistance R by fitting the pinch-off curves as described in the experimental details section. This gate-independent resistance contains mainly three contributions: contact resistance (R_c), broadening resistance (R_{Δ_b}) and SE-SU interface resistance (R_{int}). In Figure 3.19**a**, we can see that the $InAs_{0.3}Sb_{0.7}$/Al shadow junction resistance statistically increases with increasing l_s. Surprisingly, the junction resistance, R_{Δ_b} depends on the slope of the Al towards the junction, also for junctions without visible Al islands; however, the trend seems significant. For junctions with dewetted Al islands, it seems reasonable with a reduced junction transparency due to potential variations caused by Al islands across the junctions. Using standard four-probe measurements, the measured mean $R_c = 0.8$ kΩ as shown in Figure 3.19**a**. Figure 3.19**b** shows conductance saturation of the devices decrease with increased l_s. We attribute this effect to the junctions with multiple Al grains for $l_s > 500$ nm. Unexpectedly, we also observe a trend of decreasing conductance for $l_s < 250$ nm, although Al grains do not form within that range. We presume the profile of broadening within that range may play a role in the conductance deviation.

3.5 Junctions Transparency

Quantized Conductance

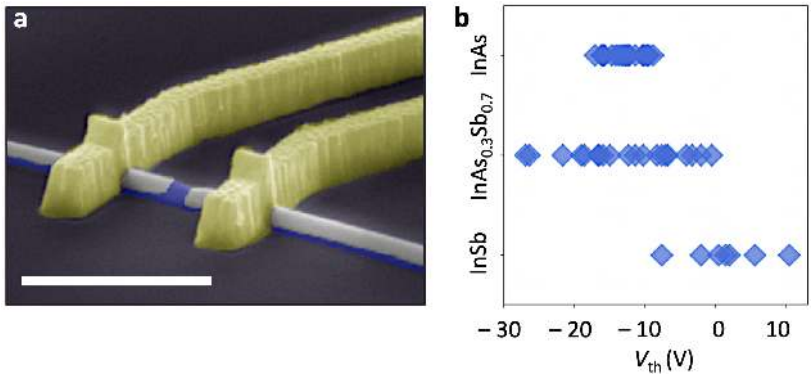

Figure 3.20: Nanowire junction devices. a, Pseudo colored SEM image of a typical single-junction back-gated device. Scale bar is 1 μm. **b**, Pinch-off voltage statistics for InAs, $InAs_{0.3}Sb_{0.7}$ and InSb NW junction devices.

We further investigate the device performances of the sharp-edged junctions for InAs, InSb, and $InAs_{0.3}Sb_{0.7}$ NWs. Pseudo-colored SEM image of a typical single shadow junction device is shown in Figure 3.20**a**. In Figure 3.20**b**, we show the pinch-off voltages for Al-based junction devices measured at 2 K. The pinch-off voltages for $InAs_{0.3}Sb_{0.7}$/Al junctions show the widest span from ~ −30V to 0V, whereas the InAs/Al junctions pinch-off in the range of ~ 0V to −10V. On the other hand, InSb/Al junction devices show pinch-off at mainly positive V_g. We ascribe the statistical differences to the band alignment between the semiconductor and the Al [228]. [1]

1: Device fabrication and measurement for NW/Al shell are performed in collaboration with Ajuan Cui and Charalampos Lampadaris. InSb/Sn device fabrication and measurements are performed by Sebastian J Pauka and Maja C Cassidy from Microsoft Station Q, Sydney.

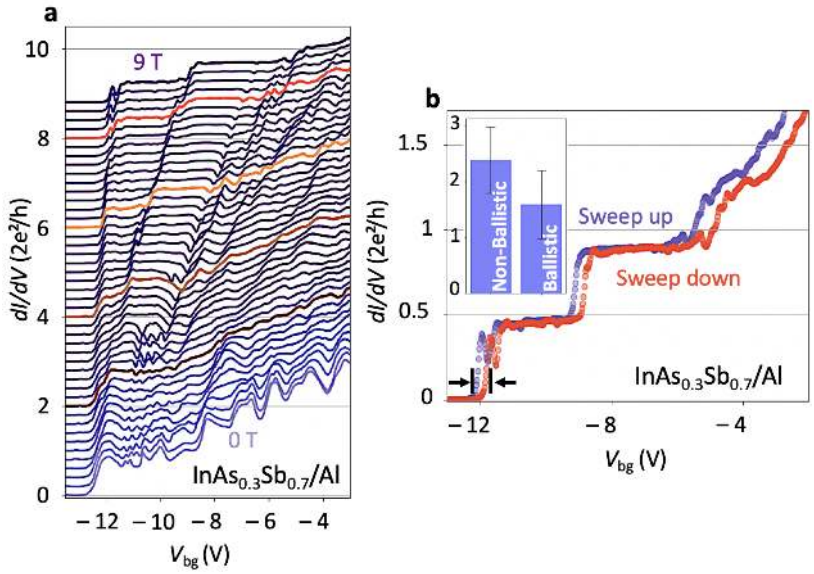

Figure 3.21: Quantized $InAs_{0.3}Sb_{0.7}$/Al NW junction. a, Differential conductance as a function of gate voltage and magnetic field of a $InAs_{0.3}Sb_{0.7}$/Al NW junction. **b**, Hysteresis of the device shown in (**a**) where sweep up and down follows closely. Inset is a comparison of a statistical value of hysteresis between quantized and non-quantized devices.

An example of quantized conductance in $InAs_{0.3}Sb_{0.7}$/Al junction device is shown in Figure 3.21**a**, where the conductance is measured as a function of V_g and magnetic field (**B**). A general trend is that the conductance plateaus are less pronounced at low **B** but gets gradually sharper with increasing field. This can be ascribed to lower electron back-scattering rates at higher **B**. The first sub-band splits into two spin-split subbands due to the Zeeman effect, which leads to an energy difference $g\mu_B\mathbf{B}$, where g is the Landé-g factor and μ_B is Bohr's magneton. For this particular $InAs_{0.3}Sb_{0.7}$/Al device, we see the emergence of the spin-split sub-bands around **B** > 2.2 T. However, we generally see the visible splitting appearing around **B**= 2-3 T. We speculate that the late emergence of visible spin-split bands is related to electron-electron interaction within the two sub-bands.

The obtained quantized values in Figure 3.21**a** are lower than the predicted Ne^2/h because of a constant contact resistance, leading to the first sun-band at of $0.45 \cdot 2e^2/h$, the second at $0.9 \cdot 2e^2/h$ and the third one is barely observed at $1.3 \pm 0.5 \cdot 2e^2/h$. Figure 3.21**b** demonstrates a hysteresis that is much smaller than sub-band spacing in the device presented in Figure 3.21**a**. The inset shows a comparison of hysteresis statistics near the pinch-off region between quantized and non-quantized devices, where the quantized devices typically exhibit a slightly smaller hysteresis ~ 1.5 V, compare to others (~ 2.3 V).

Quantized plateaus for InAs/Al and InSb/Al NW junctions under magnetic field are also observed, as showed in Figure 3.22**a** and **b**. The

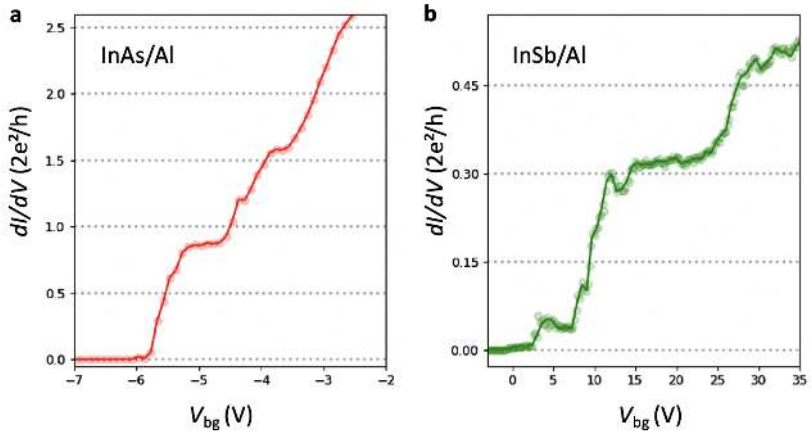

Figure 3.22: Quantized conductance on InAs/Al and InSb/Al junctions. Conductance is drawn as a function of gate voltage for InAs/Al (**a**), and InSb/Al NW (**b**) junctions. All the plots shown here are measured with 9 T magnetic field, which is applied perpendicular to the NWs. The measurement is done at 2 K and the length of the junction is ~ 100 nm.

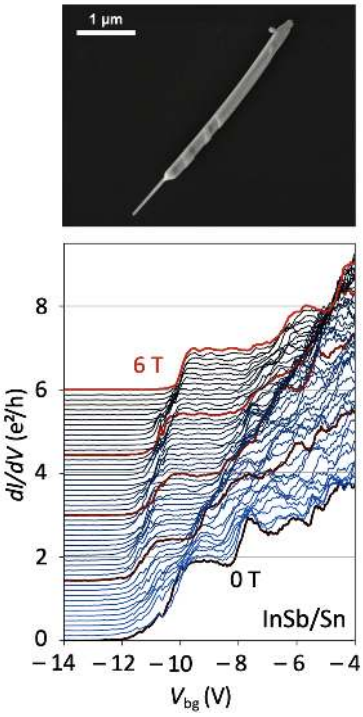

Figure 3.23: Quantized InSb/Sn junction device a, An SEM image of the NW prior to deposition of contacts. Contacts are deposited such that the only center junction is being probed. The measured dimension of this junction is 210 nm. **b**, Differential conductance as a function of gate voltage and magnetic field for InSb/Sn NW junction.

conductance plateaus do not appear at the exact value of Ne^2/h and differ between the materials. The plateaus only appear under applied magnetic field, and they become more pronounced with increased magnetic field. Two probe measurements are carried out for all these devices, so other parts in the measurement circuits also contribute to the signals. Apart from that, the difference caused by contact resistance and contact geometry among different materials may also the reason behind the deviation from e^2/h, $2e^2/h$, *etc.* As can be seen in Figure 3.22**a**, for InAs, two plateaus are identified, where the first plateau appears around $2e^2/h$. On the other hand, for InSb (Figure 3.22**b**), the plateaus are more close to e^2/h. For both, the position of the plateaus can be attributed to sub-band splitting under high magnetic field, whereas for InAs, no splitting of plateaus is observed which needs further investigation. The appearance of conductance plateaus only under magnetic field may be attributed to the disorder (structural or surface states) induced backscattering, which is suppressed by high magnetic field. Various resonances can also obscure the appearance of quantized plateaus.

In Figure 3.23**a**, SEM image of examined sharp-edge InSb/Sn junction. In Figure 3.23**b**, we show the measurement of the device with each trace offset by the value of the **B**. In contrast to the InSb/Al junctions, the devices with Sn show a negative pinch-off voltage around −10 V, caused by the different band alignment of Sn to InSb. In these devices, after the subtraction of the filter resistances in the fridge and a constant contact resistance, a clear plateau at $2e^2/h$ is visible even at zero field, suggesting a scattering length on the order of a few hundred nanometers. Furthermore, unlike the sample shown in Figure 3.21**a**, splitting of the subband is visible immediately as the field is increased. A crossing of the first two spin-split sub-bands is visible at around 2 T, characterized by the disappearance and re-emergence of a plateau at $2e^2/h$. This effect is expected due to the large Landé-g factor of InSb [148].

Low Temperature Measurements

Figure 3.25 presents low temperature ($T \sim 20$ mK) electrical measurements performed on seven $InAs_{0.3}Sb_{0.7}$/Al shadow JJs (S#1–S#7) with $l_j \sim 100$ nm. A single contact to the Al shell is fabricated from Ti/Au normal metal on either side of the shadow junction and split into separate bond-pads to allow for a pseudo four-terminal configuration, eliminating

contributions from highly resistive filters in the cryostat. The transmission of the junction is tunable by the back-gate potential V_g, and Figure 3.25**a** shows typical $V-I$-curves at $V_g = 0\,\mathrm{V}$ for sample S#1. A zero-voltage state is observed corresponding to a switching current I_C exceeding 200 nA with pronounced hysteresis between up/down sweep directions, which is commonly observed in such devices and attributed to heating effects or underdamped junction [229, 230].

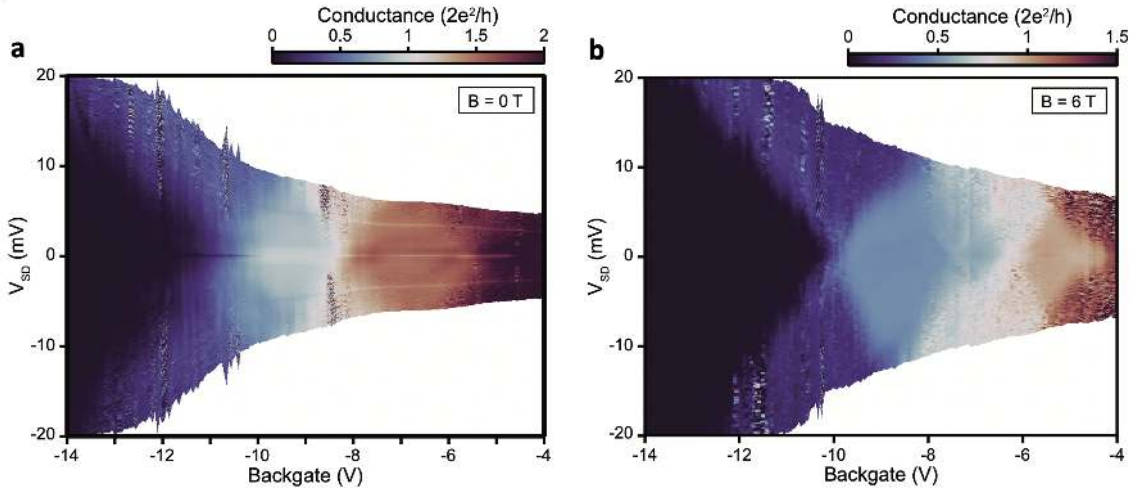

Figure 3.24: Additional measurements in InSb/Sn junction device. a, A two-terminal source-drain measurement is taken at **B**=0 T, while **b**, shows the same measurement taken at **B**=6 T. The source-drain bias (V_{SD}) at the device is extracted for both measurements using the known resistance of the filters and contacts in the fridge. In both sets of data, quantized conductance plateaus are visible, suggesting transport in the junction is ballistic on the order of a few hundred nanometres. As is expected, at zero field the first plateau has a conductance of $2e^2/h$, while at 6 T, spin degeneracy is broken leading to the emergence of a plateau at e^2/h. In the zero-field data, features relating to the superconducting shell are visible near zero bias and as two dips symmetric around zero bias.

Figure 3.25**b** shows the differential resistance as a function of I and V_g. The zero-resistance state is clearly observed, and I_C decreases with V_g as the transparency of the n-type semiconductor weak link decreases towards pinch-off at $V_g \sim -40\,\mathrm{V}$. Also shown are the extracted gate-dependence of the switching current $I_C(V_g)$ and the normal state conductance $g_N(V_g)$ measured at with a magnetic field $B_\perp = 0.3\,\mathrm{T}$ applied perpendicular so the substrate and exceeding the critical field of the superconducting leads. The product of I_C and $R_N = 1/g_N$ is a typical voltage characterizing JJs, and Figure 3.25**c** shows I_C *vs.* g_N for all devices where the range of g_N is spanned by sweeping V_g. For samples S#2-7 the curves are extracted from the data shown in Figure 3.26. The dashed line labeled KO−1 (KO−2) shows $I_C R_N = \pi\Delta/2e$ ($I_C R_N = \pi\Delta/e$) expected for a JJ in the short, quasi-ballistic and dirty (ballistic) regime with the mean-free path $l_e \ll l_j \ll \xi$ ($l_e \gtrsim l_j, l_j \ll \xi$), and a superconducting gap $\Delta = 200\,\mu\mathrm{eV}$ expected for Al and matching voltage-biased measurements discussed below. ξ is the superconducting coherence length [231]. JJs with semiconductor NWs weak links have been the subject of a large number of investigations since the original work of Doh [229] and the critical currents in these devices are generally much lower than the KO−1 and KO−2 predictions and $I_c R_n$ significantly underestimates Δ [232–234]. The origin of this suppression is unknown, but has been speculated to arise due to disorder and in-homogeneity or to heavily underdamped junctions.

For the $InAs_{0.3}Sb_{0.7}$ shadow junctions studied here the critical currents are relatively high, and samples S#1 and S#2 follow approximately the KO−1 and the ballistic KO−2 result. The remaining devices have suppressed I_C for high R_N indicating presence of channels with weak contribution to the supercurrent. At lower resistance the increase in I_C with g_N follows the KO−1 slope, consistent with additional channels with contribution to I_C, as predicted by the model. We attribute these results to the high quality of the sharp edge $InAs_{0.3}Sb_{0.7}$/Al shadow junctions and clean interface. For sample S#1, the phase-coherence is confirmed by the voltage-biased measurement in Figure 3.25**d**, which shows a clear V_g-independent subgap structure which we attribute to multiple andreev reflections (MAR) as previously studied in NW JJ [229]. The resonance resolved at lowest V_{sd} corresponds approximately to the $n = 5^{th}$ order MAR $2\Delta/ne$ process requiring five coherent andreev reflection processes. Higher order MAR processes may be present but are inaccessible in these measurements due to the cryostat line resistances ~ 6 kΩ, making the measurement an effective current-biased measurement at low applied voltages. [2]

2: Device fabrication and LT measurements of this section are performed by Lukas Stampfer from Thomas Sand group at Qdev.

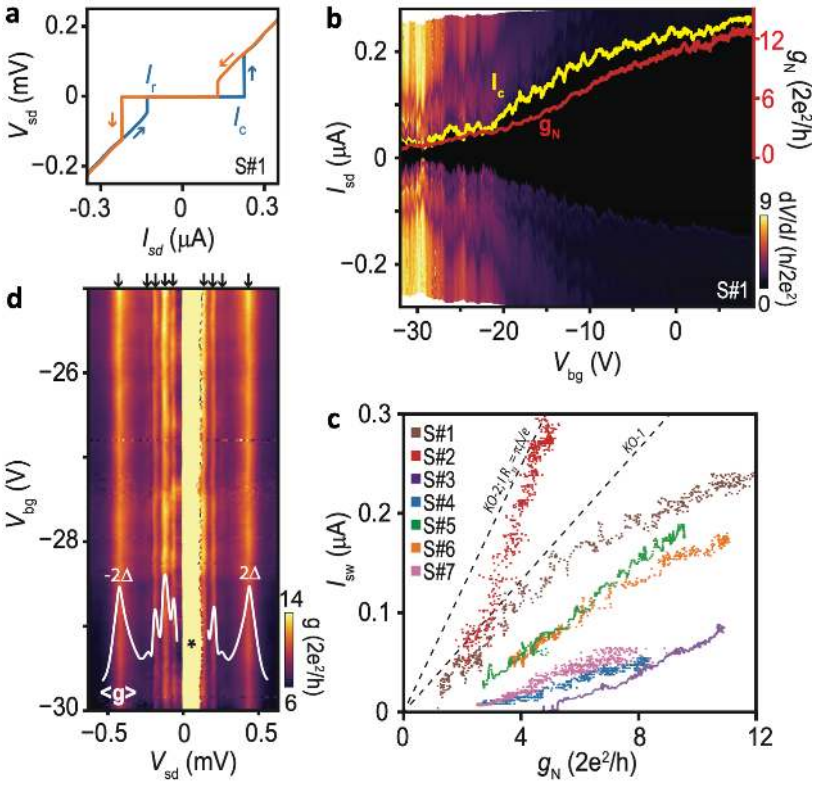

Figure 3.25: Supercurrent and multiple Andreev reflections in the sharp-edge junctions. **a**, Typical VI-curve for an $InAs_{0.3}Sb_{0.7}$/Al shadow Josephson junction (Device S#1). The switching and retrapping currents are indicated. **b**, Differential resistance as a function of current and gate potential. The black region corresponds to the zero-voltage state. I_C and normal state conductance g_N measured at $B_\perp = 0.3\,T$ are shown. **c**, I_C *vs.* g_N for all measured devices. Dashed lines are the theoretical expectations. **d**, Voltage-biased measurement of the sub-gap structure of S#1 showing resonances of multiple Andreev reflections. The high-conductance region asymmetric around zero bias (∗) is related to a supercurrent branch enabled by the finite resistance of the cryostat wiring.

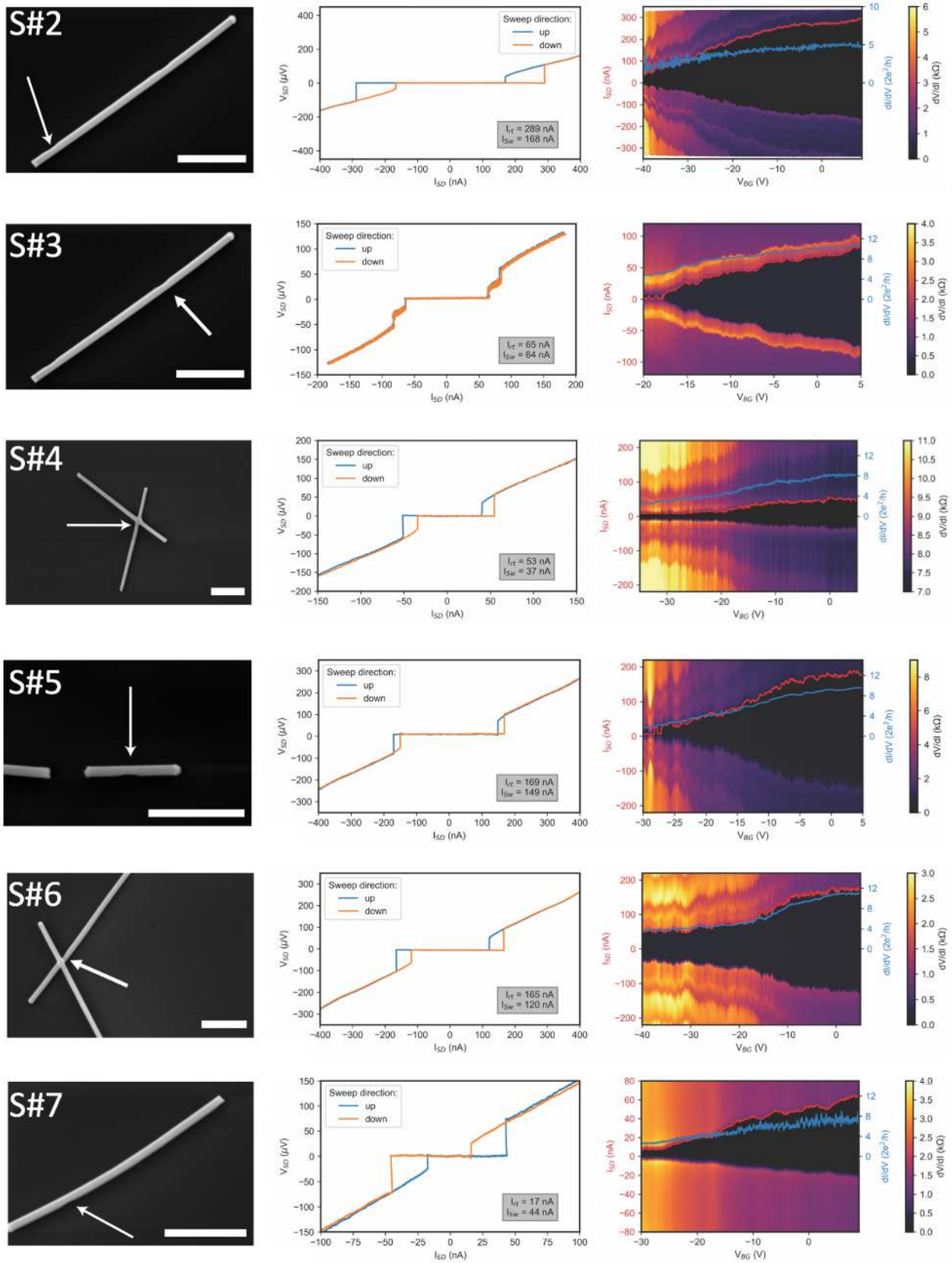

Figure 3.26: Supercurrent measurements for other devices. First column of this figure shows the SEM before metallization of the 6 other devices shown in Figure 3.25. The shadowed region is hinted with an arrow. In the case of the crosses, the merged NW is fully metalized with the corresponding contact in order to avoid floating pieces of SU close to the junction. Second column indicates the I-V characteristics of the junctions with up and down sweep at V_{bg}= 0 V. In device S#3, we note a presence of a step like feature which qualitatively looks like a Fiske step. The third column shows the differential resistances as a function of applied current and back-gate voltage.

3.6 Conclusion

In summary, we present a versatile single-step UHV crystal growth method to fabricate epitaxial SE-SU NWs with high quality gate-tunable superconducting junctions. The flexibility of the approach is exemplified with the growth of InAs, InSb, and $InAs_{0.3}Sb_{0.7}$ NWs with *in situ* shadowed junctions in Al, Sn, and Pb. Based on the performance statistics of field-effect $InAs_{0.3}Sb_{0.7}$/Al devices we show that the quality of shadowed junctions are significantly higher than the etched junctions. Furthermore, for the shadowed junctions, we demonstrate that the junction transparency depends on the junction edge profile. We conclude that the junctions with sharp edges have high transparency, exhibiting extremely large supercurrents and easily resolved quantized conductance of the lowest sub-bands. The achieved results with sharp-edge shadowing in this work can also be transferable on the scalable selective area grown (SAG) NW platform [235, 236] through either post-growth *in situ* masking or pre-fabricated substrate with nanopillar/ stencil bridge structure, which will act as a mask during SU deposition [237]. Hence, this study shows a path toward reliable gate-tunable operations in superconducting quantum networks.

3.7 Experimental Details

Substrate Fabrication

InAs (100) undoped single side polished (SSP) 500 μm thick 2-inch wafer is used to start the substrate fabrication for hybrid NW growths. Substrate preparation is discussed below:

Step 1: For exposure, we use electron sensitive co-polymer resist EL9 and spin with 4000 RPM (thickness ~ 320 nm) for 45 sec. Next, hotplate baking of the resist is performed at 185°C for 2 min to get rid of the solvent and improve the adhesion with the substrate. Lines for the trenches are exposed with EBL. For development, we dip the wafer into 1:3 MIBK: IPA for 45 sec and IPA for 30 sec. Then, oxygen plasma treatment for 2 min. **Step 2**: We use wet-etching to create (111) B faceted trenches. We etch the exposed lines to create V-shaped trenches with an angle of 54.7° using the following recipe: i) Mix H_2SO_4 (1 ml): H_2O_2 (8 ml): H_2O (80 ml) and blend for 5 min with a magnetic stirrer. ii) take 4 ml of the above mixture, mix with 400 ml of H_2O, and blend for 5 min with a magnetic stirrer. The 2-inch wafer is then dipped into the solution for 30 min (for ~ 1 μm etching) or 60 min (for ~ 2 μm etching). Afterward, cleaning of the wafer is done as follows: i) acetone for 4 min, ii) sonication for 2 min with 80 Hz frequency and 30 W power, iii) acetone for 10 sec, iv) IPA for 10 sec and finally clean with milli-q water for 30 sec. **Step 3**: Next is the exposure for Au particles. Two layers of resist are needed to coat homogeneously on the trenches. First, EL6 spinning with 4000 RPM (~ 150 nm) for 45 sec, and subsequently 1 min hotplate baking at 185°C. Second, A2 spinning with 4000 RPM (~ 60 nm) for 45 sec and similar hotplate baking. The EBL system is used for dots exposure. For post-exposure development, we dip the wafer into 1:3 MIBK: IPA for 45 sec, IPA for 30 sec, and then examine with the optical microscopy to confirm that the dots are properly aligned

with the trenches. **Step 4**: Depending on the NW diameter, 7-15 nm thick Au layer is deposited at the rate of 1 Å/s on the wafer using an e-beam evaporator. If there is a time delay between resist development and Au deposition, it is crucial to remove the native oxide before Au deposition through Hydrofluoric acid (HF) dipping or *in situ* Ar milling in the metal evaporation chamber. However, this is not needed if the Au deposition is immediately after the development. For lift-off, Au contained wafer is immersed into the acetone and kept for 10 min until the Au started lifting-off. Later, the acetone dipped sample is placed into 50°C heated bath for 1 hour and then cleaning procedure of the wafer, which is similar to step 2. Finally, the ready-to-grow 2-inch InAs substrate with trenches is cleaved into four quarters to make it adjustable with the MBE growth holder and plasma ashed for 2 min (similar to step 1) to make sure no organic particles are left on the quarter.

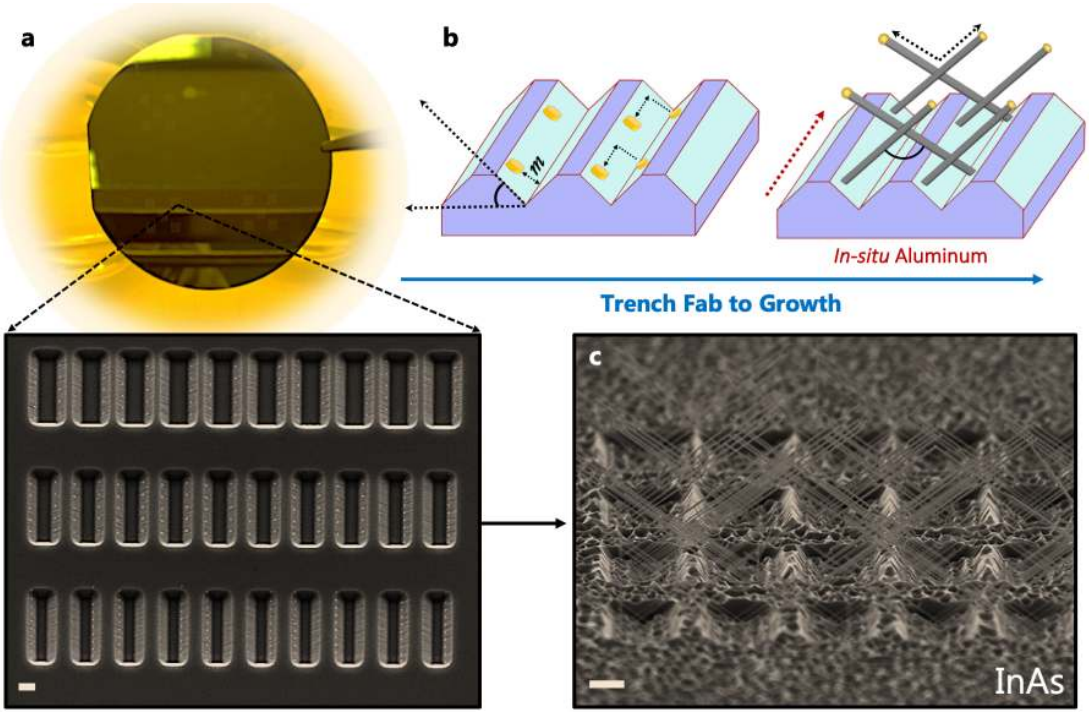

Figure 3.27: Substrate fabrication and molecular beam epitaxy of hybrid nanowires. a, An image of 2-inch wafer with lithography-defined patterns. Zoomed-in SEM image of the (111) B faceted trenches with deposited Au disks (scale bar is 1 μm). **b**, Schematic of the fabricated substrate and NW growth scheme. The angle of the etched trenches are 54.7°C. An offset (m) from the bottom of the trenches is maintained in order to avoid competition between bulk growth and NW growth in the trenches. Regarding the position of the Au, if it is close to the lower edge of the trench, the wire may not be able to grow before it gets covered by planar growth. If the catalyst is too close to the upper edge, it migrates to the (100) facet while annealing. Hence, perfectly aligned lithography to place the Au seeds in the middle of the sidewall is crucial. Red arrow is an example SU deposition direction along the trenches. **c**, InAs NWs growth from the trench substrate.

Hybrid NWs Synthesis in the Trenches.

Semiconductor-superconductor hybrid NWs are grown using the Veeco GEN II MBE system (similar to chapter 2). Before loading in the MBE chamber, the fabricated substrate (1/4 of a 2-inch wafer) is dipped into diluted HF for 10 sec, and then 20 sec of rinsing with the milli-q water to make sure the substrate is clean for loading. Initially, the sample is baked at 200°C for 2 hours in the entry/exit (EE) chamber of the MBE system,

which confirms the vaporization of remaining water molecules from the substrate and then transfer to the buffer chamber. In the buffer chamber, the substrate is degassed for 1 hour at 250°C to confirm additional cleaning before transferring into the growth chamber. In the growth chamber, the substrate is annealed for 2 min at 590°C. All the intended effusion cells are heated up and fluxes are stabilized before the growth. InAs NWs on the trench are grown with As_4 overpressure maintaining the bulk temperature at 345°C and cracker temperature at 400°C. After being annealed, the substrate is cooled down to growth temperature within 5 min (linear cooling) and stabilized for 3 min before opening the "In" shutter for the growth. Right after the NW growth, the substrate is cool down to 150°C and all the sources are set back to the base temperature. InSb NWs are grown with initial InAs NW stem where the growth procedure of stem is the same as described above. Maintaining the same substrate temperature, "As" shutter is closed and Sb shutter is opened, leading to InSb NW growth continued from the InAs stem. Finally, similar to InSb NWs, $InAs_{0.3}Sb_{0.7}$ NWs are also grown with InAs stems, where we tune the As flux for different compositions of the NWs. *in situ* Al deposition is performed in the MBE growth chamber by cooling down the substrate holder to ~ -36°C over 8-10 hours right after the NW growth. When the desired temperature is reached, the substrate is aligned to the intended deposition angle. Before the deposition, Al cell is heated 1140°C and flux is stabilized. 15 min of O_2 venting is performed while taking out the NWs sample from the MBE chamber in order to form AlO_X to avoid dewetting. Further, Sn and Pb on the NWs are grown in the UHV metal deposition chamber (with liquid nitrogen cooling) which is connected to MBE.

Structural Characterization

The morphology along with length and diameter of the grown NWs are examined with SEM. AFM is also used to characterize the surface morphology of the junctions, analyze broadening, and also to determine the thickness of SU. The atomic crystal structures of the NWs are characterized by TEM and high resolution (HR-) TEM. [3] The structural properties, including lattice constant and atomic configuration are analyzed using CrystalMaker for Windows (Ver. 9.2.7, CrystalMaker Software Ltd.). For STEM Tomography, NWs are transferred from the growth substrate to a TEM grid with a lacey carbon membrane using a micromanipulator. The grid is mounted on a Gatan tomography TEM holder, allowing tilting of samples from −70 to 70 degrees. A Thermo Fisher Scientific S/TEM Talos F200X microscope is used to acquire high-angle annular dark-field (HAADF)-STEM images at 200 kV, at steps of 1 degree. The Thermo Fisher Scientific Inspect 3D software is used for image alignment and reconstruction. 3D visualization is performed by the Thermo Fisher Scientific Avizo software.

3: TEM analysis is performed by Martin E Cachaza, Elisabetta Maria Fiordaliso, Jung-Hyun Kang and Svetlana Korneychuk.

NW Device Fabrication

The device fabrication process starts with transferring wires onto the prefabricated back-gated device chip using a micromanipulator. Two min of plasma ashing is performed before transferring NWs on the chip.

Hybrid NW devices with SE-SU junctions are fabricated as following: for InAs/Al NW devices, (1) spin resist AZ1505 on the chip with 4000 rpm for 45 sec and bake the resist at 115°C for 2 min; (2) UV lithography for source and drain electrode; (3) for development, AZ developer for 60 sec, rinse in Milli-q water for 30 sec, and later oxygen plasma treatment for 2 min; (4) to remove the oxidized NW surface, RF argon plasma milling is done for 8 min with 15 W power before depositing e-beam evaporated Ti and Au (5 and 200 nm) at the rate of 1-2 Å/s; (5) lift-off is done using acetone for 20 min; (6) cleaning procedure is done by hot bath of NMP at 80°C for 1 hour, rinsing with acetone, dipping into IPA for 10 sec, and then 2 min of oxygen plasma treatment; finally, baking the chip for 2 min at 185°C. For $InAs_{0.3}Sb_{0.7}$/Al NW devices, (1) spin electron sensitive PMMA resist (A4) on the chip with 4000 rpm for 45 sec and bake the resist at 115°C for 2 min; (2) E-beam lithography for source and drain electrode; (3) for development, 1:3 MIBK/IPA for 45 s, rinse in IPA for 30 sec, and later 30 sec of oxygen plasma treatment; (4) RF argon plasma milling is done for 5 min with 7 W power before depositing evaporated Ti and Au (5 and 250 nm) at the rate of 2 Å/s; (5) 20 min of acetone dipping for lift-off; (6) for cleaning step, rinsing with acetone, dipping into IPA for 10 sec, and then 2 min of oxygen plasma treatment. For InSb/Al NW devices, we follow the similar recipes as for $InAs_{0.3}Sb_{0.7}$/Al NW devices with following changes: in step (1) spin electron sensitive PMMA resist (A6) on the chip with 4000 rpm for 45 sec, no hot plate baking is performed after resist spinning as the InSb/Al interface is subjected to damage at high temperature, instead the sample is dried through pumping for 2 hours to get rid of the solvent of the resist; and in step (4) RF argon plasma milling for 4 min with 7 W power to remove the oxidized InSb NW surface.

NW Device Measurements

PPMS measurements. For electrical measurements, a physical property measurement system (PPMS, Quantum Design Inc.) is used with ~ 2 K measurement temperature and magnetic field up to 9 T. The device chip with daughterboard is mounted in the motherboard and loaded in the PPMS system. Then the PPMS system is pumped to a pressure lower than 0.01 mTorr and then degassing for more than 10 hours at 350 K. For InSb and $InAs_{0.3}Sb_{0.7}$ NW devices, the degassing is performed at room temperature. PPMS is then cooled down to 10 K and supply evaporated liquid helium (H_4) in the chamber to further cool down to the measurement temperature (~ 2 K).

20 mK measurements. The devices for the superconducting measurements are fabricated on degenerately doped Si substrates with 200 nm of thermal oxide. The contact areas are patterned using standard EBL. As discussed before, the contact materials, Ti/Au (5/195 nm) are evaporated after an *in situ* Argon milling process. The measurements are performed in a cryo-free dilution refrigerator at a base temperature of 20 mK. Critical current measurements are performed using standard lock-in and DC techniques with the use of a 50 kΩ shunt resistor. The clearly identifiable supercurrent shows a residual resistance. This is attributed to contact resistance and subtracted from the data set. The nature of the contact

resistance lies in the measurement not being a truly four terminal, it bypasses only the filters in the fridge, not the Ti/Au – Al contacts.

Resistance Calculation and Mobility Fit

Pinch-off curves are fitted using the formula developed in the ref. [238–240] and also shown below. The mobility values of 16 devices are extracted using the *formula fit* and the *direct transconductance method* as described ref [240], and the results we get are in agreement.

$$G(V_g) = (R + \frac{{l_j}^2}{\mu C(V_g - V_{th})})^{-1}$$

Here in the formula, R is the gate-independent resistance, C is the capacitance calculated from the cylindrical approximation with the correction for hexagonal NWs [241], l_j is the junction length and μ is the field-effect mobility.

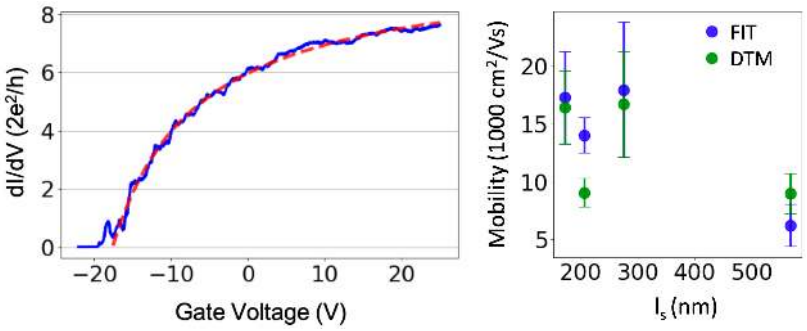

Figure 3.28: Fitting of a pinch-off curve. Blue line: forward sweep of the gate voltage and the evolution of the differential conductance in units of $2e^2/h$. Red dashed line: the fitted model. On the right, field-effect mobility as a function of interwire distances.

The equation above consists of a gate independent term (R) and a gate dependent term ($\frac{{l_j}^2}{\mu C(V_g - V_{th})}$). In our device geometry, the first term is more complex than the one described in the Ref [238–240]. These are the contact resistance (R_C), the resistance coming from the broadening of the junctions (R_{Δ_b}) and also the resistance of semiconductor-superconductor interface (R_{int}). The effect of the three gate-independent resistances on the junctions are presented before. The contact resistance is extracted from four devices using standard 4-probe measurement technique. On the other hand, The gate-dependent resistance in the equation emerges from the semiconductor segment.

Semiconductor Nanowire Networks

4

4.1 Introduction

According to the theoretical proposals [33, 51, 242–245], Majorana fermion obeys non-Abelian exchange statistics. Thus, the logic operation is possible through braiding between fermions [245]. Hybrid NWs that I have demonstrated in Chapter 2 and Chapter 3 are the platform to evidence the signature of Majorana bound states, which can appear at both ends of the NW [246]. However, for the logic operations to demonstrate functional qubits, a network is required, so that fermions' position exchange is possible without bringing them into close proximity, that can demise their property [33, 51, 242–247]. Therefore, the control synthesis of the semiconductor nanowire network plays an important role for next generation Majorana devices. Furthermore, the applications of NW networks extend into different fields, such as multi-terminal device operation [248–251], cooper-pair splitting [252, 253], optoelectronic devices [254, 255], biological sensors [256, 257] and so on. Hence, recently a significant effort is observed in developing NW networks, where two possible directions are considered: vapor-liquid-solid (VLS) grown out-of-plane NW networks [66, 84, 185, 186, 247, 258–261] and in-plane selective area grown (SAG) NW networks [149, 235, 236, 262–264]. Both approaches have their pros and cons, which will be discussed next.

Summary

In this work, we study the controlled synthesis of InSb and InAsSb nanocrosses. We analyze the conditions of nanocross growth as a function of substrate design, growth time and nanowire diameter. We also investigate the network formation for InAs NWs. Structural analysis of InAs network exhibits crystal disorder when NWs are merged. On the other hand, structural analysis of the InSb nanocrosses show single-crystalline zinc blend all over the network, which makes it interesting for multi-terminal devices. Finally, an *in situ* shadowing technique is shown to pattern the nanocrosses.

4.2 VLS and SAG Networks

VLS grown NW networks offer high crystal quality. Due to the free-standing nature, where axial growth is determined by the supersaturated catalyst, no defects from the growth substrate follows in the NWs. As mentioned in chapter 2, in VLS NWs, the strain relaxation mechanism helps to format different heterostructures with large lattice mismatch, which we cannot expect from the bulk system [7, 265]. In addition to that, VLS growth of NWs are well-studied [1, 7, 265–268], hence, an established understanding of growth dynamics helps to realize control NW networks with a variety of III-V combinations. In contrast, the growth of VLS networks require extensive fabrication effort to modify the substrate and carefully position the catalyst particles [66, 185, 247, 258, 259]. The substrate fabrication becomes more complicated to *in situ* shadow the networks. It also suffers from the limitation of the possible network design, due to the fundamental constraint of the NW growth. Besides, scalability is a crucial issue for VLS grown networks. To prepare electronic devices, the NWs require to transfer into the separate chip, and position carefully. This is a time-consuming process and in order to achieve an useful statistics on electrical measurements, a large number of NWs are required to be transferred. The degree of complexity increases for more dedicated devices with bottom-gates. All in all, unless significant

development happens toward the as-grown device fabrication with the VLS network, it will be difficult to transfer this platform into the industry. Nonetheless, VLS grown networks are essential to study the fundamental physics and material properties (due to their high crystal quality) on a single device scale.

On the other hand, SAG NWs are grown in-plane on a predefined area of the growth substrate. [1] Therefore, it offers scalability. In contrast to the VLS, SAG provides the freedom to create any kind of networks by predesigning the substrate. Also, the devices can be fabricated directly on the growth substrate. Thus, no additional step is required for transferring the NWs. Besides, due to their in-plane nature, it is possible to make in-situ devices with SAG through stencil lithography (shadow masking), after the NW growth, avoiding any resist or chemical treatment to the device. This confirms the purity of the as-grown devices. Although SAG promises scalability, the fundamental challenge remains to their crystal quality. As the NWs are grown from the template, any short of disorders during substrate fabrication will induce the defects during the NW growth. Reactive ion-assisted dry etching (RIE) is often used to define the SAG template. It is known that, RIE creates atomic-scale defects due to the energetic ion sputtering, which is difficult to get rid of [269]. Therefore, NWs can contain initial defects promoted by the template. Besides, misfit dislocations due to the lattice mismatch similar to the planar heterostructure appear in NW structures. So, it is challenging to achieve the desired crystal quality in the SAG platform. Further, a systematic study is required both on the substrate fabrication and material growth in order to achieve high crystal quality of SAG NWs. In sum, for proof of concept and fundamental study, high-quality VLS grown networks are preferable. On the other hand, for large scale applications, the SAG platform is preferable, if the high crystal quality is achieved. Similar to the previous chapters, here, I will only focus on the VLS grown NW networks.

1: Ref.[235] (Paper 7) shows details about SAG platform. This thesis will not cover the SAG growth.

In this chapter, I will demonstrate the synthesis of high yield InSb and InAsSb nanocrosses. Detailed analysis of the structural formation as a function of catalyst position and growth time will be presented. Besides, the network formation from InAs NWs and their crystal structures will be shown. [2] .

2: TEM of this chapter is performed by Jung-Hyun Kang at Center for Electron Nanoscopy, Technical University of Denmark (DTU CEN).

Remark 4.2.1 Section 4.3-4.4 and 4.7 are adapted from Paper 2. Sabbir A. Khan*, Lukas Stampfer*, Timo Mutas, Jung-Hyun Kang, Peter Krogstrup, Thomas S. Jespersen, "Multiterminal Quantized Conductance in InSb Nanocrosses" Advanced Materials (Accepted).

4.3 InSb Nanocrosses

Substrate Preparation

Similar to the Chapter 3 [3] , InAs (111)B faceted trenches are also used for creating the NW networks. The only difference is the catalyst positioning. As shown in Figure 4.1**a**, Au catalyst particles are carefully positioned on the (111)B trenches depending on the conditions of the networks.

3: See chapter 3, experimental section for detail substrate fabrication steps.

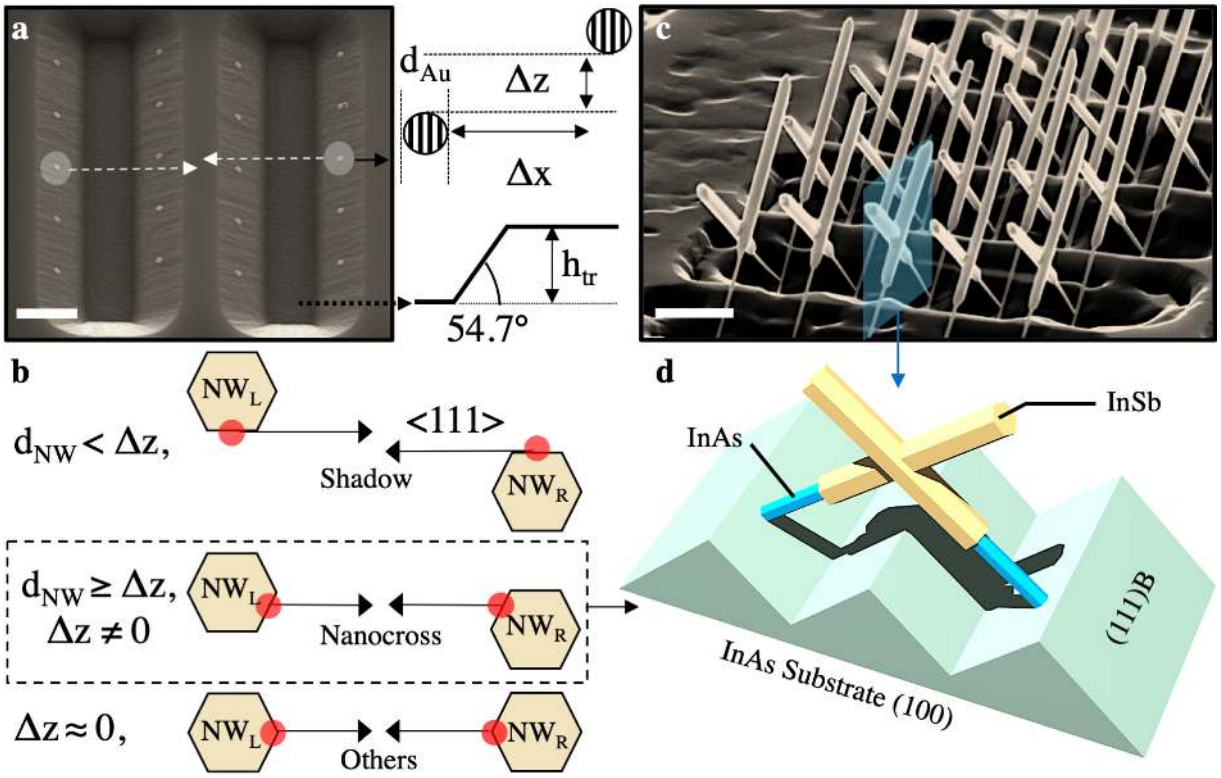

Figure 4.1: Conditions for different InSb networks. a, Tilted scanning electron micrograph (SEM) of InAs (111)B trenches with deposited Au catalyst particles. Trenches are created by wet-etching in InAs (100) substrate. Here, Δx is the distance between two Au catalysts from opposite trenches, Δz is the offset between two Au catalysts, and h_{tr} is the height or the etch depth of the trench. The schematic is not drawn to scale. **b**, Three possible schemes of the NWs, grown from the opposite directions depending on their Au positions. First, when the final diameters of the NWs (d_{NW}) are smaller than the offset of the Au catalyst ($d_{NW} < \Delta z$), then the wires are used for shadowing as elaborated in Chapter 3. Second, if the diameter of the NWs (d_{NW}) are bigger than the offset of the Au catalyst ($d_{NW} \geqslant \Delta z$ and $\Delta z \neq 0$), a nanocross can be formed. Finally, if Au catalysts are positioned face-to-face which means, NWs are grown without offset a nanoplate shape structure can be formed. Later two networks will be discussed broadly in this chapter. **c**, Tilted SEM image of InAs stem assisted InSb NWs grown from the opposite trenches. Predesigned Au positioning on the trenches confirms NWs growth direction towards each other and condition for nanocross formation. The highlighted section shows an example of proper nanocross formation, where the NWs merge through the side-wall and combined as one structure. **d**, Schematic of the nanocross from the trenches with the condition $d_{NW} > \Delta z$. Scale bars for (**a**) and (**c**) are 1 μm.

Such pre-positioning of the catalysts on the (111)B facets of the trenches locks NWs growth only in $< 111 >$ directions. That assists to control the synthesis of the NW network by tuning the lithography design, NW length, and diameter. The Au catalysts are positioned both head-to-head, where $\Delta z = 0$ and with an offset between the catalyst aiming to $d_{NW} \geqslant \Delta z$. Different catalyst positioning will lead to different network formation, which will be discussed next.

Growth of InSb Nanocrosses

As discussed in Chapter 2 and 3, Au assisted III-Sb NWs are not directly grown from the III-V substrate. InAs stem is used to confine the contact angle of the liquid catalyst and assist InSb NW growth. Hence, optimized InAs stem growth in the trench is the prerequisite to achieve uniform InSb NWs across the substrate. Detailed growth analysis of InAs NWs on the (111)B faceted trenches is discussed in Chapter 3 and Paper 1 [54]. With optimized InAs growth conditions, we first confirm the high yield of InSb growth throughout the substrate.

InSb NWs are grown from opposite < 111 > directions, hence, we can tune the position of the Au and investigate the conditions for a controlled way of creating an InSb network unlike the previous studies [66, 247]. For this, we systematically determine the trench size and Au catalyst's positioning during lithography (Figure 4.1**a**). The distance of Au in the opposite trenches (Δx), offset between Au catalysts (Δz) and height of the trench (h_{tr}) determine the conditions of the networks (as for instance, length of the stems, length of InSb segments, NWs merging point etc.). Hence, based on the Δx, Δz, and the number of catalysts, the network can be nanocross with two NWs, has-tag with four NWs, and higher order of networks from multiple trenches or multiple Au from deeper trenches. In our experiment, we only concentrate on studying nanocross, that also provides an understanding of the high order network. In the case of InSb nanocrosses from two opposite trenches, the length of the stem and InSb segment are chosen in a way that the merging happens almost in the middle of the InSb segment. Figure 4.1**a** shows an example of the arrangement of two trenches with precisely positioned Au catalysts.

Different schemes of opposite grown NWs are presented in Figure 4.1**b**, where possibility of the network formation is dependent on the Au position (Δz), the final diameter of NWs (d_{NW}). We already have elaborated in Chapter 3 about shadowing NWs by varying Au positions (where the fundamental condition is $d_{NW} < \Delta z$) and how the distance of shadowing determines the broadening of the junction and eventually junction performance. Now, if $\Delta z \neq 0$, but $d_{NW} \geqslant \Delta z$, the NWs merge from the sidewall and create a nanocross structure, as highlighted in Figure 4.1**c** with an elaborated schematic presented in Figure 4.1**d**. Please note that here, d_{NW} is the final diameter of the NW, not the diameter when NWs pass through each other initially (this will be elaborate in later section). Now, in the case of Au catalysts are positioned without offset ($\Delta z \approx 0$), as shown in Figure 4.1**c**, the NWs meet "head-to-head" and create different structures such as "nanoplate" or "nanobridge" instead of nanocrosses.

First, the growth condition of individual InSb NW on the trench is investigated. InSb growth morphology as a function of In growth rate and Sb flux conditioning is presented in Figure 4.2. A fine-tuned condition will provide the uniform morphology with a high aspect ratio, that is important to realize the control synthesis of nanocrosses and also other types of networks. Figure 4.2**a** shows four panels with different V/III ratio and their corresponding micrographs. Starting with V/III ratio 4.49 (panel (i)), where In growth rate and Sb flux are set to the highest in this experiment. High In growth rate ensures a bigger Au catalyst with rich-In concentration after switching from InAs stem to InSb segment. As a result, the diameter of the InSb increases with a bigger Au droplet. In addition to that, higher Sb flux means a high effective Sb deposition rate on the NWs facets. Since facets are nucleation limited, hence, high Sb flux may not contribute initially to the diameter. However, once the diffusion length limit is reached, high Sb flux will directly contribute to the fast radial overgrowth. Thus, both high In growth rate and more Sb effective flux will enhance the total diameter of InSb NWs.

Keeping the In growth rate same, if we decrease the Sb flux rate in panel (ii) (meaning the less effective Sb adatom to the sidewall), a drop in diameter is observed for V/III ratio 3.25. Here, the Sb flux is decreased to

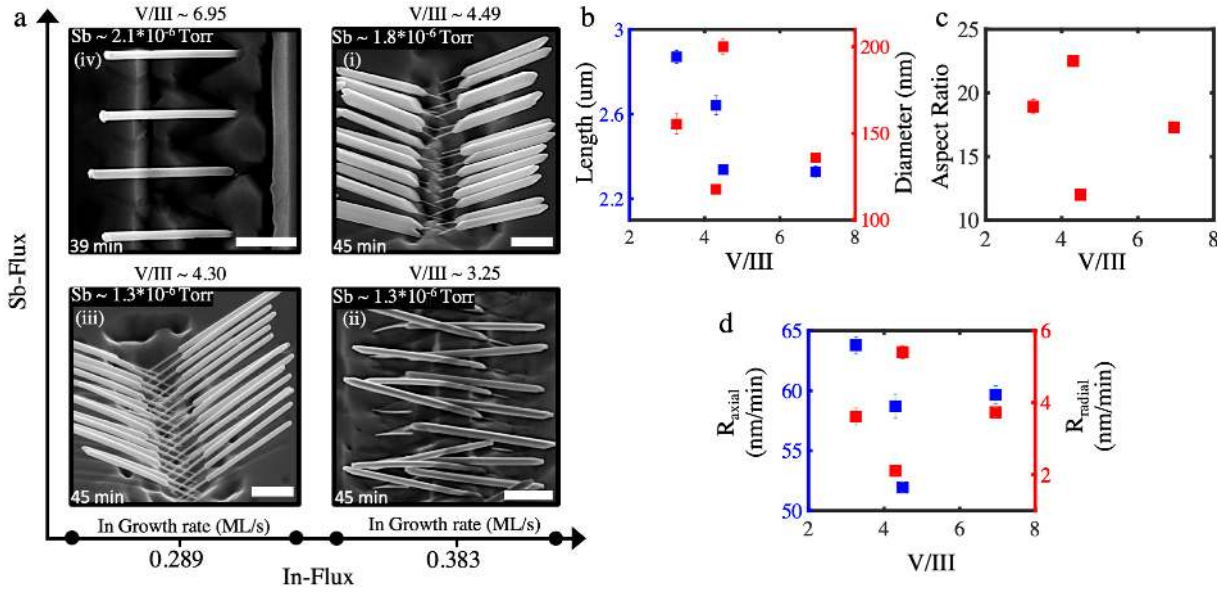

Figure 4.2: Morphology evaluation of InSb nanowires on the trench. a, InSb NW growth analysis as a function of In and Sb flux ratio. Tilted SEM images for four different conditions and corresponding growth times are presented. The growth temperature is maintained constant for all different conditions. With the highest In growth rate and Sb pressure (1.8×10^{-6} Torr, V/III ratio 4.49), the diameters of the InSb NWs are significantly larger compared to the other three conditions. On the other hand, lowering the In growth rate 0.289 ML/s with Sb pressure 1.3×10^{-6} Torr (panel (iii)) provides a high aspect ratio meaning longer length with smaller diameter compared to the other three conditions in the same growth time. The scale bars for all the images are 1 μm. **b**, Length, and diameter as a function of the V-III ratio on the same samples presented in panel (**a**). **c**, Aspect ratio as a function of V-III ratio, where V/III ratio 4.49 demonstrates the lowest aspect ratio and V/III ratio 4.30 shows the highest aspect ratio. **d**, Axial and radial growth rate as a function of V/III ratio. It is further evidence that high In and Sb flux causes larger radial growth to compare to the axial growth. Reduced Sb flux and In growth rate helps to lessen the radial growth and results in a higher aspect ratio.

1.3×10^{-6} Torr. Now maintaining Sb flux (to 1.3×10^{-6} Torr), if we lower the In growth rate to 0.289, which provides V/III ratio 4.30, in panel (iii), then, further reduced diameter is observed for same growth time. Finally, if we fix the In growth rate to 0.289 ML/s and increase Sb flux to 2.1×10^{-6} Torr from 1.3×10^{-6} Torr, that leads to the high V/III ratio 6.95 (panel (iv)). The diameter of the NWs are increased again. However, the diameters in panel (iv) are still less than the diameters in panel (i), as In growth rate is lower. That means, a higher In concentration has larger effect on NW diameters, in panel (i). Nevertheless, if we keep increasing Sb flux in panel (iv) at some point diameter will increase significantly, as it will be mostly determined by the radial growth (with high Sb flux).

Figure 4.2**b-d** show an extended data on the growth conditions and related InSb morphology. Figure 4.2**b** demonstrates statistical value of the length and diameter as a function of In and Sb flux ratio presented in Figure 4.2**a**. With low Sb flux sample (ii) and (iii) have a higher InSb length compare to the sample (i) and (iv). The highest length is observed on the sample (ii) (V/III ratio 3.25), where In growth rate is 0.383 ML/s (high). Decreasing In growth rate to 0.289 ML/s in the sample (iii), (keeping Sb flux same as sample (ii)) also decreases the InSb length. Hence, high In concentration has a positive effect on length if Sb flux is low. However, as discussed before, high In growth rate also increase the diameter. If we look into the diameter scale, samples with a high In growth rate (i) and (ii) have diameters in the higher end, which is expected. Sample (iii) and (iv) with In growth rate of 0.289 ML/s has diameters in the lower side further evidence of In flux effect on the diameter. Sample (iii) has the lowest diameter among the four, as both In and Sb flux are low. Accumulating

length and diameter in Figure 4.2**c**, we can conclude that sample (iii) has the highest aspect ratio and sample (i) has the lowest aspect ratio, as also evident in the SEM image of Figure 4.2**a**. Finally, we also analyzed the axial and radial growth rates for those four samples, as shown in Figure 4.2**d**. The highest axial rate is achieved for sample (ii) and the highest radial growth is achieved for sample (i), which are consistent with Figure 4.2**b**. On the other hand, the sample (iii) has the lowest radial growth and marginally high axial rate. Considering all the scenarios, we choose the growth conditions of the sample (iii) (V/III ratio 4.30 with In growth rate 0.289 ML/s) for our InSb nanocross experiments.

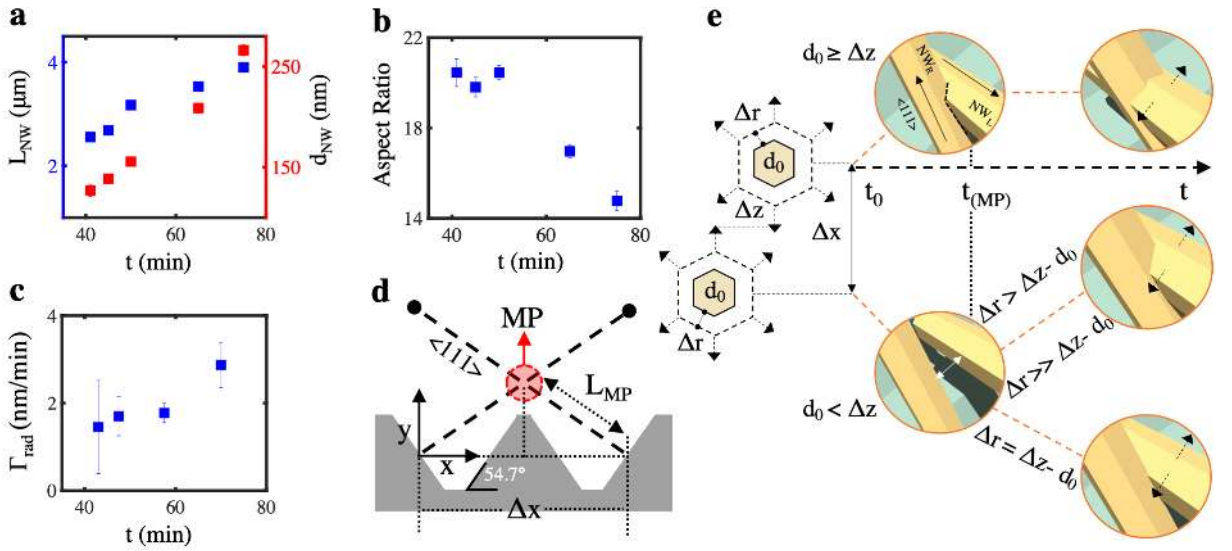

Figure 4.3: Understanding InSb nanocross formation. a, Length and diameter as a function of growth time. Here, the In growth rate is fixed to 0.289 ML/s. **b**, Aspect ratio as a function of growth time while maintaining other growth conditions fixed. **c**, Radial growth rate as a function of growth time. **d**, Schematic of the nanocross geometry, where Δx is the trench-to-trench distance between the Au catalysts, MP is the point where NWs merge or cross each other and L_{MP} is the length of the NW before merging. **e**, Schematic of the evolution of NWs to merge and form nanocrosses. Here, d_0 is the initial diameter of the InSb NW without radial growth, Δr is the thickness of the radial growth, Δz is the offset between two Au catalyst. In the growth time scale, t_0 is the time when growth starts, $t_{(MP)}$ is the time when merging happens or NWs pass through each other and t is the final growth time. Here, three different merging possibilities are shown depending on the growth condition, which will be discussed in detail in the text.

Figure 4.3**a**- **c** show further analysis with growth conditions presented in Figure 4.2**a**-(iii). We measured the average InSb length and diameter from the trenches with Δx = 4.5 μm and pitch size of 970 nm between Au catalysts at different growth times, as shown in Figure 4.3**a**. Not only does the NW length but also the diameter increases with growth time. As the growth evolves, the diameter of the NWs increases significantly compared to the length, which is also evident from the decaying trend of aspect ratio data over a long growth period, as shown in Figure 4.3**b**. As briefly discussed above, InSb NW growth is determined by axial growth and radial growth. It is initiated by axial growth via the liquid-solid transition, with an initial diameter d_0. The initial diameter of the InSb segment is determined by the volume of the Au, the contact angle, and the supersaturation of the Au with In and Sb. [4] This Au catalyst assisted growth helps InSb to keep growing axially until a certain period. In the later stage, due to the diffusion length limit, the supersaturation in the Au catalyst gets limited, and eventually, the axial growth of the NWs slows down. As a result, the length of the NWs doesn't increase linearly,

4: See chapter 2 for a detailed explanation of the switching from InAs to InSb, Au shape-changing before starting InSb growth and diameter determination.

as shown in Figure 4.3**a**.

On the other hand, initially, the incorporation rate of the adatom on the sidewall is close to zero due to the nucleation barrier. After a certain growth time, the radial growth begins, presumably by overcoming a critical adatom density that initiates growth on the side facets. In other words, all the adatoms can not reach the Au catalyst when the NW length becomes comparable to the incorporation limited diffusion length λ. Hence, the radial growth rate (Γ_{rad}) of the InSb segment is expected to increase once the NW length is much longer than λ. The measured diameter is shown in the Figure 4.3**a**, together with the radial growth rate in Figure 4.3**c**, where the diameter in long growth run is mostly dominated by increased radial growth. In general, radial growth of the NWs can be divided into three stages: no radial growth ($L << \lambda$), transition stage ($L \approx \lambda$), and constant radial growth ($L >> \lambda$). From the radial growth rate data in this study (from 43 to 70 minutes), we conclude the main part of the InSb growth resides in the transition stage (see Figure 4.3**c**). Experimentally we do not have the data where the radial growth rate completely saturates. In fact, such data will require a long growth time in the given conditions we are analyzing. Also, such a long growth run is not the core focus of the experiment here. We are particularly interested in controlling the radial growth rate, in order to design the Δx and Δz through appropriate substrate fabrication and thereby improve the dimensions and yield of the InSb nanocrosses.

A model for determining the NWs merging position (MP) for nanocrosses is shown in Figure 4.3**d**. Here, L_{MP} is the length of the NWs before merging. MP and L_{MP} directly depends on the Au catalysts distances from trench to trench, Δx. L_{MP} can be expressed as, $L_{MP} = \Delta x/2 \cos\theta$, where, $\theta = 35.3°$ and the coordinate of the merging point is MP = $(\Delta x/2, \Delta x \cos 54.7°/2)$. Based on the Δx and the axial growth rate of given growth condition, we can control the L_{MP} and merge the NWs in our intended position (in our case, $L_{MP} \approx 2.8\ \mu$m). In Figure 4.3**e**, we discuss about the conditions of Δz to control the formation of nanocrosses, by imaging the different scenarios as a function of growth time. For control synthesis, Δz can be directly related to the radial growth rate.

The nanocross growth formation from initial growth time (t_0) to final growth time (t) is shown in Figure 4.3**e**. Post-growth analysis reveals how the NCs can be fully formed, partially intersected, or slightly touched at the side-facets (also can be seen in Figure 4.1**c**). The appearance of any of these situations are dependent on initial diameter, d_0 and thickness of radial growth, Δr. To form a NC the axial growth front needs to pass the opposing NW at the MP. We consider two scenarios, when NWs pass each other with diameter d_0, either it is the $d_0 \geq \Delta z$ or $d_0 < \Delta z$. As illustrated, total diameter of the InSb NW is a combination of initial diameter during axial growth and thickness of the radial growth, $d_{NW} = d_0 + 2\int \Gamma_{rad} t dt$. Since, the NWs are grown from Au catalysts (in the same lithography step) with similar diameter and volume, we can assume that the initial diameter during axial growth is identical for both sides of the NWs in the trench. Now, assuming that if $L_{MP} < \lambda$ radial growth is negligible until the NWs reach the MP. In this case, for $d_0 \geq \Delta z$, the opposing NWs side-facets may slightly connect at t_{MP} with d_0, and then radial overgrowth of both NWs assist them to merge properly in the subsequent growth time. On the other hand, if $d_0 < \Delta z$, then NWs pass each other

in close proximity but do not merge as shown in Figure 4.3**e**. In such case, the subsequent radial growth leading to thicker nanowires with diameter d_t determines whether the NWs connect to form NCs. Such as, if $\Delta r > \Delta z - d_0$, then NWs can overcome the interwire distance and connect each other to create NCs (considering the radial growth rate of both NWs are almost equal). However, if the radial growth for both NWs are not equal (which means, one NW remains thinner than the other one), then, Δr for thicker NW require to be significantly large, $\Delta r >> \Delta z - d_0$ in order to form a NCs. Furthermore, if $\Delta r = \Delta z - d_0$, the NWs get enough radial thickness just to marginally touch each other through the side-facets instead of intersecting.

Structural Analysis of InSb Nanocrosses

Figure 4.4**a** shows an SEM image where all the NWs are merged as nanocrosses due to the enhanced materials consumption from the sidewall, as elaborated in Figure 4.3**e**. Here, the lithography defined Δx and Δz are respectively 4.5 μm and $\approx$ 188 $\pm$ 0.06 nm. Based on this, we grow the InSb segment for 75 min, which provides 3.90 $\pm$ 0.06 μm long InSb segment with a diameter of 266 $\pm$ 5.64 nm. As a result, all the opposite directional NWs radially overcome the Δz spacing and connect through the sidewall demonstrating high yield synthesis of InSb nanocrosses. Apart from the InSb segment, the length of InAs plays a role to engineer the meeting point of the NWs. Here, we grow $\approx$1.5 μm of InAs segment before InSb to position the nanocross merging roughly in the middle.

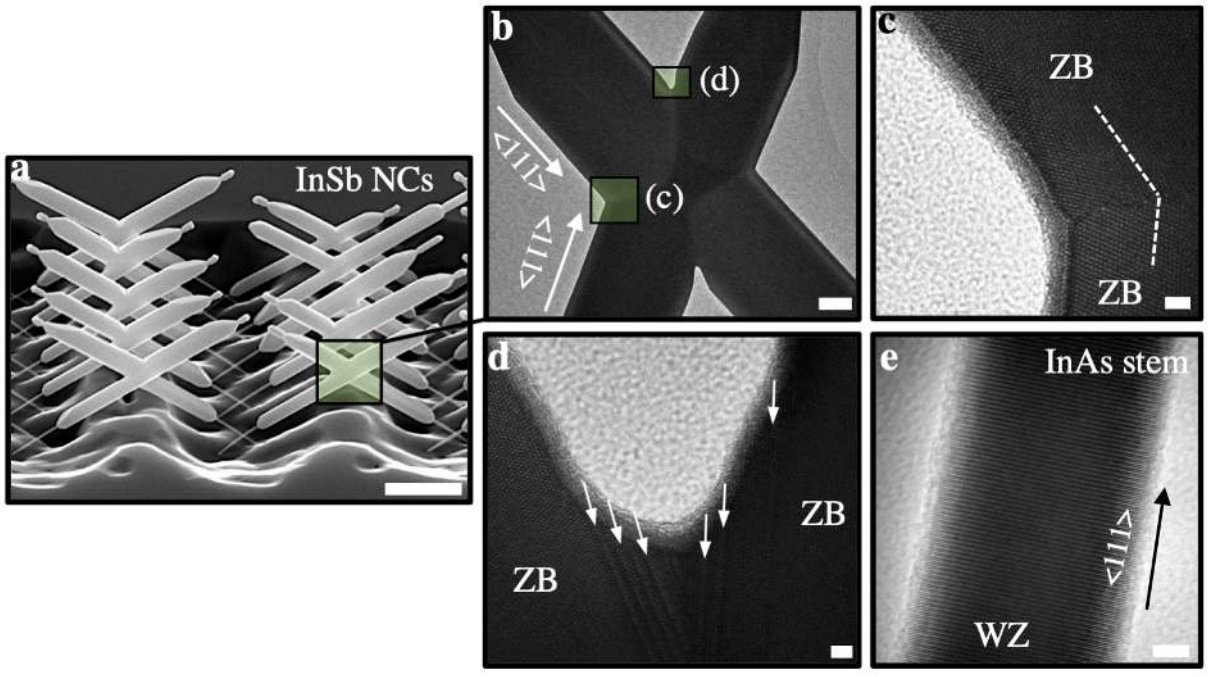

Figure 4.4: TEM analysis of the InSb nanocrosses. a, Tilted SEM image of InSb nanocrosses, where all the NWs are crossed with assistance of the radial growth in longer growth time as the schematic is shown in Figure 4.3**e**. Scale bar is 1 μm. **b**, Representative TEM of a nanocross. Scale bar is 100 nm. **c**, High resolution TEM from highlighted section of (**b**) confirming ZB crystal structure before and after merging. **d**, Highlighted TEM of the curved section from (**b**). Couple of stacking faults are observed only at the edge (indicated by white arrow) of merged section. On the other hand, pure ZB structures maintains to the center of the merged section and in all arms. **e**, Representative TEM image of the pure WZ InAs stem. Scale bars for (**c**) and (**d**) are 2 nm, and (**e**) is 5 nm.

TEM analysis of the nanocrosses are presented in Figure 4.4(**b-e**). Figure 4.4**b** shows an overall structure of the nanocross under TEM inspection, which confirms all four arms and the merged segment in the middle maintain the same crystal structure and no significant stacking-fault or other crystal defect is observed along with the structure. A high contrast section in the middle is observed in the TEM due to the higher thickness. Single crystalline quality throughout the crossed structure is an essential element to achieve a ballistic multiterminal device. Figure 4.4**c** shows high-resolution TEM (HR-TEM) image of the transition between two arms magnified from Figure 4.4**b**. We can see that the defect-free Zinc blend (ZB) crystal phase maintains despite merging from opposite directions and also seems to be independent of the InSb NW aspect ratio [127]. Here, a twin-plane is observed in the merging place of two NWs. This can be attributed to the merging of two ZB NWs with different stacking sequences. Figure 4.4**d** exhibits HR-TEM from the highlighted curved section from Figure 4.4**b**. It appears that multiple stacking faults (indicated with arrows) occurred at the boundary after crossing the area, which we also presume to be due to the slight misalignment during merging. However, such defects do not seem to have appeared along the arms and core middle section. Figure 4.4**e** shows the HR-TEM image of WZ InAs stem without any disorders. InAs stems get thinner with longer InSb growth time due to the As decomposition. Further, misfit dislocation can be observed within a few layers from InAs transition to InSb, which is due to the structural relaxation mechanism while shifting from WZ InAs to ZB InSb. Such interface analysis and relaxation mechanisms are elaborated in chapter 2. [5]

5: See chapter 2 for detail analysis on InAs-InSb interface

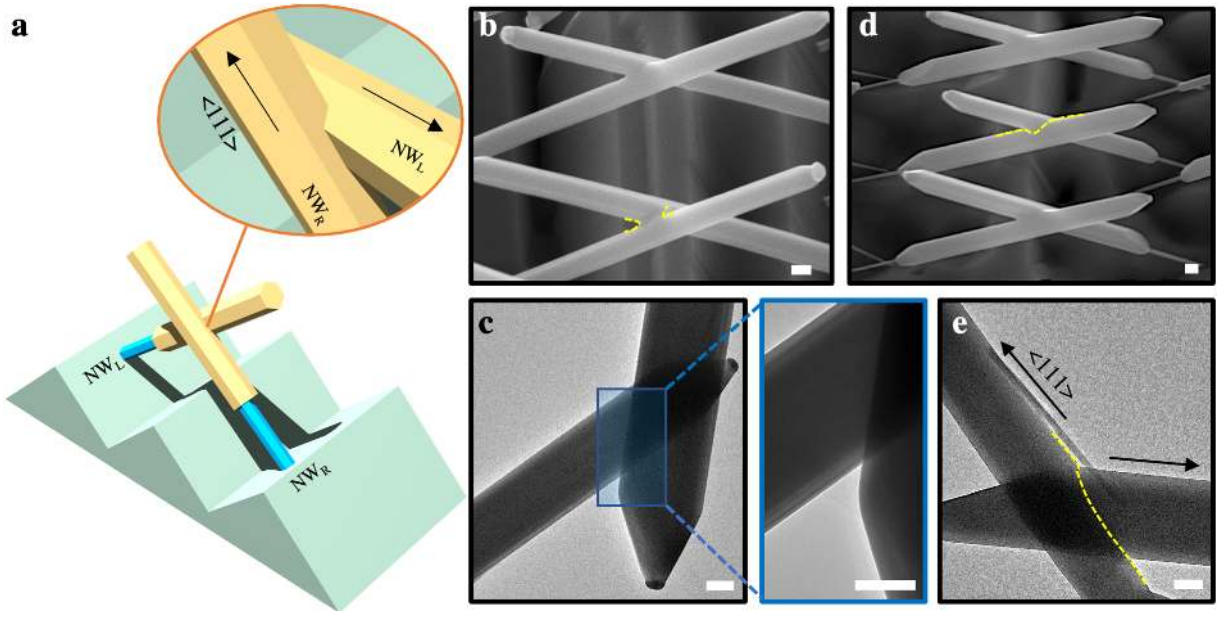

Figure 4.5: Structural analysis of marginally overlapped and partially intersected InSb nanocrosses. a, Schematic of the opposite directional InSb NWs partially intersected through the sidewall due to radial growth. **b**, Tilted SEM image of InSb nanocrosses, where NWs are moderately meet (or overlap) each other through the facets when final InSb diameter is reached. **c**, TEM analysis of the similar nanocross, as shown in panel (**b**), where NWs are slightly touched but not intersected through each other. The magnified TEM image in the right confirms the overlapping, as no intersection is observed. **d**, Tilted SEM image of the nanocrosses, where NWs are marginally intersected from the sidewall after final growth time. **e**, TEM image of the similar nanocross. It is clearly observed that NWs are intersected to each other, unlike the previous one. Scale bars are 100 nm.

Structural analysis of the overlapped and partially merged nanocrosses are presented in Figure 4.5. If the lithography position of Au catalysts and diameter of the NWs are chosen in a way that $d_{NW} \approx \Delta z$ (final diameter of NWs), then NWs create networks by overlapping through the sidewall in the merging point as shown in the SEM image of Figure 4.5**b**. However, the NWs do not completely intersect with each other. Here the NWs are crossing from the very close proximity with the initial axial diameter and then radial overgrowth of both NWs helps them to get connected. Since the wires just touch from the boundary of the diameter, presumably no crystal defect is induced in any of the wires. The period of the overlapping can be anytime from between NWs passing each other to NWs reaching their maximum length. Figure 4.5**c** shows a TEM image of two overlapped NWs and the magnified TEM section confirms no intersecting through the sidewall. In Figure 4.5**d** shows NWs that marginally intersect from the side facets at final growth time. Here, the yellow dotted line shows the merged zone inside the NW. Outside the equal radial overgrowth of both NWs, if the diameter of one of the NW gets significantly thicker due to the local condition that may also lead to a partial intersection as discussed in Figure 4.3**e**. A TEM image of such structure is shown in Figure 4.5**e**, where a clear intersection area is shown by a dotted yellow line. Such an intersection also does not change the crystal structure after converging and maintains the ZB crystal phase as we can see in the TEM image. However, some crystal defects (twining) may appear in the section where NWs intersect.

4.4 InSb Nanoplate and Other Nanostructures

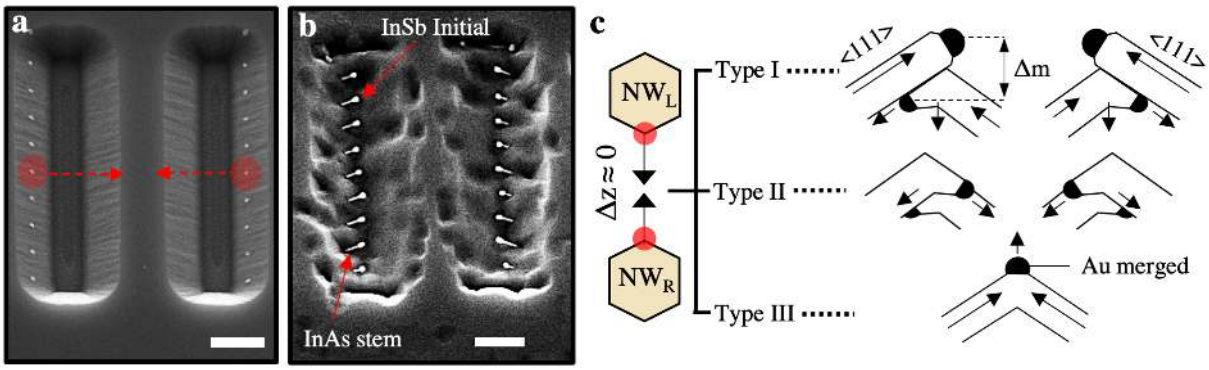

Figure 4.6: Head-to-head Au catalyst position. a, Tilted SEM image of the trenches, where the Au catalysts are lithographically positioned without any offset. **b**, Initial InSb section grown with InAs stem. **c**, Schematic of the three possible types of nanostructure formation when InSb NWs are grown head-to-head towards each other. Here, Δm is the distance of the merging point from the Au catalyst. Scale bars for (**a**) and (**b**) are 1 μm.

As we mentioned at the beginning of this chapter, the types of InSb NW networks depend on the corresponding Au position and NWs meeting point. Hence, playing with the Au catalyst position and knowing the optimized growth conditions provide freedom to control the synthesis of other types of InSb nanostructures (in addition to nanocrosses). We use the same optimized growth condition discussed in Figure 4.2. Now, if the Au droplets are placed head-to-head, different types of nanostructure

formation are observed in the post-growth analysis. Figure 4.6**a** presents an example of a prepared substrate where all the Au catalysts in the opposite trenches are positioned face-to-face. Figure 4.6**b** shows InAs assisted the initial InSb segments, where all the opposite NWs are growing towards each other. Next, in Figure 4.6**c** shows three different categories of InSb nanostructures we observed for design $\Delta z \approx 0$. In "Type-I", NWs colloid on each other's sidewall with an offset in the axial direction, Δm. In this case, one NW continues growing in the <111> direction, whereas the other one slides through the opposite wire facet after the collision and continues growing. In the "Type-II" situation, Δm is smaller compared to "Type-I", and NWs meet approximately at the top of each other. After merging, Au catalysts slide through each other side-facets and create a bridge-like structure. Finally, in "Type-III", $\Delta m \approx 0$, which means that with the same growth rate both of the NWs meet at their Au catalysts. As a result, Au catalysts merge into a single droplet and in the long growth run continue growing in a kinetically driven direction. We counted 321 networks to understand the statistical distribution of different types and the result is presented in Figure 4.7. As we can see in the histogram, "Type-I" is the largest number of nanostructures we observed in our experiment. On the other hand, "Type-III" is the smallest portion observed. In addition to these three types, some random directional networks are also observed which are challenging to classify under a category (mentioned as "Others"). Further details of each type are discussed in the following sections.

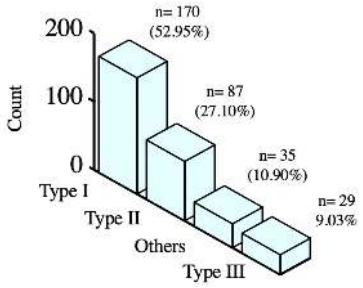

Figure 4.7: Formation of different types of network. Histogram presents percentage of different types of InSb structures created from Au catalyst positioned without offset. Total 321 data are counted.

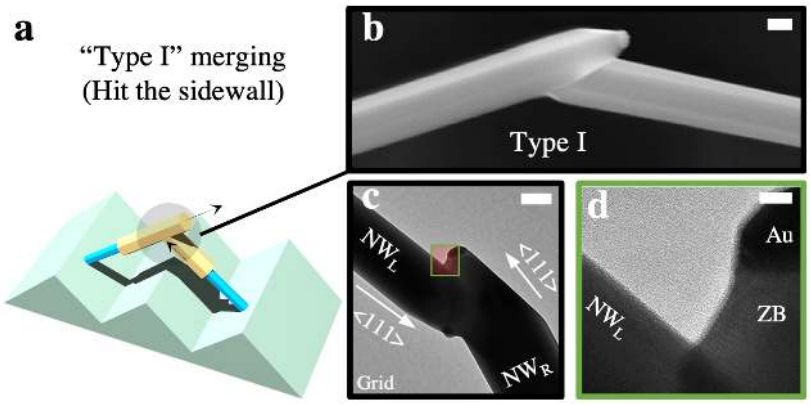

Figure 4.8: "Type-I" merging. a, Schematic of the "Type-I" InSb network. Here, one NW hit on the side-wall of another NW with an offset. **b**, Tilted SEM image of the "Type-I" merging. **c**, TEM analysis of the similar phenomena, where Au catalysts are well separated from each other after merging. **d**, Magnified highlighted section from panel **c**. Scale bars for (**b**), (**c**), (**d**) are 100, 50 and 5 nm respectively.

"Type-I" merging: Nanoplate with Elongated Arm

In the first scenario, we are going to discuss when one NW in the pair hits on the sidewall of another NW, whereas the other one keeps growing in <111> direction. A schematic of such side-wall hitting ("Type-I" merging) is shown in Figure 4.8**a** and an example SEM image is shown in Figure 4.8**b**. Pair of both NWs are grown from the Au catalysts that are deposited in the same growth process and intended to have the identical volume. However, the volume can still differ from each other depending on the e-beam Au deposition and lift-off efficiency. As a result, the growth rate of the opposite NWs may differ in some cases. It is reported that, NWs with bigger Au droplet leads to the slower growth rate compared

to the smaller Au droplet [270, 271]. In addition to that, local growth conditions such as flux distribution, adatom diffusion, and materials sharing between the wires may also deviate the supersaturation condition of the Au catalyst, eventually lead to the variation of the NW growth rate. So, the faster-grown NW passes the meeting point (MP) earlier than its counterpart, which leads the other NW to hit into the sidewall, when it reaches the meeting point. The distance Δm is directly dependent on the axial growth rate of the InSb NW. Further, this Δm is a crucial parameter to determine the nanostructure. TEM analysis of the similar structure is presented in Figure 4.8**c**, where NW_L meets NW_R's sidewall with an axial offset from Au (NW_R) catalyst. As we can see from the TEM, the direction of NW_R's Au catalyst is independent of the "Type-I" merging. The change we observed in NW_R after merging is highlighted in Figure 4.8**d**, where the shape of the neck beneath the Au catalyst is enhanced. Additional materials consumption may happen in the neck due to the adatom collection from NW_L's facets and also from the solidified materials layers precipitated from supersaturated NW_R Au catalyst. Figure 4.8**c** also shows the initial phase of NW_L Au catalyst's transformation from <111> to a new direction (opposite) connected to the sidewall of NW_R. Au catalyst of NW_L initially hits on the sidewall with <111> direction. Since the direction creates an obtuse angle to the sidewall of NW_R, the Au catalyst gets unstable after merging and continuous nucleation process pushed down the Au catalyst into the (111)A facet as a new growth direction of NW_L.

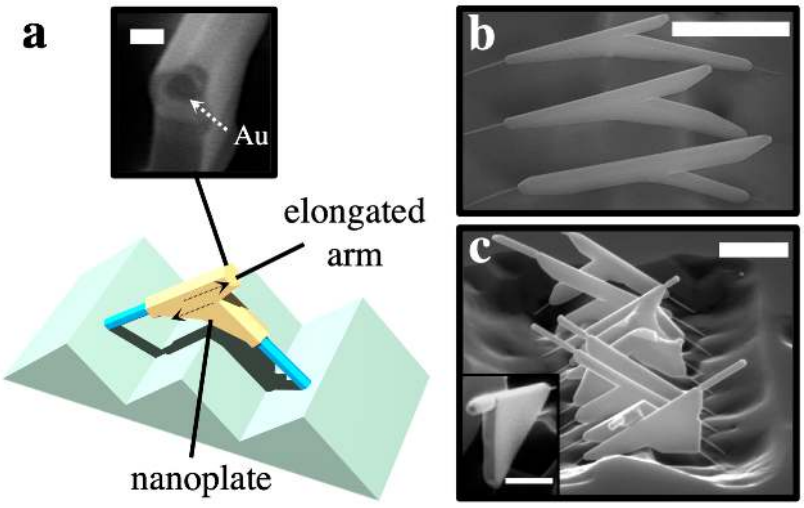

Figure 4.9: InSb nanoplate with elongated arm. a, Schematic of the InSb nanoplate with a long arm. Inset SEM image demonstrates the top view of the elongated arm. **b**, Tilted SEM image, where all the arms are in the same direction. **c**, Tilted SEM image, where arms are shown two different directions demonstrating domination of kinetics of the Au catalyst to determine the direction of the arm. Inset is the top view demonstrating the triangular nanoplate section. Scale bar for (**a**) is 100 nm. Scale bars for (**b**) and (**c**) are 1 μm.

For a long growth run, one NW keeps growing in <111> direction, and the other one crawl down to the sidewall and grow an additional structure attached with the NW, as depicted with arrows in Figure 4.9**a**. For a clear understanding of the Au droplet position in <111> direction, the long arm is shown in the inset of Figure 4.9**a**. In post-growth analysis, we observe both NWs lead to a final structure, which is analogous to two dimensional (2D) nanoplate with elongated arm as illustrated in the schematic Figure 4.9**a** and in the SEM images Figure 4.9**b** and Figure 4.9**c**. Apparently, there are two growth processes running in parallel; one, nanoplate formation, and the other one is standard NW growth. Nanoplate formation is driven by the Au droplet with changed direction

and the associated structure with it, whereas the long arm is grown by the droplet that unconditional to the merging.

As we have addressed previously, InSb NW growth is driven by both axial and radial growth, and after a certain period, the radial growth rate increases significantly compared to the axial growth rate. Here, similar to the nanocross formation, the axial growth defines the skeleton of the nanostructure by assisting NW pair to connect with each other. After that, the radial growth rate plays a significant role especially to form a nanoplate. Based on that, we can divide InSb nanoplate formation into three stages. In the initial stage, after changing the direction (with (111)A facet), Au droplet keeps growing as a secondary NW connected to the side facet of NW_L (in the schematic of Figure 4.9**a**). In this phase, the growth is mainly driven by the catalyst and side facet, which is still nucleation limited. The length of this secondary NW on the sidewall defines the actual frame of the nanoplate. As we can see in Figure 4.9**c**, different size of the nameplates depending on the position of the merging and the length that secondary NW traveled. In the next stage, during the growth time domain, when radial growth dominates the InSb structure with increased adatom density, both primary and secondary directions of NW_R [6] (respectively <111> and crawling down to the (111)A facet of NW_L) grow thicker. It is presumed that the secondary arm of NW_R collects more materials compared to the primary arm as it is adjoined with the NW_L, which means the radial growth is also significantly large. An increase in the growth rate of such crawling NW was also reported in earlier research [222]. In the final stage, the overgrowth from both arms help to connect with each other and create a nanoplate structure. A top view example of 2D nanoplate is shown in inset of Figure 4.9**c**.

6: NW_L and NW_R are considered from the schematic of Figure 4.9**a**.

On the other hand, Au catalyst growth of NW_L is independent of the merging, hence, NW_L grows as an elongated arm. Which NW in a pair will continue as an elongated arm completely depends on their corresponding growth rate. In some cases, this growth rate seems to be organised, as shown in Figure 4.9**b** and in other cases it is more random, as shown in Figure 4.9**c**. It is reported that, such a 2D structure of InSb demonstrates defect-free crystal quality owing to the intrinsic ZB crystal nature of InSb nanowires [272–275]. We can predict that high crystal quality InSb nanoplate will be an interesting materials platform for different quantum transport experiments.

"Type-II" merging: Nanoplate without Arm

Now we are going to discuss the second set of nanostructures shown in Figure 4.10**a** that appears due to the "Type-II" merging. According to the statistics shown in Figure 4.7, "Type-II" merging is the second-highest number of structures we counted. "Type-II" merging occurs when growth rates of the paired NWs do not vary significantly, which means instead of connecting from the sidewall, NWs connect proximity to the top of their length. However, Au droplets of NW_L and NW_R do not coalesce. Different scenarios may appear depending on where the Au droplets connect and the kinetic direction after that, which also defines the final

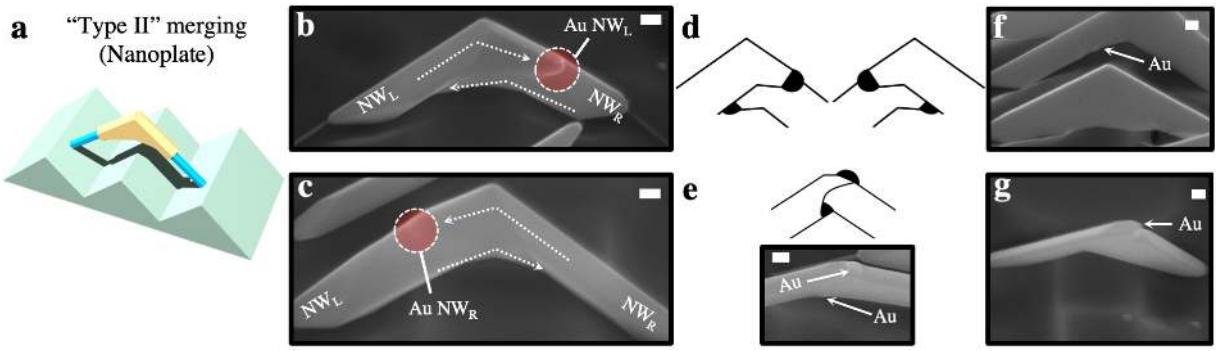

Figure 4.10: InSb network with "Type-II" merging. a, Schematic of the InSb network created after "Type-II" merging. **b**, Tilted SEM image of InSb network where Au catalysts of NW_L and NW_R slide through each other facets after the meeting. The highlighted red circle shows the Au catalyst's position after the final growth time. **c**, SEM image shows the similar phenomena as (**b**), but in the opposite directions. **d**, Schematic of the Au position to create network shown in panel (**b**) and (**c**). **e**, Schematic and inset SEM shows the condition, where Au catalysts sit on the top and bottom facets of the NWs instead of side facets. **f**, Tilted SEM image of the nanoplate where upper NW slides on $(10\bar{1})$ and $(0\bar{1}\bar{1})$ facets and at the same time bottom NW crawl through (011) and $(\bar{1}01)$ facets in opposite <111> directions. **g**, Tilted SEM image of the nanoplate structure, where Au catalyst of NW_L stays in the top facet, whereas the NW_R catalyst crawl through the sidewall similar to other conditions.

growth structure. After connecting in proximity, both Au catalysts may change their growth direction to [-1-1-1] and slide to each other side facets. SEM images and schematic of such event is displayed in Figure 4.10**b-d**. In Figure 4.10**b**, we can see the NW growth in <111> direction terminates after the collision and growth continues in new catalyst's direction. Au catalyst of the NW_L is highlighted with a red circle, that is sliding on the NW_R side facet and the arrow shows the trail of the NW_L growth. NW_R growth follows on the other side of the NW_L, as indicated with the second arrow. It's clear from the SEM images and from the sketch in Figure 4.10**d**, unlike "Type-I" merging condition, here the Au catalysts do not crawl through (011) or $(\bar{1}01)$ facets, instead catalysts slide in one of the four facets: (110), $(10\bar{1})$, $(\bar{1}\bar{1}0)$ or $(0\bar{1}\bar{1})$. In Figure 4.10**c**, we see the similar phenomena where NW_R Au catalyst is visible from the viewing angle. In both cases, enhanced facet growth of both NWs conjointly creates a nanoplate structure without any elongated arm.

The next case we observed, when Au catalyst of NW_R (or NW_L) connects just beneath the Au catalyst of NW_L (or NW_R). A schematic of such a scenario is shown in Figure 4.10**e** and experimental observation of such event is presented in the SEM below. This incident is very similar to the one depicted in "Type-I" merging (see Figure 4.8), hence it is expected that one catalyst will continue in [111] direction and another one will change in [-1-1-1] direction. However, the difference appears in Figure 4.10**e** is that the position of Au, and its interface with the facet after merging. In Figure 4.8, the upper Au catalyst and its corresponding solid interface still directed to the [111]. On the other hand, in Figure 4.10**e**, after connection, the upper Au catalyst get relaxed in the interface of $(10\bar{1})$ and $(0\bar{1}\bar{1})$ facets and no (111)B interface is remained to grow. As a result, with continuous nucleation upper catalyst may continue growing in [-1-1-1] direction on $(10\bar{1})$ and $(0\bar{1}\bar{1})$ facets interface. Similar to "Type-I", the bottom catalyst slides and continue growing on (011) and $(\bar{1}01)$ facets. In the end, with radial overgrowth of each NWs, a nanoplate like structure is formed, which is shown in Figure 4.10**f**. In other cases, we also have seen, after merging and upon reaching to new facet-interface, the upper Au catalyst does not assist on the NW growth any longer as shown in Figure 4.10**g**. It's presumably due to the reason that the contact angle of the Au catalyst

with the new interface is not favorable to the axial growth anymore, however, the radial growth through adatom collection continues.

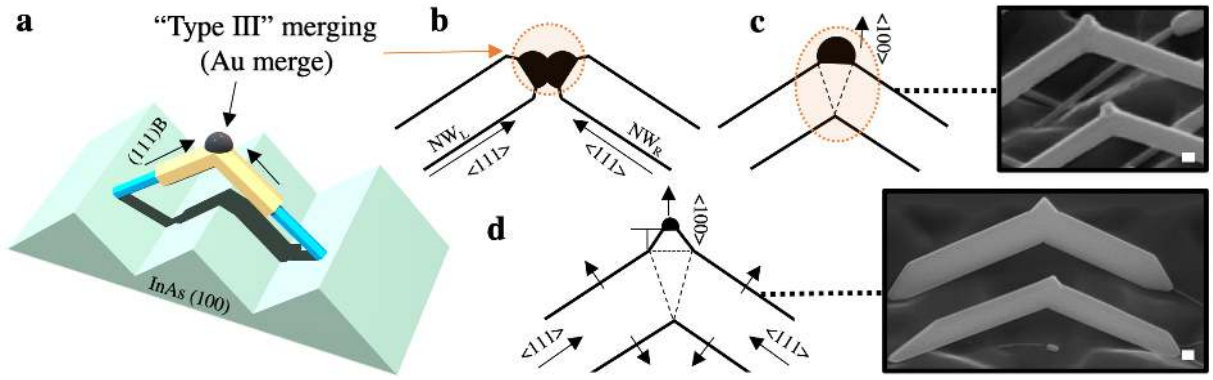

Figure 4.11: "Type-III" merging with InSb network. a, Schematic of the "Type-III" merging. Here, Δz and Δm are zero, as a result, Au droplets of both NWs merge. **b**, Initial stage of the merging, where two Au droplets meet. **c**, Second stage of the merging, where Au droplets are combined into one. On the right, SEM image of such structure. **d**, In the last stage, Au droplet assists growing in < 100 > direction for longer growth time. SEM image on the right shows similar results in long growth time. Scale bars for (**c**) and (**d**) are 100 nm.

"Type-III" merging: Nanobridge

Finally, the last kind of merging ("Type-III") that we observe is presented in Figure 4.11, where Δz and Δm are zero, which lead to a condition of 'tip-to-tip' merging. In our counting, "Type-III" merging is the lowest number that appeared during the growth. Furthermore, "Type-III" merging is mostly observed when the wires are merged "head-to-head" from long distance trenches ($\Delta x \approx 6\mu m$). The schematic of "Type-III" merging is shown in Figure 4.11**a**. The nanostructure formation, when $\Delta m = 0$, can be divided into three phases. In the initial phase, the NWs with identical growth rates meet almost at the middle of the trenches, as shown in Figure 4.11**a**. At this point, the Au droplets of both NWs come in contact with each other, and the droplets coalescence process starts. The coalescence process of two Au droplets and the relaxation mechanisms depend on the contact angle of the liquids with solids, droplet size and the contact line between the droplets [276]. However, the coalescence process to reach the final single droplet stage is much more complicated in our case. This is because, the Au droplets are continuously collecting materials, and the solids beneath the droplets are also evolving. An atomic-scale analysis of the Au droplets coalescence process of NWs can be an interesting research project, and will probably require *in situ* TEM examination. However, it was not the focus and capability of this research.

In the next phase, after relaxation of the coalescence process, the combined Au droplet reaches its final volume. Both <111> directional NWs are entirely merged and created a nanobridge structure. Also, the (111) interfaces of this new Au droplet diminish completely. As the <111> directional growth completely terminates, Au droplet is now positioned on the (100) facet, as shown in the sketch in Figure 4.11**b** and the SEM image on the right. After the termination of the <111> growth, a triangular shape interface is observed beneath the <100> directional Au catalyst (see schematic in Figure 4.11**c**). Similar triangular interfaces are also observed

in Si and InAs NWs [222, 277]. In the final phase, a triangular overgrowth in the <100> direction is observed, as shown with an arrow in Figure 4.11**d**. However, <100> directional growth in the VLS NW is not very common. Furthermore, it has been reported that [222, 259, 261], after coalesce, the Au catalyst gets bigger. But after the long growth time, Au catalyst size gets smaller as illustrated in Figure 4.11**d**. During the extended period, nucleation from Au catalyst gets limited, as a result, catalyst volume decays with time. Consequently, catalyst driven growth segment becomes very short (see the triangular segment in the SEM image of Figure 4.11**d**). Conversely, <111> directional arms of the nanobridge get significantly thick due to the enhanced adatom collection. In brief, head-to-head merging with $\Delta m = 0$ results in Au droplets convergence, that along with the overgrown arms lead to a nanobridge structure.

4.5 InAs Nanowire Networks

In this section, we will discuss InAs NWs related networks. Several researchers have reported VLS grown InAs network formation on InAs, InP and Si substrates [66, 222, 258, 260, 261, 278–280]. So far, InAs network formation has been studied both in an arbitrary way directly from the substrate [66, 260, 261] and control positioning on the tilted facets [222]. In our experiment, we will study the control way of forming InAs networks. The fundamental growth mechanism of Au assisted InAs NWs network is comparable to the InSb network. However, the main difference in growth kinetics is the adatom assisted radial growth, which is significantly high for the InSb NWs due to the diffusion length limit. Thus, with distinct growth dynamics, the final morphology of the InAs network is also different than the InSb one. Study of synthesizing single WZ crystalline and ZB inclusion of InAs nanocross depending on the growth geometry is reported by Krizek et. al [66]. It is demonstrated that, if the WZ InAs NWs are grown from different ZB basis, then the difference in initial crystal orientation leads to the incoherent merging, which results in ZB area inclusion in the nanocrosses. On the other hand, if the NW couples are originated from the same WZ basis (by kinking InAs NW), then the possibility of single-crystalline InAs nanocrosses increases [66]. We will concentrate our study on appearance of different InAs networks, when the catalysts are positioned head-to-head. Depending on the distance between the Au catalysts (Δx), different types of InAs junctions are observed.

Networks from Two Trenches

Figure 4.12 shows two kinds of junctions when $\Delta x \approx 4\mu$m. As we discussed earlier, Au catalysts of both NWs may coalesce if the growth rates are the same. Otherwise, Au catalyst of one NW may hit into the side-wall of another NW. Figure 4.12 **a** shows InAs NW networks, which are the result of tip-to-tip catalyst merging. Similar to what we discussed in the InSb case ("Type-III" merging, see Figure 4.11), Au catalysts come close to each other and the coalesce process begins. At the same time (111) interface diminish, and a new interface is introduced beneath the Au catalyst. Eventually, the Au catalyst is pushed into one of the wire's legs

and continued to crawl that direction. However, unlike Figure 4.11 **d**, no growth in <100> direction is observed for InAs case. Similar phenomena are reported in previous reports [222, 258, 260] and step-by-step catalyst position during and after merging is shown by Dalacu et. al [222]. In Figure 4.12 **b**, shows the junctions, where the Au catalyst hit the sidewall of opposite NW due to the difference in growth rate. As expected, after hitting, the Au catalysts slide down to it's supporting NW in [-1-1-1] direction. Since the catalysts are lithographically defined, we can produce the network in well-organized manner, as shown in In Figure 4.12 **a** and **b**, unlike the previous arbitrary studies [66, 258, 260, 261, 281].

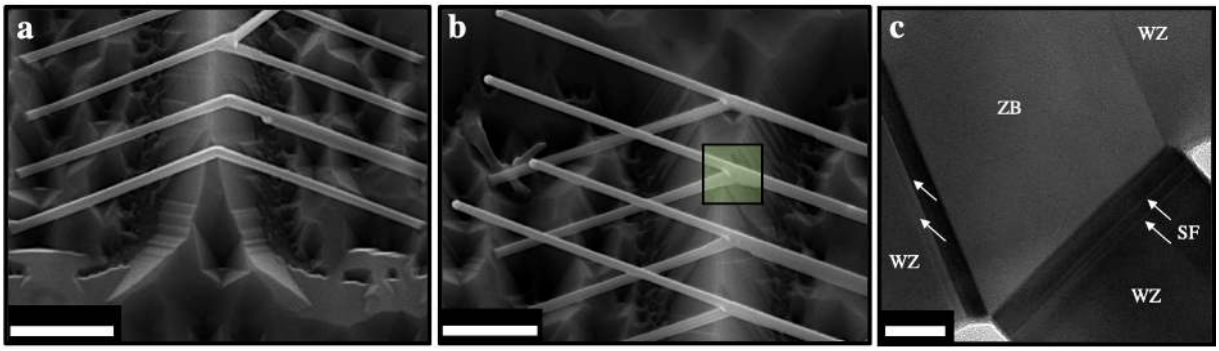

Figure 4.12: InAs network from two neighbouring trenches. a, SEM image of the junctions, where the NWs meet tip-to-tip and Au catalysts merge into one. Later, the merged catalyst choose to slide into one of the NWs' arms. **b**, SEM image of the "T"-shaped junctions, where one catalyst hit the sidewall of another one and crawl down to [-1-1-1] direction. **c**, TEM image of the junction interface from similar NW highlighted from (**c**). A trapezoidal ZB inclusion is observed after merging. A couple of stacking faults (indicated with arrows) are observed close to the boundary area of the ZB segment. Scale bars for (**a**) and (**b**) are 1 μm and (**c**) is 20 nm.

Unlike InSb networks, a significant crystal reconstruction is observed during the merging of InAs NW. As InSb is already grown with the cubic structure, during merging it is kinetically unfavorable to change the crystal structure. On the other hand, InAs WZ NWs are grown from opposite <111> directional ZB basis, which means crystal sequencing of both WZ NWs may not be the same. Hence, when both NWs meet (either at the side-wall or the top), the crystal structure immediately alters into the more energetically favorable ZB structure in the interface. Eventually, capillary penetration of the ZB crystal structure propagates into the diameter of the secondary NW, and the trapezoidal area of the ZB structure is observed, as shown in the HR-TEM image of Figure 4.12 **c**. Later, in the continuous growth period, ZB propagation stops, and the crystal switch back into the WZ phase, which is the predominant phase of InAs NWs. This switching from WZ-ZB-WZ can also be attributed to the supersaturation and the contact angle of the Au catalyst during and after merging. During merging, the triple-phase line shifts from the edge of the NW side facet, which means that the nucleation position also moves from the edge. This condition favors the ZB structure [120], hence, we observe a shift from WZ to ZB. Later, the position of the triple-phase restores at the edge, as a result [-1-1-1] directional sliding NW switch back to WZ structure. A similar incident is also reported by Kang et. al [260], where they initially observed partial penetration of Au with a rough interface into another NW and later, ZB crystal propagate into the "hit" NW. We observe the boundary of the transition is atomically sharp, which is also seen by others [66, 260]. The size of the trapezoidal area is

dependent on the diameter of both NWs, penetration of the Au droplet into the second NW, and the interface between them. If the diameter of "hit" NW is significantly larger than the "hitting" NW, then the ZB structure may not propagate into the whole area of the diameter. We presume, for the same reason, WZ to ZB switching phenomena is also true for the new interface generated when Au catalysts coalesce in the "V"-shaped junction shown in Figure 4.12 **a**. However, the ZB inclusion is supposedly a triangular shape for Figure 4.12 **a** interface due to the elbow structure. We do not have TEM inspection for Figure 4.12 **a** interface, however the evidence of our prediction can be validated by the TEM demonstration from Ref.[260].

Networks from Single Trench

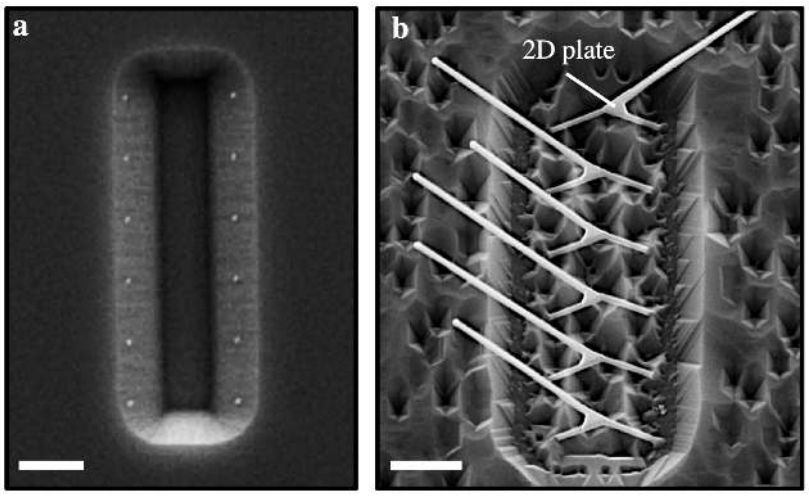

Figure 4.13: InAs network from one trench. a, SEM image of the single trench with Au catalysts positioned in both side of the (111) facets. Au catalysts are placed head-to-head. **b**, Tilted SEM image of the "y"-shaped InAs network with a 2D nanoplate overgrown area in the junction. Scale bars for (**a**) and (**b**) are 1 μm.

We are now going to discuss the InAs junctions grown from the same trench. In this case, the distance between the Au catalysts is approximately 2 μm as shown in Figure 4.13 **a**. Grown "y"-shaped InAs junctions are shown in Figure 4.13**b**. In contrast to the "T"-shaped junction formation that we have discussed in Figure 4.12**b**, here, the opposite NWs meet in a very early stage due to the close distance. Also, we haven't observed the catalyst crawling to each other's arms. Thus, it can be assumed that the growth rates of both NWs are equal, and NWs meet at the tip-to-tip condition. Au catalysts are merged as one and continued growing in <111> direction, unlike the previous junctions. An increase in diameter is observed in the post-merged <111> directed arm due to the bigger Au droplet. Also <111> continued arm seems to be slightly bent from their initial growth direction. This bending is occurred due to the post-merging re-position of the Au catalyst with a new interface and later continued growing from that. Furthermore, we observe a two dimensional (2D) plate formation in the merging point, as indicated in Figure 4.13**b**. We attribute this 2D plate to the high adatom incorporation in the given time of the junction area. The junction is formatted at the early stage of the growth and, in long run, collected adatoms from both NWs' arms accumulated in the junction area, which overcomes the nucleation barrier of the facets. As a result, an overgrown 2D plate junction area is observed.

Long Distance Networks

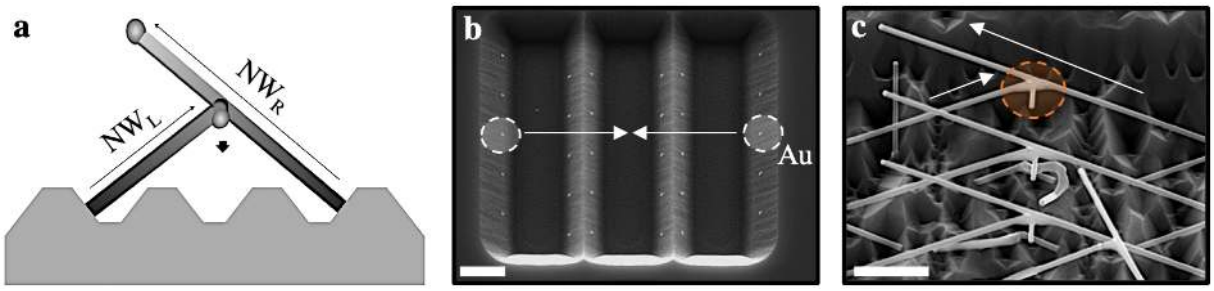

Figure 4.14: Formation of branched InAs NW. a, Schematic of the branched InAs NWs junction, where opposite <111> directional NWs merge from the side and a third new directional NW grows in parallel to the substrate (<110> direction). **b**, SEM image of the three parallel trenches with EBL positioned Au catalysts. Dotted highlighted Au from the last trenches are positioned "head to head" to merge and form a network. **c**, SEM image of the grown brunched NWs, where the orange highlighted NW grows in <110> direction after merging. Scale bars are 1 μm.

Finally, an interesting phenomenon we observe when the NWs are merged from long distance. SEM image of three parallel trenches are displayed in Figure 4.14**b**, where "head-to-head" Au catalysts are positioned in the opposite (111) facets approximately 6 μm apart, as highlighted with the dotted circle. NWs pair grown on <111> direction has an uneven growth rate, as a result, one NW passes the merging point (usually the middle of the trenches) faster than the other one, which leads to the other NW hit on the sidewall of the longer NW. Unlike the previous scenarios, the "hitting" NW doesn't crawl down to the "hit" NWs facet, rather choose a completely new direction of NW growth, as shown in the schematic of Figure 4.14**a** and SEM image of Figure 4.14**c**. Such <110> direction, which is parallel to the substrate, is quite unusual for the VLS grown NWs. Nevertheless, it is very reproducible for the NWs grown from the trenches shown in Figure 4.14**b** and **c**. A similar new NW branch from arbitrary catalyst position is observed and analyzed in Ref. [260, 261], where they demonstrated that after merging, the third possible direction can either be in <001> direction perpendicular to the substrate or <110> direction parallel to the substrate, similar to our case. They have also argued, in some cases, after merging, the Au catalyst may split into two and one slides through the sidewall, whereas the other one initiates a new branch. However, judging from our networks, we haven't observed any such scenario. After merging, the modified interface between Au and beneath material is the driving force for the new Au direction. As we mentioned before, crystal phase change appears from WZ to ZB in the post-merging interface, which helps Au droplet to re-position in a new energetically favorable crystal plane [261]. The complete mechanism behind this unusual <110> directional new branch of NW growth is not conclusive and requires a detailed investigation of the interface during Au merging on the sidewall, which can lead to a new way of branching NWs. Few other arbitrary and non-reproducible networks from long-distance merging are also observed. An example TEM analysis of such branched InAs junction is presented in Figure 4.15**a-i**. However, due to their random nature, it is complicated to draw a proper analysis.

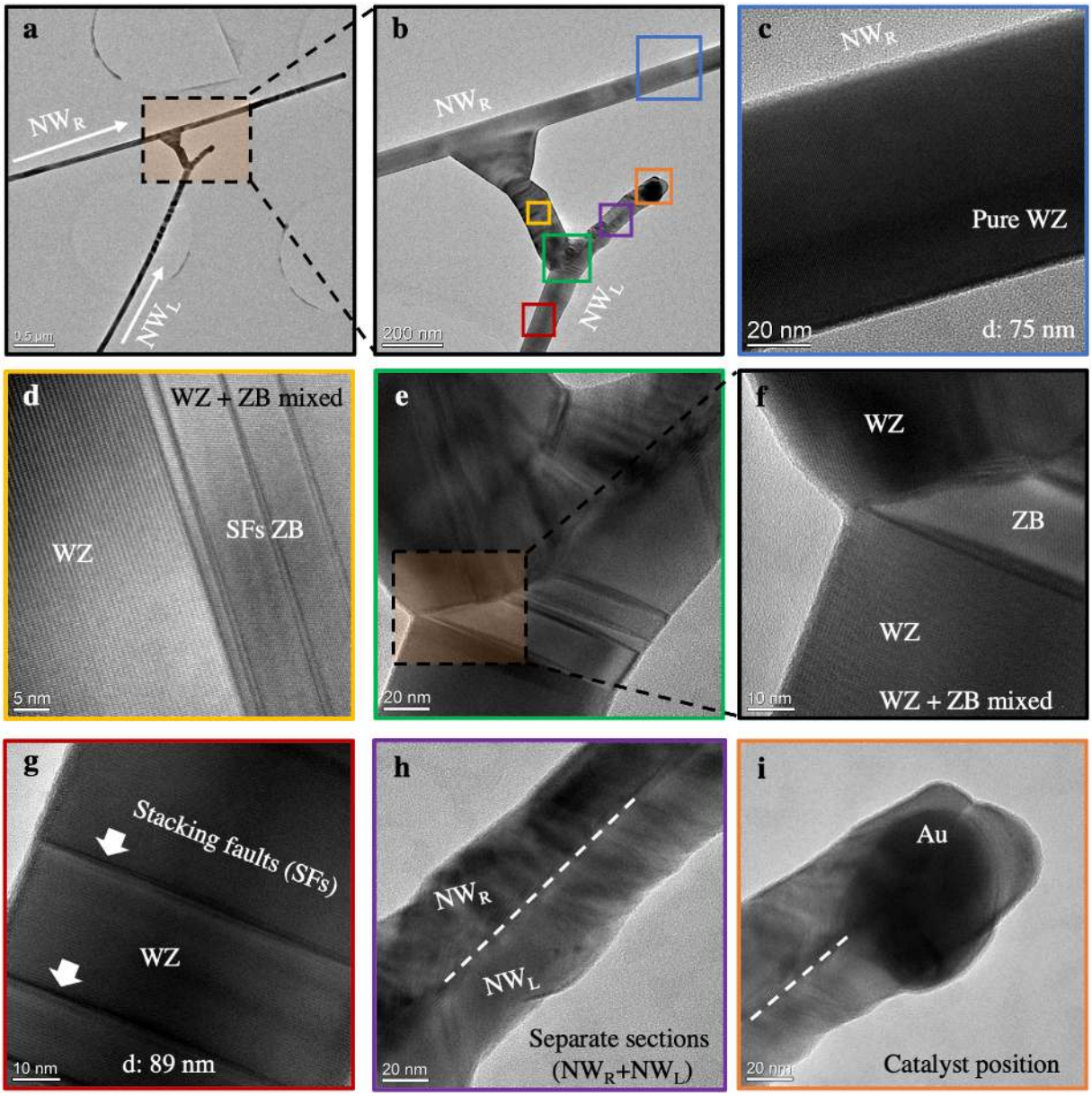

Figure 4.15: Crystal structure of an arbitrary branched InAs NW junction. a, TEM image of a branched InAs NW junction in the grid. **b**, Magnified TEM image of the junction area. Coloured boxes are our sections of interest, where we will perform high-resolution TEM and present in later panels. **c**, HR-TEM image in the segment of InAs NW_R, which is uninfluenced to merging and shows pure WZ crystal structure. **d**, Coexistence of WZ and ZB crystal structure after merging, which is also shown in Ref.[261]. Here Shockley partial dislocation leads to a couple of stacking faults induced in the structure during transition [282]. **e**, Interface between NW_L and the junction area. Although merged, a clear distinction between NW_L and NW_R is observed. Several stacking faults are also appeared in the process of relaxing the crystal structure. **f**, Magnified TEM image of the interface section reveals the transformation of two WZ structures into ZB while merging. **g**, HR-TEM from NW_L before merging. The NW shows mostly WZ crystal structure with the inclusion of several stacking faults. **h**, HR-TEM of the junction progression after merging. The clear distinction between NW_L and NW_R (which initiated in the interface, shown in panel (**e**)) continues. A dotted line in the contrast area is indicated. The growth of both NW segments side by side is a unique phenomenon. **h**, Au catalyst position at the top of the branched NW. The separation between both structures continues beneath the catalyst.

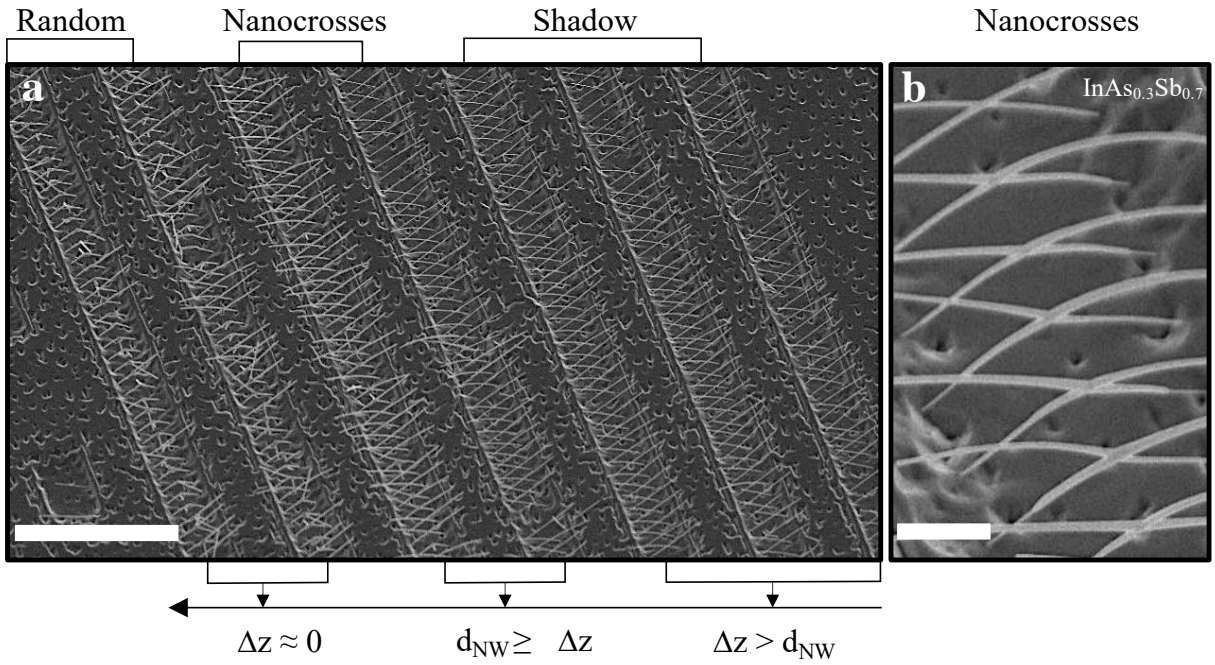

Figure 4.16: Nanocrosses with InAsSb NWs. a, Tilted SEM image of the InAsSb NW growth on the trenches, where the spacing between the catalysts are different from right to left. Based on that, NCs are created only on the sections where $d_{NW} \geq \Delta z$. **b**, Tilted SEM image of the magnified InAsSb nanocrosses, where less radial overgrowth is observed compared to InSb. Scale bars for (**a**) and (**b**) are 10 μm and 1μm respectively.

4.6 InAsSb Nanocrosses

Here, we will discuss InAsSb NW-based nanocrosses. We have already presented InAsSb NW growth on the trenches in Chapter 3. It has been shown that a composition of 70% Sb and 30% As provides single-crystalline ZB InAsSb NW, which leads to high-performance devices. Hence, to maintain high-quality single-crystalline ZB InAsSb NC formation, we stick to the same composition. Similar to the previous section, InAsSb NWs are grown with InAs stem from (111)B trenches, as shown in Figure 4.16**a**-**b**. Typical InAs segment is grown for 12 min maintaining As/In ratio ~ 9.78. Later, the Sb flux is introduced in the system with optimal Sb/In flux ratio ~ 4.30 and In growth rate 0.289 ML/s, which is expected to provide a high aspect ratio and uniform morphology of the Sb based NWs on the trenches.[7] Simultaneously, As to In ratio is lowered to 2.04 by tuning the As valve opening, which helps us to achieve the right composition in the InAsSb NW. Standard InAsSb segment is grown for 30-35 min providing the length of 4-4.5 μm long NW with diameter varies from 100-150 nm. The diameter variance depends on the catalyst size, which is usually varied from one growth section to another. Besides, depending on the spacing of the opposite Au catalyst (Δz), occasionally a radial overgrowth is performed after the InAsSb NWs growth, that also enhances the diameter of the InAsSb NW. Radial growth is performed with As_2 (contrary to the NW growth, which is performed with As_4) by cracking As molecules in the cracker cell at high temperature. For this, after the InAsSb growth, the As cell temperature is elevated to 700 °C and stabilized for 15 min, and then 10 min As_2 assisted overgrowth is

7: See Figure 4.2 for aspect ratio and morphology analysis with respect to Sb/In ratio.

performed confirming all the intended NWs are merged properly.

Figure 4.16**a** shows high yield InAsSb NW growth on the parallel trenches, where the Au catalysts are positioned in ~3 μm lateral distance (Δx) on the trench opening. The Δz [8] between the catalysts are varied from right to left. In the rightmost three trenches, InAsSb NW diameters are smaller than Δz, ($\Delta z > d_{NW}$), hence NWs are not merged. In the next two trenches $d_{NW} \geq \Delta z$, which leads to the formation of InAsSb NCs following the similar radial growth assisted mechanism, as elaborated in InSb cases. However, unlike InSb cases, a reduced radial overgrowth is observed in the InAsSb NW growth, as shown in Figure 4.16**b**. This reduced radial growth can be attributed to the increased diffusion length of adatoms on the NW sidewall assisted by the presence of As.With As, adatom incorporation in the Au catalyst increases, as a result, tapering-free axial growth is longer than the InSb NWs, but shorter than InAs NWs. For long growth run, with high Sb concentration (70% Sb here) of InAsSb NWs, a tapering profile is usually observed, that is related to the increased Sb incorporation on the NW sidewall. In addition to that, a gradual transition from InAs stem to InAsSb NW is observed (unlike InSb case). This is due to the continuous As inclusion to InAs stems through direct impingement and diffusion from the substrate. Finally, in the leftmost two trenches of Figure 4.16**a**, $\Delta z \approx 0$, hence, the coupled NWs grow face-to-face and after merging, different scenarios appear depending on the droplet kinetics. As the radial growth of the InAsSb is limited, leading to the low growth rate in the side-facets, therefore, no nanoplate formation is observed (unlike InSb). In most of the cases, head-to-head collision of the InAsSb with same growth rates (combined catalyst) causes random directional network. Thus, cannot be categorized like the previous two investigated NWs. However, in a few cases where the growth rates of both sides are different, similarities of network formation with InAs NWs are observed.

8: See Figure 4.1 for the trench and Au position schematic

Remark 4.6.1 The InAsSb NCs presented in this section is part of the research project of "Paper 8" (In Preparation).

4.7 Shadowing VLS Nanocrosses

Substrate Preparation

We use a bridge on top of the trenches to shadow the nanocrosses while depositing superconductors. [9] The idea of bridge fabrication to use as a shadow method is adapted from recently published work related to *in situ* patterning [69]. Similar to the trench fabrication, InAs (100) wafer is used for preparing the substrate. The preparation is divided into four main steps: Masking, developing bridges, creating trenches, and finally, positioning Au catalysts. In total, three lithography steps and two etching processes are involved in the development. Starting with the first step, which is masking the InAs substrate. Either SiO_x or Si_3N_4 can be used for masking. However, for an easier wet-etching process, we use SiO_x. 150 nm of SiO_x is deposited on top of InAs substrate using plasma-enhanced chemical vapor deposition (PECVD) system, as shown in Figure 4.17**a**. For fabricating the bridges, we pattern the intended bridge area on the mask with an EBL system and develop with standard MIBK and IPA

9: The bridge substrate project for nanocross shadowing is developed in collaboration with the Thomas Sand group at Niels Bohr Institute.

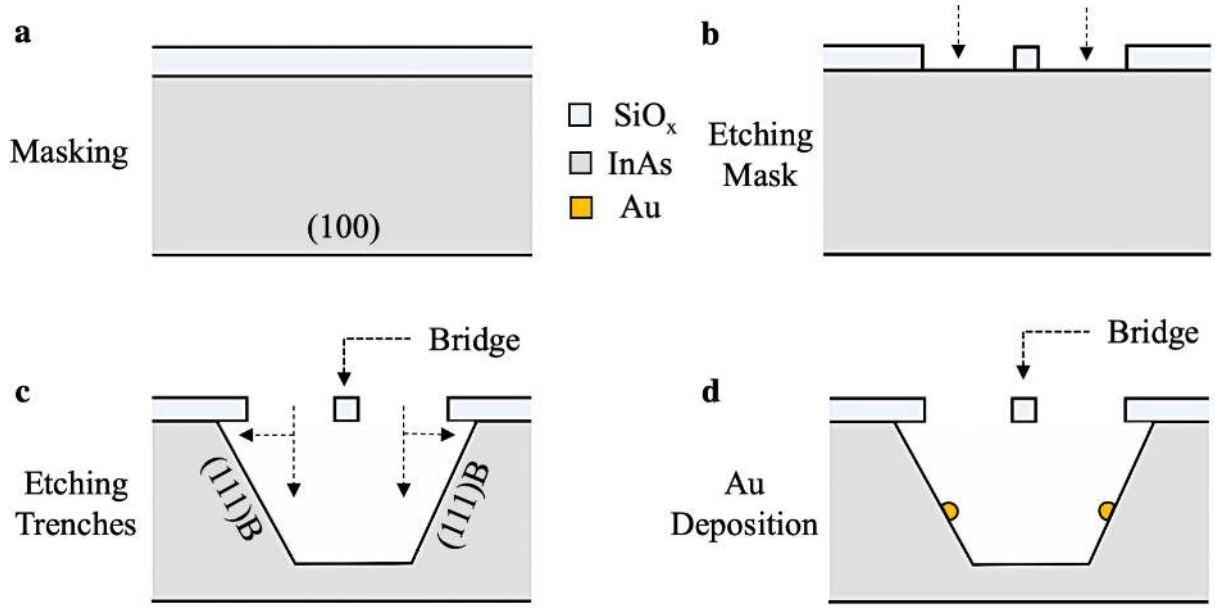

Figure 4.17: Substrate preparation for nanocross shadowing. a, Schematic of the InAs (100) wafer, where 150 nm of PECVD SiO_x is deposited for masking. In the right, color codes are mentioned for different materials. **b**, First electron beam lithography (EBL) is used for defining the pattern for the bridges. Buffered HF is used to remove the SiO_x from the developed area. As a result, the bridge for shadowing is formed. **c**, Second EBL process is used to pattern the area to make the trenches. Sulfuric acid based wet-etching is used to etch the developed area and create (111)B facted trenches [54]. **d**, Third EBL process is used to define the position of the Au catalyst on the (111)B faceted wall. E-beam evaporation is used to deposit the Au film. After lift-off, only developed areas are left with Au catalysts.

dipping (see previous experimental sections for development recipes). Next, buffered hydrofluoric acid is used to etch the SiO_x mask from developed area, which leaves the expected patterned SiO_x bridge, shown as cross-sectional view in Figure 4.17**b**. Then, the substrate is cleaned to remove the unintended resist and etch residues. For creating the trenches beneath the bridges, we use a second EBL process to define the trench area and developed the resist after lithography. Next, we use sulfuric and hydrogen peroxide acid-based wet-etching process to etch the trenches as described in chapter 3. [10] . As depicted in Figure 4.17**c**, the etching process is anisotropic [283], hence, a lateral etching beneath the SiO_x mask is observed. After this stage, the substrate has (111)B faceted trenches with a bridge on top for shadowing. In the final step for Au deposition, we use the third EBL process to define the position of the Au catalysts and develop the resist. Next, the e-beam evaporation system is used to deposit Au film on the substrate (see the previous chapter for details). Subsequently, the lift-off process is performed, which removes the unintended Au film leaving only the Au disks that will be used as a catalyst during the growth, shown in Figure 4.17**d**. Finally, a careful cleaning procedure and ashing is performed to make sure all the resist residue is removed before loading in the MBE. Here HF based etching is not used before loading in the MBE, as it can damage the bridge structures.

10: See chapter 3 for detailed fabrication steps and recipes.

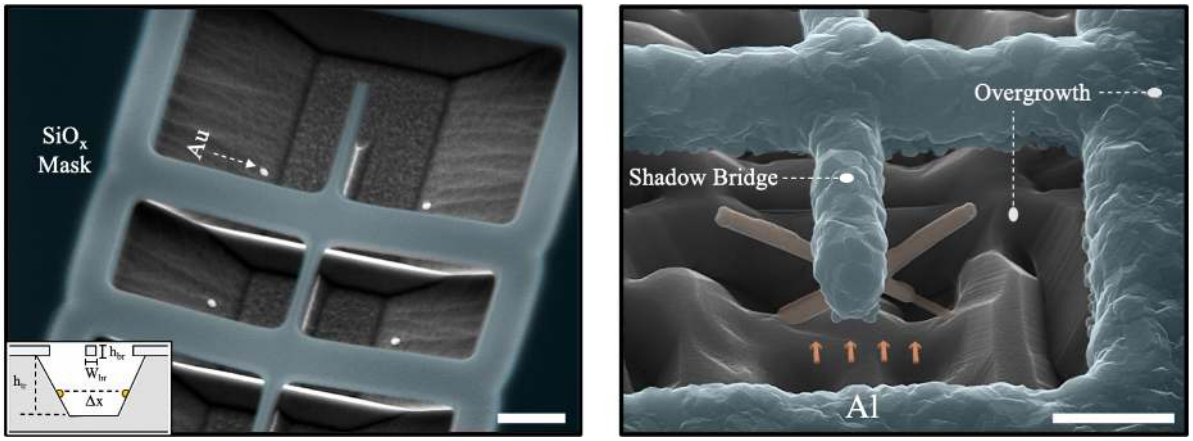

Figure 4.18: Shadowing InSb nanocrosses with Al. a, Tilted SEM image of the fabricated substrate. Related parameters for the shadow geometry is shown in the inset. **b**, Tilted SEM image of the shadowed nanocross. The arrows show the direction of the Al deposition. Indicated dotted lines show the shadow bar and the overgrowth on SiO_x mask. Scale bars for (**a**) and (**b**) are 1 μm.

Nanocrosses Growth and Shadowing

For multi-terminal Josephson junctions, we require to pattern the NCs with a superconductor. However, shadowing complex network structures, such as nanocross is not yet demonstrated in the literature. Hence, we investigate *in situ* procedure with bridges to shadow the intersection area of the nanocrosses. *In situ* superconductor growth on semiconductor and their optimal deposition conditions are demonstrated in chapter 2. Further in chapter 3, we discussed the patterning of the superconductors by *in situ* shadowing along with fine-tuning and geometry for controlled shadowing. Based on that, Figure 4.18**a** [11] shows the fabricated SiO_x bridge with trenches, where the Au catalysts are deposited (shown with arrow). Similar to the previous shadow study, the geometry of the bridge structure is crucial to realize both the nanocross growth and the shadowing in desired place. The position of the Au catalyst, Δx depends on the depth of the trenches, h_{tr}, which is again determined from the merging point (L_{MP}). In this case, we set $h_{tr} > L_{MP}$, so that the intersection of nanocrosses (where we would like to have our shadow) stays beneath the shadow bar. Hence, unlike trenches discussed in chapter 2 and previous sections in this chapter, the trenches here etched deeper (etched for 1.5 hr that may provide approximately 2μm deep trench). The etch efficiency of the solution may decrease due to the SiO_x mask, compared to the unmasked trenches. Further, the merging point (MP) requires to be exactly under the shadow bar. We lithographically position the cross-bar in the middle of the length of Δx. The width of the shadow bar, W_{br} is a crucial parameter to define the size of the shadow junction. Depending on the fabricated W_{br}, we decide the diameter of the NW, which determines the intersected area of the nanocross. If $W_{br} > d_{NW}$, then the shadowed area will be extended to the individual arms. On the other hand, If $W_{br} \leqslant d_{NW}$, the shadowed area is expected to be confined within the intersected area.

11: The nanocross substrate fabrication and SEM imaging is performed by Lukas Stampfer from Niels Bohr Institute. The recipe is adapted from Ref. [54, 69].

Nanocross growth with shadowing is shown in Figure 4.18**b**. Here, for demonstration of the process, InSb nanocross growth and Al deposition are shown. The NW growth conditions under the bridge are different compared to the normal trench growth discussed above. Hence, the optimal growth conditions from the normal trenches [12] , are not effective

12: See chapter 3 for InAs NW, and nanocross section in this chapter for InSb NW growth conditions

with the bridges. As a result, we observe a yield issue in the growth, shown in Figure 4.18**b**. Since the substrate is completely covered by SiO_x, which changes the local growth temperature, that affects the growth outcome and the morphology of the NWs. Here, we observe a significant overgrowth both in the trenches and on top of the oxide mask. Overgrowth on the oxide mask can be attributed to the non-selective temperature window of operation. Enhanced planar overgrowth in the trenches compare to the previous chapter can be due to the confinement of the trenches with the oxide mask. This leads to high adatom density inside the box. As a result, the nucleation sites increase in the trenches, leading to high planar growth and also hinders the NWs growth. The arrows in Figure 4.18**b** show the direction of the Al deposition. The deposition direction is carefully adjusted so that the Al get blocked in the shadow bar. Furthermore, the overgrowth on the shadow bar has an adverse effect on the shadowing. As discussed before, the shadow size and broadening are directly dependent on the angle of deposition, shadowing object, and the distance of shadow position from the shadow object. Here, the shadow size is a function of the initial width of the shadow bar, the overgrowth SiO_x mask, and the broadening due to the geometry. In this growth, the overgrown bar with the angle of deposition lead to long broadening in the edge profile and non-optimal shadow size. [13] For control shadow condition, first we have to eliminate the overgrowth on the mask and grow NWs selectively. A possible direction can be covering the trenches with an oxide mask and create openings only for Au catalysts. This will help to investigate the optimal temperature, which will ensure the selectivity both on shadow bars and trenches [284]. This research requires further development and currently ongoing.

13: Understanding the co-relation of edge-profile evolution and deposition geometry is elaborated in Chapter 3.

4.8 Conclusion

In conclusion, we presented the control synthesis of InSb, InAs, and InAsSb nanowire network by engineering the Au catalyst positions. First, we showed the tuning of InSb NWs morphology on the (111)B trenches by varying the V/III ratio, which helped us to find the optimal conditions. We showed that an offset between the Au catalysts is required to create NCs. Investigating the time-dependent radial and axial growth of InSb NWs, we explained the detail growth dynamics of forming InSb NCs and nanoplates. Structural analysis of InSb NCs showed ZB single crystal quality even after merging, which is essential for multi-terminal ballistic transport. Next, we showed nanoplate and nanobridge formation from head-to-head Au position. Depending on the growth rate of paired NWs, we found three types of merging conditions, which lead to different structures. Further, InAsSb NW growth is also performed from the trenches by varying Au positions, which exhibited radial growth assisted network formation similar to InSb. Unlike III-Sb, InAs networks demonstrated less domination to the radial growth, leading to the different structural outcomes. We analyzed InAs network formation from head-to-head Au position. Here, we found the distance between the Au in opposite tranches determines the structure of the network. Varying this trench distance, we manage to create V-shaped, T-shaped, y-shaped, and also a new directional branched network. Structural analysis of InAs NWs showed a ZB inclusion in the merged area, which we attributed

to the changed contact angle and triple-phase line during Au collision. Finally, we demonstrated the *in situ* shadow technique to pattern NCs with superconductors, which may unveil a high-quality platform for NW based multi-terminal Josephson junction. Here, we exhibited the junction with Al, however, the experiment can be extended to any other superconductors.

Conclusion and Outlook 5

In this thesis, I have divided the development of my research project into three core segments. Initially, MBE-grown semiconductor-superconductor hybrid NWs have been demonstrated. Going forward, a single-step *in situ* method have been developed to obtain semi-super hybrid NWs with the shadowed junctions. Finally, I have presented semiconductor NW networks and revealed an advanced technique to shadow nanocrosses for multi-terminal devices. In this chapter, I am going to sketch the core outcomes from each chapter, associated challenges and will try to connect them with future development.

Hybridization

Why Hybrid? Majorana bound state is expected to appear in a hybrid system of semiconductor NW (strong SOI and Landé-g factor) coupled with a superconductor (S-wave). Besides, high crystal quality and disorder-free interface between hybrid is essential. These motivated us to study MBE-grown high-quality SE-SU material platform.

Key Results. First, we demonstrated the VLS-grown InAs and InSb NWs. With optimized growth conditions, it has been shown that InAs exhibits WZ crystal structure and InSb exhibits pure ZB crystal structure. As InSb has been grown from InAs stem, a study on the InAs-InSb interface is also presented, which is vital to understand the growth mechanism. Next, we demonstrated hybridization of both NWs with Al and Sn. To confirm the high interface quality, SU depositions have been performed *in situ* after the NW growth. With Al, we showed the uniform thin film on both InAs and InSb NWs, where a thin film of as low as 3.5 nm has been demonstrated. In the final section, we showed a continuous Sn film formation on InSb NW. However, on the InAs NW surface, Sn film exhibited dewetted islands. In the structural analysis, $\alpha - \mathbf{Sn}$ supremacy in the Sn shell has been observed in the presented growth condition. Whereas, in the device demonstration, we found superconducting transition of the Sn shell. It is believed that the presence of superconducting $\beta - \mathbf{Sn}$ phases proximitize the neighboring $\alpha - \mathbf{Sn}$ phases, resulting in a superconducting shell.

Challenges and Next Step

In this two-layer system of semiconductor and superconductor, the challenges are present in both layers. Disorder in one layer can be detrimental for the whole system. Hence, proper tuning is required considering the crystal quality, interfacial domain matching, surface and grain boundary energy, etc. Moreover, a wide range of material combinations are possible to explore. On the semiconductor side, InSb and InAsSb are preferable material systems as both exhibit defect-free single-crystal quality and compatible with the standard device fabrication steps. Other semiconductors with high spin-orbit coupling can also be explored, such as PbTe nanowires. On the superconductor

side, Sn and Pb seem to be an interesting platform on III-V NW to investigate further. The issue with Sn is that, the cohabitation of both phases can be a bottleneck for the device yield. Particularly, devices for topological superconductivity ($\beta - \mathbf{Sn}$) and topological insulator ($\alpha - \mathbf{Sn}$), a well-defined single phase would be desired. Hence, our ongoing research is directed to the tuning of growth parameters to control synthesis of Sn-phase on semiconductor NWs, which will open up Sn's application in multiple research areas. Besides, Pb (high T_c) combined with single-crystalline InSb NW is another promising platform that we are currently investigating. Apart from single element superconductors, inorganic compound materials can also be explored for high T_c superconductivity (such as MgB_2). However, the challenge that appears with compound superconductors is to grow uniformly on III-V NW surface by finding an interfacial domain match.

Shadowing

Why Shadowing? The disorder-free junctions are crucial to realize Josephson Junction in gate tunable transmons qubits, spectroscopy devices, superconducting Majorana islands, and other kinds of hybrid NW based quantum devices. The conventional approach of creating a junction in the hybrid NW is to remove the superconducting segment by a top-down etching process. Such metal etching is not always controllable and damages the SE-SU interface, sometimes leave metal residues, which eventually detrimental to the device performances. In chapter 3, we attempted to resolve this issue by *in situ* shadowing the hybrid NWs in a single-step growth process.

Key Results. We used NWs to shadow each other during hybridization by growing them from opposite <111> directions with a lateral spacing. Such single-step shadowing avoids any post-processing of NW to create a junction. We manifested the versatility of the process by growing InAs, InSb, and InAsSb NWs and creating shadow junctions with Al, Sn, and Pb. Growing NWs from the mask-free trenches can be challenging due to the competition between planar growth and the NW growth. Hence, we developed a growth map with temperature window and appropriate flux ratio ($T_G \sim$ 401-415°C with V/III ratio ~ 9-10.5), where the highest yield with uniform morphology can be achieved. With full control over the synthesis and geometry of shadowing, we managed to create multiple superconducting islands with different sizes on a single NW. In-depth analysis was performed on the shadowed junction and unveiled that junctions performance depends on the junction morphology, which is determined by the material kinetics and shadowing geometry. The shadow-edge profile primarily relies on whether the adatoms follow the "hit and stick" model or they are kinetically active. If the adatom follows the "hit and stick" model then junction edge is a function of interwire distance, deposition system geometry. We experimented with varying the inter-wire distances and showed that the sharp-edge junction can be achieved with short interwire distance. Besides, the transition of the edge profile (from gradient to step-like profile) is also determined by the flux distribution from the source, where using EBPVD we showed it can differ from materials to materials. It's because, when adatoms are mobile (which means the temperature is not low enough) then adatom migration length for a given material plays a crucial role in determining the junction

profile. It is found that InSb/Sn exhibits the sharpest junction profile. Demonstrating NW devices with different junction profiles revealed that the sharp-edge junction show low resistance with repeatable quantized conductance for all type of NWs. Furthermore, low-temperature measurements on these sharp-edge junctions exhibited a large supercurrent. Finally, a statistical comparison of *in situ* shadowed and etched NW devices showed superior performance of the shadowed NW devices, which validates our efforts toward in vacuo fabrication of the quantum materials.

Challenges and Next Step

Our findings clearly show the importance of fabricating quantum materials and devices *in situ*. However, we only have performed a fundamental study, whereas plenty of development and engineering yet to be done. For instance, the next possible challenge I can think of is to fabricate a complete VLS NW device *in situ*. A 3D structure is required for that, allowing to pattern the NW from different sides. Concerns may appear regarding the control fabrication of such 3D structures and their persistence during the growth process. Another challenge I see is to transfer shadow lithography in the scalable devices. Going forward, we have to consider a scalable material platform for the development of quantum computation. Hence, using *in situ* stencil lithography technique can be a possible direction to pursue. Right after the materials growth (2DEG or SAG), a stencil mask can be used to selectively deposit SU, dielectric materials, and contact electrodes on the grown structure. In this way, full device fabrication on the scalable platform can be performed in an ultra-high vacuum.

Networks

Why Network? Semiconductor nanowire (NW) network is a crucial material platform for exploring Majorana braiding operation [33, 51, 243, 244]. However, the use of such networks can also be expanded in multi-terminal quantum devices and other areas like, optoelectronic devices, biological sensors, photovoltaics etc. All this factors motivated us to study control synthesis of semiconductor NW networks, which we discussed in Chapter 4.

Key Results. We demonstrated VLS grown InSb, InAs, and InAsSb NW networks. It is observed that network formation and their types are highly dependent on the catalyst position and growth conditions. Starting with InSb NWs, if the Au catalysts are placed with an offset, NWs grow and pass each other without intersecting. Later, radial overgrowth assists them to merge and form nanocrosses. Depending on the radial growth rate, the NCs can be slightly overlapped, partially intersected, or properly merged. Such InSb NCs exhibit defect-free ZB crystal quality. Furthermore, if the catalyst particles are placed head to head, InSb NWs seem to form other types of structures such as nanoplates (with or without an arm) or nanobridges. InAsSb NWs also follow the similar NC formation mechanism as InSb. In the case of WZ InAs NWs, head-to-head catalyst positioning leads to V-shaped, T-shaped, y-shaped, and also a new directional branched network, where inclusion of well-defined ZB crystal segment in the merging area is observed. Lastly, we demonstrated

an advanced architecture to shadow nanocrosses with a bridge, providing a platform for multi-terminal Josephson junction devices.

Challenges and Next Step

Addressing the scalability issue is the main challenge for VLS grown networks, which is hindering its progress towards technology. An approach to attain scalability with kinked VLS NW is reported earlier [285]. However, the controlled kinking direction, maintaining crystal quality, and reliable fabrication process become an issue. If the kinking direction is controlled, then various possibilities can be explored. An idea can be, growing the NWs in the etched trench or hole and kink them after the trench (or hole) height, which will make the device fabrication process similar to SAG. As a potential material, InAs-InSb can be used for high crystal quality, and kink after the InAs segment, which has been shown before [247]. In this case, patterning with superconductor will also be possible using shadow-wall. This project may require efforts to overcome challenges in both the growth and the fabrication side. On the other hand, the SAG NW networks inherently provide scalability. In combination with *in situ* stencil lithography, it already promises in vacuo platform for large-scale quantum devices. However, the drawback is in the crystal quality, which relates to the substrate lattice mismatch leading to the misfit dislocation in the SAG structure (much like planar heterostructure). Hence, focusing on the SAG platform to improve the crystal quality should be highly considered as the next step for the quantum network. Providing the existing advancement in the semiconductor industry, my best guess would be SAG NWs on silicon platform as a promising direction to be able to integrate with the present technology. In short, VLS grown networks provide high crystal quality for fundamental academic research and SAG networks will provide scalability. Hence, we should consider synergistic progress on both material platform.

Bibliography

Here are the references in citation order.

[1] Anna Fontcuberta i Morral, Shadi A Dayeh, and Chennupati Jagadish. *Semiconductor Nanowires I: Growth and Theory*. Academic Press, 2015 (cited on pages 1, 71).

[2] Neil P Dasgupta et al. '25th anniversary article: semiconductor nanowires–synthesis, characterization, and applications'. In: *Advanced materials* 26.14 (2014), pp. 2137–2184 (cited on pages 1, 2).

[3] Anqi Zhang, Gengfeng Zheng, and Charles M Lieber. *Nanowires: Building blocks for nanoscience and nanotechnology*. Springer, 2016 (cited on pages 1, 8, 10).

[4] Vladimir G Dubrovskii. *Vapor–Liquid–Solid Growth of Nanowires (Chapter 4). in: Nucleation theory and growth of nanostructures*. Springer, 2014 (cited on pages 1, 10–14, 18).

[5] Jordi Arbiol and Qihua Xiong. *Semiconductor Nanowires: Materials, Synthesis, Characterization and Applications*. Elsevier, 2015 (cited on pages 1, 2).

[6] Claes Thelander et al. 'Nanowire-based one-dimensional electronics'. In: *Materials today* 9.10 (2006), pp. 28–35 (cited on page 1).

[7] PC McIntyre and A Fontcuberta i Morral. 'Semiconductor nanowires: to grow or not to grow?' In: *Materials Today Nano* 9 (2020), p. 100058 (cited on pages 1, 14, 71).

[8] Charles Lieber et al. *Semiconductor nanowires: from next-generation electronics to sustainable energy*. Royal Society of Chemistry, 2014 (cited on page 1).

[9] RS Wagner and s WC Ellis. 'Vapor-liquid-solid mechanism of single crystal growth'. In: *Applied physics letters* 4.5 (1964), pp. 89–90 (cited on pages 1, 10, 11).

[10] Magnus Heurlin et al. 'Continuous gas-phase synthesis of nanowires with tunable properties'. In: *Nature* 492.7427 (2012), pp. 90–94 (cited on page 1).

[11] Yu Huang and Charles M Lieber. 'Integrated nanoscale electronics and optoelectronics: Exploring nanoscale science and technology through semiconductor nanowires'. In: *Pure and Applied Chemistry* 76.12 (2004), pp. 2051–2068 (cited on page 1).

[12] Yi Cui et al. 'High performance silicon nanowire field effect transistors'. In: *Nano letters* 3.2 (2003), pp. 149–152 (cited on page 1).

[13] Josh Goldberger et al. 'Silicon vertically integrated nanowire field effect transistors'. In: *Nano letters* 6.5 (2006), pp. 973–977 (cited on page 1).

[14] Ho-Young Cha et al. 'Gallium nitride nanowire nonvolatile memory device'. In: *Journal of applied physics* 100.2 (2006), p. 024307 (cited on page 1).

[15] MT Björk et al. 'Nanowire resonant tunneling diodes'. In: *Applied Physics Letters* 81.23 (2002), pp. 4458–4460 (cited on page 1).

[16] K Q. Peng, Z P. Huang, and Jing Zhu. 'Fabrication of large-area silicon nanowire p–n junction diode arrays'. In: *Advanced Materials* 16.1 (2004), pp. 73–76 (cited on page 1).

[17] Oliver Hayden, Andrew B Greytak, and David C Bell. 'Core–shell nanowire light-emitting diodes'. In: *Advanced Materials* 17.6 (2005), pp. 701–704 (cited on page 1).

[18] Eric M Gallo et al. 'Picosecond response times in GaAs/AlGaAs core/shell nanowire-based photodetectors'. In: *Applied Physics Letters* 98.24 (2011), p. 241113 (cited on page 1).

[19] Zhiyong Fan and Jia G Lu. 'Gate-refreshable nanowire chemical sensors'. In: *Applied Physics Letters* 86.12 (2005), p. 123510 (cited on page 1).

[20] Yi Cui et al. 'Nanowire nanosensors for highly sensitive and selective detection of biological and chemical species'. In: *science* 293.5533 (2001), pp. 1289–1292 (cited on page 1).

[21] Peter Krogstrup et al. 'Single-nanowire solar cells beyond the Shockley–Queisser limit'. In: *Nature Photonics* 7.4 (2013), pp. 306–310 (cited on page 2).

[22] L Tsakalakos et al. 'Silicon nanowire solar cells'. In: *Applied physics letters* 91.23 (2007), p. 233117 (cited on page 2).

[23] Francisco Domınguez-Adame et al. 'Nanowires: A route to efficient thermoelectric devices'. In: *Physica E: Low-dimensional Systems and Nanostructures* 113 (2019), pp. 213–225 (cited on page 2).

[24] XL Feng et al. 'Very high frequency silicon nanowire electromechanical resonators'. In: *Nano Letters* 7.7 (2007), pp. 1953–1959 (cited on page 2).

[25] Xudong Wang et al. 'Piezoelectric field effect transistor and nanoforce sensor based on a single ZnO nanowire'. In: *Nano letters* 6.12 (2006), pp. 2768–2772 (cited on page 2).

[26] Candace K Chan et al. 'Solution-grown silicon nanowires for lithium-ion battery anodes'. In: *ACS nano* 4.3 (2010), pp. 1443–1450 (cited on page 2).

[27] Chong Liu, Neil P Dasgupta, and Peidong Yang. 'Semiconductor nanowires for artificial photosynthesis'. In: *Chemistry of Materials* 26.1 (2014), pp. 415–422 (cited on page 2).

[28] Yuval Oreg, Gil Refael, and Felix von Oppen. 'Helical liquids and Majorana bound states in quantum wires'. In: *Physical Review Letters* 105.17 (2010), p. 177002 (cited on pages 2–4, 7, 47).

[29] Roman M. Lutchyn, Jay D. Sau, and S. Das Sarma. 'Majorana fermions and a topological phase transition in semiconductor-superconductor heterostructures'. In: *Physical Review Letters* 105.7 (2010), p. 077001 (cited on pages 2–4, 7, 22, 47).

[30] V. Mourik et al. 'Signatures of Majorana Fermions in Hybrid Superconductor-Semiconductor Nanowire Devices'. In: *Science* 336 (2012), pp. 1003–1007 (cited on pages 2, 7, 47).

[31] Leonid P. Rokhinson, Xinyu Liu, and Jacek K. Furdyna. 'The fractional a.c. Josephson effect in a semiconductor–superconductor nanowire as a signature of Majorana particles'. In: *Nature Physics* 8 (2012), pp. 795–799 (cited on pages 2, 7, 47).

[32] MT Deng et al. 'Majorana bound state in a coupled quantum-dot hybrid-nanowire system'. In: *Science* 354.6319 (2016), pp. 1557–1562 (cited on page 2).

[33] Hao Zhang et al. 'Next steps of quantum transport in Majorana nanowire devices'. In: *Nature Communications* 10.1 (2019), pp. 1–7 (cited on pages 2, 71, 99).

[34] Elsa Prada et al. 'From Andreev to Majorana bound states in hybrid superconductor–semiconductor nanowires'. In: *Nature Reviews Physics* (2020), pp. 1–20 (cited on pages 2, 22).

[35] SM Frolov, MJ Manfra, and JD Sau. 'Topological superconductivity in hybrid devices'. In: *Nature Physics* 16.7 (2020), pp. 718–724 (cited on page 2).

[36] Paul Adrien Maurice Dirac. 'The quantum theory of the electron'. In: *Proceedings of the Royal Society of London. Series A, Containing Papers of a Mathematical and Physical Character* 117.778 (1928), pp. 610–624 (cited on page 2).

[37] E. Majorana. 'Teoria simmetrica dell'elettrone e del positrone'. In: *Nuovo Cimento* 5 (1937), pp. 171–184 (cited on page 2).

[38] Liang Fu and Charles L Kane. 'Superconducting proximity effect and Majorana fermions at the surface of a topological insulator'. In: *Physical review letters* 100.9 (2008), p. 096407 (cited on pages 2, 4).

[39] Roman M Lutchyn, Jay D Sau, and S Das Sarma. 'Majorana fermions and a topological phase transition in semiconductor-superconductor heterostructures'. In: *Physical Review Letters* 105.7 (2010), p. 077001 (cited on page 2).

[40] Martin Leijnse and Karsten Flensberg. 'Introduction to topological superconductivity and Majorana fermions'. In: *Semiconductor Science and Technology* 27.12 (2012), p. 124003 (cited on pages 3, 5).

[41] Leon N Cooper. 'Bound electron pairs in a degenerate Fermi gas'. In: *Physical Review* 104.4 (1956), p. 1189 (cited on page 3).

[42] Sergey Frolov. *Quantum Transport, Lecture 20: Majorana fermions*. https://www.youtube.com/watch?v=7OUkHkmPGbY. Apr. 2013 (cited on pages 3–5).

[43] GE Volovik. 'Fermion zero modes on vortices in chiral superconductors'. In: *Journal of Experimental and Theoretical Physics Letters* 70.9 (1999), pp. 609–614 (cited on pages 3, 5).

[44] A Yu Kitaev. 'Unpaired Majorana fermions in quantum wires'. In: *Physics-Uspekhi* 44 (2001), pp. 131–136 (cited on pages 3, 7, 22).

[45] Sven Marian Albrecht. 'Quasiparticle Dynamics and Exponential Protection in Majorana Islands'. PhD thesis. The Niels Bohr Institute, Faculty of Science, University of Copenhagen, 2016 (cited on page 5).

[46] I Van Weperen. 'Quantum Transport in Indium Antimonide Nanowires: Investigating building blocks for Majorana devices'. In: (2014) (cited on pages 4, 6).

[47] Saulius Vaitiekenas. 'From Topological to Anomalous Quantum Phases in Hybrid Nanowires'. PhD thesis. Niels Bohr Institute, Faculty of Science, University of Copenhagen, 2019 (cited on page 4).

[48] Yu Liu et al. 'Semiconductor–ferromagnetic insulator–superconductor nanowires: stray field and exchange field'. In: *Nano Letters* 20.1 (2019), pp. 456–462 (cited on pages 4, 47).

[49] S Vaitiekėnas et al. 'Zero-bias peaks at zero magnetic field in ferromagnetic hybrid nanowires'. In: *Nature Physics* (2020), pp. 1–5 (cited on page 4).

[50] Jay D Sau, Sumanta Tewari, and S Das Sarma. 'Experimental and materials considerations for the topological superconducting state in electron-and hole-doped semiconductors: Searching for non-Abelian Majorana modes in 1D nanowires and 2D heterostructures'. In: *Physical Review B* 85.6 (2012), p. 064512 (cited on page 6).

[51] R. M. Lutchyn et al. 'Majorana zero modes in superconductor–semiconductor heterostructures'. In: *Nature Reviews Materials* 3 (2018), pp. 52–68 (cited on pages 7, 17, 22, 47, 71, 99).

[52] P Krogstrup et al. 'Epitaxy of semiconductor–superconductor nanowires'. In: *Nature Materials* 14.4 (2015), pp. 400–406 (cited on pages 7, 12, 23, 25, 28–30, 32, 33, 35, 38, 47, 51, 53, 58).

[53] Sasa Gazibegovic et al. 'Epitaxy of advanced nanowire quantum devices'. In: *Nature* 548.7668 (2017), pp. 434–438 (cited on page 7).

[54] Sabbir A Khan et al. 'Highly Transparent Gatable Superconducting Shadow Junctions'. In: *ACS nano* (2020) (cited on pages 7, 17, 20, 21, 32, 35, 40, 47, 73, 93, 94).

[55] Anindya Das et al. 'Zero-bias peaks and splitting in an Al–InAs nanowire topological superconductor as a signature of Majorana fermions'. In: *Nature Physics* 8 (2012), pp. 887–895 (cited on pages 7, 47).

[56] MT Deng et al. 'Anomalous zero-bias conductance peak in a Nb–InSb nanowire–Nb hybrid device'. In: *Nano Letters* 12 (2012), pp. 6414–6419 (cited on pages 7, 47).

[57] A. D. K. Finck et al. 'Anomalous modulation of a zero-bias peak in a hybrid nanowire-superconductor device'. In: *Physical Review Letters* 110 (2013), p. 126406 (cited on pages 7, 47).

[58] M. T. Deng et al. 'Majorana bound state in a coupled quantum-dot hybrid-nanowire system'. In: *Science* 354 (2016), pp. 1557–1562 (cited on pages 7, 47).

[59] H. Zhang et al. 'Quantized Majorana conductance'. In: *Nature* 556 (2018), pp. 74–79 (cited on pages 7, 47).

[60] Jun Chen et al. 'Experimental phase diagram of zero-bias conductance peaks in superconductor/semiconductor nanowire devices'. In: *Science advances* 3 (2017) (cited on pages 7, 47).

[61] Önder Gül et al. 'Ballistic Majorana nanowire devices'. In: *Nature nanotechnology* 13 (2018), pp. 192–197 (cited on pages 7, 47).

[62] Hao Zhang et al. 'Ballistic superconductivity in semiconductor nanowires'. In: *Nature communications* 8.1 (2017), pp. 1–7 (cited on page 7).

[63] Önder Gül et al. 'Hard superconducting gap in InSb nanowires'. In: *Nano letters* 17.4 (2017), pp. 2690–2696 (cited on page 7).

[64] W Chang et al. 'Hard gap in epitaxial semiconductor–superconductor nanowires'. In: *Nature Nanotechnology* 10.3 (2015), pp. 232–236 (cited on pages 7, 29, 54, 56).

[65] David Johannes Thoen et al. 'Superconducting NbTin Thin Films With Highly Uniform Properties Over a 100 mm Wafer'. In: *IEEE Transactions on Applied Superconductivity* 27.4 (2016), pp. 1–5 (cited on page 7).

[66] Filip Krizek et al. 'Growth of InAs wurtzite nanocrosses from hexagonal and cubic basis'. In: *Nano Letters* 17 (2017), pp. 6090–6096 (cited on pages 7, 47, 59, 71, 74, 86, 87).

[67] Nicholas A Güsken et al. 'MBE growth of Al/InAs and Nb/InAs superconducting hybrid nanowire structures'. In: *Nanoscale* 9.43 (2017), pp. 16735–16741 (cited on pages 7, 30).

[68] Martin Bjergfelt et al. 'Superconducting vanadium/indium-arsenide hybrid nanowires'. In: *Nanotechnology* 30.29 (2019), p. 294005 (cited on page 7).

[69] Damon J Carrad et al. 'Shadow lithography for in-situ growth of generic semiconductor/superconductor devices'. In: *arXiv preprint arXiv:1911.00460* (2019) (cited on pages 7, 47, 92, 94).

[70] Thomas Kanne et al. 'Epitaxial Pb on InAs nanowires'. In: *arXiv preprint arXiv:2002.11641* (2020) (cited on pages 7, 8, 26–28, 30, 34, 38).

[71] M Pendharkar et al. 'Parity-preserving and magnetic field resilient superconductivity in indium antimonide nanowires with tin shells'. In: *arXiv preprint arXiv:1912.06071* (2019) (cited on pages 7, 32, 33, 35, 37, 38, 40, 41, 51).

[72] WJ De Haas, J De Boer, and GJ Van den Berg. 'The electrical resistance of cadmium, thallium and tin at low temperatures'. In: *Physica* 2.1-12 (1935), pp. 453–459 (cited on pages 7, 33).

[73] B. T. Matthias, T. H. Geballe, and V. B. Compton. 'Superconductivity'. In: *Rev. Mod. Phys.* 35 (1 Jan. 1963), pp. 1–22 (cited on page 8).

[74] Julian Eisenstein. 'Superconducting Elements'. In: *Rev. Mod. Phys.* 26 (3 July 1954), pp. 277–291 (cited on page 8).

[75] R. D. Chaudhari. 'Critical Magnetic Fields in Superconducting Films of Indium'. In: *Phys. Rev.* 151 (1 Nov. 1966), pp. 96–100 (cited on page 8).

[76] GW Webb, F Marsiglio, and JE Hirsch. 'Superconductivity in the elements, alloys and simple compounds'. In: *Physica C: Superconductivity and its applications* 514 (2015), pp. 17–27 (cited on page 8).

[77] Aaron Wexler and William S. Corak. 'Superconductivity of Vanadium'. In: *Phys. Rev.* 85 (1 Jan. 1952), pp. 85–90 (cited on page 8).

[78] S. T. Sekula and R. H. Kernohan. 'Magnetic Properties of Superconducting Vanadium'. In: *Phys. Rev. B* 5 (3 Feb. 1972), pp. 904–911 (cited on page 8).

[79] L Schubert et al. 'Silicon nanowhiskers grown on< 111> Si substrates by molecular-beam epitaxy'. In: *Applied Physics Letters* 84.24 (2004), pp. 4968–4970 (cited on page 8).

[80] Jeffrey Y Tsao. *Materials fundamentals of molecular beam epitaxy*. Academic Press, 2012 (cited on page 8).

[81] Dr Faebian Bastiman. *Epitaxy Explained*. https://faebianbastiman.wordpress.com/. Nov. 2020 (cited on page 9).

[82] SVT Associatesv. *Valved Sources and Cracking Sources*. https://www.svta.com/valved-cracking-sources-mbe-system.html. Nov. 2020 (cited on page 10).

[83] Dr Eberl MBE-Komponenten. *Beam Flux Monitor*. https://www.mbe-komponenten.de/products/mbe-components/equipment/bfm.php. Nov. 2020 (cited on page 10).

[84] Kimberly A Dick et al. 'Synthesis of branched'nanotrees' by controlled seeding of multiple branching events'. In: *Nature materials* 3.6 (2004), pp. 380–384 (cited on pages 11, 71).

[85] Jean-Christophe Harmand et al. 'Atomic step flow on a nanofacet'. In: *Physical review letters* 121.16 (2018), p. 166101 (cited on pages 11, 12, 14).

[86] EI Givargizov. 'Fundamental aspects of VLS growth'. In: *Vapour Growth and Epitaxy*. Elsevier, 1975, pp. 20–30 (cited on pages 11, 14).

[87] Peter Krogstrup et al. 'Advances in the theory of III–V nanowire growth dynamics'. In: *Journal of Physics D: Applied Physics* 46.31 (2013), p. 313001 (cited on pages 11–14, 25, 58).

[88] Ning Wang, Y Cai, and RQ Zhang. 'Growth of nanowires'. In: *Materials Science and Engineering: R: Reports* 60.1-6 (2008), pp. 1–51 (cited on pages 11, 14).

[89] Jonas Johansson et al. 'Mass transport model for semiconductor nanowire growth'. In: *The Journal of Physical Chemistry B* 109.28 (2005), pp. 13567–13571 (cited on pages 11, 14).

[90] KW Schwarz and J Tersoff. 'Multiplicity of steady modes of nanowire growth'. In: *Nano letters* 12.3 (2012), pp. 1329–1332 (cited on pages 11, 14).

[91] VG Dubrovskii et al. 'Growth kinetics and crystal structure of semiconductor nanowires'. In: *Physical Review B* 78.23 (2008), p. 235301 (cited on pages 11, 12, 14).

[92] KW Schwarz and J Tersoff. 'Elementary processes in nanowire growth'. In: *Nano letters* 11.2 (2011), pp. 316–320 (cited on pages 11, 14).

[93] KW Schwarz and J Tersoff. 'From droplets to nanowires: Dynamics of vapor-liquid-solid growth'. In: *Physical review letters* 102.20 (2009), p. 206101 (cited on pages 11, 14, 18).

[94] Günter Schmid and Benedetto Corain. 'Nanoparticulated gold: syntheses, structures, electronics, and reactivities'. In: *European Journal of Inorganic Chemistry* 2003.17 (2003), pp. 3081–3098 (cited on page 11).

[95] Jonas Johansson et al. 'Effects of supersaturation on the crystal structure of gold seeded III- V nanowires'. In: *Crystal Growth and Design* 9.2 (2009), pp. 766–773 (cited on page 12).

[96] Daniel Jacobsson et al. 'Interface dynamics and crystal phase switching in GaAs nanowires'. In: *Nature* 531.7594 (2016), pp. 317–322 (cited on pages 12, 14).

[97] Y-C Chou et al. 'Atomic-scale variability and control of III-V nanowire growth kinetics'. In: *Science* 343.6168 (2014), pp. 281–284 (cited on pages 12, 14).

[98] Carina B Maliakkal et al. 'In situ analysis of catalyst composition during gold catalyzed GaAs nanowire growth'. In: *Nature communications* 10.1 (2019), pp. 1–9 (cited on pages 12, 14).

[99] Filip Krizek. 'Semiconductor Nanowire Networks Grown by Molecular Beam Epitaxy: Vapor-liquid-solid and Selective Area Growth'. PhD thesis. The Niels Bohr Institute, Faculty of Science, University of Copenhagen, 2018 (cited on pages 12, 14).

[100] Xu Zhang et al. 'Analytical study of elastic relaxation and plastic deformation in nanostructures on lattice mismatched substrates'. In: *Crystal growth & design* 11.12 (2011), pp. 5441–5448 (cited on page 14).

[101] Morten Hannibal Madsen et al. 'Experimental determination of adatom diffusion lengths for growth of InAs nanowires'. In: *Journal of crystal growth* 364 (2013), pp. 16–22 (cited on pages 14, 16).

[102] Zhi Zhang et al. 'Quality of epitaxial InAs nanowires controlled by catalyst size in molecular beam epitaxy'. In: *Applied Physics Letters* 103.7 (2013), p. 073109 (cited on page 14).

[103] Maria Tchernycheva et al. 'Au-assisted molecular beam epitaxy of InAs nanowires: Growth and theoretical analysis'. In: *Journal of Applied Physics* 102.9 (2007), p. 094313 (cited on page 14).

[104] Mattias Borg et al. 'Vertical III–V nanowire device integration on Si (100)'. In: *Nano letters* 14.4 (2014), pp. 1914–1920 (cited on page 14).

[105] Peter Offermans, Mercedes Crego-Calama, and Sywert H Brongersma. 'Gas detection with vertical InAs nanowire arrays'. In: *Nano letters* 10.7 (2010), pp. 2412–2415 (cited on page 14).

[106] Bang Li et al. 'Self-catalyzed growth of InAs nanowires on InP substrate'. In: *Nanoscale research letters* 12.1 (2017), pp. 1–5 (cited on page 14).

[107] Guoqiang Zhang et al. 'Au-free InAs nanowires grown in In-particle-assisted vapor-liquid-solid mode: growth, structure, and electrical property'. In: *AIP Advances* 3.5 (2013), p. 052107 (cited on page 14).

[108] MH Sun et al. 'Photoluminescence properties of InAs nanowires grown on GaAs and Si substrates'. In: *Nanotechnology* 21.33 (2010), p. 335705 (cited on page 14).

[109] David Forbes et al. 'Au-catalyst-free epitaxy of InAs nanowires'. In: *Journal of crystal growth* 312.8 (2010), pp. 1391–1395 (cited on page 14).

[110] M Teng Soo et al. 'Growth of catalyst-free epitaxial InAs nanowires on Si wafers using metallic masks'. In: *Nano letters* 16.7 (2016), pp. 4189–4193 (cited on page 14).

[111] Katsuhiro Tomioka et al. 'Control of InAs nanowire growth directions on Si'. In: *Nano letters* 8.10 (2008), pp. 3475–3480 (cited on page 14).

[112] Bernhard Mandl et al. 'Self-seeded, position-controlled InAs nanowire growth on Si: A growth parameter study'. In: *Journal of crystal growth* 334.1 (2011), pp. 51–56 (cited on page 14).

[113] H Jeong et al. 'Growth kinetics of silicon nanowires by platinum assisted vapour–liquid–solid mechanism'. In: *Chemical Physics Letters* 467.4-6 (2009), pp. 331–334 (cited on page 14).

[114] Alexander T Vogel et al. 'Ag-assisted CBE growth of ordered InSb nanowire arrays'. In: *Nanotechnology* 22.1 (2010), p. 015605 (cited on page 14).

[115] Jordi Arbiol et al. 'Influence of Cu as a catalyst on the properties of silicon nanowires synthesized by the vapour–solid–solid mechanism'. In: *Nanotechnology* 18.30 (2007), p. 305606 (cited on page 14).

[116] Reza R Zamani et al. 'Polarity and growth directions in Sn-seeded GaSb nanowires'. In: *Nanoscale* 9.9 (2017), pp. 3159–3168 (cited on page 14).

[117] Morgan C Putnam et al. 'Secondary ion mass spectrometry of vapor- liquid- solid grown, Au-catalyzed, Si wires'. In: *Nano letters* 8.10 (2008), pp. 3109–3113 (cited on page 15).

[118] Colin M Hessel, Andrew T Heitsch, and Brian A Korgel. 'Gold seed removal from the tips of silicon nanorods'. In: *Nano letters* 10.1 (2010), pp. 176–180 (cited on page 15).

[119] Frank Glas, Jean-Christophe Harmand, and Gilles Patriarche. 'Why does wurtzite form in nanowires of III-V zinc blende semiconductors?' In: *Physical review letters* 99.14 (2007), p. 146101 (cited on page 16).

[120] Peter Krogstrup et al. 'Impact of the liquid phase shape on the structure of III-V nanowires'. In: *Physical review letters* 106.12 (2011), p. 125505 (cited on pages 16, 18, 87).

[121] I Vurgaftman, J R Meyer, and L R Ram-Mohan. 'Band parameters for III–V compound semiconductors and their alloys'. In: *Journal of applied physics* 89.11 (2001), pp. 5815–5875 (cited on pages 16, 18).

[122] B Mattias Borg and Lars-Erik Wernersson. 'Synthesis and properties of antimonide nanowires'. In: *Nanotechnology* 24.20 (2013), p. 202001 (cited on pages 16–19).

[123] Hongzhi Chen et al. 'Infrared detection using an InSb nanowire'. In: *IEEE Nanotechnology Materials and Devices Conference*. IEEE. 2009, pp. 212–216 (cited on page 17).

[124] S Nadj-Perge et al. 'Spectroscopy of spin-orbit quantum bits in indium antimonide nanowires'. In: *Physical review letters* 108.16 (2012), p. 166801 (cited on page 17).

[125] M Shafa et al. 'Indium antimonide nanowires: synthesis and properties Nanoscale Res'. In: *Nanoscale Res. Lett.* 11 (2016), p. 164 (cited on page 17).

[126] Philippe Caroff et al. 'High-quality InAs/InSb nanowire heterostructures grown by metal–organic vapor-phase epitaxy'. In: *Small* 4.7 (2008), pp. 878–882 (cited on pages 17–20).

[127] Sébastien R Plissard et al. 'From InSb nanowires to nanocubes: looking for the sweet spot'. In: *Nano letters* 12.4 (2012), pp. 1794–1798 (cited on pages 17, 18, 79).

[128] Lorenzo Lugani et al. 'Growth mechanism of InAs–InSb heterostructured nanowires grown by chemical beam epitaxy'. In: *Journal of crystal growth* 323.1 (2011), pp. 304–306 (cited on pages 17, 18).

[129] CM Fetzer et al. 'The use of a surfactant (Sb) to induce triple period ordering in GaInP'. In: *Applied Physics Letters* 76.11 (2000), pp. 1440–1442 (cited on page 17).

[130] RR Wixom, LW Rieth, and GB Stringfellow. 'Sb and Bi surfactant effects on homo-epitaxy of GaAs on (001) patterned substrates'. In: *Journal of crystal growth* 265.3-4 (2004), pp. 367–374 (cited on page 17).

[131] P Moriarty et al. 'Sb-induced GaAs (111) B surface reconstructions: success and failure of the electron-counting rule'. In: *Surface science* 365.3 (1996), pp. L663–L668 (cited on page 18).

[132] LJ Whitman et al. 'Metallic III-V (001) surfaces: Violations of the electron counting model'. In: *Physical review letters* 79.4 (1997), p. 693 (cited on page 18).

[133] Jeffery Houze et al. 'Structure of AlSb (001) and GaSb (001) surfaces under extreme Sb-rich conditions'. In: *Physical Review B* 76.20 (2007), p. 205303 (cited on page 18).

[134] VA Nebol'Sin and AA Shchetinin. 'Role of surface energy in the vapor–liquid–solid growth of silicon'. In: *Inorganic materials* 39.9 (2003), pp. 899–903 (cited on page 18).

[135] Luna Namazi. *From understanding to realizing novel III-Sb materials via nanowires*. Lund University, 2018 (cited on page 18).

[136] Mattias Borg. *Antimonide Heterostructure Nanowires-Growth, Physics and Devices*. Lund University, 2012 (cited on pages 18, 19).

[137] Robert M Biefeld. 'The metal-organic chemical vapor deposition and properties of III–V antimony-based semiconductor materials'. In: *Materials Science and Engineering: R: Reports* 36.4 (2002), pp. 105–142 (cited on page 18).

[138] Guoqiang Zhang et al. 'Telecom-band lasing in single InP/InAs heterostructure nanowires at room temperature'. In: *Science advances* 5.2 (2019), eaat8896 (cited on page 18).

[139] Jonathan P Boulanger and Ray R LaPierre. 'Polytype formation in GaAs/GaP axial nanowire heterostructures'. In: *Journal of crystal growth* 332.1 (2011), pp. 21–26 (cited on page 18).

[140] Jonas Johansson and Kimberly A Dick. 'Recent advances in semiconductor nanowire heterostructures'. In: *CrystEngComm* 13.24 (2011), pp. 7175–7184 (cited on page 18).

[141] YN Guo et al. 'Structural characteristics of Ga Sb/ Ga As nanowire heterostructures grown by metal-organic chemical vapor deposition'. In: *Applied physics letters* 89.23 (2006), p. 231917 (cited on page 18).

[142] Kimberly A Dick. 'A review of nanowire growth promoted by alloys and non-alloying elements with emphasis on Au-assisted III–V nanowires'. In: *Progress in Crystal Growth and Characterization of Materials* 54.3-4 (2008), pp. 138–173 (cited on page 19).

[143] Luna Namazi et al. 'Realization of wurtzite GaSb using InAs nanowire templates'. In: *Advanced Functional Materials* 28.28 (2018), p. 1800512 (cited on page 20).

[144] Marıa de la Mata et al. 'Atomic scale strain relaxation in axial semiconductor III–V nanowire heterostructures'. In: *Nano Letters* 14.11 (2014), pp. 6614–6620 (cited on page 20).

[145] Sepideh Gorji Ghalamestani. *Realization of Complex III-V Nanoscale Heterostructures*. Citeseer, 2014 (cited on page 20).

[146] Philippe Caroff et al. 'InSb heterostructure nanowires: MOVPE growth under extreme lattice mismatch'. In: *Nanotechnology* 20.49 (2009), p. 495606 (cited on page 20).

[147] B Mattias Borg et al. 'Enhanced Sb incorporation in InAsSb nanowires grown by metalorganic vapor phase epitaxy'. In: *Applied Physics Letters* 98.11 (2011), p. 113104 (cited on page 20).

[148] Ilse van Weperen et al. 'Quantized conductance in an InSb nanowire'. In: *Nano letters* 13.2 (2013), pp. 387–391 (cited on pages 21, 62).

[149] Pavel Aseev et al. 'Ballistic InSb nanowires and networks via metal-sown selective area growth'. In: *Nano letters* 19.12 (2019), pp. 9102–9111 (cited on pages 21, 71).

[150] Juan Carlos Estrada Saldaña et al. 'Split-channel ballistic transport in an InSb nanowire'. In: *Nano Letters* 18.4 (2018), pp. 2282–2287 (cited on page 21).

[151] S Li et al. 'Coherent charge transport in ballistic InSb nanowire Josephson junctions'. In: *Scientific reports* 6 (2016), p. 24822 (cited on page 21).

[152] Sen Li et al. 'Ballistic transport and quantum interference in InSb nanowire devices'. In: *Chinese Physics B* 26.2 (2017), p. 027305 (cited on page 21).

[153] H Gottschalk, G Patzer, and H Alexander. 'Stacking fault energy and ionicity of cubic III–V compounds'. In: *physica status solidi (a)* 45.1 (1978), pp. 207–217 (cited on page 21).

[154] Tomoki Yamashita et al. 'Theoretical investigations on the formation of wurtzite segments in group III–V semiconductor nanowires'. In: *Applied surface science* 254.23 (2008), pp. 7668–7671 (cited on page 21).

[155] Toru Akiyama et al. 'An empirical potential approach to wurtzite–zinc-blende polytypism in group III–V semiconductor nanowires'. In: *Japanese journal of applied physics* 45.3L (2006), p. L275 (cited on pages 21, 22).

[156] Jonas Johansson et al. 'Diameter dependence of the wurtzite- zinc blende transition in InAs nanowires'. In: *The Journal of Physical Chemistry C* 114.9 (2010), pp. 3837–3842 (cited on page 22).

[157] NV Sibirev et al. 'Surface energy and crystal structure of nanowhiskers of III–V semiconductor compounds'. In: *Physics of the Solid State* 52.7 (2010), pp. 1531–1538 (cited on page 22).

[158] Sepideh Gorji Ghalamestani, Sebastian Lehmann, and Kimberly A Dick. 'Can antimonide-based nanowires form wurtzite crystal structure?' In: *Nanoscale* 8.5 (2016), pp. 2778–2786 (cited on page 22).

[159] Bernhard Mandl et al. 'Crystal structure control in Au-free self-seeded InSb wire growth'. In: *Nanotechnology* 22.14 (2011), p. 145603 (cited on page 22).

[160] Daniel Magnfält. 'Fundamental processes in thin film growth: The origin of compressive stress and the dynamics of the early growth stages'. PhD thesis. Linköping University Electronic Press, 2014 (cited on pages 23, 25–27).

[161] K Reichelt. 'Nucleation and growth of thin films'. In: *Vacuum* 38.12 (1988), pp. 1083–1099 (cited on pages 22, 24, 25).

[162] M Harsdorff. 'Heterogeneous nucleation and growth of thin films'. In: *Thin Solid Films* 90.1 (1982), pp. 1–14 (cited on page 22).

[163] DW Pashley and MJ Stowell. 'Nucleation and growth of thin films as observed in the electron microscope'. In: *Journal of Vacuum Science and Technology* 3.3 (1966), pp. 156–166 (cited on page 22).

[164] JA Venables. 'Nucleation and growth of thin films: recent progress'. In: *Vacuum* 33.10-12 (1983), pp. 701–705 (cited on page 22).

[165] Richard W Vook. 'Nucleation and growth of thin films'. In: *Optical engineering* 23.3 (1984), pp. 343–349 (cited on page 22).

[166] JA Venables. 'Nucleation and growth processes in thin film formation'. In: *Journal of Vacuum Science & Technology B: Microelectronics Processing and Phenomena* 4.4 (1986), pp. 870–873 (cited on page 22).

[167] Martin Leijnse and Karsten Flensberg. 'Introduction to topological superconductivity and Majorana fermions'. In: *Semiconductor Science and Technology* 27.12 (2012), p. 124003 (cited on pages 22, 47).

[168] Tudor D Stanescu and Sumanta Tewari. 'Majorana fermions in semiconductor nanowires: fundamentals, modeling, and experiment'. In: *Journal of Physics: Condensed Matter* 25.23 (2013), p. 233201 (cited on pages 22, 47).

[169] Grazyna Antczak and Gert Ehrlich. *Surface diffusion: metals, metal atoms, and clusters*. Cambridge University Press, 2010 (cited on page 24).

[170] T. 1961-author.(Thomas) Michely. *Islands, Mounds, and Atoms: Patterns and Processes in Crystal Growth Far from Equilibrium*. Springer. (cited on page 24).

[171] H Van Beijeren et al. 'Structure and Dynamics of Surfaces II'. In: *Topics in Current Physics*. Vol. 43. Springer Berlin, 1987 (cited on page 24).

[172] AA Koryakin, SA Kukushkin, and AV Redkov. 'Nucleation and growth mechanisms of CdTe thin films on silicon substrates with silicon carbide buffer layers.' In: *Materials Physics & Mechanics* 32.3 (2017) (cited on page 25).

[173] Zhenyu Zhang and Max G Lagally. 'Atomistic processes in the early stages of thin-film growth'. In: *Science* 276.5311 (1997), pp. 377–383 (cited on page 25).

[174] Thomas Michely and Joachim Krug. *Islands, mounds and atoms*. Vol. 42. Springer Science & Business Media, 2012 (cited on pages 25, 26).

[175] Rossitza Pentcheva et al. 'Non-Arrhenius behavior of the island density in metal heteroepitaxy: Co on Cu (001)'. In: *Physical review letters* 90.7 (2003), p. 076101 (cited on page 26).

[176] W Oswald. 'Studien uber die Bildung und Umwandlung fester Korper'. In: *Z. Phys. Chem* 22 (1897), pp. 289–330 (cited on page 26).

[177] Terry Threlfall. 'Structural and thermodynamic explanations of Ostwald's rule'. In: *Organic process research & development* 7.6 (2003), pp. 1017–1027 (cited on page 26).

[178] C Ratsch and JA Venables. 'Nucleation theory and the early stages of thin film growth'. In: *Journal of Vacuum Science & Technology A: Vacuum, Surfaces, and Films* 21.5 (2003), S96–S109 (cited on page 26).

[179] Kenjiro Oura et al. *Surface science: an introduction*. Springer Science & Business Media, 2013 (cited on page 26).

[180] Koenraad GF Janssens et al. 'Computing the mobility of grain boundaries'. In: *Nature materials* 5.2 (2006), pp. 124–127 (cited on page 27).

[181] Carl V Thompson. 'Structure evolution during processing of polycrystalline films'. In: *Annual review of materials science* 30.1 (2000), pp. 159–190 (cited on page 27).

[182] FA Nichols and WW Mullins. 'Morphological changes of a surface of revolution due to capillarity-induced surface diffusion'. In: *Journal of Applied Physics* 36.6 (1965), pp. 1826–1835 (cited on page 27).

[183] C. V Thompson, J. Floro, and H. I. Smith. 'Epitaxial grain growth in thin films'. In: *Journal of Applied Physics* 67.9 (1990), p. 4099 (cited on page 28).

[184] Joachim E Sestoft et al. 'Engineering Hybrid Epitaxial InAsSb/Al Nanowire Materials for Stronger Topological Protection'. In: *Physical Review Materials* 2 (2018), p. 044202 (cited on pages 29, 47, 51, 54).

[185] Sasa Gazibegovic et al. 'Epitaxy of advanced nanowire quantum devices'. In: *Nature* 548 (2017), p. 434 (cited on pages 29, 47, 48, 71).

[186] Jung-Hyun Kang et al. 'Robust Epitaxial Al Coating of Reclined InAs Nanowires'. In: *Nano Letters* (2017) (cited on pages 30, 71).

[187] Candice Thomas et al. 'Toward durable Al-InSb hybrid heterostructures via epitaxy of 2ML interfacial InAs screening layers'. In: *Physical Review Materials* 3.12 (2019), p. 124202 (cited on page 32).

[188] RR Dean and CJ Thwaites. 'Tinplate and Tin Coating Technology'. In: *JOM* 39.8 (1987), pp. 42–45 (cited on page 32).

[189] Man-Fai Ng and Teck L Tan. 'Unveiling stable group IV alloy nanowires via a comprehensive search and their electronic band characteristics'. In: *Nano letters* 13.10 (2013), pp. 4951–4956 (cited on page 32).

[190] Sebastian Küfner et al. 'Structural and electronic properties of α-tin nanocrystals from first principles'. In: *Physical Review B* 87.23 (2013), p. 235307 (cited on page 32).

[191] Sebastian Küfner et al. 'Optical absorption and emission of α-Sn nanocrystals from first principles'. In: *Nanotechnology* 24.40 (2013), p. 405702 (cited on page 32).

[192] Harvey Black. *Getting the lead out of electronics*. 2005 (cited on page 32).

[193] Nicolas G Hörmann, Axel Gross, and Payam Kaghazchi. 'Semiconductor–metal transition induced by nanoscale stabilization'. In: *Physical Chemistry Chemical Physics* 17.8 (2015), pp. 5569–5573 (cited on pages 32, 33).

[194] Zhengyuan Tu et al. 'Fast ion transport at solid–solid interfaces in hybrid battery anodes'. In: *Nature Energy* 3.4 (2018), pp. 310–316 (cited on page 32).

[195] Cai-Zhi Xu et al. 'Elemental topological Dirac semimetal: α-Sn on InSb (111)'. In: *Physical review letters* 118.14 (2017), p. 146402 (cited on pages 32, 33).

[196] Yoshiyuki Ohtsubo et al. 'Dirac cone with helical spin polarization in ultrathin α-Sn (001) films'. In: *Physical review letters* 111.21 (2013), p. 216401 (cited on pages 32, 33).

[197] GA Busch and R Kebn. 'Semiconducting properties of gray tin'. In: *Solid State Physics*. Vol. 11. Elsevier, 1960, pp. 1–40 (cited on pages 32, 33).

[198] AW Ewald and ON Tufte. 'Gray tin single crystals'. In: *Journal of Applied Physics* 29.7 (1958), pp. 1007–1009 (cited on pages 32, 33).

[199] Steven Groves and William Paul. 'Band structure of gray tin'. In: *Physical Review Letters* 11.5 (1963), p. 194 (cited on pages 32, 33).

[200] RFC Farrow et al. 'The growth of metastable, heteroepitaxial films of α-Sn by metal beam epitaxy'. In: *Journal of Crystal Growth* 54.3 (1981), pp. 507–518 (cited on pages 32, 33).

[201] Fleur Legrain and Sergei Manzhos. 'Understanding the difference in cohesive energies between alpha and beta tin in DFT calculations'. In: *AIP Advances* 6.4 (2016), p. 045116 (cited on pages 32, 33).

[202] I Didschuns et al. 'Superconductivity in Sn films on InSb (110) taking account of the film morphology and structure'. In: *Physica C: Superconductivity* 377.1-2 (2002), pp. 89–95 (cited on pages 32, 33, 41).

[203] Alexandr Mikhailovich Molodets and Sergei Sergeevich Nabatov. 'Thermodynamic potentials, diagram of state, and phase transitions of tin on shock compression'. In: *High Temperature* 38.5 (2000), pp. 715–721 (cited on pages 32, 33).

[204] Reginald W Smith. 'The α (semiconductor) ag β (metal) transition in tin'. In: *Journal of the Less Common Metals* 114.1 (1985), pp. 69–80 (cited on pages 32, 33).

[205] Huanhuan Song et al. 'Thermal stability enhancement in epitaxial alpha tin films by strain engineering'. In: *Advanced Engineering Materials* 21.10 (2019), p. 1900410 (cited on page 33).

[206] N Oehl et al. 'Critical size for the β-to α-transformation in tin nanoparticles after lithium insertion and extraction'. In: *CrystEngComm* 17.19 (2015), pp. 3695–3700 (cited on page 33).

[207] Harmut Höchst and Isaac Hernández Calderón. 'Microscopic electronic structure and growth mode of Sn/InSb (111) interfaces'. In: *Journal of Vacuum Science & Technology A: Vacuum, Surfaces, and Films* 3.3 (1985), pp. 911–914 (cited on page 33).

[208] Elena Magnano et al. 'Growth morphology and electronic properties of Sn deposited on different InSb surfaces'. In: *Surface science* 433 (1999), pp. 387–391 (cited on page 33).

[209] Kelly Houben et al. 'In situ study of the α-Sn to β-Sn phase transition in low-dimensional systems: Phonon behavior and thermodynamic properties'. In: *Phys. Rev. B* 100 (7 Aug. 2019), p. 075408 (cited on page 37).

[210] Lucas Casparis et al. 'Superconducting gatemon qubit based on a proximitized two-dimensional electron gas'. In: *Nature Nanotechnology* 13.10 (2018), pp. 915–919 (cited on page 47).

[211] T. W. Larsen et al. 'Semiconductor-nanowire-based superconducting qubit'. In: *Physical Review Letters* 115.12 (2015), p. 127001 (cited on pages 47, 56).

[212] Torsten Karzig et al. 'Scalable designs for quasiparticle-poisoning-protected topological quantum computation with Majorana zero modes'. In: *Physical Review B* 95.23 (2017), p. 235305 (cited on page 47).

[213] Chetan Nayak et al. 'Non-Abelian anyons and topological quantum computation'. In: *Reviews of Modern Physics* 80.3 (2008), p. 1083 (cited on page 47).

[214] David Aasen et al. 'Milestones toward Majorana-based quantum computing'. In: *Physical Review X* 6.3 (2016), p. 031016 (cited on page 47).

[215] Filip Krizek et al. 'Field effect enhancement in buffered quantum nanowire networks'. In: *Physical Review. Materials* 2 (2018), p. 093401 (cited on page 47).

[216] Stephen T Gill et al. 'Selective-area superconductor epitaxy to ballistic semiconductor nanowires'. In: *Nano Letters* 18.10 (2018), pp. 6121–6128 (cited on page 47).

[217] Chun-Xiao Liu, Jay D. Sau, and S. Das Sarma. 'Distinguishing topological Majorana bound states from trivial Andreev bound states: Proposed tests through differential tunneling conductance spectroscopy'. In: *Physical Review B* 97 (2018), p. 214502 (cited on page 47).

[218] Eduardo JH Lee et al. 'Spin-resolved Andreev levels and parity crossings in hybrid superconductor–semiconductor nanostructures'. In: *Nature Nanotechnology* 9 (2014), p. 79 (cited on page 47).

[219] Haining Pan and S. Das Sarma. 'Zero-bias conductance peaks in Majorana nanowires: the good, the bad, and the ugly'. In: *arXiv:1910.11413* (2019) (cited on page 47).

[220] S. M. Albrecht et al. 'Exponential protection of zero modes in Majorana islands'. In: *Nature* 531 (2016), pp. 206–210 (cited on page 47).

[221] Fabrizio Nichele et al. 'Scaling of Majorana zero-bias conductance peaks'. In: *Physical Review Letters* 119 (2017), p. 136803 (cited on page 47).

[222] Dan. Dalacu et al. 'Droplet dynamics in controlled InAs nanowire interconnections'. In: *Nano Letters* 13 (2013), p. 2676 (cited on pages 48, 59, 83, 86, 87).

[223] P. Caroff et al. 'High-quality InAs/InSb nanowire heterostructures grown by metal–organic vapor-phase epitaxy'. In: *Small* 4 (2008), pp. 878–882 (cited on page 50).

[224] Georg W. Winkler et al. 'Topological Phases in $InAs_{1-x}Sb_x$: From Novel Topological Semimetal to Majorana Wire'. In: *Physical Review Letters* 117 (7 Aug. 2016), p. 076403 (cited on page 51).

[225] Heidi Potts et al. 'From twinning to pure zincblende catalyst-free InAs (Sb) nanowires'. In: *Nano Letters* 16.1 (2016), pp. 637–643 (cited on page 51).

[226] Lars Vegard. 'Die konstitution der mischkristalle und die raumfüllung der atome'. In: *Zeitschrift für Physik* 5.1 (1921), pp. 17–26 (cited on page 51).

[227] Sven Marian Albrecht et al. 'Exponential protection of zero modes in Majorana islands'. In: *Nature* 531.7593 (2016), pp. 206–209 (cited on page 56).

[228] Sergej Schuwalow et al. 'Band bending profile and band offset extraction at semiconductor-metal interfaces'. In: *arXiv preprint arXiv:1910.02735* (2019) (cited on page 61).

[229] Yong-Joo Doh et al. 'Tunable supercurrent through semiconductor nanowires'. In: *science* 309.5732 (2005), pp. 272–275 (cited on pages 63, 64).

[230] Hervé Courtois et al. 'Origin of hysteresis in a proximity Josephson junction'. In: *Physical Review Letters* 101.6 (2008), p. 067002 (cited on page 63).

[231] IO Kulik and AN Omel'Yanchuk. 'Properties of superconducting microbridges in the pure limit'. In: *Sov. J. Low Temp. Phys.(Engl. Transl.);(United States)* 3.7 (1977) (cited on page 63).

[232] Jie Xiang et al. 'Ge/Si nanowire mesoscopic Josephson junctions'. In: *Nature Nanotechnology* 1.3 (2006), p. 208 (cited on page 63).

[233] HA Nilsson et al. 'Supercurrent and multiple Andreev reflections in an InSb nanowire Josephson junction'. In: *Nano Letters* 12.1 (2012), pp. 228–233 (cited on page 63).

[234] Kaveh Gharavi et al. 'Nb/InAs nanowire proximity junctions from Josephson to quantum dot regimes'. In: *Nanotechnology* 28.8 (2017), p. 085202 (cited on page 63).

[235] Filip Krizek et al. 'Field Effect Enhancement in Buffered Quantum Nanowire Networks'. In: *Physical Review Materials* 2.9 (2018), p. 093401 (cited on pages 66, 71, 72).

[236] Martin Friedl et al. 'Template-Assisted Scalable Nanowire Networks'. In: *Nano Lett.* 18.4 (2018), pp. 2666–2671 (cited on pages 66, 71).

[237] Peter Schüffelgen et al. 'Selective area growth and stencil lithography for in situ fabricated quantum devices'. In: *Nature Nanotechnology* 14.9 (2019), pp. 825–831 (cited on page 66).

[238] Seyoung Kim et al. 'Realization of a High Mobility Dual-Gated Graphene Field-Effect Transistor with Al_2O_3 Dielectric'. In: *Appl. Phys. Lett.* 94.6 (2009), p. 062107 (cited on page 70).

[239] Önder Gül et al. 'Towards high mobility InSb nanowire devices'. In: *Nanotechnology* 26.21 (2015), p. 215202 (cited on page 70).

[240] Hua Zhong et al. 'Comparison of Mobility Extraction Methods Based on Field-Effect Measurements for Graphene'. In: *AIP Advances* 5.5 (2015), p. 057136 (cited on page 70).

[241] Olaf Wunnicke. 'Gate Capacitance of Back-Gated Nanowire Field-Effect Transistors'. In: *Appl. Phys. Lett.* 89.8 (2006), p. 083102 (cited on page 70).

[242] Jason Alicea et al. 'Non-Abelian statistics and topological quantum information processing in 1D wire networks'. In: *Nature Physics* 7.5 (2011), pp. 412–417 (cited on page 71).

[243] Sankar Das Sarma, Michael Freedman, and Chetan Nayak. 'Majorana zero modes and topological quantum computation'. In: *npj Quantum Information* 1.1 (2015), pp. 1–13 (cited on pages 71, 99).

[244] Z-Y Xue. 'Detecting non-Abelian statistics of Majorana fermions in quantum nanowire networks'. In: *JETP letters* 94.3 (2011), p. 213 (cited on pages 71, 99).

[245] Fenner Harper, Aakash Pushp, and Rahul Roy. 'Majorana braiding in realistic nanowire Y-junctions and tuning forks'. In: *Physical Review Research* 1.3 (2019), p. 033207 (cited on page 71).

[246] Xiong-Jun Liu, Chris LM Wong, and Kam Tuen Law. 'Non-abelian majorana doublets in time-reversal-invariant topological superconductors'. In: *Physical Review X* 4.2 (2014), p. 021018 (cited on page 71).

[247] Sébastien R Plissard et al. 'Formation and electronic properties of InSb nanocrosses'. In: *Nature Nanotechnology* 8.11 (2013), p. 859 (cited on pages 71, 74, 100).

[248] Natalia Pankratova et al. 'Multiterminal Josephson Effect'. In: *Physical Review X* 10.3 (2020), p. 031051 (cited on page 71).

[249] Roman-Pascal Riwar et al. 'Multi-terminal Josephson junctions as topological matter'. In: *Nature communications* 7.1 (2016), pp. 1–5 (cited on page 71).

[250] P Samuelsson et al. 'Nonequilibrium Josephson effect in mesoscopic ballistic multiterminal SNS junctions'. In: *Physical Review B* 62.2 (2000), p. 1319 (cited on page 71).

[251] A Zazunov et al. 'Josephson effect in multiterminal topological junctions'. In: *Physical Review B* 96.2 (2017), p. 024516 (cited on page 71).

[252] Lukas Hofstetter et al. 'Cooper pair splitter realized in a two-quantum-dot Y-junction'. In: *Nature* 461.7266 (2009), pp. 960–963 (cited on page 71).

[253] Anindya Das et al. 'High-efficiency Cooper pair splitting demonstrated by two-particle conductance resonance and positive noise cross-correlation'. In: *Nature communications* 3.1 (2012), pp. 1–6 (cited on page 71).

[254] Chuanwei Cheng and Hong Jin Fan. 'Branched nanowires: synthesis and energy applications'. In: *Nano Today* 7.4 (2012), pp. 327–343 (cited on page 71).

[255] Matthew J Bierman and Song Jin. 'Potential applications of hierarchical branching nanowires in solar energy conversion'. In: *Energy & Environmental Science* 2.10 (2009), pp. 1050–1059 (cited on page 71).

[256] Xiaocheng Jiang et al. 'Rational growth of branched nanowire heterostructures with synthetically encoded properties and function'. In: *Proceedings of the National Academy of Sciences* 108.30 (2011), pp. 12212–12216 (cited on page 71).

[257] Bozhi Tian et al. 'Macroporous nanowire nanoelectronic scaffolds for synthetic tissues'. In: *Nature materials* 11.11 (2012), pp. 986–994 (cited on page 71).

[258] Torsten Rieger et al. 'Crystal phase transformation in self-assembled InAs nanowire junctions on patterned Si substrates'. In: *Nano letters* 16.3 (2016), pp. 1933–1941 (cited on pages 71, 86, 87).

[259] Diana Car et al. 'Rationally designed single-crystalline nanowire networks'. In: *Advanced Materials* 26.28 (2014), pp. 4875–4879 (cited on pages 71, 86).

[260] Jung-Hyun Kang et al. 'Crystal structure and transport in merged InAs nanowires MBE grown on (001) InAs'. In: *Nano Letters* 13.11 (2013), pp. 5190–5196 (cited on pages 71, 86–89).

[261] Jung-Hyun Kang et al. 'Wurtzite/Zinc-Blende 'K'-shape InAs Nanowires with Embedded Two-Dimensional Wurtzite Plates'. In: *Nano letters* 17.1 (2017), pp. 531–537 (cited on pages 71, 86, 87, 89, 90).

[262] Johannes Gooth et al. 'Ballistic one-dimensional InAs nanowire cross-junction interconnects'. In: *Nano Letters* 17.4 (2017), pp. 2596–2602 (cited on page 71).

[263] Pavel Aseev et al. 'Selectivity map for molecular beam epitaxy of advanced III–V quantum nanowire networks'. In: *Nano letters* 19.1 (2018), pp. 218–227 (cited on page 71).

[264] Roy LM Op het Veld et al. 'In-plane selective area InSb–Al nanowire quantum networks'. In: *Communications Physics* 3.1 (2020), pp. 1–7 (cited on page 71).

[265] Lucas Güniat, Philippe Caroff, and Anna Fontcuberta i Morral. 'Vapor phase growth of semiconductor nanowires: key developments and open questions'. In: *Chemical reviews* 119.15 (2019), pp. 8958–8971 (cited on page 71).

[266] Chen Zhang et al. 'A review of III–V planar nanowire arrays: selective lateral VLS epitaxy and 3D transistors'. In: *Journal of Physics D: Applied Physics* 50.39 (2017), p. 393001 (cited on page 71).

[267] Seth A Fortuna and Xiuling Li. 'Metal-catalyzed semiconductor nanowires: a review on the control of growth directions'. In: *Semiconductor Science and Technology* 25.2 (2010), p. 024005 (cited on page 71).

[268] Hyun D Park and SM Prokes. 'Study of nanowire growth mechanisms: VLS and Si assisted'. In: *One-Dimensional Nanostructures*. Springer, 2008, pp. 1–15 (cited on page 71).

[269] SJ Pearton. 'Reactive ion etching of III–V semiconductors'. In: *International Journal of Modern Physics B* 8.14 (1994), pp. 1781–1876 (cited on page 72).

[270] Dan Dalacu et al. 'Selective-area vapour–liquid–solid growth of InP nanowires'. In: *Nanotechnology* 20.39 (2009), p. 395602 (cited on page 82).

[271] Dan Dalacu et al. 'Selective-area vapor-liquid-solid growth of tunable InAsP quantum dots in nanowires'. In: *Applied Physics Letters* 98.25 (2011), p. 251101 (cited on page 82).

[272] Dong Pan et al. 'Free-standing two-dimensional single-crystalline InSb nanosheets'. In: *Nano letters* 16.2 (2016), pp. 834–841 (cited on page 83).

[273] Marıa De La Mata et al. 'Twin-induced InSb nanosails: a convenient high mobility quantum system'. In: *Nano letters* 16.2 (2016), pp. 825–833 (cited on page 83).

[274] Isha Verma et al. 'Morphology control of single-crystal InSb nanostructures by tuning the growth parameters'. In: *Nanotechnology* (2020) (cited on page 83).

[275] Sasa Gazibegovic et al. 'Bottom-Up Grown 2D InSb Nanostructures'. In: *Advanced Materials* 31.14 (2019), p. 1808181 (cited on page 83).

[276] Jing Jin et al. 'Coalescence processes of droplets and liquid marbles'. In: *Micromachines* 8.11 (2017), p. 336 (cited on page 85).

[277] Bozhi Tian et al. 'Single-crystalline kinked semiconductor nanowire superstructures'. In: *Nature nanotechnology* 4.12 (2009), pp. 824–829 (cited on page 86).

[278] Martin Aagesen et al. 'Molecular beam epitaxy growth of free-standing plane-parallel InAs nanoplates'. In: *Nature nanotechnology* 2.12 (2007), pp. 761–764 (cited on page 86).

[279] Sebastian Heedt et al. 'Electronic Properties of Complex Self-Assembled InAs Nanowire Networks'. In: *Advanced Electronic Materials* 2.6 (2016), p. 1500460 (cited on page 86).

[280] Sonia Conesa-Boj et al. 'Vertical "III–V" V-Shaped Nanomembranes Epitaxially Grown on a Patterned Si [001] Substrate and Their Enhanced Light Scattering'. In: *ACS nano* 6.12 (2012), pp. 10982–10991 (cited on page 86).

[281] Yanming Wang, Tomáš Šikola, and Miroslav Kolıbal. 'Collector Droplet Behavior during Formation of Nanowire Junctions'. In: *The Journal of Physical Chemistry Letters* 11.16 (2020), pp. 6498–6504 (cited on page 87).

[282] He Zheng et al. 'Dynamic process of phase transition from wurtzite to zinc blende structure in InAs nanowires'. In: *Nano letters* 13.12 (2013), pp. 6023–6027 (cited on page 90).

[283] DB Lee. 'Anisotropic etching of silicon'. In: *Journal of Applied physics* 40.11 (1969), pp. 4569–4574 (cited on page 93).

[284] Qian Gao et al. 'Simultaneous selective-area and vapor–liquid–solid growth of InP nanowire arrays'. In: *Nano letters* 16.7 (2016), pp. 4361–4367 (cited on page 95).

[285] Peter Krogstrup et al. *Network of nanostructures as grown on a substrate*. US Patent 10,669,647. 2020 (cited on page 100).